May 2025
RESULTS
REPORT 1

Lower Buzzards Bay Sedimentation & Gooseberry Causeway Impact Study; Westport River Inlet and East Beach

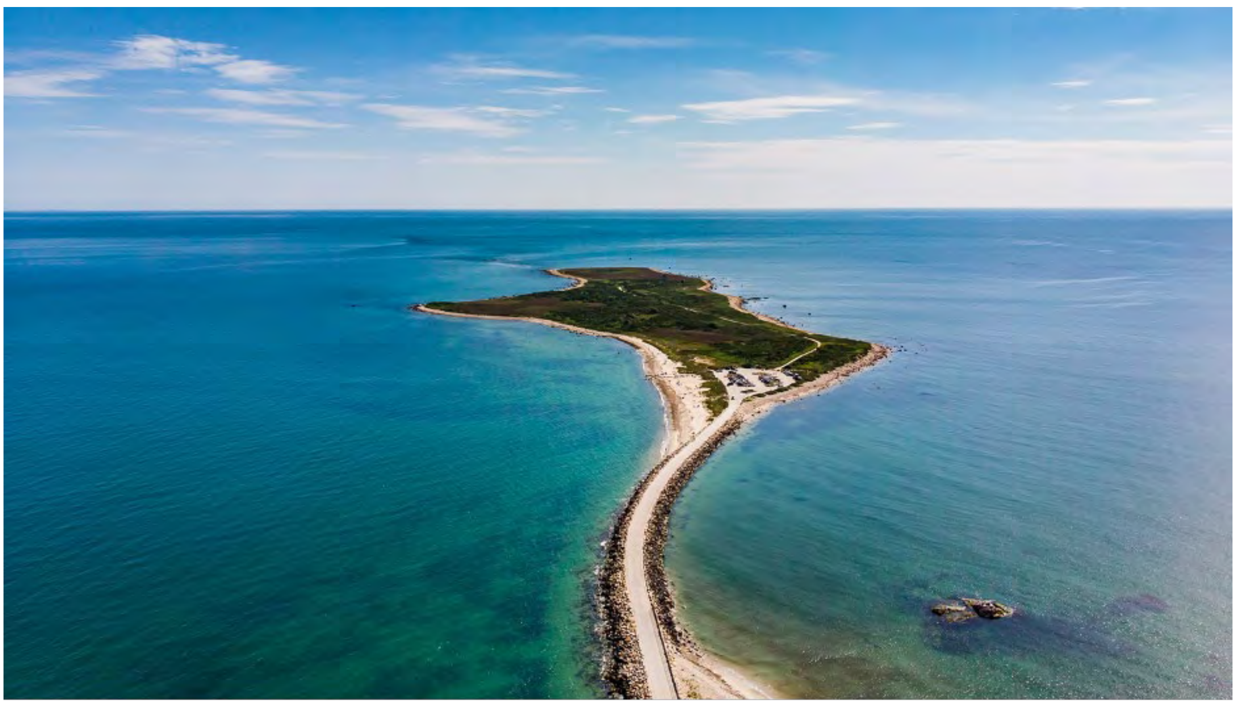

Zoe Hughes[1], Duncan FitzGerald[1], Sergio Fagherazzi[1], Tansir Asik[1], Danghan Xie[2], Silke Tas[3], Christopher Hein[4], Anna van Dongon[4] and Matt Shultz[5].

[1]Boston University; [2]Scripps Institute of Oceanography; [3]Wageningen University and Research; [4]Virginia Institute of Marine Science; [5]Woods Hole Group.

1 Executive Summary

The primary goals of this project are to assess coastal resilience along the shorelines of Westport and Dartmouth, considering the impact of human structures and climate change on water circulation and sediment transport patterns. This includes identifying any direct impacts of Gooseberry Neck Causeway on nearby coastlines and environments. We collected extensive field data, allowing us to develop numerical models to determine rates of sediment transport and the connectivity of beach units along the shoreline. This approach has been used to assess how the present system functions including the impact of the Causeway, as well as examining potential for change in the future with changing climate.

Primary findings include insights into the natural water and sediment circulation patterns along Horseneck, East and Little Beaches as well as the volumes of sediment that move between areas under fair weather and storm conditions. Specific findings include:

1.1 Postglacial Sediment Movement

Sedimentary and geophysical data along with geomorphological mapping reveal that sediments transported offshore during postglacial low-water periods (~10-13 K years ago) have been reworked and migrated onshore with rising sea levels over time scales ranging from hundreds to thousands of years. This process has led to the formation of Horesneck beach and other barriers, and the infilling of bays that, today, we think of as static features. However, as sea level rise continues or accelerates, this evolutionary trend is expected to continue with beaches gradually retreating towards the mainland, squeezing and filling in the bays that exist in their lee.

1.2 Westport River Inlet

- **Causeway Influence:** The Gooseberry Causeway has negligible effects on water circulation at the Westport River mouth, with consistent circulation patterns regardless of its presence.
- **Sediment Transport:** Anti-clockwise circulation west of Gooseberry Island drives sediment transport from east to west along Horseneck Beach, promoting the accretion of the spit at the barrier island's western end (the east side of the inlet). Tidal flow, however, limits substantial sand accumulation and spit extension into the inlet, despite occasional need for navigational dredging inside the inlet.
- **Tidal Prism Impact:** The tidal prism, which governs water flushing, is unaffected by the storm-induced anti-clockwise circulation created in the bay outside the inlet by Gooseberry Neck. Thus, Gooseberry Neck Island exerts little influence on water quality inside the Westport Rivers.

1.3 East Beach

- **Causeway Influence:** The Gooseberry Causeway does not accelerate erosion at East Beach. Natural, storm processes are the primary drivers of erosion. The model indicated that in the absence of a causeway there would not have been sufficient sediment contributed to East Beach to have maintained a sandy beach, nor would recovery to a sandy beach be possible if the causeway was removed now.
- **Sediment Dynamics:** During major storms, the absence of a causeway would allow minor sediment transport from Horseneck Beach to East beach across the tombolo. This flux of sediment would be minor compared to overall easterly transport of sediment towards Allens Pond, and in light of sea level rise, the depletion or disconnection of the beach to offshore sand reservoirs.

1.4 *Climate* Change and Sea Level Rise

- **Future Sediment Movement:** Rising sea levels will shift circulation cells closer to the shore, intensifying erosion and sediment transport. Conversely, if storms intensify, stronger storm-driven currents will move offshore, which could mediate the increase in coastal erosion.
- **Causeway Influence:** The Gooseberry Causeway has a minimal impact on sediment transport under sea level rise. Coastal morphology (i.e., the presence of Gooseberry Island), rather than the causeway, shapes observed water and sediment circulation patterns.
- **Marsh Accretion:** Salt marsh accretion rates will lag behind sea level rise. As marshes become submerged, the tidal prism will expand, increasing open water areas, exchange, and size of inlet openings.

TABLE OF CONTENTS

2 List of Figures

3 List of Tables

4 Introduction

4.1 Background and motivation

The Buzzards Bay Coalition, the Towns of Westport and Dartmouth, and local residents are concerned with overall coastal resilience, including the impacts of human structures and climate change on water circulation and sedimentation patterns. Particular interest lies in the direct impacts of the Gooseberry Neck Causeway on nearby coastlines and environments (Figure 1). This includes specific outcomes such as erosion along East Beach, and potential barrier breaching into the Let, spit dynamics along Allens Pond, and shoaling at the mouth to Slocums River. More general issues include receding shorelines, decreasing tidal exchange between bays and the coastal ocean, degrading marshes, and harbor shoaling. These concerns have led to a series of scientific questions that include a focus on the Gooseberry Neck Causeway and its effects on coastal processes and the resulting shoreline trends and water circulation patterns in the area between and adjacent to the Westport and Slocums Rivers (Figure 2).

Figure 1. Locations of sites of interest in study region from the Westport Inlet to Mishaum Point.

The area considered in this study stretches along the Westport-South Dartmouth shoreline from the Westport Inlet to Mishaum Point, which is the eastern boundary of Slocums

Embayment (Figure 1). This is a complex shoreline comprising three tidal inlets (Westport Rivers, Allens Pond and Slocums River) and four distinct beach areas (Horseneck Beach, East Beach, Little Beach and Slocums Embayment), separated by headlands (Gooseberry Neck and Barney Joy's Head). The direct connectivity between Horseneck Beach and East Beach was interrupted by the construction of a causeway to Gooseberry Neck Island in the 1940s, and the connectivity of Little Beach and Allens Pond with the embayment containing Slocums River Inlet is uncertain. As such, these subregions could be considered as individual coastal cells, however, event-driven sediment transport potentially pushes pulses of sediment across tidal inlets, along beaches, and past headlands/islands. Understanding the contemporary issues along the shoreline and determining potential action to improve resilience is of increasing concern in the face of a changing climate. Our primary aim has been, therefore, to improve the understanding of the transport patterns along the shore, including how the morphological units interact, the conditions required for sediment to move between sections of shoreline and how human modifications continue to influence shoreline evolution.

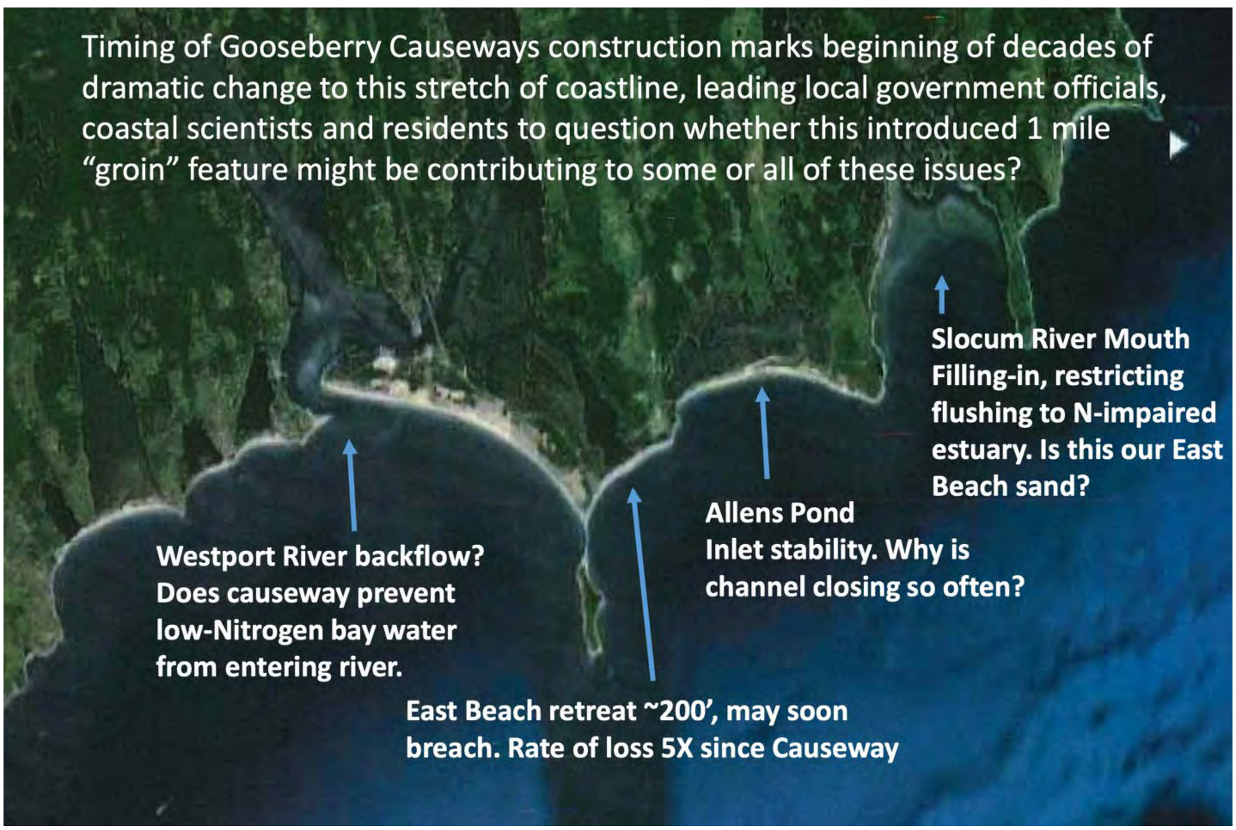

Figure 2. Aerial view of the project area and brief description of the questions and major issues that are being addressed in this study.

To more readily understand local shoreline change, specific project components and related objectives were defined:

4.2 Specific objectives

This project was centered around several environmental issues that collectively may be linked to changes in wave energy, nearshore circulation, and sediment transport potentially resulting from hardening of the causeway linking Horseneck Beach to Gooseberry Island (Figure 1). These form the basis for individual objectives:

1. Westport River Estuary- We will assess the possibility that the Gooseberry Causeway has disrupted nearshore currents and tidal exchange between the estuary and coastal ocean at Westport Inlet. Obstruction of flow could be linked to increased residence times of nutrients/fecal coliforms and reducing overall water quality. Fluxes of sediment and nutrients will also impact salt marsh, and so there is concern about the sustainability of the wetlands and of how tidal exchange is influencing net sand transport into and out of the Westport Inlet.

2. East Beach- The stretch of shore immediately east of the Causeway is sediment starved, and the once sandy beach has been transformed into a steep cobble beach. During major storms, sediment is transported across East Beach Road building washover fans onto the adjacent marsh. This process represents a permanent loss of sediment from the beach system resulting in erosion and shoreline retreat and thus, a narrowing of the land available for summer resident use. As the barrier narrows, there is concern that a major storm will cut a channel across East Beach opening the Let. We will assess this concern and investigate potential links to the Causeway and determine whether it inhibits the movement of sand from west to east thereby inhibiting sand nourishment to East Beach.

3. Climate Change- The warming of Earth is ultimately causing an acceleration in the rate of sea-level rise (SLR) as well as increased storminess. Climate models tell us that warmer ocean waters are increasing the magnitude and frequency of tropical storms. In addition, these models indicate that there will be a tendency of tropical storms (including hurricanes) to track up the East Coast and the forward velocity of these will slow down. Collectively, we can expect greater storm impacts in the future leading to increased sediment transport and probable shoreline erosion. Moreover, the sustainability of marshes is in jeopardy due to their inability to keep pace with SLR. A major question is can we predict how the project area will be impacted by Climate Change?

5 Approach and methods

The Westport-South Dartmouth coastline is a complex, integrated system. It includes multiple tidal inlets, mixed-sediment beaches, headlands, a tombolo system and extensive human development. The complex morphology of the system means that event-driven sediment transport is very important in translating pulses of sediment across tidal inlets, along beaches, and past headlands/islands. This occurs because storm surges create deeper water at the shore, allowing larger storm waves to break in these areas. Greater wave energy means that wave-driven sand transport occurs at exponentially higher rates than under normal conditions. In addition, regions normally controlled by tidal currents become dominated by wave-driven sediment transport. Examining the impact of high-energy events and assessing the magnitude of the storms that produce transport between different zones is, therefore, critical for understanding the long-term evolution of the shoreline.

Addressing our objectives and predicting existing and future sedimentation patterns along this section of coast requires a study that couples observations with numerical modeling. Modeling allows us to replicate the hydrodynamic and sediment-transport conditions on a scale large enough to answer our questions, at a level of detail that could not be accomplished through observation alone and including conditions that rarely occur or are hard to observe (e.g., large storms). Developing a model that covers this broad section of coast provides us with a tool to study existing flow conditions and also enables us to project into the future to examine higher sea level conditions, as well as the short-term impacts of major storms.

For a numerical model to provide meaningful results, it needs to be well-tested and grounded in real data. For this reason, we have undertaken extensive research collating previous studies to determine the present understanding of the system, obtained the highest quality existing data, and supplemented where existing data were sparse by conducting a rigorous field campaign (Figure 3). Data acquisition was designed to:

1) provide inputs to the modeling effort (bathymetric data, sediment data, water levels, wind and current measurements),
2) calibrate and test the model, and
3) obtain an understanding of the longer-term geomorphology of the region and the dominant hydrodynamic and sedimentation processes.

Data were assessed geospatially using Geographic Information System (GIS) techniques; this allows us to view spatial patterns but has also allowed analysis of historical images and elevation data to determine rates of change and to calculate the volumes of sand removed or gained in certain critical zones.

Modeling a large area or 'domain' (such as the white rectangle in Figure 1) allows the necessary connectivity between coastal cells and has the benefit of allowing us to address all of our scientific questions using a single grid. However, this also requires a coarser resolution than needed to obtain realistic answers for some of our questions. The modeling solution has therefore included higher resolution grids be developed and 'nested' within the larger domain. These smaller models use the larger grid to provide some input along their boundaries but require their own inputs and calibration. Nested models have been used to look in detail at the areas around the Causeway, Westport Inlet, Allens Pond Inlet, and Slocums River Embayment.

Details of each step of the study are documented below, providing a breakdown of the specific tasks required to answer the questions driving this research.

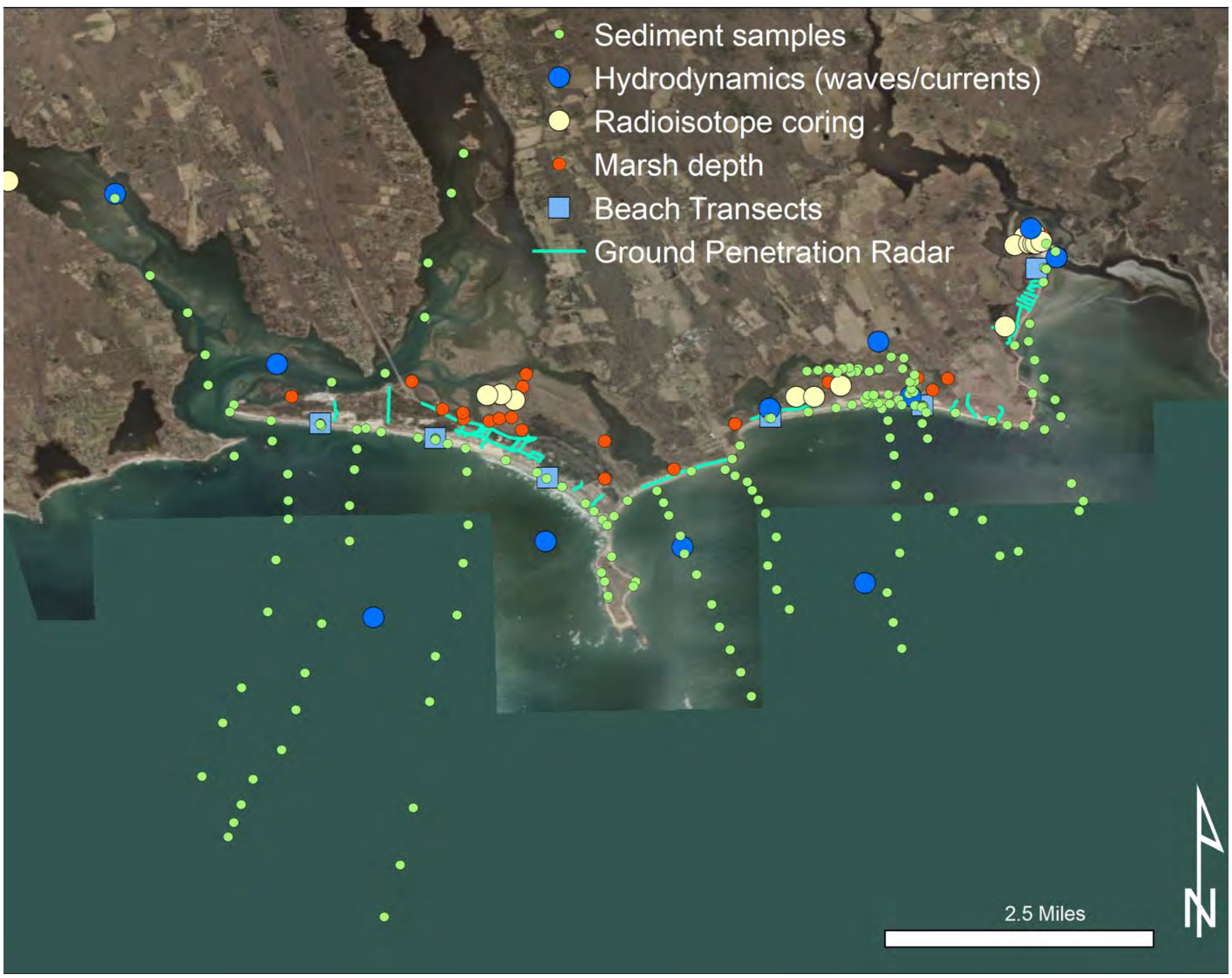

Figure 3. Data collected during Project Years 1 and 2 provided input for the numerical models and allowed us to develop further understanding of how the system originally evolved.

5.1 Data acquisition

5.1.1 Geologic framework and exogenous data sets.

In addition to fieldwork, we interrogated existing literature to obtain geologic information concerning the sedimentology, geomorphology, and glacial geology of the region. For example, acquiring sediment data from onshore and offshore surficial maps which document the types and distribution of sedimentary deposits in the project area. This information helps to inform the modeling (e.g., how deep should a sand bank be?) but has also provided an understanding of sediment reservoirs and paleo-pathways of sediment transport and deposition. This provides the research and model with broader context and allows a more complete interpretation of observations. In addition to geologic context, many of the data sets that we have used were acquired from government agencies including aerial photography, bathymetry, LiDAR, river discharges, sediment maps and model boundary drivers such as tides, winds and waves. Details are provided in the relevant sections.

5.1.2 Field and lab observations and analyses

As described below, a variety of field and laboratory data have been collected both in support of the modeling effort, as well as to provide insight into active processes responsible for modern and historical coastal change.

5.1.2.1 Historical aerial image and volume change analyses

To assess changes in coastal geomorphology, we made use of remotely sensed data including time series of aerial and satellite images and LiDAR (high resolution laser backscatter data providing elevation). Time series analyses concentrated on three regions, which represent different sediment reservoirs: 1) West Horseneck Beach - Westport River Inlet, deltas and intertidal flats, 2) Allens Pond Inlet, and 3) Slocums River Inlet. We obtained images from USGS Earth Explorer and Google Earth, and LiDAR data were downloaded from the National Center for Environmental Information (NCEI). Details of the available dates of data are provided in Table 1. Images were georeferenced to provide a time series of planform change from 1938 to the present. These changes were assessed for cyclic and interlinked behavior and for net erosional-depositional changes. Time series of aerial images provide important information concerning the planform evolution of the system. However, to quantify volumes of sediment in certain sectors of the study area, and create topographic and bathymetric inputs for the model, we also made use of high resolution topographic and LiDAR surveys (Table 1, Figure 4).

Table 1. Images and LiDAR data obtained for historical analyses.

Year	Data Type	Source
1938	Aerial Photograph	USGS
1961	Aerial Photograph	USGS
1974	Aerial Photograph	USGS
1995	Aerial Photograph	USGS
2003	Aerial Photograph	USGS
2006	Aerial Photograph	USGS
2012	Aerial Photograph	USGS
2013	Aerial Photograph	USGS
2021	Aerial Photograph	USGS
2005	LiDAR	NCEI
2006	LiDAR	NCEI
2007	LiDAR	NCEI
2010	LiDAR	NCEI
2012	LiDAR	NCEI
2013	LiDAR	NCEI
2015	LiDAR	NCEI
2018	LiDAR	NCEI

Some of the LiDAR DEM (Digital Elevation Model) did not include subaqueous data, although they were taken around low tide to include as much as possible of the intertidal zone and covered different areas (Figure 4). Therefore, care was taken to allow consistent comparison with these older data sets, the lowest elevation that was included in all LIDAR DEM comparisons was -0.4 m NAVD88 (MLW is -0.58 m NAVD88, NOAA, 2023). The LIDAR data sets were also corrected for differences in the Geoid used for processing the raw data. This was done using the parking lot in Demarest Lloyd State Park as a georeferenced plane to correct the data to the same reference elevation (Figure 5). Care was also taken when using the Continuously Updated Digital Elevation Model (CUDEM) as, although it combines the most recent LiDAR and hydrographic data, the latter may be decades (or greater) old. As a consequence, we employed bathymetric data, collected by the team at Woods Hole Group, to confirm the reliability of the Westport Inlet and offshore depth data and were able to correct the CUDEM where needed. However, Figure 6 illustrates that, over the majority of the domain, the bathymetry from the CUDEM showed remarkable similarity to the field data, with the 30 % of the differences falling in the +/- 0.2 m range and a standard deviation of 0.48 m. This suggests that for much of the comparison, the difference between the data sets falls within the uncertainty expected in either data set due to factors such as waves during data collection, error, vegetation impacting LiDAR or acoustic signals during measurement or the impact of binning and gridding the data at the compared resolution (~ 3m horizontal spacing). The key areas with larger differences were located, as would be expected, in areas within bays or channels, particularly in the vicinity of the ebb and flood tidal deltas that form close to inlets. Bathymetric updates were made where necessary.

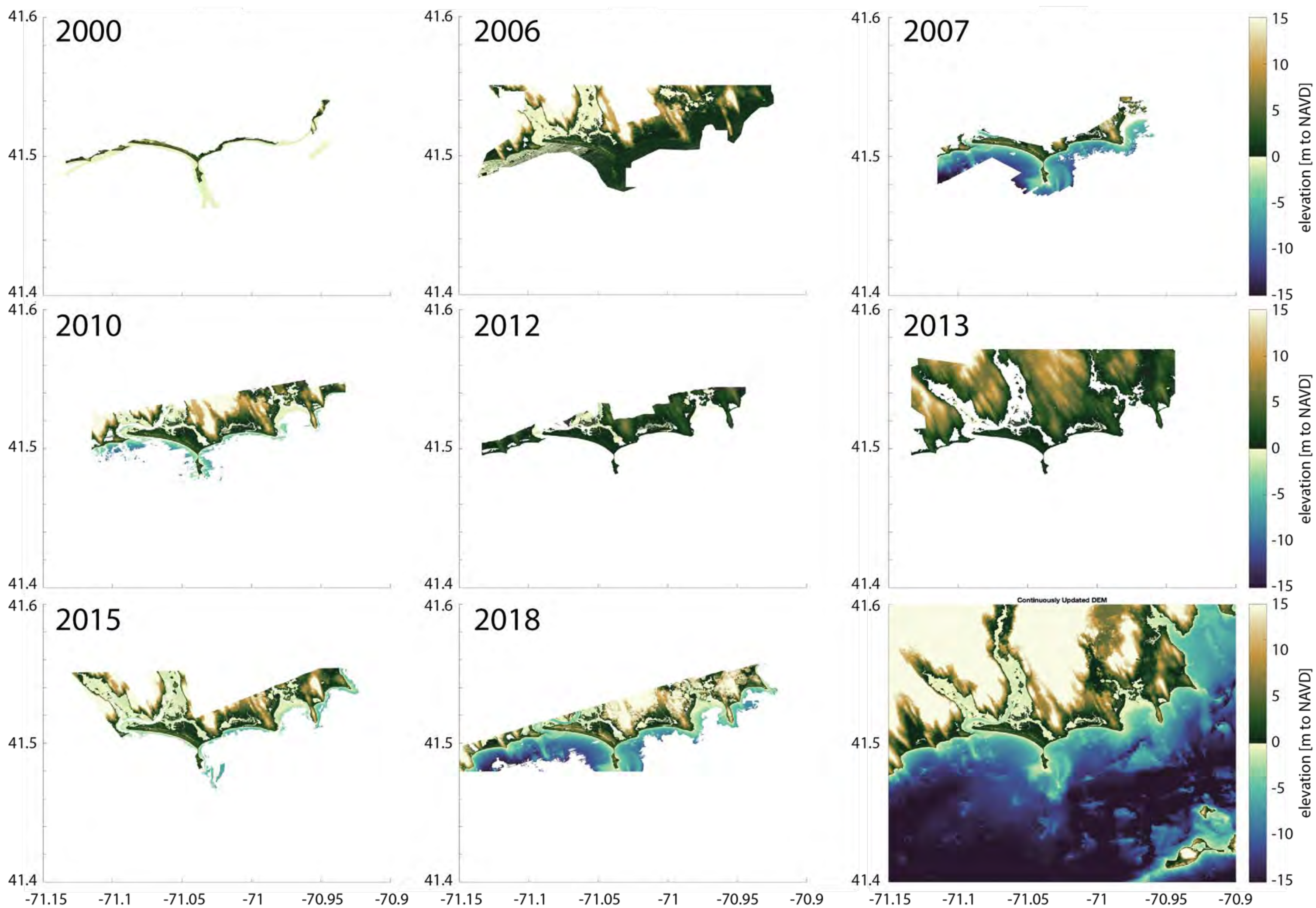

Figure 4. Coverage of the available LiDAR data for the lower Buzzards Bay area and the Constantly Updated DEM used for the model (in the bottom right panel), all plotted with the same color axis. Some data sets include the shallow water data others cover only subaerial regions. Comparisons were made using data sets where the sub-aqueous data were available. The CUDEM uses LiDAR data combined with the most recently available hydrographic data.

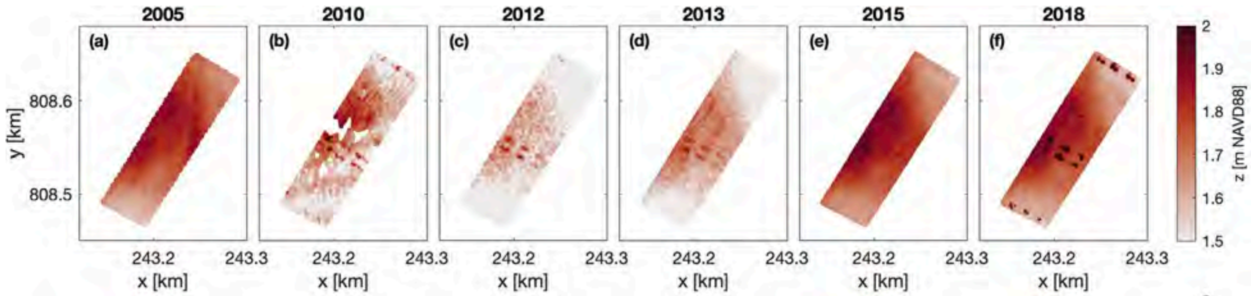

Figure 5. Example correction from Demarest Lloyd State Park parking lot (a-f). Parking lot elevation before geoid correction.

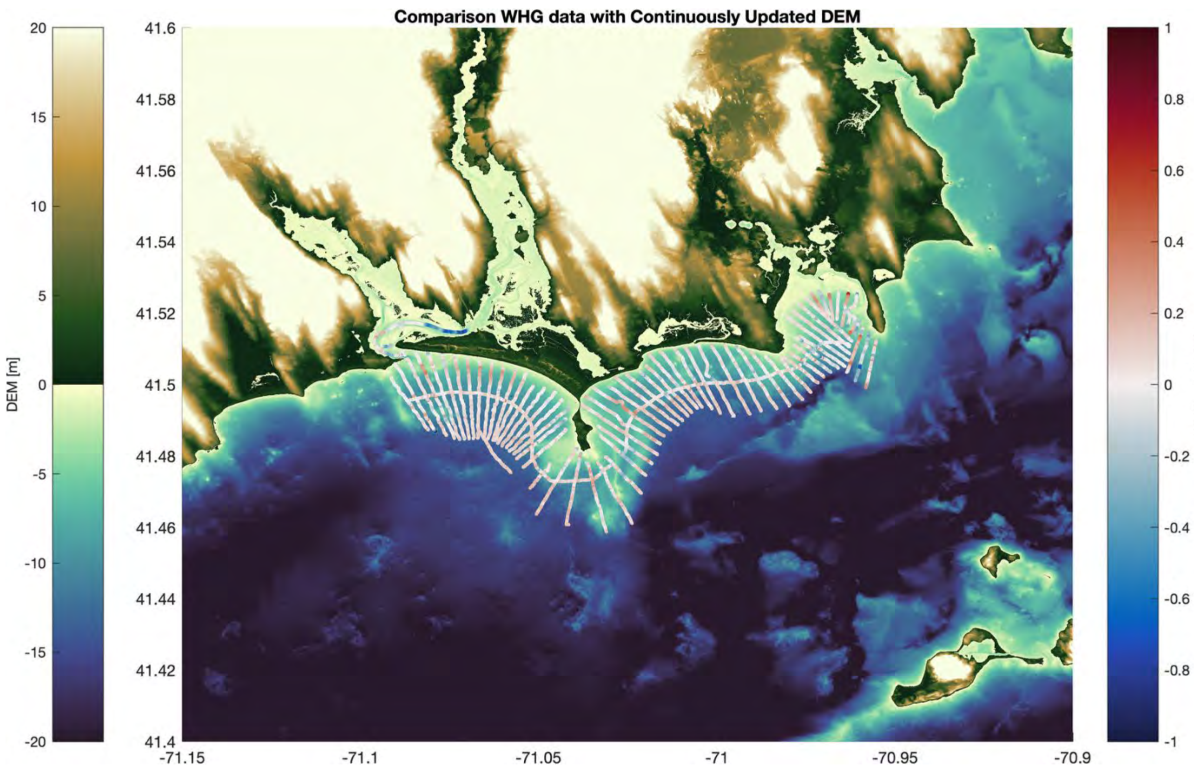

Figure 6. A comparison of the CUDEM and the bathymetric data collected in the field. The lines on the plot represent the vessel track lines during collection (illustration coverage) and the color represents the difference between the field data and the CUDEM. Spatially. the colors are dominated by white (0 difference) and light colors (within =+/- 0.2 m from zero), with dark areas with differences over +/-0.5 m only occurring close to the edge of the ebb tidal deltas outside of Westport or Slocums inlets – regions were a large amount of variability and change would be expected.

5.1.2.2 Mapping

After an examination of the project shoreline during Year 1, we observed a heterogeneous and highly variable shore that has been impacted by storms, human structures, dredging, stabilization efforts, and additional human modifications. It was apparent that to fully understand the complexity of the study area and be able to model the various coastal cells, it would be necessary to map the project shoreline from Acoaxet Point to Slocums River Embayment. This entailed walking the entire exposed ocean shoreline, taking precise waypoints using GPS (global positioning systems), photographs, and gathering sediment samples to characterize different beach environments. We recorded beach morphology (i.e., width and slope) and dune morphology (size and extent, eroding scarps, paleo-scarps), presence of prograding beach ridges, sediment composition, human structures, bedrock and till exposures, gravel beaches, wetland type (i.e., salt marsh, isolated freshwater pond, etc.), and Piping Plover and Least Tern nesting areas.

This information was then transferred from detailed field notes and instruments into Geographic Information System (GIS) software. At this point the data were further augmented with details interpreted from high-resolution vertical aerial photographs (i.e., features that could not be observed in the field). The field data were integrated over a series of aerial photographs. These data have been used to create a geodatabase and can be opened by end users in GIS software. The data can then be displayed directly on the photographs including photographs and text explaining the character of the shoreline as well as unique features or processes (i.e., bedforms, dune blow-outs); these can be used to generate outreach posters to disseminate information and findings.

5.1.2.3 Sediment characterization

To predict and quantify sediment movement along coast during day-to-day conditions as well as during extratropical cyclones and major hurricanes, it was necessary to collect grain-size data along the beaches and in the nearshore. This was one of the major tasks in the geomorphic-sedimentologic mapping of shore. Over 200 sediment samples were collected throughout the study region. A series were collected along the shoreline concurrently with site mapping. Locations of the samples taken throughout the study area are shown on Figure 3. To determine whether sand was moving from the beaches through the inlets and into the bays we undertook sampling in inner channels and shoals. Finally, to better understand the potential for cross-shore transport (sand exchange between beaches and offshore), particularly during major storms, we collected bed samples offshore of Horseneck, East and Little Beaches (Figure 3, Figure 7). Onshore, samples of ~100-200g were collected by hand from the beach surface, bagged and returned to the lab for analysis. Offshore samples were collected using a ponar grab (Figure 7). Successful grabs that returned sediment were emptied into sample bags and returned to the lab for analysis.

Figure 7. A). View of Ponar Grab sampler after being lifted to the surface. Note that the apparatus is closed, B). Grab being opened to retrieve sand sampled, C). Example sample in labeled sample bag.

Dry sand samples from the supratidal beach and dunes were analyzed directly. Samples obtained from underwater environments that were stored in a refrigerator were washed with fresh water to remove salt and to break up clusters of sediments that could affect the subsequent granulometric analyses. All samples (after washing for submerged ones, same day of collection for subaerial) were placed in a drying oven, a procedure lasting one to several days at a temperature of 60 °C (140 °F).

A granulometric analysis of the sediment was performed using a mechanical sieving method (RO-TAP sieve shaker; Figure 8) that consists of a nested sieved that collected increasingly smaller grain sizes toward the bottom of the stack. The Ro-tap was run for approximately 10 minutes using a mesh size ranging from ϕ[1]= 0.0 to ϕ = 4.0 (corresponding from coarse sand to coarse silt). The sediment fraction captured in each sieve and the catcher pan at the bottom of the stack was transferred to individual beakers and weighed on a digital scale. Lastly, the samples were placed into their original bag and stored as a permanent record.

Figure 8. View of Ro-tap with nested brass sieves.

Granulometric analysis allows statistical characterization of the sand samples, which can be used to determine the origin and sediment transport trends or potential. We have applied the Folk and Ward (1957) classification method to determine the following sedimentological and statistical characterization of the sample population[2]:

- **Mean**: the average grain-size. It is calculated as follows:

$$Mean\ \varphi = (\varphi 16 + \varphi 50 + \varphi 84)/3 \qquad (1)$$

---

[1] Where φ is $-\log_2(d)$, d=grain diameter in mm.

[2] Modified from Professor C. Rigsby, East Carolina University

where 16, 50, and 84 represent the size at 16, 50, and 84 percent of the sample by weight. Mean is measured in phi units and is the most widely compared parameter.

- **Median** (D_{50}): corresponds to the 50th percentile on a cumulative curve. It shows that half of the sample population is larger, and half is smaller than the D_{50}.
- **Sorting**: is a method of measuring the grain-size variation of a sample by encompassing the largest parts of the size distribution as measured from a cumulative curve. Folk (1968) presented a verbal classification scale for sorting: very well sorted, moderately well sorted, moderately sorted, poorly sorted, very poorly sorted.
- **Skewness:** it measures the degree to which a cumulative curve approaches symmetry. Two samples may have the same average grain size and sorting but may be quite different in their degree of symmetry. Symmetrical curves have a skewness equal to 0.00; those with a large proportion of fine material are positively skewed and those with a relatively large proportion of coarse material are negatively skewed.
- **Kurtosis**: is a measure of "peakedness" of a curve. Kurtosis of 1.00 is a curve with the sorting in the tails equal to the sorting in the central portion (mesokurtic). If a sample curve is better sorted in the central part than in the tails, the curve is said to be excessively peaked, or leptokurtic. If the sample curve is better sorted in the tails than in the central portion, the curve is flat peaked or platykurtic.

Statistical analyses have been calculated using a combination of MATLAB and Excel. The analyses have contributed to determining sediment transport trends and provide input parameters for the hydrodynamic and sediment transport modeling.

5.1.2.4 Radioisotopic dating

The future sustainability of marsh within the Westport River Estuary and behind Allens Pond Spit is largely dependent on the ability of the marshes to accrete vertically at a rate apace with accelerated SLR. Determination of marsh accretion rates during the past 50–100 years as well as the relative contributions of organic matter and mineral sediment to that accretion allows for estimation of the likely threshold rates of SLR that these marshes can withstand. Moreover, these accretion rates provide a key input for projecting the extent of marshes in future-looking model runs. The accretion rate dictates the areal extent of marshes versus the open-water area of the bay and controls the volume of the tide needed to fill the bays with the rising tide. This is called the tidal prism, and this volume dictates the velocity that ebb, and flood currents move through tidal inlets and thus contributes to hydrodynamics and sediment-transport trends (e.g., the balance of storm waves and tidal flows, sand input versus export and beach barrier width).

We collected twelve, 25-cm diameter sediment cores, each 60–80 cm long, at the lower reaches of the Westport Rivers (Figure 3). Long-term marsh accretion rates were determined from cores through down-core radioisotopic lead and cesium (^{210}Pb, ^{137}Cs) dating. These short-lived radionuclides have a strong affinity for soil and sediment particles, making them suitable tracers in saltmarsh environments (i.e., Kemp et al 2012; Corbett and Walsh 2015). ^{210}Pb is a naturally occurring radioactive nuclide element that is constantly replenished at the Earth's surface and, once buried (for example in saltmarsh peats) begins to decay at a known rate of 22.2 years, allowing for estimation of time since burial. ^{137}Cs is a product of atmospheric thermonuclear testing that occurred during the mid-1940s to mid-1970s, and was deposited across Earth's surface, peaking in concentration in the 1963–1964 period.

Cores were fully described and photographed in the field and sectioned (2-cm depth intervals from the surface to 30 cm, followed by 5-cm depth intervals from 30 to 55 cm; total of 20 samples per core). In the laboratory aliquots of each sample were extracted and analyzed for organic content (loss-on-ignition) and bulk density. Remaining samples were dried, homogenized, packed into petri dishes, wax-sealed, and analyzed for ^{210}Pb and ^{137}Cs contents using a suite of LeGe and BeGe gamma detectors at the VIMS Radioisotope Lab. After conducting a down-core analysis of concentrations of radioisotopic ^{137}Cs and excess ^{210}Pb, soil bulk density, and loss-on-ignition (LOI), we calculated multi-decadal accretion rates and changes in the organic-matter composition of the marshes through time. ^{210}Pb-based accretion rates (covering an estimated 60–100-year period) were calculated based on the constant-flux-constant-supply (CFCS) method (Appleby 2001; Corbett and Walsh 2015).

Values of accretion excess (AE_c), a dimensionless measure of marsh vertical accretion rate normalized by the sea-level rise rate contemporaneous with the accretion period, were calculated to assess the relative "health" of the marsh; that is, whether the marsh was accreting at a rate that kept pace with sea-level rise (i.e., if $AE_c \geq 1.0$) or was losing vertical resilience over the measured timeframe $AE_c < 1.0$).

5.1.2.5 Marsh Peat Cores

In addition to the cores for radioisotopic dating, a network of twenty-six, 2 cm-radius, Dutch auger cores was taken in the marshes behind Horseneck and East Beach (Figure 9). The purpose of these cores was to determine thickness of the peat and depth to the underlying substrate, which in most cases is sand. In protected coastal environments, marsh grass will begin colonization when the tidal flat builds to an elevation of approximately mean sea level and thus we can use the Engelhart and Horton (2012) sea-level curve (Figure 9) to approximate the age of marsh formation. These data provide a framework for understanding barrier evolution in this region and help us project how this system will respond in a regime of accelerating sea-level rise.

Figure 9. A.) Location of the Dutch auger cores used to determine depth to the sand substrate. B.) Sea-level curve for southeastern Massachusetts (from Engelhart and Horton, 2012) allowing us to determine an approximate age for a certain depth below the surface, allowing peat thicknesses to be translated to age. Note that over the last 1000 years (1 ka BP), sea level rose ~1 m, meaning sea level rise has been ~1 mm/yr.

Real Time Kinematic Differential GPS surveys

Real Time Kinematics DGPS (RTK) is a survey tool used to obtain an accurate location of the coring sites and a highly accurate elevation of the sites (+/- 2 cm). To evaluate the response of the marsh platform to various forcings and determine how these factors may affect vertical growth rates, it is vitally important to know where the cores were collected and their exact elevation. In addition to providing RTK data for marsh coring sites, measurements were also taken throughout the study area to augment the LIDAR and bathymetric data input for implementing the hydrodynamic modeling runs.

5.1.2.6 Beach morphology and dynamics

Beach profiling.

In the first year of the project, in advance of fall and winter storms that typically cause erosion of the beach, scarping of the dunes, and overwashing, we set up six beach profile stations, with three (#4, 5 and 6) recording change along Horseneck beach (Figure 10, Table 2). These sites were revisited a total of 4 times during the project, most notably before and after significant storms in January 2023. We also took photographs to document compositional changes to the beach. The profiles were evenly spaced along Horseneck Beach (Figure 10). A detailed description of the profiles is provided in Appendix A.

Figure 10. Beach profile sites across the entire study site. Sites, 4, 5 and 6 were set up to characterize erosion on Horesneck beach.

Table 2. Coordinates for the Beach Profile Stations (see accompanying map above)

ID	Location	Latitude	Longitude
Site 4	East Side Horseneck Beach	41.50222	-71.04681
Site 5	Central Horseneck Beach	41.50751	-71.06203
Site 6	West Side Horseneck Beach	41.5094	-71.07762

We used the Emery Beach Profile methodology because it is expedient and produces quantitative information and reproducible results. The profile stations consist of two metal fence posts, semi-permanently positioned in the dunes. The two stakes are aligned perpendicular to the trend of the beach and provide a means of resurveying the profile along the same traverse.

Ground-penetrating radar

To provide needed information about the development of the system and the thickness of sand units (i.e., beach, barrier and dune systems) to inform the modeling we employed Ground-Penetrating Radar (GPR). GPR is a technique that provides an X-ray view of the sedimentary layers beneath the ground surface. These data complimented the extensive data collection throughout the system. The transects collected along Horseneck beach are shown in Figure 11.

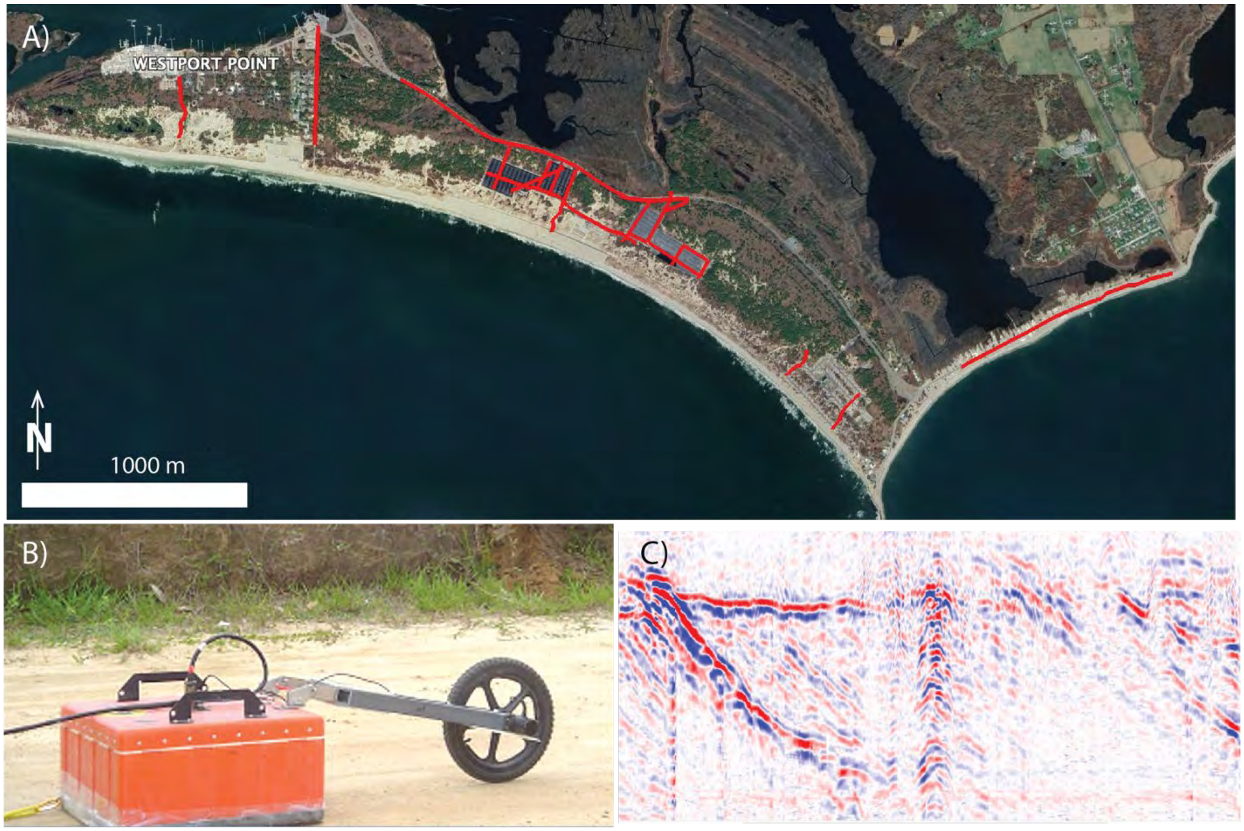

Figure 11. A) GPR transects collected in Westport running either shore parallel or cross-shore allow a detailed understanding of how the barrier developed, how thick the sand lens might be and provide details of former tidal inlet openings in the barrier. B). View of the GPR transceiver (orange box) and wheel assembly. The wheel turns to initiate the transceiver and collection of data. C). In the cross-shore record above, the blue and red dipping lines indicate beach progradation as sediment was being deposited along the shoreline. Each reflector represents a former position of the beach and foreshore.

The transceiver (orange box, Figure 11 B) is dragged along the ground surface usually consisting of fields, pathways, or paved roadways. The character and orientation of the radar reflectors (Figure 11 C) can be interpreted as to the type of sedimentary processes responsible for their formation. For example, we used this instrument to study beach and dune progradation along the Horseneck Beach and to identify a previous inlet location. This information can help us to understand how the barrier developed and how much sand is contained in this sand reservoir.

5.1.2.7 Hydrodynamic data collection

A series of instrument deployments in the offshore and backbarrier provided insights into the water level, wave and tidal conditions across the study areas. These data have been used as calibration input data for the modeling, as well as informing our understanding of the hydrodynamics and sediment transport within this complex system.

Simultaneous deployments were made at 12 locations in the study domain between October 2022 and January 2023 (Figure 12), of which 7 focused on the Westport region, however all of the instruments were considered in the calibration of the largest model domain. Westport deployments included two water level sensors (Onset Hobos) recording at 5 second intervals throughout the deployment, one was paired with a conductivity monitor to assess salinity variability in backbarrier (and indicator of water quality). These instruments measured tidal water level and temperature. An acoustic current meters, also measuring water depth and temperature but additionally measuring water velocity, was deployed close to the mouths of Westport Rivers. Two RBR water level-wave sensors were deployed either side of the Gooseberry Causeway close to shore in conjunction with a deployment by Woods Hole Group of two more acoustic current meters, recording waves, currents and water levels.

Once retrieved, data were downloaded from the instruments in the labs at BU and Woods Hole, examined for issues, and water surface data were post processed to provide wave and tide characteristics throughout the deployment. Of the twelve instruments most recorded adequately (Table 3), a water level sensor and salinity meter in Westport River and the RBR on the west side of the inlet were lost (moved or taken from their deployment sites) and one instrument in Allens Pond did not record successfully for the entire period of the deployment. The current meter in Westport inlet did not provide full velocity data, despite providing water level data. A further deployment was made to supplement the missing velocity data where needed.

Table 3. Instrument deployment details.

ID	Variables recorded	Position	Latitude	Longitude	Start	End	Note
WL7	d	West Branch	41.54041	-71.10536	10/4/22 20:00	12/5/22 8:43	
WL3	d, ppt	East Branch	41.54598	-71.05813	10/4/22 20:00		Lost
WNP	d, u	Westport channel	41.517396	-71.083514	10/7/22 20:00	11/22/22 11:49	
BUN1	d, u	Westport channel	41.531808	-70.978257	10/4/22 20:00	10/7/22 17:30	d only
RBR1	d, H	East Gooseberry	41.4927082	-71.02878	10/7/22 20:00	11/22/22 0:00	
RBR2	d, H	West Gooseberry	41.493469	-71.047245	10/7/22 20:00		Lost
WHG1	d, H, u	East Gooseberry	41.487821	-71.004132	10/6/22 16:00	1/11/23 14:08	
WHG2	d, H, u	West Gooseberry	41.483214	-71.070477	10/6/22 16:00	1/11/23 16:00	Partial loss

d = water depth, H = wave data, u = water velocity, ppt = salinity

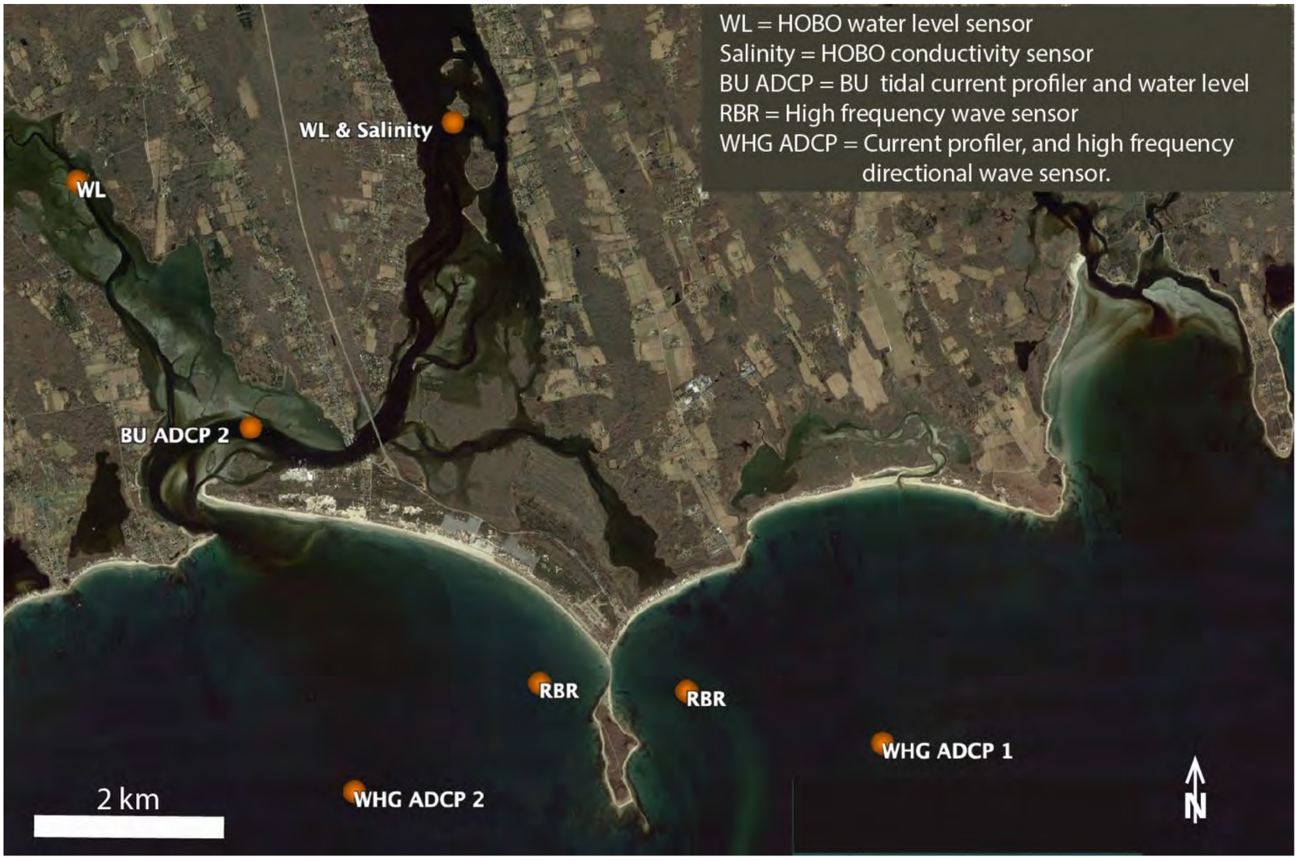

Figure 12. Location of instruments deployed within the project area measuring water levels (tides), waves, and currents.

The sensors provided sufficient synchronous data across the Westport River system, Allens Pond, and Slocums River Embayment to provide a good characterization of the hydrodynamics. Further, several high energy events were recorded (including a storm over the 8-15th November 2022 and Winter Storm Elliot in December 2022). Together, the data provide information about the wave and flow regime and have been used to test and train the models. In addition to the calibration data, we have been able to assess local shallow water waves on both sides of the Causeway using high-frequency measurements, providing direct observational data concerning the influence that Gooseberry Neck has on the nearshore wave climate.

5.1.2.8 Bathymetric surveys

One of the important input parameters for initializing hydrodynamic models is bathymetry (depth), because it controls shoaling of the tidal wave, wave refraction, geometry of tidal channels, and strength and direction of tidal currents. Ultimately, all these physical factors determine sediment transport trends and surge levels during storms. For intertidal areas we use LIDAR surveys, which have a high degree of accuracy and resolution. Although NOAA (National Oceanic Atmospheric Administration) publishes nautical charts for some of the project areas, this bathymetry is often too coarse scale for detailed modeling, or in the case of tidal inlets, the bathymetry has changed because of growth of shoals, shifting channels, or dredging activity. Consequently, Woods Hole Group collected supplementary highly accurate bathymetry throughout the offshore and within the lower portions of the estuaries (Figure 13). These single beam data allowed us to improve the digital elevation model (DEM) that was used to interpolate the bathymetry across the modelled domain (see also Figure 6). These data were collected in late Fall 2023.

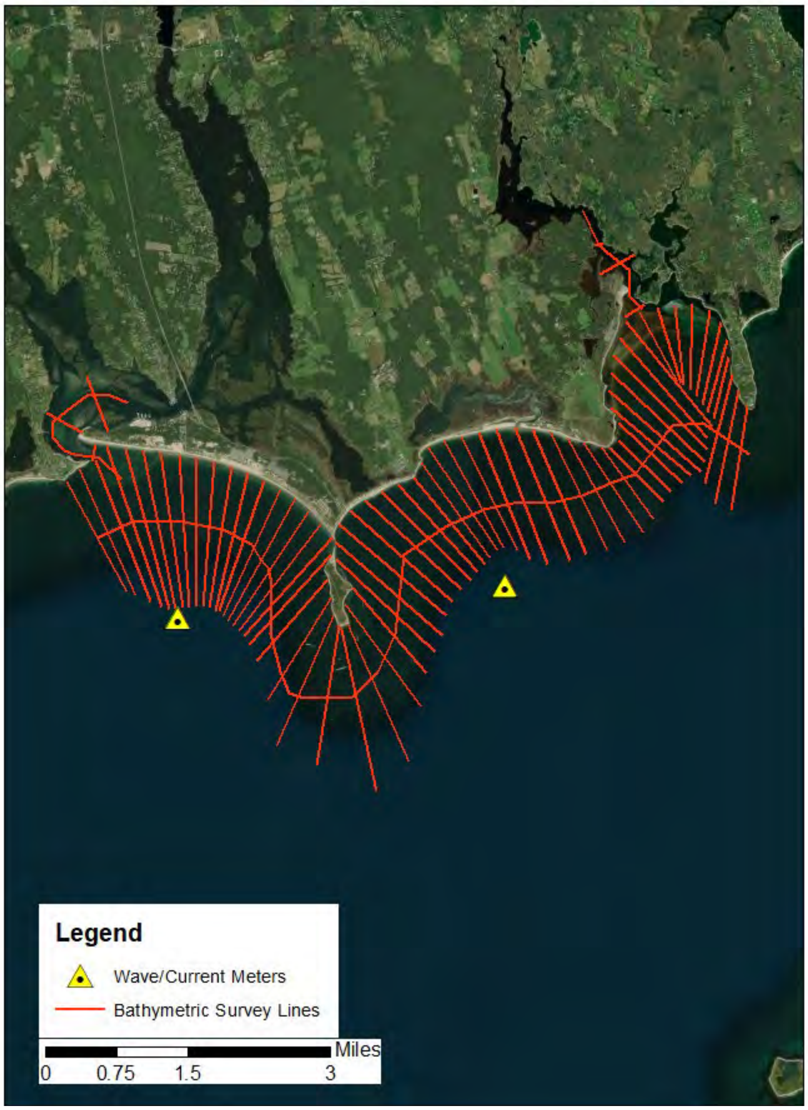

Figure 13. Single beam transects conducted by Wood Hole Group.

5.2 Modeling

Modeling has been undertaken using the Delft3D model (Lesser et al., 2004), which simulates currents from tides and meteorology (Delft3D-FLOW) and waves (Delft3D-WAVE) in concert, allowing us to simulate complex interactions of waves and currents at high resolution. Delft3D-FLOW solves the unsteady shallow water equations (Lesser et al., 2004) and Delft3D-WAVE uses the third-generation numerical wave model SWAN (Booij et al., 1999). These models (FLOW and WAVE) are coupled, feeding information back and forth as they run. Delft3D has been successfully used for sediment transport simulations around headlands (Vieira da Silva et al., 2016; McCarroll et al., 2018; George et al., 2019). Model boundary conditions are derived from the North Atlantic Coast Comprehensive Study (NACCS), a coastal storm wave and water level modelling study of the US North Atlantic coast. Delft3D is considered a top-performing model and reliable when well calibrated. The model also provides estimates of sediment transport, including how erosion and deposition change the bed level. The sediment module also allowed us to assess the source of sediment as it passes set assessment points (in this case, the position of the causeway or Barney's Joy Point). Five model domains were developed to allow us to include offshore conditions and larger scale circulations in the regional model, but to focus down to a high resolution in areas of interest such as the causeway. Figure 14 shows the large wave (dashed black) and current (black) domains of the regional model and the 4 nested grids (in color).

This report will discuss results from the following 3 modeling domains:

1) A large regional grid (comprising an extensive wave grid and a smaller grid to model the tides, thus allowing stable generation of wave-current conditions in the area of interest). Near the shoreline and island, this grid resolution was 40 m by 40 m, gradually extending to 40 m by 80 m at the southern seaward and northern landward boundaries in the cross-shore direction.
2) A high-resolution model of the Causeway (10 m resolution)
3) A high-resolution model of Westport Inlet (20 m resolution).

The southern boundary of the WAVE domain is located offshore to avoid strong bed level gradients at the boundary, as well as to avoid any sheltering effects of the nearby islands. Its exact position was chosen close to an output point of a calibration point (discussed below). The lateral boundaries of the WAVE domain were chosen in order to limit boundary effects and wave shadow zones in the region of interest. Grid cell size varies from 80 m near the boundaries to 40 m in the region of interest. The FLOW domain was extended far enough to the south to capture the flow into and out of Buzzards Bay. The lateral boundaries extend slightly beyond the region of interest, and the northern boundary allows for the inclusion of a reasonable tidal prism inside the Westport Rivers. The model was run to provide depth-averaged values for variables, e.g., velocity or suspended sediment.

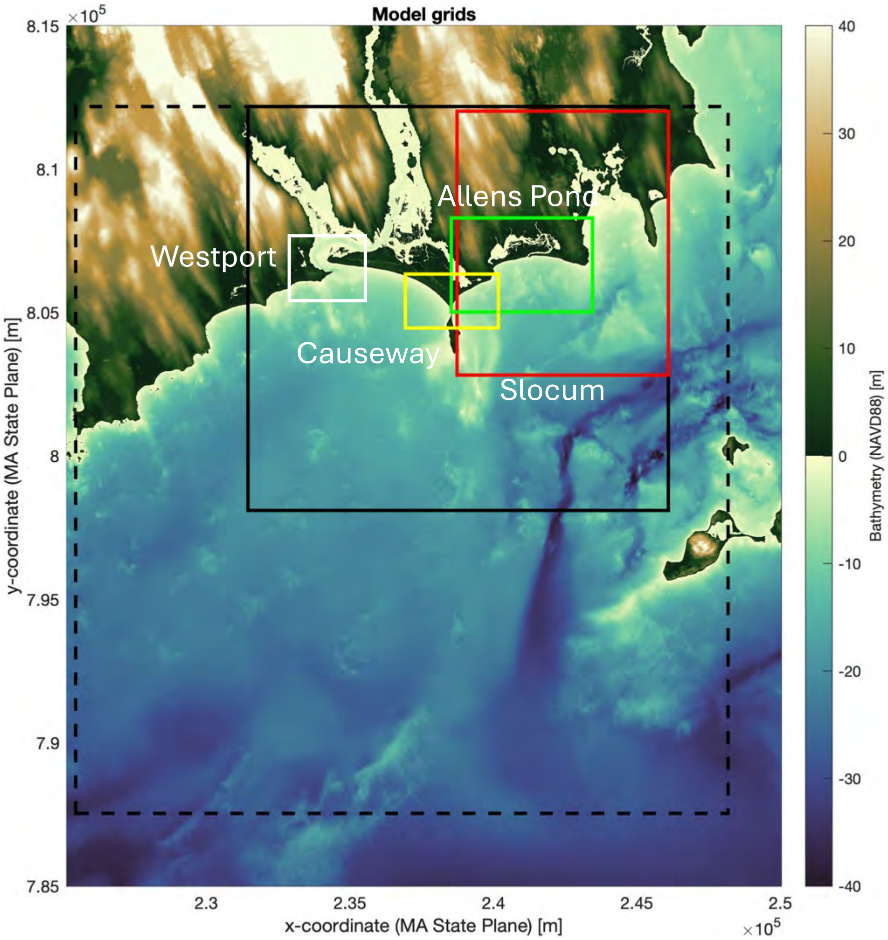

Figure 14. The Regional wave (dashed) and flow grids are shown in black; the causeway grid is shown in yellow, and Westport grid is shown here in white. Also shown here are the Allens Pond grid in green and the Slocums grid shown in red which will be the subject of Report 2.

5.2.1 Model inputs

Bathymetry data for all of the models is based on the Continuously Updated Digital Elevation Model (Cooperative Institute for Research in Environmental Sciences (CIRES) at the University of Colorado, Boulder, 2014; Amante et al., 2023). This bathymetry was validated with point measurements collected in September 2023. These data have a horizontal resolution (i.e., spacing) of 3 m in our study area, which is a finer resolution than any of the model grids.

The model domain consists of 469 × 389 grid cells (X × Y directions), with one offshore water level boundary and two alongshore Neumann boundaries. The river discharge boundary conditions were based on stream gauge data from the USGS discharge monitoring network.

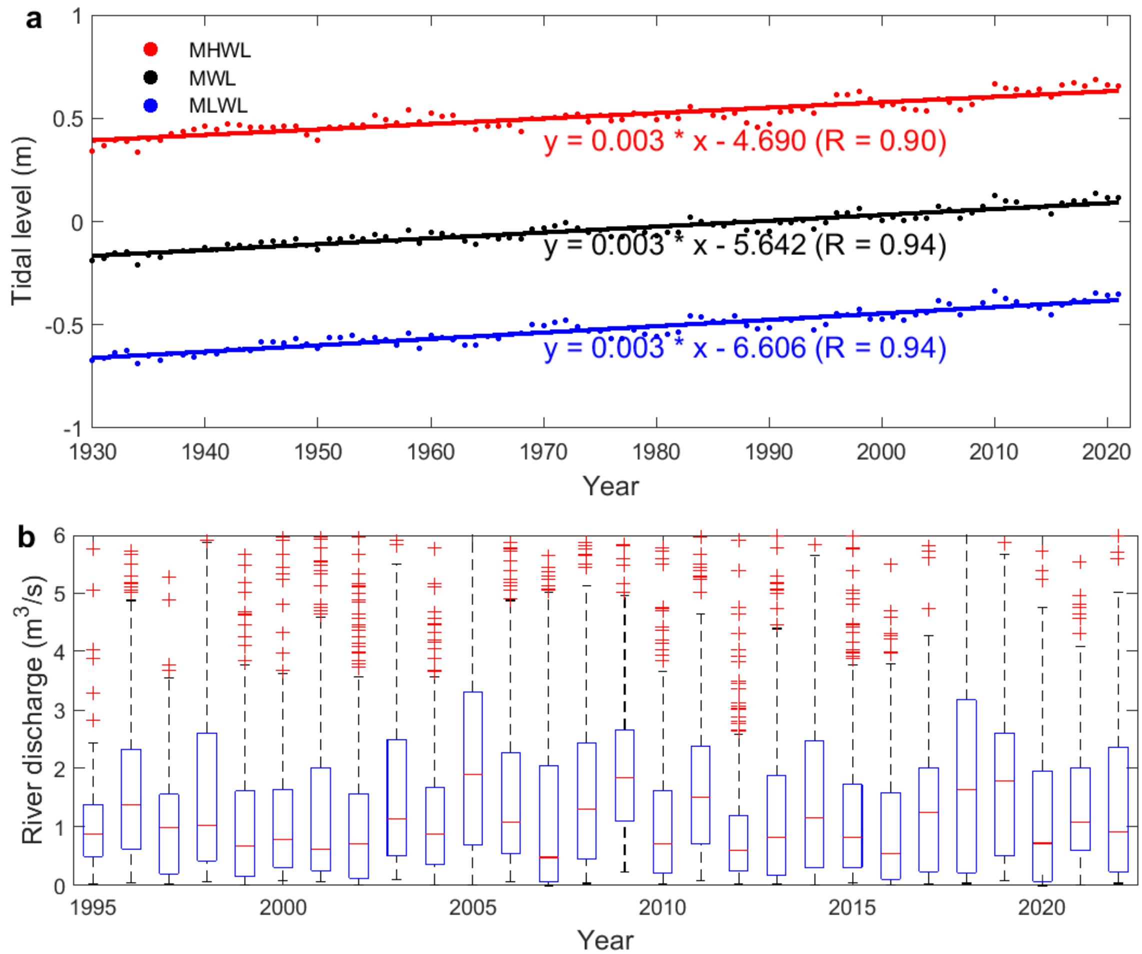

Figure 15. Observed tidal level and river discharge. a) Mean tidal levels at the Newport tidal gauge (Station No.: 8452660; https://tidesandcurrents.noaa.gov). Red, black, and blue points represent annually mean high tide, annually mean water level and annually mean low tide, respectively. Linear interpolation is applied separately for the three tidal signals. The data covers the period from 1930 to 2021. b) Statistics of annual river discharge measured at the Paskamanset River near South Dartmouth, Massachusetts, USA (Station No. 01105933, Location: 41°35'07"N, 70°59'27"W; https://waterdata.usgs.gov/ma/nwis/rt). The red line within each box represents the median value of the river discharge annual samples, and the extension of two whiskers above and below the box represents the upper quartile (75%) and lower quartile (25%) of river discharge datasets, between which the most representative data is located.

Discharge from Westport River was set to a constant value of 2 m^3/s based on the only local stream gauge 01105933 (Figure 15) which was located 5 km upstream of the model domain in the Paskamanset River (US Geological Survey, 2023), which flows into Slocums River. This value was chosen because it represented a moderately high flow in Slocums (being an approximate mean of the annual upper quartile flow). No flow data is available for Westport, but gauges nearby in similar watersheds (based on terrain and geology) have similar flow rates to the Paskamanset River (USGS gauge 01109070 Segreganset River, 01109060, Threemile River at North Dighton). Estimates of the flow into the head of the East and West branches of the Westport River estuary by the Massachusetts Estuaries Project (Walters et al, 2013), suggest total inputs to the system from multiple diffuse sources total approximately an average of 5 m^3/s, with values closer to 2 m^3/s from the watersheds at the head of the estuaries. However, these values are significantly smaller than the volumes of water exchanged with the ocean during a tide in both systems and are expected to have negligible impact on the hydrodynamics and sediment dynamics of the shoreline. As such, the decision was made to use the same input for Westport River as Slocums River.

A domain wide map of sediment grain size was used for the model based on data from usSEABED (Foster et al, 2016). The range in grain size for Buzzards Bay from the usSEABED is divided into gravel, sand and mud, as shown in (Figure 16a). The sediment map was refined and validated using sediment samples collected as part of our field campaign (Figure 16a). In addition to validating by observation, we also used the CUDEM to determine a ’roughness’ parameter by looking at the standard deviation of the elevation spatially (Figure 16b). This indicated smoother (sandy) or rougher (rocky) areas which showed a good spatial correlation with the interpolated usSEABED data.

The system is dominated by sand, which varies along the shorelines from fine to coarse sand. A spatially uniform Chézy bed roughness of 50 $m^{1/2}/$ s is used in the model, consistent with modelling studies in similar sandy environments (Brakenhoff et al., 2020). The sediment specific density and dry bed density are set to 2650 and 1600 kg/m^3, respectively (Xie et al., 2023).

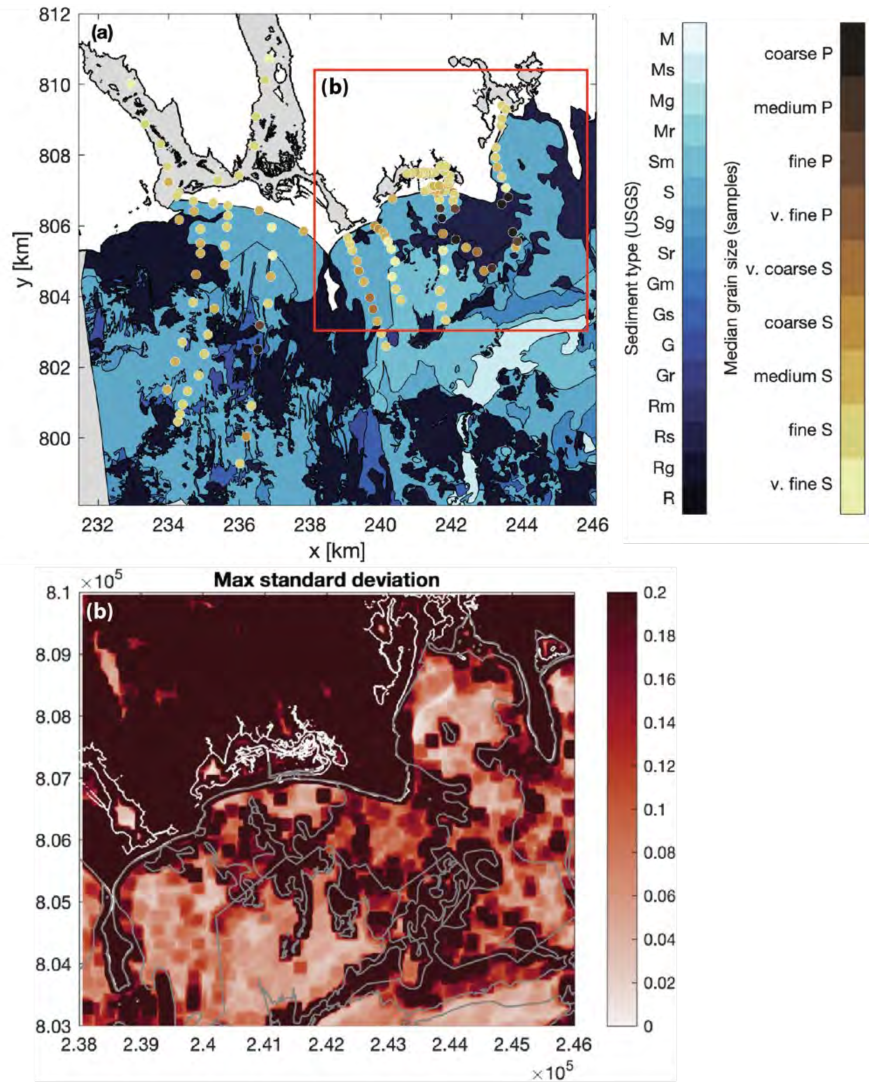

Figure 16. (a): Sediment type based on USGS sediment texture map of Buzzards Bay (usSEABED; Foster et al., 2016, in blue shades). Median grain size based on sediment samples from this study in yellow-brown dots. For the usSEABED data, sediment type is defined after Barnhardt et al, (1998): M = mud, S= sand, G = gravel. R = rock or boulder, dominant texture (>50%) is indicated using upper case, subordinate texture (<50%) is indicated with lower case; e.g., Gm is >50% gravel with some mud; (b) inset shown as red square on (a), illustrating spatial agreement between roughness calculated as standard deviation of elevation data and the usSEABED data shown in (a) with the outlines of different sediment zones from (Foster et al., 2016) shown as grey lines. Dark areas, with high roughness, correlate well with the bare/rocky areas. Sandy regions correlate with the smoother areas.

5.2.2 Boundary conditions

Boundary conditions, such as currents, wind and waves, were obtained from the North Atlantic Comprehensive Coastal Study (NACCS), within the Coastal Hazards System (CHS), a model specifically designed to capture the impact of fast-moving storms on ocean hydrodynamics. The modelling domain of the NACCS encompasses the western North Atlantic, the Gulf of Mexico and the western extent of the Caribbean Sea, which is far beyond our current model domain. It utilizes a range of grid resolutions, from 40 km in the Caribbean Sea to 10 m along the Northeast shoreline and estuaries, to simulate various hydrodynamic conditions. NACCS was calibrated based on a series of offshore buoy stations (Cialone et al., 2015). This regional model provides hourly model outputs at specific locations (Figure 17 A) both near the shoreline and offshore by simulating different hydrodynamic drivers, such as the presence or absence of storms, astronomical tides, and sea level rise (SLR). Over forty NACCS output locations sit within our Regional Model Domain. The outputs of NACCS include a series of historical and synthetic storms. The validation of NACCS was conducted under several historical storm events, with good agreement between model simulations and hydrodynamic data, such as water level and wave height, collected from nearly 60 buoy stations (Cialone et al., 2015).

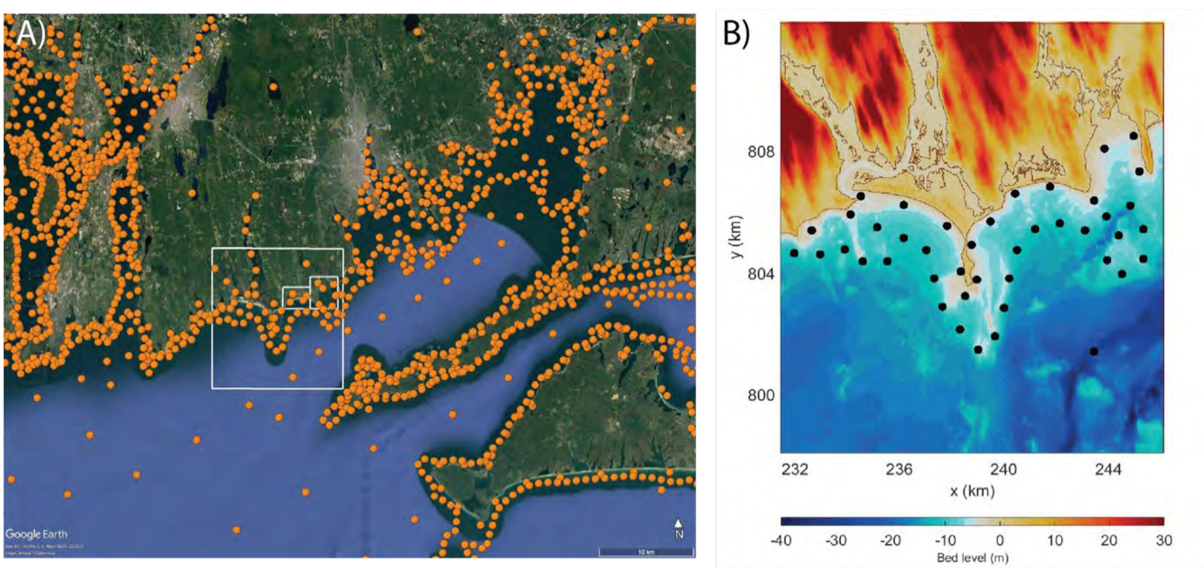

Figure 17. A) NACCS output locations throughout Buzzards Bay. B) NACCS sites within the regional model domain which were used to provide 43 validation points to supplement the validation using field observations.

5.2.3 Model calibration and validation

Our models were validated using a combination of our field data (waves, currents and water levels) and the regional NACCS model. The regional domain has been validated using 1) two ADCPs (Figures 18 and 19) and 43 validation points extracted from NACCS

(Figure 17 B, 20 and 21). To evaluate our model performance, we calculated the model skill index using the validation approach proposed by Willmott (1981). The skill index is defined as:

$$Skill = 1 - \frac{\sum |X_D - X_S|^2}{\sum (|X_D - \overline{X_S}| + |X_S - \overline{X_S}|)^2} \quad (2)$$

where X_D is the refined Delft3D model output and X_S is either the measured data or the data points extracted from the regional model (CHS), both of which are applied here at an hourly interval. $\overline{X_S}$ is the temporal average of the data points from measurements of the regional model (CHS). The skill index is a metric used to evaluate the performance of models in predicting the behavior of a system. It ranges between 0 and 1, where 1 indicates a perfect match between the model output and reference samples, and 0 indicates a complete failure to capture the expected behavior. Previous research in coastal hydrodynamic simulations suggests that a skill index higher than 0.7 to 0.8 represents a reasonable prediction, particularly for wave heights (Warner et al., 2005; Zhu & Wiberg, 2022).

We first compare the model results with data collected by ADCPs. Two ADCPs were installed in October 2022, recording water level and wave signals (e.g., wave height, wave period and wave direction) hourly through the end of December 2022 (Figure 12). During this period Buzzards Bay was impacted by Winter Storm Elliott at the end of December. Therefore, we ran the model to simulate the observation period of Storm Elliott. Our model demonstrates high agreement with the observation data, particularly in terms of the water level and wave height (Figures 18 a-b and Figures 19 a-b). Since our model did not consider spatial variation in wind effects, the simulated wave period and direction show less accuracy (Figures 18 c-f and Figures 19 c-f). Water level and wave height show an excellent calibration, according to skill, root mean squared error (RMS) and mean absolute error (MAE). The wave period and direction are shown for both the mean wave direction and the peak wave direction. These data are more prone to error due to 1) magnetic direction corrections and frame interference in the field data; 2) uncertainty introduced during spectral analyses and binning the data. However, particularly for the mean wave periods, the calibration is reasonable. The absolute error demonstrates a constant offset between the measured and modelled data, likely due to the errors mentioned above. Based on this calibration, the model is considered fit for purpose.

We then compare the model output with the calibrated results of NACCS at 43 points within our research domain (Figures 20 and 21), using a real storm event - Hurricane Irene in 2011. The storm is one of the major events that has impacted Buzzards Bay in the last decade (Marsooli & Lin, 2018). Additionally, hydrodynamic data to drive the models were available at the buoy station offshore (Station BUZM3/44085; water depth 21 m) and were used to calibrate CHS. Here, we calculated the skill indices for water level, wave height, velocity magnitude, and wave period by comparing the outputs of the two models. Results indicate that our local refined model can effectively capture changes in water level, wave height, and velocity during storms, similar to the NACCS model (Figure 20). However,

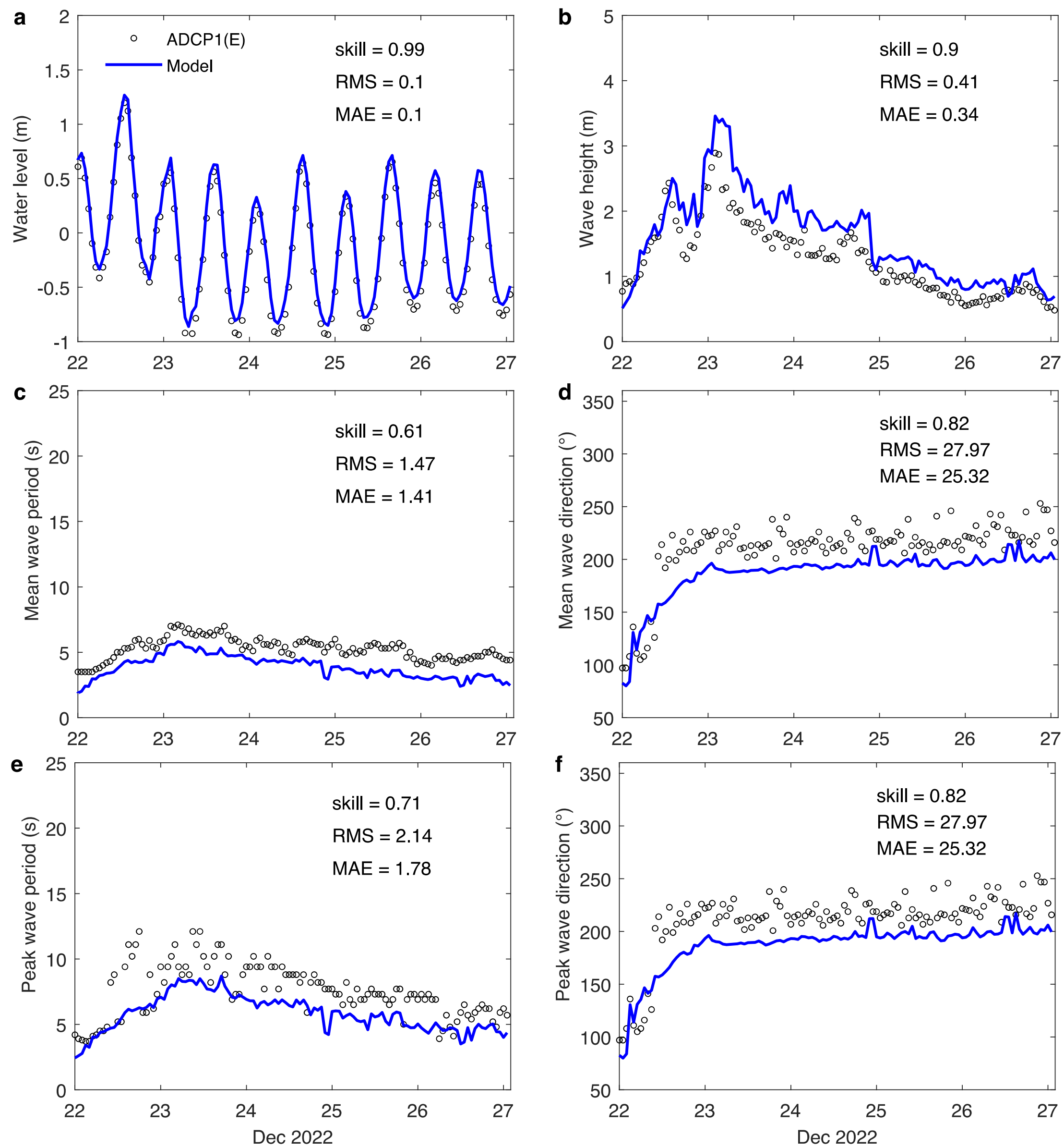

Figure 18. Comparison between the local Delft3D model and observation data at the site of ADCP1 during Winter Storm Elliott 2022: a) water level, b) wave height, c) wave period and d) wave direction.

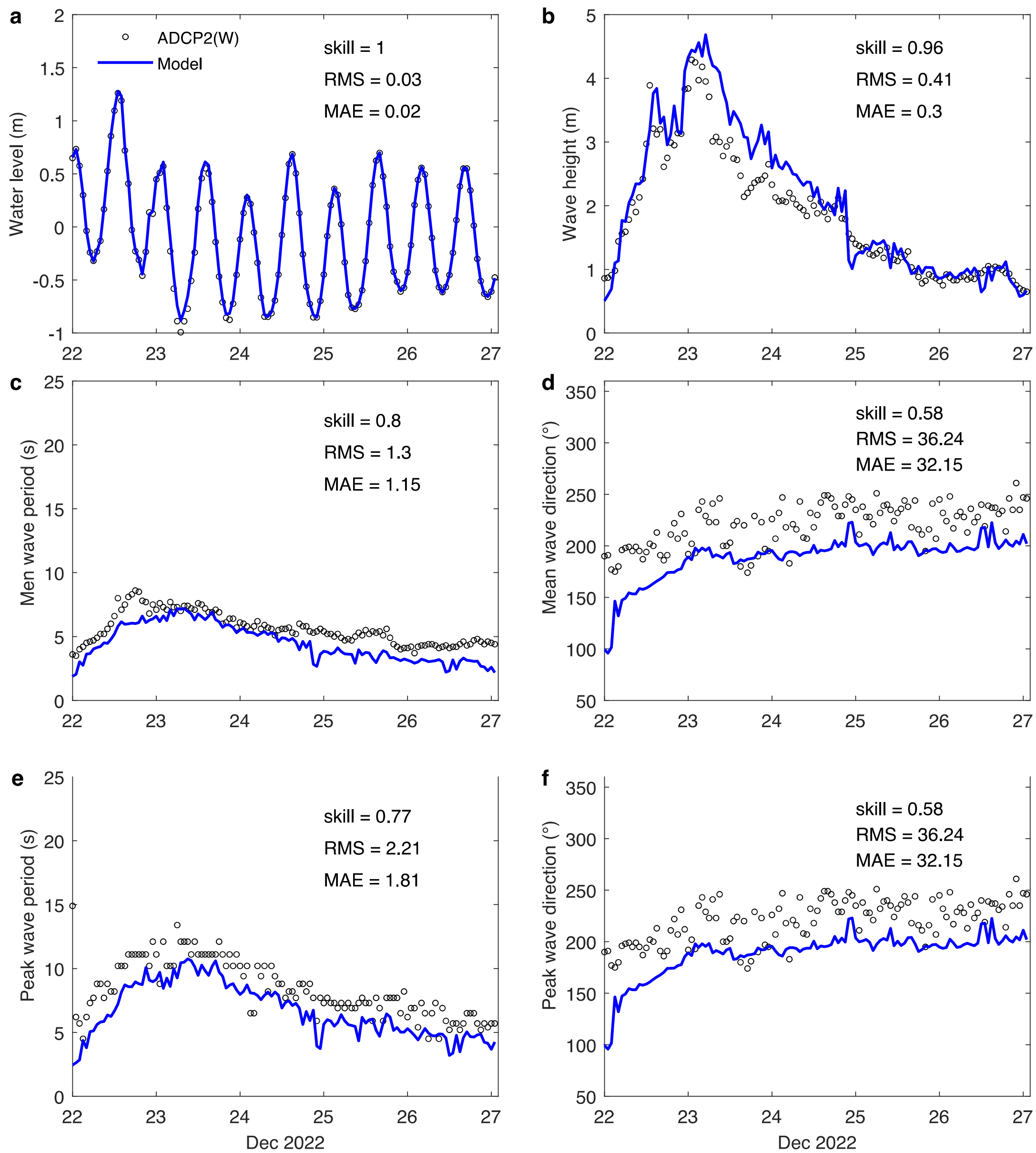

Figure 19. Comparison between the local Delft3D model and observation data at the site of ADCP2 during Winter Storm Elliott 2022: a) water level, b) wave height, c) mean wave period and d) mean wave direction, e) peak wave period and d) peak wave direction. Root mean squared error and mean absolute error are also provided to allow a further evaluation of the skill metric.

some areas close to the shoreline exhibit lower correlations for velocity, possibly due to inconsistent bathymetry settings between the two models. However, in general skill assessment for water level and wave height consistently greater than 0.92 (complete agreement = 1). As an example, a detailed comparison of the four hydrodynamic parameters can be seen in Fig. 21 for the point highlighted with a rectangle in Figure 20.

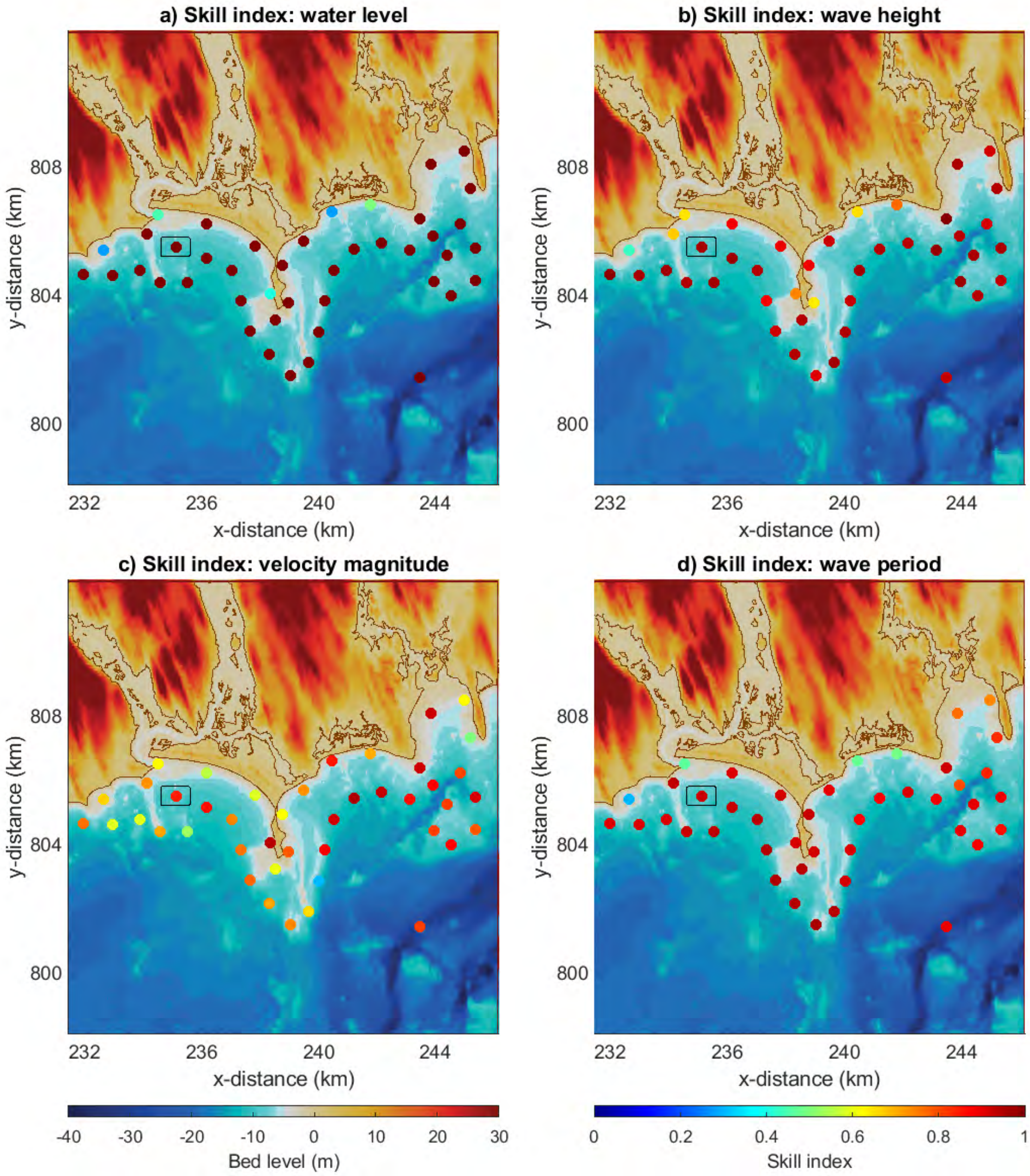

Figure 20. Comparisons of hydrodynamic outputs between the local model (Delft3D) and the regional model (NACCS Coastal Hazards System) based on tropical cyclone Irene between 27 August and 30 August 2011. The comparison parameters include a) water level, b) wave height, c) velocity and d) wave period.

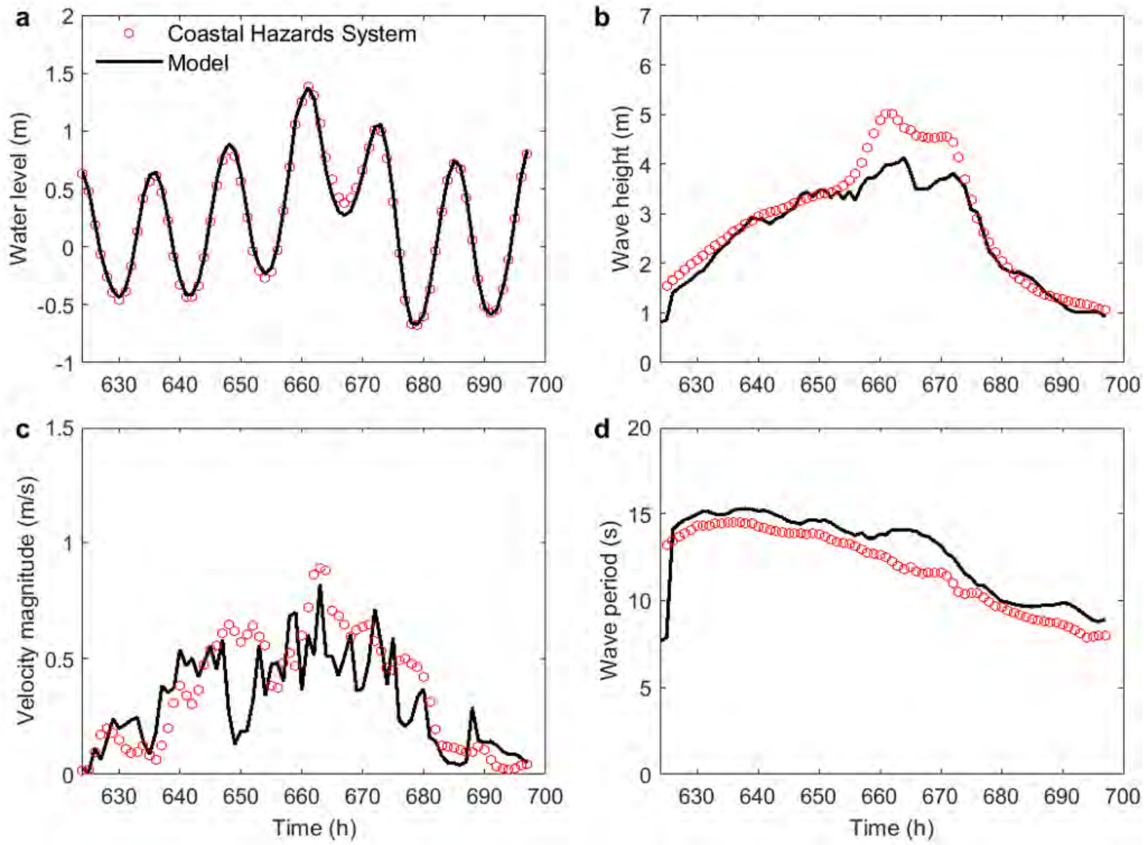

Figure 21. Detailed comparison between the local Delft3D model and large scale CHS model outputs during tropical cyclone Irene in 2011: a) water level, b) wave height, c) velocity and d) wave period.

5.2.4 Simulations

A set of simulations were run to answer each of the specific objectives. The larger, regional grid has allowed the assessment of sediment transport patterns within two zones: 1) Westport Inlet, and 2) East Beach. For each grid, or each objective a *base line scenario* was run to assess the general flow and sediment transport patterns in each zone and to provide a reference (a control) to compare to other experimental scenarios (noted on figure axes or in captions). For most objectives, by running a set of specified significant wave height and wave direction conditions (e.g., 5 wave heights and 5 wave directions, i.e., 25 conditions), a technique successfully used by Mariotti et al. (2010), we can determine sediment transport fluxes along the shoreline and, by looking at return frequency of the experimental conditions, we can assess the related mid to long-term morphological changes. This is done by looking at differences in sediment fluxes and erosional-depositional patterns, which is then extrapolated to a longer timescale using local climate data (based on the frequency of the experimental conditions).

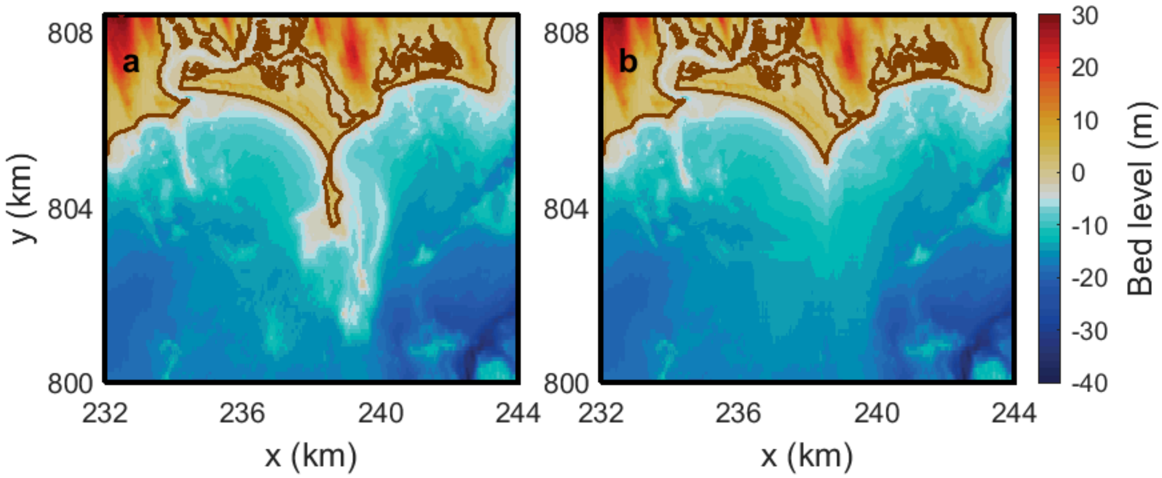

Figure 22. Bathymetry with (a) and without (b) coastal headland for model simulations. To remove the coastal headland from the system, the elevation of the headland zone was lowered until it matched the nearby bathymetry outside of the headland zone.

1) The island: Identical scenarios were run using a version of the model in which we artificially remove the Gooseberry Island from the model (Figure 22).

2) The Causeway: Identical scenarios were run using a version of the model in which we artificially remove the Gooseberry Causeway from the model (Figure 23 and 24).

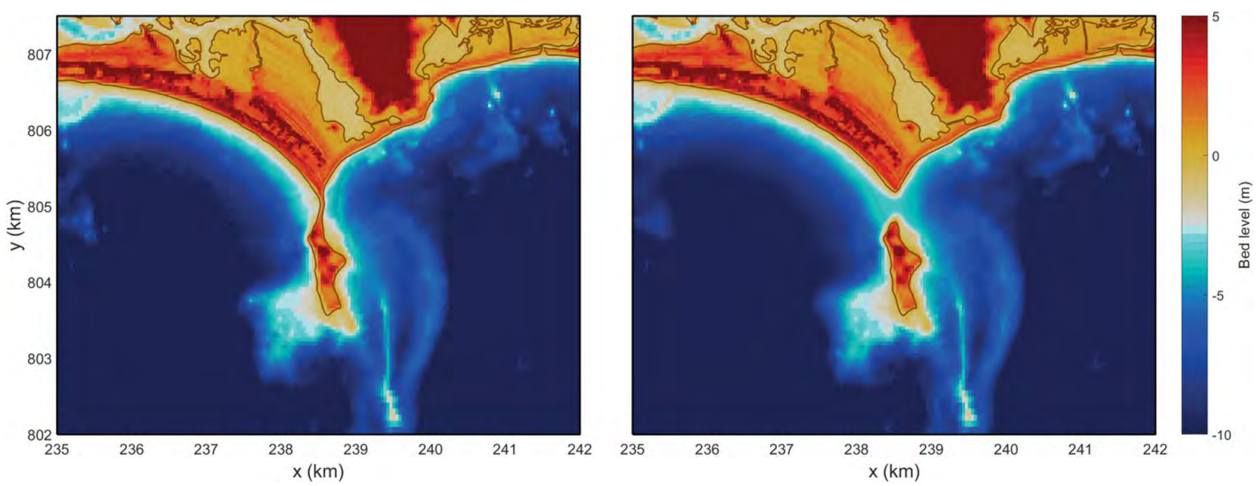

Figure 23. Bathymetry with (a) and without (b) the causeway for model simulations. To remove the causeway from the system, the elevation of the tombolo was lowered to emulate the bathymetry over the tombolo before the causeway was built (see Figure 24 for detail).

This has allowed us to evaluate the influence of both the Island and the causeway on flow patterns and consequent sediment fluxes and bathymetric and morphologic changes under a variety of wave and water level conditions. We examine systemwide impacts of the Causeway using the Regional Model grid, however, we also use a fine scale model to examine nearshore wave dynamics and sediment fluxes around the Causeway. This allows us to look in detail at how the Causeway impacts waves and longshore sediment fluxes. The scenarios that were run are summarized in Table 4.

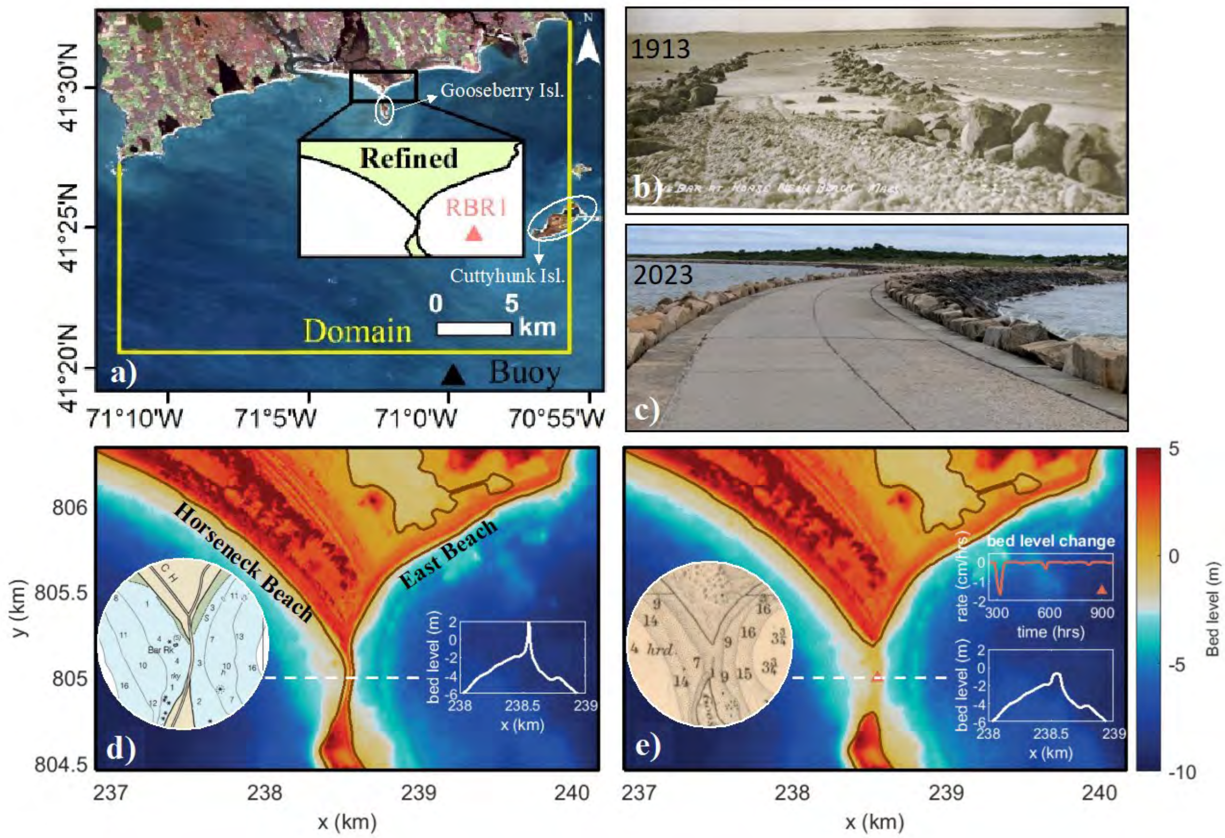

Figure 24. Maps and photos showing the study area (a) Delft3D-FLOW domain is overlayed with a Delft3D-WAVE domain (yellow box). The focus area of this research is modelled with a refined sub-domain (black box), the red triangle shows the location of the RBR® pressure sensor deployed on the east side of the causeway to measure storm tides and significant wave heights for model validation. Black triangle shows the location of an offshore buoy (Station BUZM3/44085; water depth 21 m) recording wave conditions (wave heights, wave period and wave direction) for model setups. (b) Ground photograph looking southward to Gooseberry Island in 1913 (Clamflats, 2019), (c) Ground photograph looking southward to Gooseberry Island in 2023 (Danghan Xie, August 2023). (d) Current bathymetry with a causeway and (e) bathymetry without causeway. Two historical sea charts in panels (d-e) depict the depth around the tombolo at different times (NOAA, 2024). The line plots inset in these panels show the elevation across the causeway and tombolo, with modeled rate of bed level change after the bathymetry was altered to represent pre-causeway conditions until equilibrium state was reached, shown in panel e. The bed level in the two domains is comparable with the sea charts in 2016 (d) and 1892 (e).

Table 4. Scenarios run to examine the impact of the causeway on sediment transport from Horseneck Beach to East Beach.

Scenario name	Description	Storm surge value (m) [bin range]	Wave height value (m) [bin range]	Wave direction value (°) [bin range]	Number of storms	Joint probability
REF	Baseline conditions	0.65 [0.56-0.74]	4 [3.8-4.8]	185 [180-200]	8	8%
Surge +	Water level elevated by storm surge	1.25 [> 0.74]	4 [3.8-4.8]	185 [180-200]	1	1%
SW wave	Waves from the SW	0.65 [0.56-0.74]	4 [3.8-4.8]	215 [200-220]	3	3%
Wave +	Large waves	0.65 [0.56-0.74]	8.5 [> 6.8]	185 [180-200]	2	2%
Elliott	Conditions during Winter Storm Elliott	0.45 [0.38-0.56]	5.3 [4.8-5.8]	193 [180-200]	2	2%
Irene	Conditions during Hurricane Irene	0.71 [0.56-0.74]	8.7 [> 6.8]	191 [180-200]	2	2%
Bob	Conditions during Hurricane Bob	2.77 [> 0.74]	8.8 [> 6.8]	176 [160-180]	2	2%

3) Climate change: The impact of a changing climate was examined using two approaches. The first by considering sea level rise (SLR) and, secondly, by considering increased storm intensity. The impacts of SLR were evaluated by modeling conditions under four scenarios: 0.25, 0.5, 0.75 and 1m rise. These represent a range of potential future conditions (Table 5, for Newport RI tide gauge from the Interagency Sea Level Rise Prediction Tool (https://sealevel.nasa.gov/task-force-scenario-tool/), including low rates of sea level rise in 2050 (0.25 m rise), high rates of sea level rise in 2050, moderate sea level rise in 2070 and low rates of SLR in 2100 (0.5 m rise), moderately high sea level rise in 2070 (0.75 m rise). The 1 m rise represents the outcome of high rates of sea level rise in 2070 or moderate rates in 2100. This is considered probably the most pertinent or likely of the SLR scenarios. Increasing storm intensity was assessed by increasing wave height (Table 6).

Table 5. Sea level rise predictions in m of total change with reference to 2018 sea level (i.e., the date of the most recent LiDAR data in the model DEM).

Median SL	2050	2070	2100	2150
Low	0.26	0.36	0.47	0.67
IntLow	0.30	0.46	0.66	1.06
Int	0.34	0.58	1.12	2.10
IntHigh	0.40	0.75	1.49	2.49
High	0.43	0.91	1.92	3.46

Table 6. Scenarios run to look at the impact of Gooseberry Neck Island and sea level rise on shoreline erosion patterns.

No.	Group	Peak storm wave height (m)	Sea-level rise (m)	Headland	Note
1	Non-climate change	8	0	Yes	Reference
2				No	
3	Larger storm waves	10	0	Yes	SW10m
4				No	
5		12		Yes	SW12m
6				No	
7		14		Yes	SW14m
8				No	
9		16		Yes	SW16m
10				No	
11	Sea-level rise	8	0.25	Yes	SLR0.25m
12				No	
13			0.5	Yes	SLR0.5m
14				No	
15			0.75	Yes	SLR0.75m
16				No	
17			1	Yes	SLR1m
18				No	

6 Results

The following section summarizes and interprets the results of the data acquisition and modeling activities. The final sub section synthesizes these results.

6.1 Geologic framework and exogenous data sets

6.1.1 Regional geology assessment

The regional geology has been heavily influenced by the last glaciation which ended around 11,000 years ago. Concurrently, as the continental ice sheet retreated, meltwater streams flowed to the ocean raising sea level. Offshore surface sediment data aids in our understanding concerning how sand moved onshore during the marine transgression following deglaciation (caused by rising sea level) and where this sand was deposited. In other words, this provides insight into the source of the beach sediment and the size of that original reservoir of sand, whether it is finite and if it is, when did/will it be exhausted.

Both a general and a more detailed US Geological Survey (USGS) surficial sediment map of the Westport and South Dartmouth region are provided in Figure 25. The major sedimentary units include: 1. Sand and Gravel (orange), 2. Thin Till (light green), 3. Thick Till (darker green), and Wetland Peats (lavender/purple). As seen in the Figure, the deposits tend to be elongated in a north-south direction, which coincides with the structural grain of the region. In the geologic past (542- 416 million years ago) closure of the Iapetus Ocean (predecessor of the Atlantic) caused a continental-continental collision resulting in compression generating folded rocks. Fluvial erosion of this landscape produced ridges and valleys that were subsequently modified by several episodes of Pleistocene glaciation. The valleys became the sites of river drainage and estuary development, and the ridges now extend seaward forming peninsulas and submerged ledges and bedrock ridges.

The detailed map of Westport (Figure 25 inset) reveals that sand and gravel sediment border both sides of the Westport and Slocums River Estuaries. It is reasonable to believe that glacial meltwater streams were responsible for depositing these sediments and it is also likely that similar types of deposits were formed in the offshore region. The sediment map in Figure 26 was constructed from bottom samples collected throughout western Buzzards Bay (Figure 27). As these maps demonstrate, much of the region offshore of Horseneck Beach consists of sand and gravel, whereas the promontories separating these areas are rocky or bedrock.

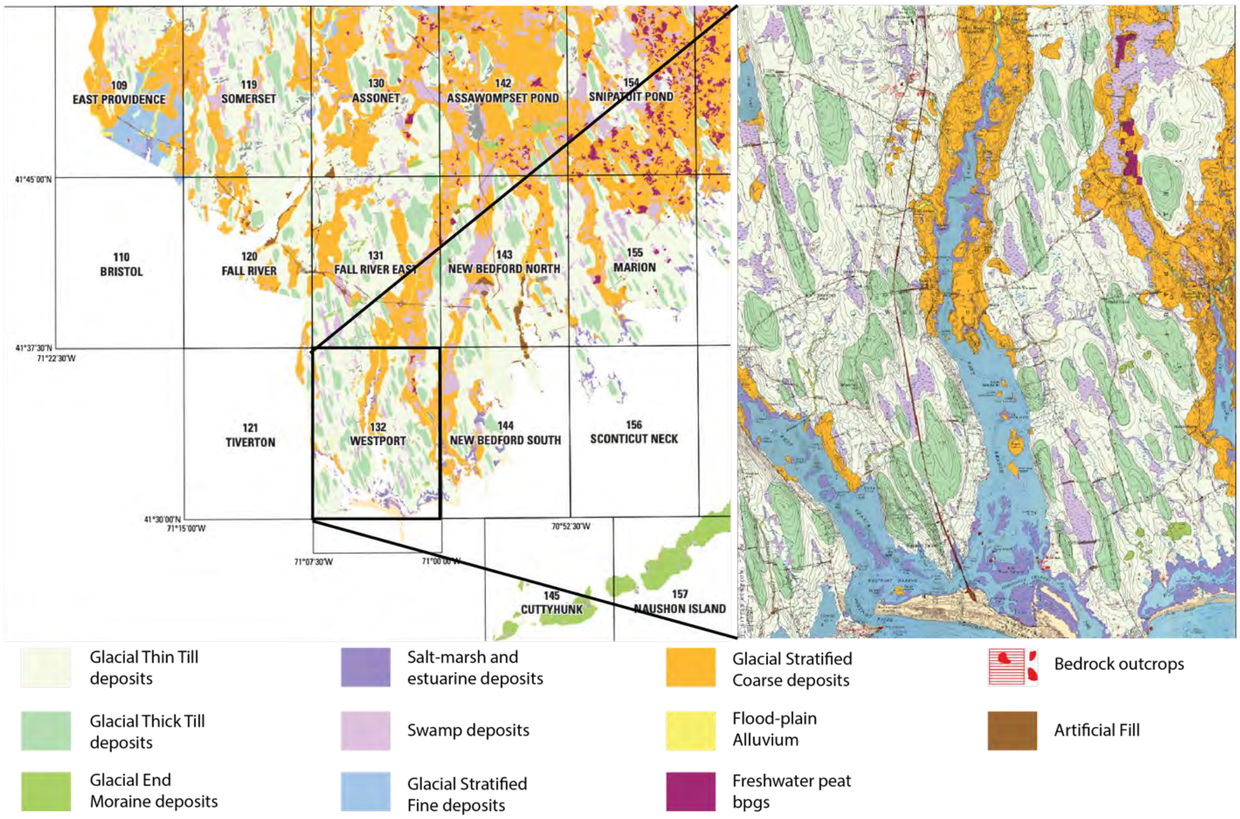

Figure 25. Surficial deposits in the Westport and South Dartmouth region. A general view of the area and inset detailed map of Westport River Estuary (modified from Stone et al, 2018). The primary unit of note is the Glacial Stratified Coarse deposits that line the valley sides. These are described by Stone et al 2018 as: Glacial Stratified Coarse deposits which “consist of gravel deposits, sand and gravel deposits, and sand deposits, not differentiated in this report. Gravel deposits are composed of at least 50 percent gravel-size clasts; cobbles and boulders predominate; minor amounts of sand occur within gravel beds, and sand comprises a few separate layers. Gravel layers generally are poorly sorted, and bedding commonly is distorted and faulted due to post-depositional collapse related to melting of ice. Sand and gravel deposits occur as mixtures of gravel and sand within individual layers and as layers of sand alternating with layers of gravel. Sand and gravel layers generally range between 25 and 50 percent gravel particles and between 50 and 75 percent sand particles. Layers are well sorted to poorly sorted; bedding may be distorted and faulted due to post-depositional collapse. Sand deposits are composed mainly of very coarse to fine sand, commonly in well-sorted layers. Coarser layers may contain up to 25 percent gravel particles, generally granules and pebbles; finer layers may contain some very fine sand, silt, and clay”

The presence of extensive sand and gravel accumulations along the estuarine valleys and general footprint of the offshore sand and gravel deposits suggest that the abundance of sand comprising the Horseneck barriers is a product of the onshore reworking of glacial-fluvial sediment composed of a high sand content. The abundance and maturity of the barrier sediment (well-sorted, high quartz sand) indicate that the sand was moved onshore preferentially while most of the gravel remained offshore as a lag deposit.

We have used USGS data in Buzzards Bay to examine the offshore sedimentary deposits and evaluate where the sand came from that formed the vast sand reservoirs that occur onshore. This has been essential in constructing the numerical models and to project into the future if we can expect more sand to be coming onshore or if the process has reversed and we will be losing sand to the offshore. Our dataset is taken from a report by Foster et al (2016) entitled: *Shallow Geology, Sea-Floor Texture, and Physiographic Zones of Buzzards Bay, Massachusetts* that uses acoustic backscatter, bathymetry, and seismic-reflection profile data to map the surficial sediments and the shallow stratigraphy of the region. A second older report by O'Hara and Oldale (1980) titled: *Maps Showing Geology and Shallow Structure of Eastern Rhode Island Sound and Vineyard Sound, Massachusetts* provides subsurface information. Finally, a report by Ford and Vos (2010) titled: *Seafloor Sediment Composition in Massachusetts Determined Using Point Data* gives us widely spaced grain-size information.

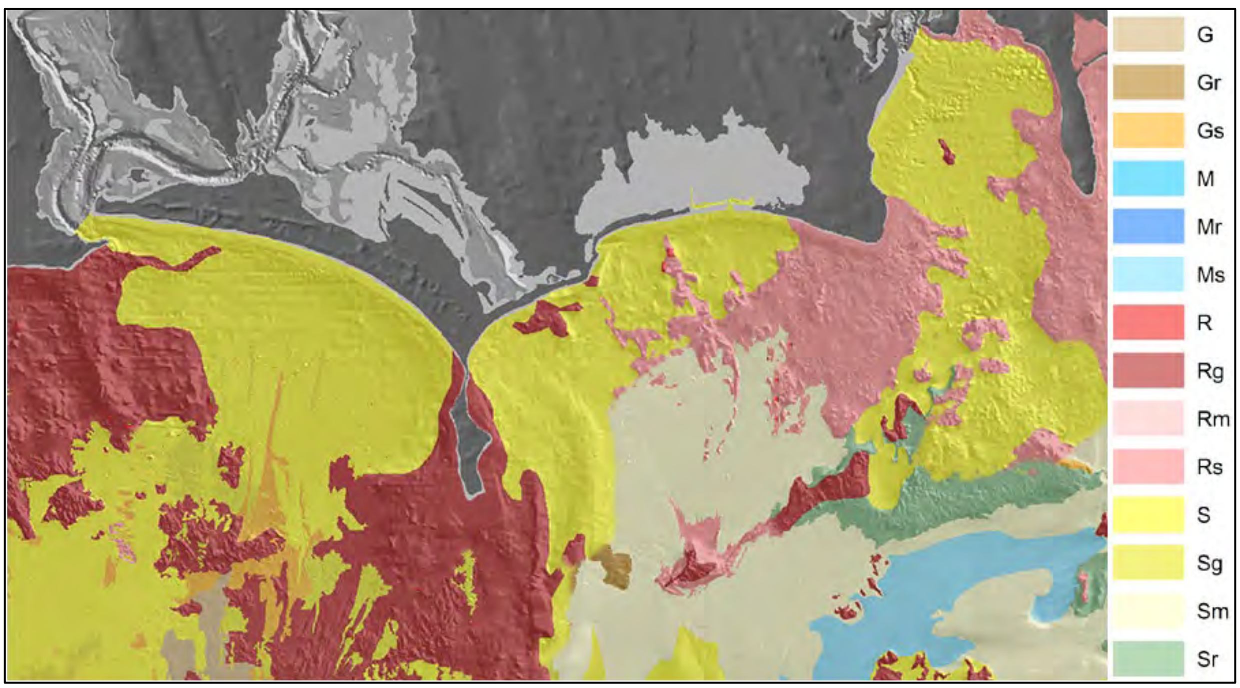

Figure 26. Sediment map of the project area. Note the abundance of sand and gravel. M or m = mud, S or s = sand, G or g = gravel. R or r = rock or boulder, dominant texture (>50%) is indicated using upper case, subordinate texture (<50%) is indicated with lower case, e.g., Gm is >50% gravel with some mud. Clip from Foster et al (2016).

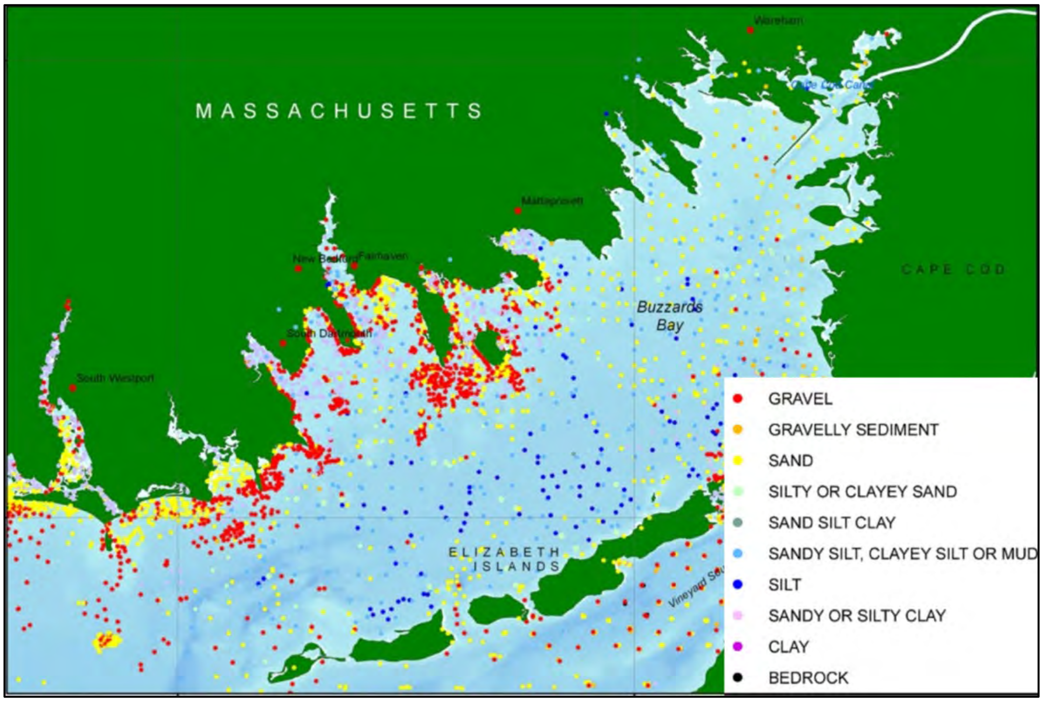

Figure 27. Distribution of different sediment types based on bottom samples.

Shallow seismic (both Boomer and Chirp) profiles along with side-scan sonar and single-beam surveys have been utilized to map the bottom in the vicinity of the project area (O'Hara and Oldale, 1980; Foster et al 2016). O'Hara and Oldale (1980) used this information to produce two maps that help corroborate our interpretation concerning the early history of the Horseneck barrier and Westport estuarine complex. Figure 28 a is a structure contour map of the glacial drift (Wisconsinan glacial sediments). Essentially, this is the depth to the glacial sediment surface following deglaciation and includes the surface cut by fluvial erosion as meltwaters streams flowed from the retreating ice sheet. It is important to note that one of the major drainage systems that developed following deglaciation, depicted by the dashed lines in Figure 28 a, trended northward toward the East Branch of Westport River Estuary. Likewise, one of the thickest post-glacial sedimentary deposits (Holocene sediments) coincides with former drainage valleys (Figure 28 b). The sediments that filled these valleys commonly consist of sand, silt, and clay associated with fluvial and estuarine deposition during the Holocene transgression (rising sea level). The surface of these deposits was subsequently reworked by waves and tides and topographically flattened (Figure 28 and 29).

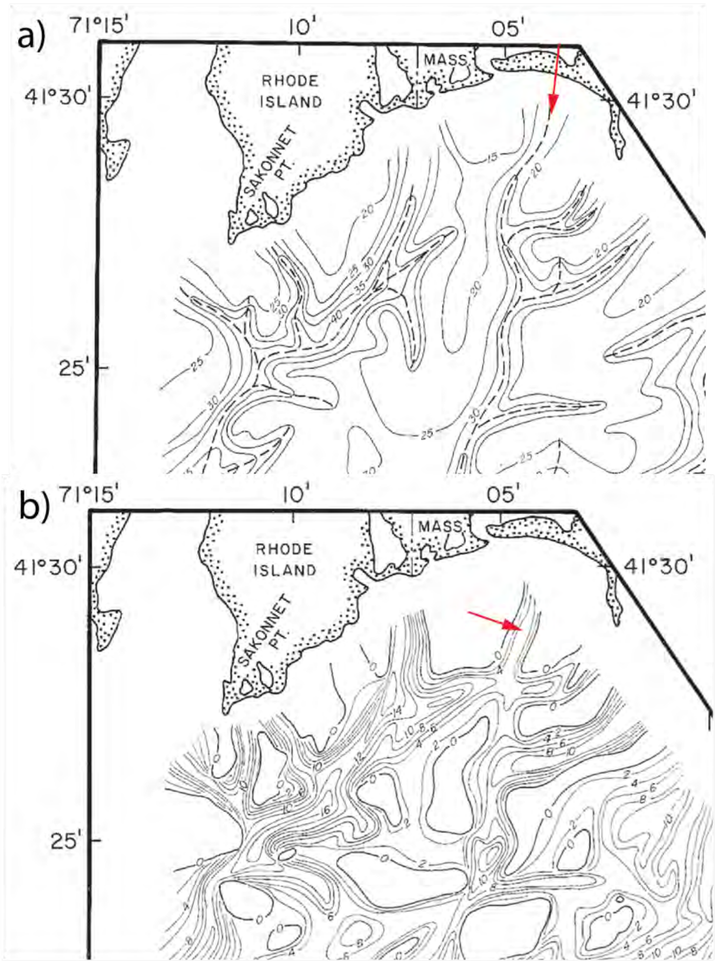

Figure 28. Maps produced from interpretation of shallow seismic profiles and sediment core data. a). Structure contour map of Pleistocene surface indicating former drainage with one system heading toward paleo-estuary opening (red arrow). b). Holocene sediment thickness map showing a buried channel leading to mid-Horseneck Beach (O'Hara and Oldale, 1980).

The stratigraphic section given in Figure 29 was derived from extensive shallow seismic and coring data (O'Hara and Oldale, 1980). It indicates that thick glacial-fluvial sand and gravels deposited during deglaciation underlie extensive areas offshore of Horseneck Beach. This sediment is overlain by fluvial and estuarine deposits, which consists of sand and other sediment reworked from glacial deposits as well as estuarine sediment that accumulated as sea level was rising during the Holocene transgression. A vibra-core taken 4 km southwest of Gooseberry Island (Figure 30) demonstrates that thick (~ 2.5 m) sand exists in the offshore and that this deposit is an example of the unit that is described in Figure 29 as being the Holocene fluvial and estuarine sediment (Qfe).

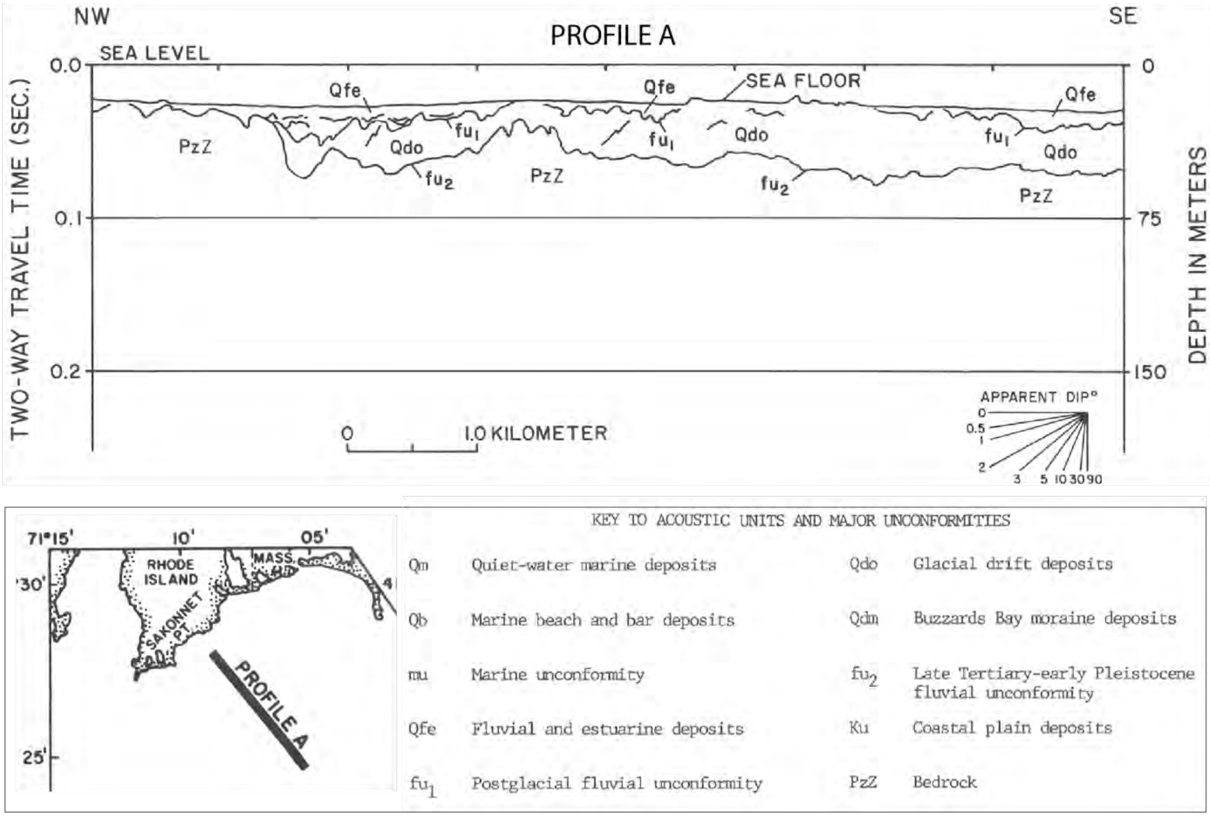

Figure 29. Stratigraphic cross section offshore of Horseneck Beach (O’Hara & Oldale, 1980). Note the fluvial and estuarine deposits overlying thick stratified outwash sediment that contains extensive sand.

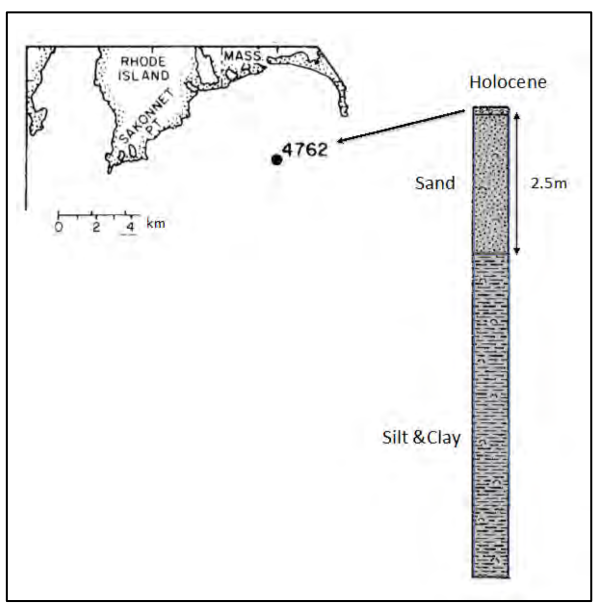

Figure 30. Sediment core from O’Hara and Oldale (1980) revealing extensive offshore sand deposits. This finding is consistent with our offshore sampling.

To summarize the regional geology assessment, the bedrock fabric of Buzzards Bay has produced a pronounced headland and embayment coast. This led to the deposition of glacial-fluvial sand and fine gravel in offshore valleys during deglaciation. As the icesheet retreated and water was added back to ocean basins, sea level rose, and waves reworked the offshore deposits into a broad, landward moving sand sheet. Eventually, the rate of sea-level rise slowed, and the landward migrating sand became pinned to bedrock promontories forming low barriers and elongating spits. Specifically, this means that: 1) Westport River at one point flowed past where Horseneck Beach now sits and (along with other nearby rivers) deposited sediments offshore of the modern-day coastline; and 2) that Horseneck Beach was created through the landward transport of glacial sand and gravel, previously deposited offshore, onto the beach with coarser sand and gravel left behind offshore. The onshore movement of sand is a response to rising sea levels. As water depth increased, sand deposits located below the depth of wave influence became immobile. More importantly, as the mobile offshore sand source has diminished in volume, it has allowed gravel to mobilize and invade beaches.

6.2 Field and laboratory analyses

6.2.1 Sediment characterization

The sediment samples collected throughout the project region demonstrate the wide variety of settings within this coastline. A generally fining of sediment can be seen along Horseneck beach towards Westport inlet (Figure 31), with coarser sediments on and around the headlands (e.g., Gooseberry Neck Island). In the areas of sand, the sand is often moderately to well sorted, implying that it has been transported and reworked, indicating glacio-fluvial sources, likely having been reworked from offshore. However, there are also areas of bedrock, boulders or course sediment, and poorly sorted sediment that would be expected in glaciated terrain.

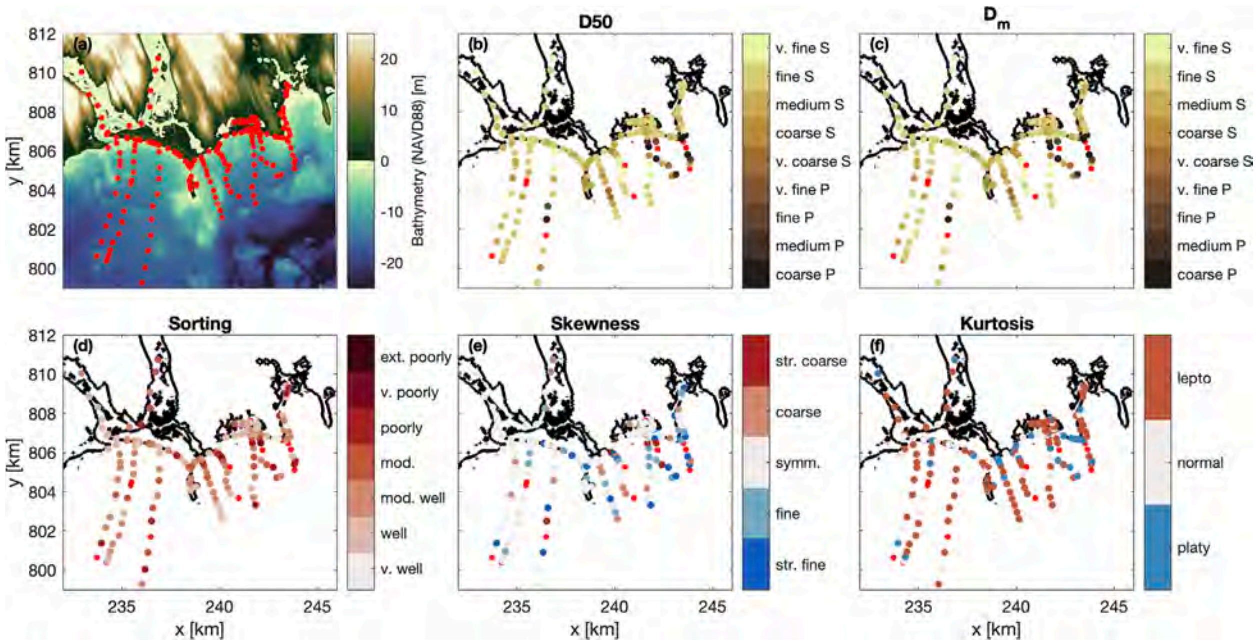

Figure 31. (a) 200 sediment sampling locations around the project area and their properties: (b) median grain size diameter, (c) mean grain size diameter, (d) sorting, (e) skewness, and (f) kurtosis.

Analysis of the beach and offshore grain size datasets suggests that sand is present from the beach to several kilometers offshore, which is consistent with the USGS surficial studies (Figure 26 to 30) and the usSEABED data (Figure 16). It also shows that the offshore in this region is not characterized by seaward fining in grain size common to many coasts. This likely reflects the wide range in composition of glacial sediments that were reworked during the Holocene transgression. These data have been used to select grain size values in the modelling.

Examples of the type of variability observed along Gooseberry Island are illustrated in Figure 32. In some localities long-term erosion has exposed till scarps, whereas in other regions an abundance of sand has built sandy wide beaches and barriers in front of freshwater wetlands. This range in sediment abundance at Gooseberry Island appears to be a product of differential wave exposure, shoreline setting (headland versus embayment), and proximity to the onshore migration of sand.

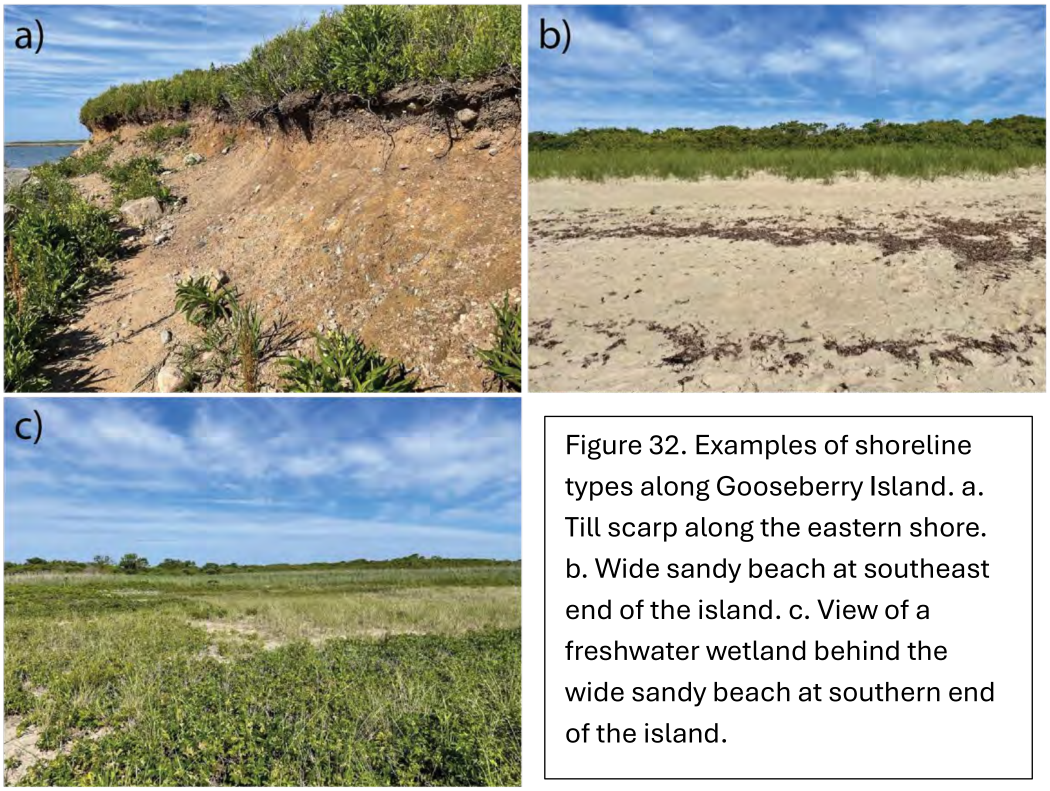

Figure 32. Examples of shoreline types along Gooseberry Island. a. Till scarp along the eastern shore. b. Wide sandy beach at southeast end of the island. c. View of a freshwater wetland behind the wide sandy beach at southern end of the island.

6.2.2 Radioisotopic dating and marsh accretion

Measurement of marsh accretion is used for two purposes. First, it allows us to project a reasonable marsh platform elevation in modeling of future scenarios. Secondly, it provides us with an assessment of the overall stability and resilience of the marshes in the system. The marshes are valuable ecosystems providing services such as nurseries for juvenile fish stocks (supporting commercial and recreational fishing), buffering of the mainland from storms, carbon sequestration and supporting tourism such as birding and water sports. Further to this, because changes in the marsh platform area can significantly impact tidal prism, loss of saltmarsh is associated with expanding tidal inlets and thinning and shortening of barrier islands. Thus, marsh accretion rates can provide an insight into the long-term stability of the entire beach barrier system.

Radioisotopic dating of the marsh sediment cores (Full data in Table A1, Appendix A) indicate accretion rates ranging from 1.21 to 3.54 mm/yr, corresponding to Accretion Excess (AE_c) values of 0.38–1.29 (Figure 33). AE_c has been calculated based on the sea level rise observed over the same period as the accretion rate calculation (see methods described above), which varies depending on a large number of variables.

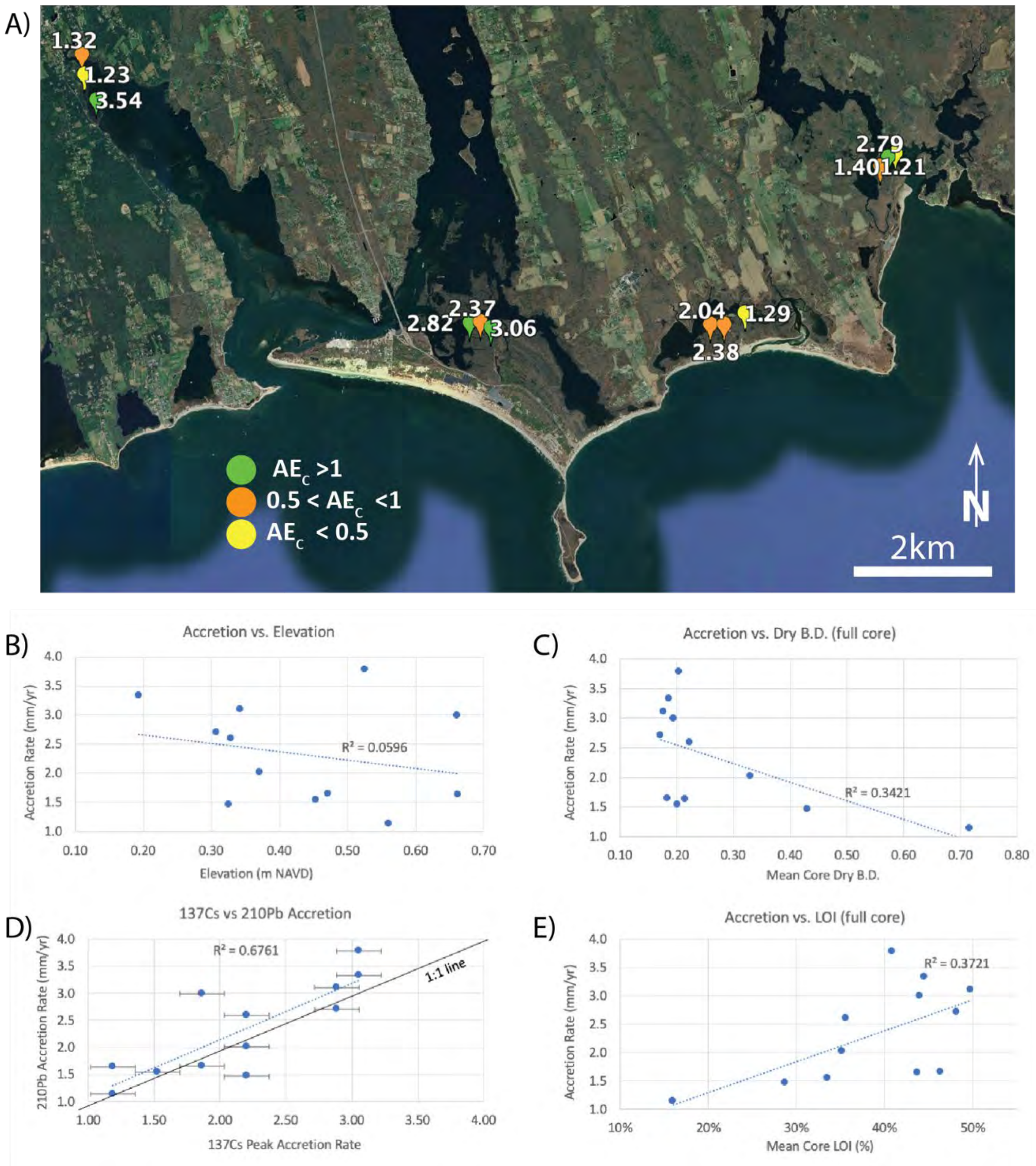

Figure 33. A) Map of sampling sites for salt marsh accretion rates, labeled with accretion rate in mm/yr and colored according to Accretion Excess (above current sea level rise) obtained from radioisotopic dating. B) Demonstrates no relationship between elevation and accretion within the narrow range of elevations that were sampled. C) Illustrates a negative relationship between accretion and bulk density, D) shows the agreement between the cesium and lead dating techniques and panel E) indicates a relationship between accretion and organic accumulation (where LOI, or loss on ignition, provides a measure of the organic carbon lost during a high temperature burn).

Overall, the system-wide average rate of marsh accretion is only 2.12 mm/yr (AE_c: 0.81), suggesting these marshes are struggling to keep pace with sea-level rise, which is presently occurring at between 2.97 mm/yr (Newport, RI, NOAA gauge 8452660, NOAA 2025) and 3.13 mm/yr (Wood Hole, MA, NOAA gauge 8447930, NOAA 2025). These marshes are highly organic-rich, as revealed by high loss-on-ignition (median down-core average: 38.8 % by weight, which is about 85% organic by volume) with low soil bulk density (median down-core average: 0.27 g/cm) values, suggesting that these marshes rely more on belowground biomass production than surficial deposition of allochthonous sediment input for survival. These results contribute evidence that New England salt marshes are receiving low terrestrial sediment inputs, and thus, are more prone to drowning.

There is a long-standing assumption that marshes at higher elevations in the tidal frame (e.g., nearer to mean high water) will grow slower than those at lower elevation with respect to mean sea level that are flooded more often, because with that flooding water comes sediment to aid vertical accretion and nutrients to aid marsh growth. However, for the sampled marshes in Westport, MA, marsh elevation and accretion rates do not have a significant relationship ($R^2 = 0.06$, suggesting a nonexistent correlation). This suggests that the small differences in elevation (microtopography) across the salt marshes are not the primary factor driving marsh resilience to sea-level rise. This reflects the fact that the range of elevation across the sampled marshes is minimal: marshes at our sampling sites were located between 0.077 and 0.546 m above mean sea level, a range of only 47 cm in a location where the tidal range is closer to 100 cm. The data do, however, reveal that marsh accretion rates have a stronger, albeit statistically insignificant, negative correlation with average bulk density ($R^2 = 0.34$) and positive correlation with organic content ($R^2 = 0.37$). This means that, at least to some degree, the areas of the marsh growing fastest are those producing organic peats at the fastest rates.

To summarize, the rate of marsh accretion in Westport is low compared to sea level rise, and strongly dependent on biomass production. Area of AEc lower than 1 are at risk of not keeping pace with sea level rise, particularly if sea level rise continues to accelerate.

6.2.3 Morphological evolution of the shoreline

6.2.3.1 Beach profiles

Beach profiling provides useful information to help validate model findings on erosion by quantifying how much sand is lost from the beach face and dunes during large storms, and how far the system retreats. It also allows comparisons of stability amongst different regions of the coastline. To gain these insights, beach profiles were installed and surveyed before and after Winter Storm Elliott to provide information on how the beach changes during a storm. Winter Storm Elliot on 23 December 2022 was an intense storm having an annual exceedance probability of 10% (a once in 10-year storm). Comparing measurements taken on November 29th 2022 and on January 3rd 2023 during a falling tide provides a cross-sectional view of Winter Storm Elliott impacts (Figure 34). Photos taken at the same time document sedimentological and morphological changes to the beach and dune system (Figure 35).

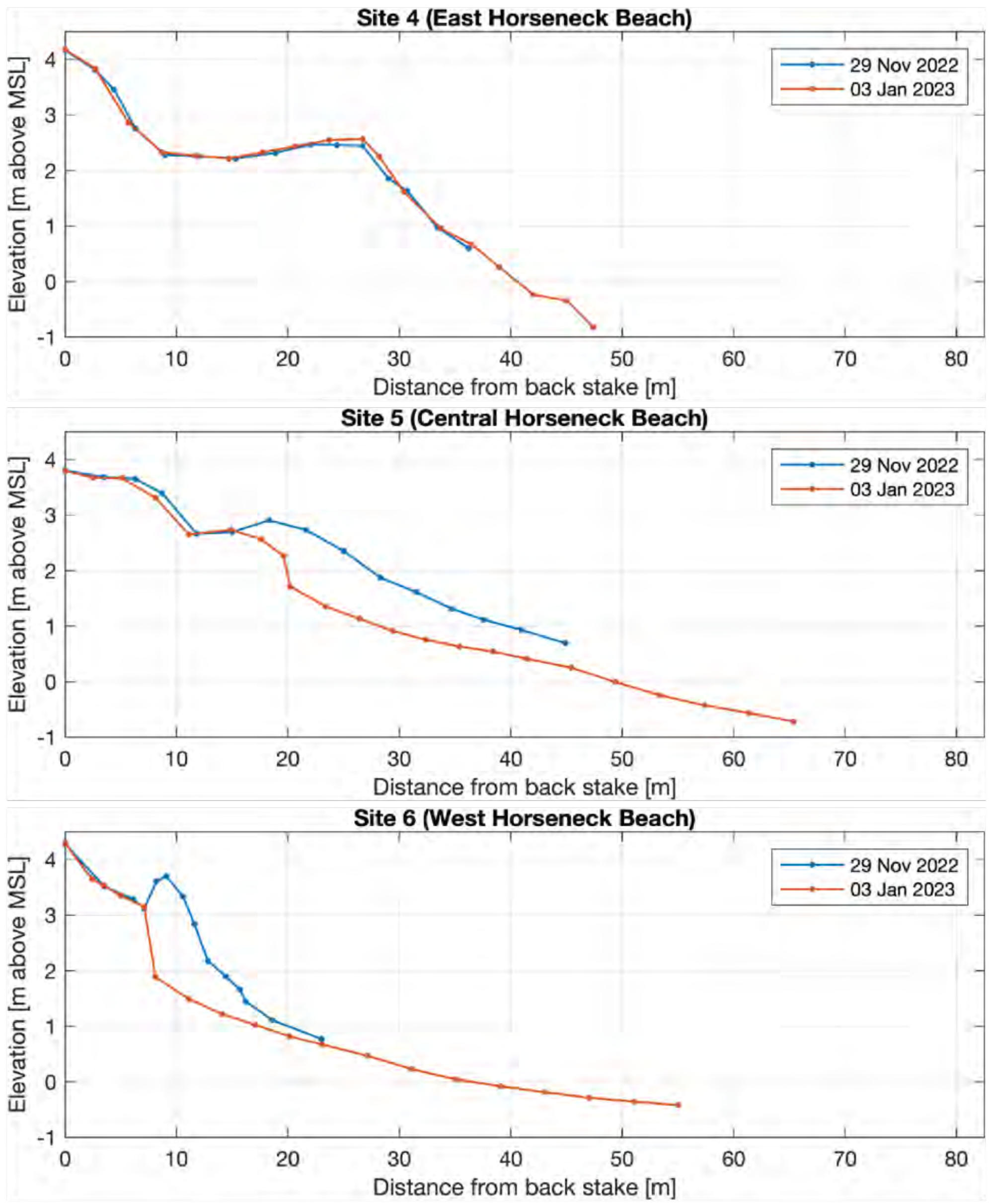

Figure 34. Beach profile changes during a winter storm presented for the three survey sites along Horseneck Beach (4, 5 and 6). Survey site locations shown in Figure 10. Accompanying photos of these sites are shown in Figure 35.

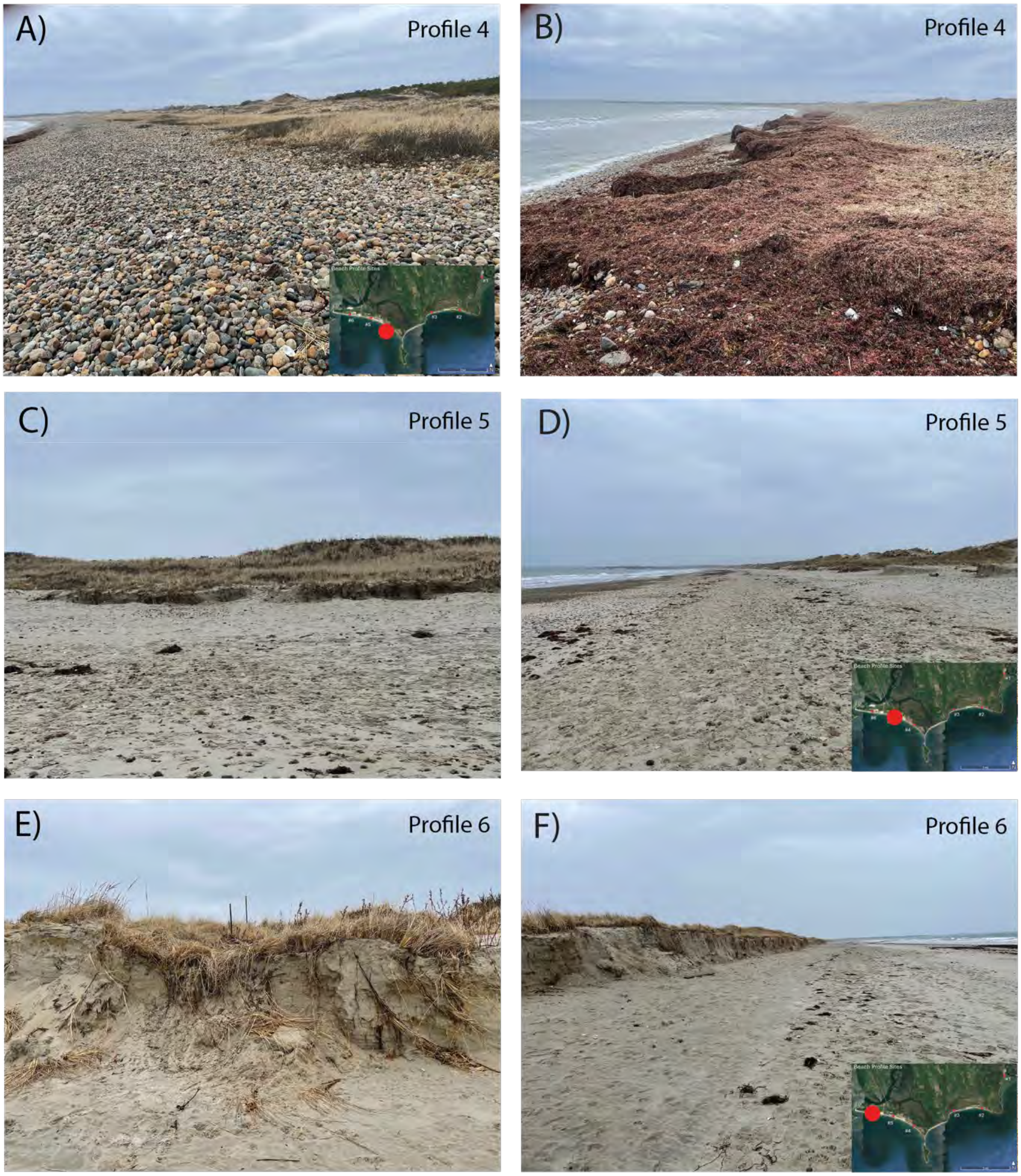

Figure 35. A) Site 4. Gravel berm invading the landward dunes. B) Site 4. Concentration of seaweed along the lower berm after the storm. C) Site 5 Dune scarp resulting from 7 m of dune retreat during storm Elliot. D) Site 5. View of the eroded beach following storm Elliot in 2023. E) Site 6. Photo of foredune scarp and beach profile stakes. F) Site 6. Longshore view of the eroded dune ridge.

The trends for the three profiles were consistent and can largely be explained based on beach composition. Beaches composed of gravel and made up mostly of rounded cobbles underwent very little change, whereas beaches consisting predominantly of sand experienced both vertical erosion and retreat of the landward foredune if present.

Site #4 is located along Horseneck Beach just west of the RV parking area. This site consists entirely of gravel and the profile exhibited very little change (Figures 34 A and 35 A). The major change was accumulation of seaweed (Figure 35 B).

Site #5 is located just west of the main Horseneck Beach parking lot region within the dunes. This section of beach and dunes experienced significant erosion during the winter of 2023 (Figure 34 B). The beach underwent a meter of vertical erosion, and the dune retreated 7 m (Figures 35 C and D).

Site #6 is positioned at the western end of Horseneck Beach consisting of a sandy beach backed by a well-formed dune ridge. After the storm, the foredune had retreated 5 m and the beach underwent 2 m of vertical erosion (Figure 34 C, Figure 35 E and F).

Winter Storm Elliot provided an excellent opportunity to record major storm wave and tidal conditions and observe their effects along the Westport and South Dartmouth shorelines. Observations concerning the storm are summarized below:

1. Winter Storm Elliot produced onshore winds ranging between 50 and 60 mph, water levels 1 m above mean high tide elevation, and offshore waves heights reaching 6 m.
2. Waves overtopped East Beach and water flowed into the Let carrying sand and gravel and debris onto the roadway and adjacent marsh.
3. Sandy beaches were eroded, whereas gravel beaches were mostly stable. Sandy beaches underwent more than a meter of vertical erosion and foredunes ridges retreated up to 7 m producing vertical scarps. On the west side of Slocums River Inlet, the dune was flattened.
4. Where foredunes were absent, overwash was a major process consisting of sand aprons deposited on the marsh surface at Slocums River Inlet and gravel ridges and fans deposited in back dunal areas elsewhere.

6.2.3.2 Peat depth and marsh evolution

There were two important trends that we learned from examining the salt marsh peat thickness across the study region (Figure 36). First, the pervasive sand unit that underlies most of the marsh peat indicates that much of marsh formed coincident with the widespread onshore movement of sand that occurred about 3,500-1,000 years ago. The depth to this sand falls within two major ranges: shallow (42 to 128 cm) and deep (> 200 cm). There is one outlier to this trend (eastern Allens Pond, 156 cm), which can be explained by the fact that this core was collected next to a mainland peninsula and marsh developed relatively early because it was an upland site. The relatively thin marsh peat locations have formed on broad sand sheets behind the present barriers, marking the leading edge of sand transgression into the embayments between the major peninsulas. This transgressive sand partly enclosed the landward bays and estuaries and served as a stable platform upon which the barrier systems originated and prograded seaward. The thick peats (> 200 m) are all found next to major estuaries or at sites of former tidal inlets or tidal channels. Because of the relatively deep elevation of these former valleys, saltwater intruded into these estuaries earlier during the marine transgression and marshes developed early at these sites. Note that the thicker peats are located 1. at the western end of Horseneck Beach next to the major pathway of Westport Estuary, 2. at the entrance to the Let (former discharge channel of the East Branch of Westport Estuary), 3. next to Slocums River Estuary, and 4. at the location of a former tidal channel to proto-Allens Pond.

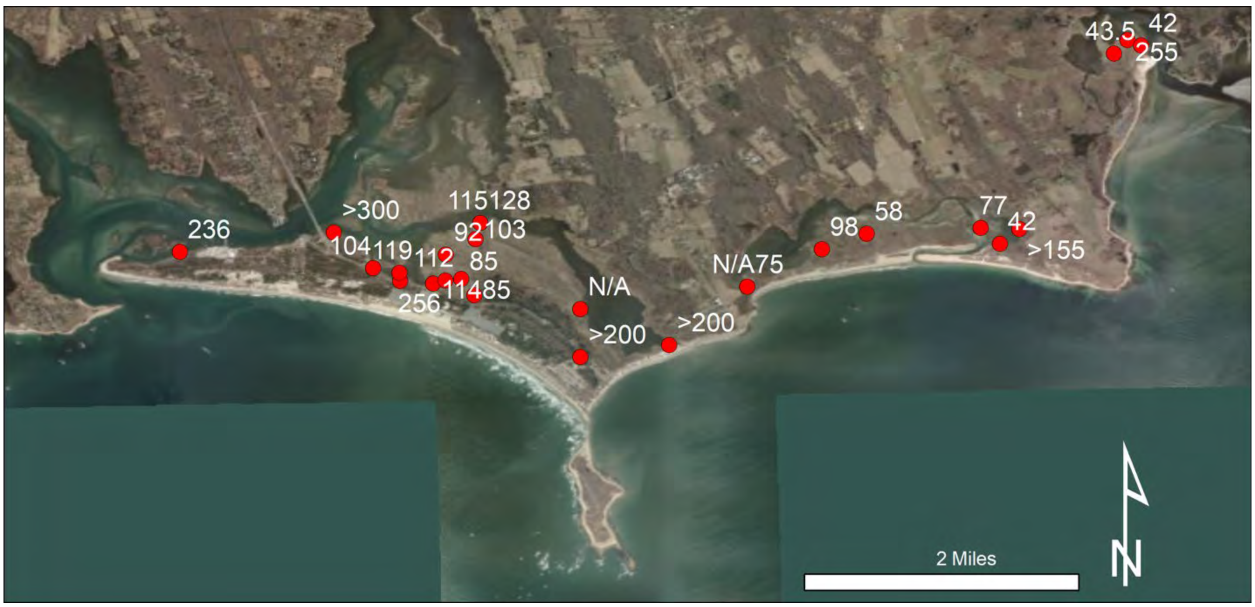

Figure 36. Depth of peat above sand layer in the study region, determined from coring.

These data help us better understand the distribution of sand and evolution of the system during post glacial sea level rise by providing insight into how much marsh has had time to develop on top of the underlying sand lens. This illustrates where deeper channels or offshore river systems existed in the past, having been filled in by coastal processes (sand movement onshore and bay infilling). These results have also allowed us to design the modeling domains with appropriate thicknesses of sand and gravel.

6.2.3.3 Barrier evolution and stability

Understanding the evolution of the coast, such as the opening and closing of previous inlets or widening or narrowing of barriers, aids in determining long term (100s of years) sediment transport patterns and predictions of barrier and shoreline stability in the future. Ground-penetrating radar (GPR) produces an X-ray view of the sedimentary layers, and glacial contacts below the surface. GPR has provided a tool for interpreting the accretionary history of the shoreline and has been particularly useful in determining barrier evolution, inlet closure, and sand thicknesses. Coverage of GPR transects throughout the project area is given in Figure 3 above.

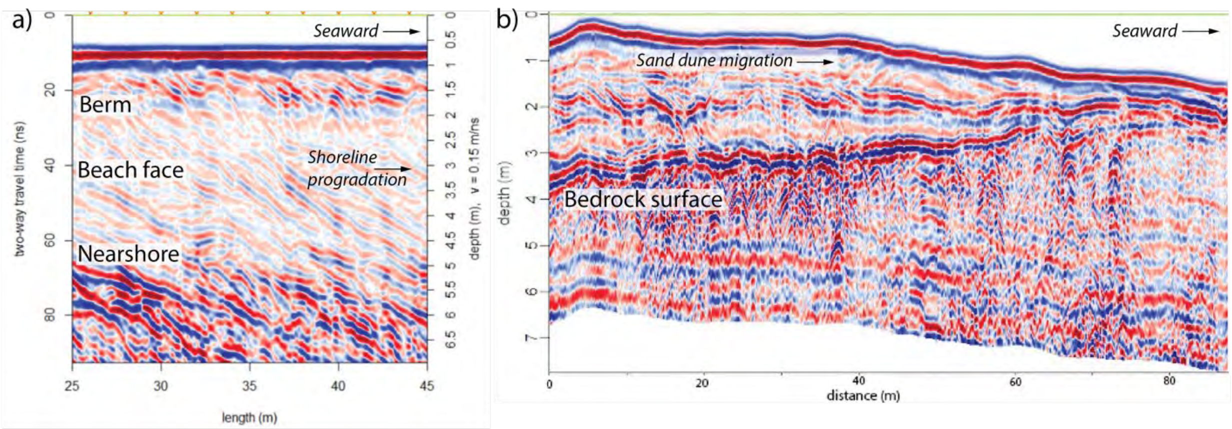

Figure 37. a) Ground-penetrating radar profile illustrating shoreline progradation. Offshore features underlie 'onshore' features as the shoreline builds seaward. b) Beach out-building (seaward dipping reflectors) over a till or bedrock surface identified by the strong reflectors

The surficial geomorphology map for Southeastern Massachusetts shows extensive sand and gravel deposits in Westport and Slocums River valleys; it is highly likely that similar sediment was laid down in the seaward extensions of these valleys (now offshore). Following deglaciation and retreat of the continental ice sheet, sea level began rising precipitously (~ 1 cm/yr; Figure 8b). By 5,000 yrs before present the transgressing sea intercepted the offshore glacial-fluvial sediment, and the attendant wave action began reworking the finer fraction of these deposits onshore, consisting primarily of sand and fine gravel (granules). By about 3,500 yrs ago, the rate of sea-level rise began to slow to ~1 - 2 mm/yr (Figure 8b) and the onshore movement of sand out-paced rising sea level. During this time, sand began stacking up forming beaches, barriers, and spits. Each of these prograding shorelines exhibits a distinctive geophysical signature. As seen in Figure 37a from Horseneck Beach, repetitive seaward dipping reflectors are indicative of a prograding sequence replicating: (bottom) flatter reflectors of offshore, (middle) more steeply dipping reflectors representing the beachface and nearshore, and finally (top) low gradient berm (gently dipping reflectors). The reflectors are formed by changes in grain size, composition, packing, and other physical and geotechnical properties. A second GPR profile in the Barney's Joy region illustrates a 3-m thick beach progradation unit overlying a till or bedrock surface, which is represented by the sharp reflectors produced by a strong energy return (Figure 37b). A third profile, taken in the western end of Horseneck Beach perpendicular to the trend of the barrier can be seen in Figure 42c. It shows a seaward prograding barrier (seaward dipping reflectors) over-printed by more steeply landward-dipping reflectors produced by the onshore migration of a very large sand dune. From this we can conclude that, for a long time, since about 3,500 years before present, the landward movement of sand and slow SLR has allowed the shoreline to prograde, with sediment being moved by waves from offshore into the widening barrier beach system. This trend has changed recently, with SLR accelerating to ~3 mm/yr, significantly impacting onshore-offshore sediment transport processes.

Paleo-entrance to Westport River Estuary

A comprehensive set of GPR profiles was collected in the mid-barrier Horseneck Beach parking lot area and along John Reed Road (Figure 38) for the purpose of documenting barrier progradation and exploring the former eastern entrance to the Westport River. A profile along John Reed Road captured a 250-m wide and 5.7-m deep channel located at the eastern side of the paleo-estuary (Figure 39; see location in Figure 38), which has similar dimensions to that of the present-day Westport River Inlet at Acoaxet Point.

Figure 38. A network of GPR transects was collected within the parking lot and along John Reed Road. The yellow lines represent “dip” profiles perpendicular to barrier progradation and the blue lines are “strike” transects taken parallel to the barrier trend. The green lines are GPR profiles taken obliquely to sedimentation patterns.

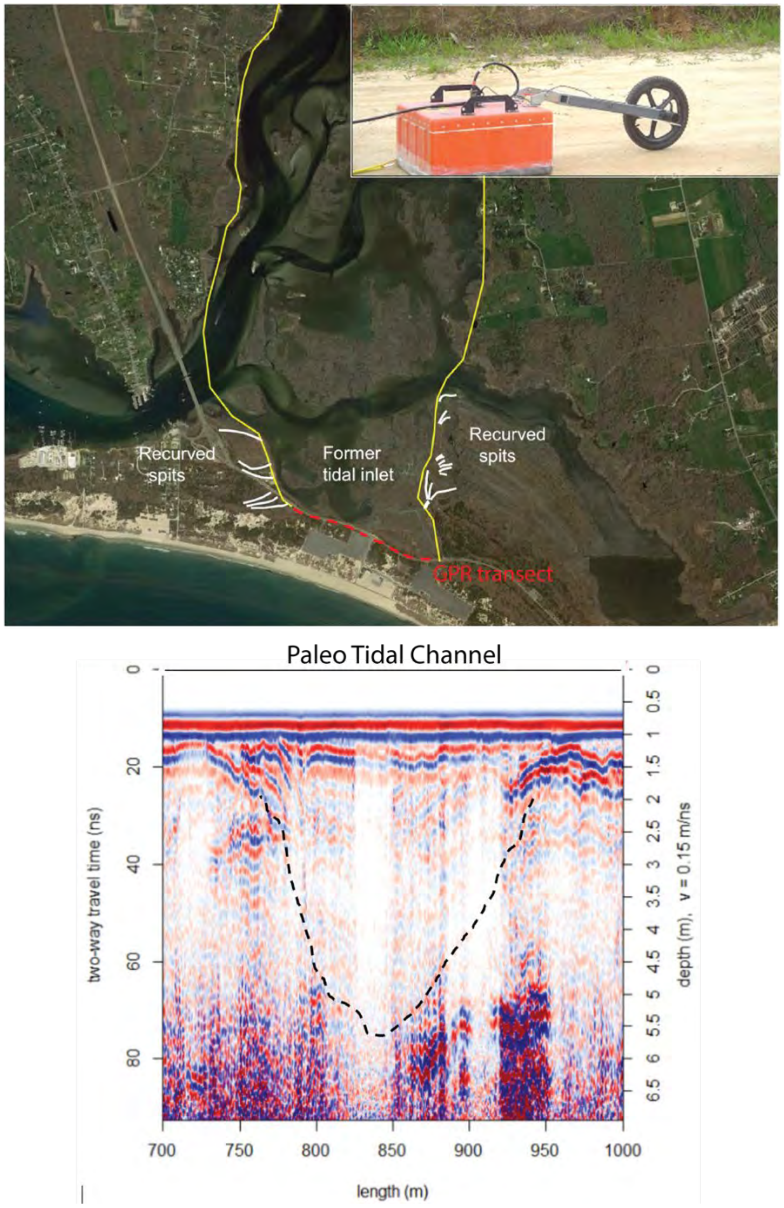

Figure 39. a) The location of a former tidal inlet that existed prior to formation of the Horseneck barrier (red dashed line). Recurved spit ridges on both sides of this reentrant suggest that this was a site of paleo-discharge from the Westport River. This is confirmed by the ground-penetrating radar profile in b) showing a paleo-channel (delineated by the dashed black line). The faint lines within the outlined channel show how the channel gradually filled with sediment.

Interpretation of the GPR, aided by analyses of aerial photographs, indicates the former entrance of the East Branch of Westport River Estuary once flowed through what is now the middle of Horseneck Beach. The overall size of the opening can be delineated from the presence of paleo-recurved beach ridges that exist on either side of a broad marsh and tidal channel system north of Route 88 (Figure 39a). These recurved ridges are typical of features formed as waves refracted into the estuary transporting sand along the flanks of the channel. Beach ridges that developed *within* Westport River Estuary were formed during a lower stand of sea level. Today, rising sea level has partly drowned many of these ridges, allowing marsh to grow atop them and in inter-ridge swales (see Figure 40). The paleo-tidal inlet closed before the Let to its east. This will have occurred because of the onshore movement of large quantities of sand during the Holocene transgression described above and because the infilling of the bay. From this we can conclude that over time, as the barrier formed, the bay behind it filled in and the amount of water flowing into and out of the bay each tide (the tidal prism) reduced. Once closed there was not enough tidal prism to reopen the inlet.

Figure 40. Delineation of inlet-associated channel-aligned beach ridges on the eastside of the paleo-tidal inlet/estuary.

Figure 41. Annotated images (from Google Earth) showing a) the western end of the Horseneck barrier displaying a series of recurved ridges indicating a westerly extension of the barrier (350 m) through spit accretion, this can also be seen in b) which provides context for the location of images a and c; and c) showing prograding beach ridges aligned with the backbarrier which show the earliest development of Horseneck Beach.

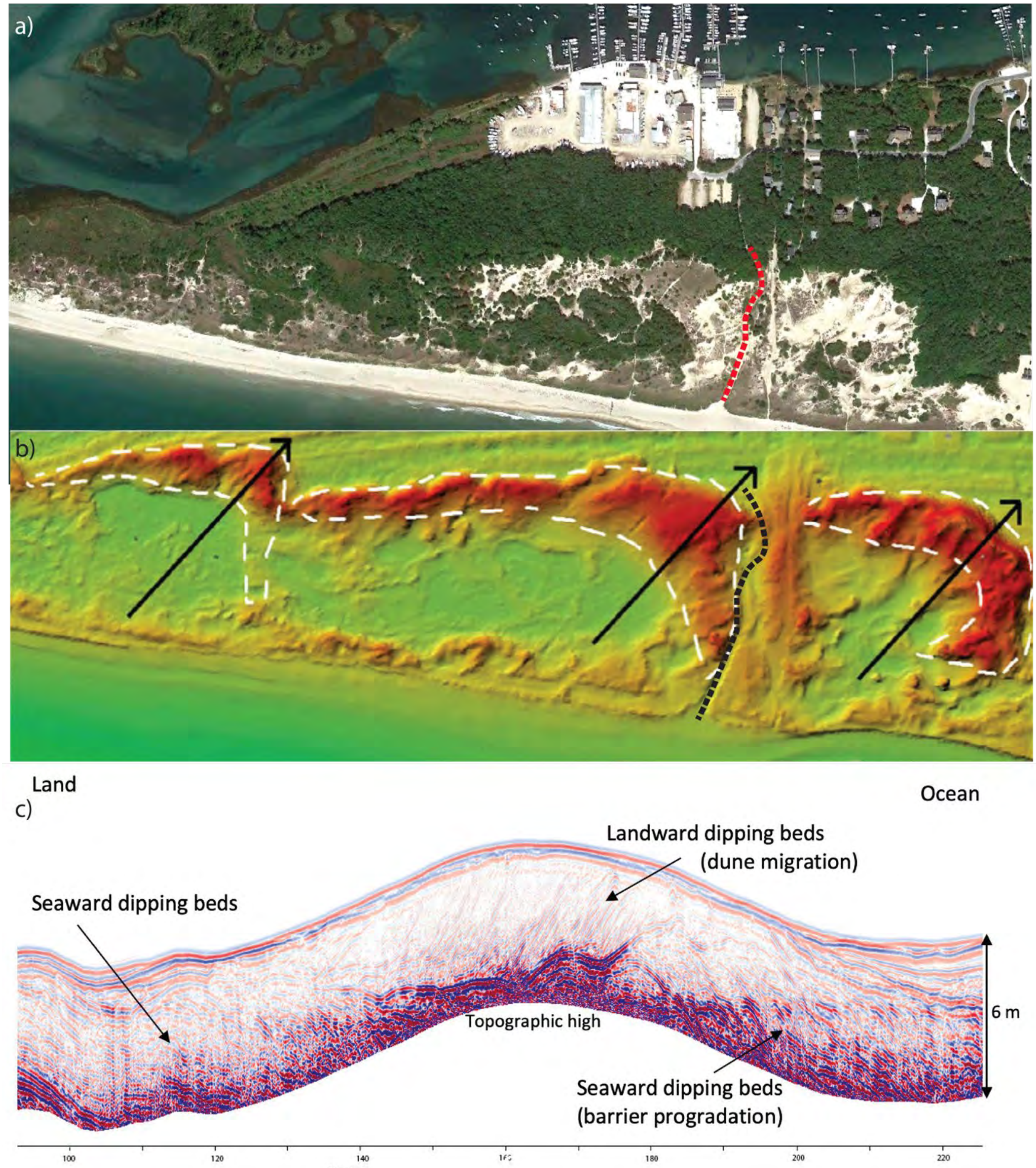

Figure 42. The development of large arcuate dunes on the western end of Horseneck Beach, shown in a) an aerial image with a GPR transect shown as a red dashed line, b) LiDAR, where the shape of the dunes is outlines in a white dashed line and the direction of migration and growth is indicated by the black arrow and the GPR transect is shown as a black dashed line, and c) GPR data, where landward dipping dune reflectors can be seen overlying seaward dipping prograding barrier reflectors as the dune migrates away from the beach.

Westport barrier progradation and spit accretion:

Although human modifications and dune migration have masked much of the evolutionary development of Horseneck Beach and surrounding region, there is still evidence of its early history preserved along the backside of the barrier (Figure 41, 42). Next to Tripps Boat Yard there is a series of prograding beach ridges indicating that western Horseneck Beach evolved in a manner similar to the eastern end of the barrier (Figure 41c). Following establishment of the barrier core, the barrier lengthened through spit accretion as evidence by the recurves shown in Figure 41a. Narrowing of Westport River Inlet may have been a result of a decreasing tidal prism caused by tidal flat building and marsh development. Figure 42 illustrates the fate of the large volumes of sand that have moved westward along Horseneck beach. This sand has created the massive dune system that has formed on the western end of Horseneck barrier (shown in an aerial image and a LiDAR image, Figures 42 a and b respectively). Figure 42 c shows a GPR profile taken across the western end of Horseneck Beach perpendicular to the trend of the barrier (shown as a dash line on Figure 42 a and b). The record shows a seaward prograding barrier (seaward dipping reflectors) over-printed by more steeply landward-dipping reflectors produced by the onshore migration of a very large sand dune. The cuspate dunes seen in these images hold an enormous about of fine sand.

These findings indicate that the west of Horseneck beach is a sink for sand that has been moved westward and that the end of the spit has a history of lengthening. Fine sediment has also been moved onto the barrier by wind creating massive dunes. When the island lengthened it caused the Westport inlet to narrow. As with the paleo inlet, this happened in response to the bay filling in with marsh and fine sediment. It is now the remaining inlet in the system and it remains open in equilibrium with the present tidal prism (D'Alpaos et al, 2009) by 1) moving sand into the bay around the point of the spit (recurve spit progradation) 2) moving sediment onto the flood tidal delta (within the bay) and 3) moving sand onto the ebb delta (offshore) where waves can move it across to Acoaxet and west of the Knubble through inlet bypassing.

East Beach evolution and stability

East Beach was formed when landward moving sand and gravel closed off the inlet at the entrance to the Let and as the tidal prism to maintain the inlet reduced. GPR from the region shows the gradual infilling of a wide, shallow channel (~130 m wide, 3 m deep; Appendix A, Figure A7). The Let has since filled with fine sediment and is now uniformly flat and shallow, with evidence of the tidal channel that once flowed there completely erased by infilling. The 2018 LiDAR data (Figure 43 A and B) penetrated to depths of almost 15 m in some areas. This allows a comparative look at the depth of shallow regions of the Westport estuary and offshore. There are no longer any signs of the channel that must once have connected the inlet that once opened through East Beach into the Let. The bed is uniformly about 0.8 m below NAVD88, or 0.92 m below mean sea level. Sediment brought down the river and into the bay collects in this low energy area. However, the water also shallows just behind the barrier, (shown more clearly in Figure 43 B in which the depth range displayed has been reduced to allow focus on the depths between 2 and -2 m below NADV1988) particularly in the middle section. Here the seabed is shoaling, indicative of sedimentation from the from the seaward side of the barrier, reaching the Let either as the wind blows finer sediment across the barrier, or as coarser sediment is washed over by storm waves. This has allowed sections of the marsh to grow by as much as 15 m into the bay.

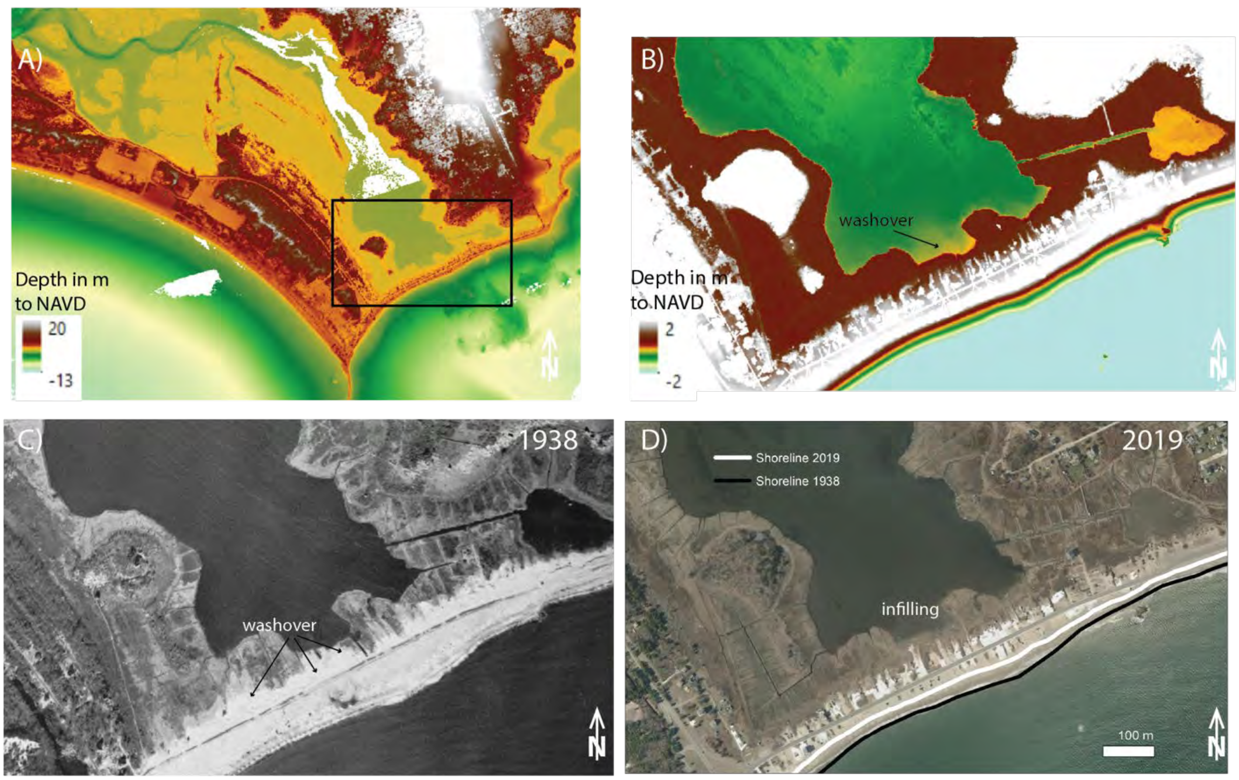

Figure 43 East Beach and the Let. A) LiDAR with color range set to highlight dunes and channels around East Beach, an area of no data (white) can be seen in the middle of the Let where reflection or roughness of the surface prevented the LiDAR from penetrating the water surface, the Let is shallow and previous tidal channels have been filled in. The black rectangle shows the outline of images B, C and D. B) Refining the elevations of interest to provide high resolution elevation within the Let and on the back of the barrier, shallowing towards the beach can be seen, indicating that the area is receiving sediment most likely from washover events, C) Aerial image from 1938 (post Hurricane) and D) Aerial image from 2019 showing a change in position of the front and back of the barrier.

Figure 43C shows the beach shortly after the Hurricane of 1938. Sandy sediment and pebbles from the foreshore were washed across the barrier, flattening dunes and destroying homes. By 2019, much of that sand had either been blown or washed into the Let or stabilized by vegetation (Figure 43D). The front side of the barrier retreated by approximately 25 to 35 meters along the shoreline—an average of 0.4 meters per year—consistent with observations by Massachusetts Coastal Zone Management (Figure 43D). These observations support the conclusion that the barrier is retreating in response to sea level rise, a process known as barrier rollover (Lorenzo-Trueba and Ashton, 2014).

East Beach is composed chiefly of gravel and has been actively rolling over itself since at least 1938. Most of the beachface and supratidal surface consist of gravel and scattered patches of sand, based on sediment sampling. Cores taken behind the barrier in the marsh encounter gravel at shallow depths (<1 m). As previously discussed, the Let is shallow and has been significantly cut off from the Westport River Estuary by sedimentation and marsh expansion.

Although concerns have been raised about potential breaching of East Beach, most new tidal inlets typically originate from the backside of the barrier. Were a cut to form through the barrier during a storm, there would be minimal tidal flow to sustain it due to constrictions and the shallow nature of the former channel. The likelihood of a permanent breach forming through the Let is extremely low. Additionally, the lack of pronounced low-lying areas along the barrier further reduces the potential for even temporary breaches.

Loss of sand and a shift toward a more gravel-dominated system is likely as offshore sand resources become exhausted or immobilized by increasing water depth with sea level rise. However, historical imagery shows that the beach has long exhibited coarse sediment, including gravel dunes and berms, even prior to the 1938 hurricane. These images suggest that the Hurricane of 1938 transported significant amounts of sandy sediment from the nearshore zone onto the gravel barrier system (Appendix A, Figure A8).

To summarize, East Beach is a low, gravel-based barrier that is gradually responding to sea level rise through the process of rollover. It is expected to continue retreating at a similar pace. As sand is moved over and along the barrier, coarser sand—and eventually gravel—is likely to move onshore as finer sand sources are depleted.

6.3 Numerical Modeling

6.3.1 Westport and East Beach circulation

To examine the impact of Gooseberry Neck, and specifically the causeway itself, we began by examining existing circulation patterns and the impact of the headland itself on the conditions at the shore. The examination of the headland impact is published in Xie et al (2023, attached in Appendix B). We showed that under storm conditions, the headland itself is responsible for large near-shore circulation cells. These wave-generated flows moved from offshore, along the sides of the island and then turned along shore as they reached the mainland (clockwise on the east of the Island and anticlockwise on the west of the Island, for example see Figure 44 b). These circulation cells were triggered by *large waves events*, were often complex with the number of cells and the exact position with respect to the mainland differed dependent on wave height and length, and sea level. Transport along Horseneck Beach was commonly directed towards the west, against the direction from which the waves were actually approaching. This pattern of transport is validated by the growth of the west end of the Horseneck Beach spit (i.e., the eastern side of the Westport inlet) and the buildup of large dunes in that region. Gooseberry Island was found, as with most headlands, to be a focus of wave energy and high bed shear stress (a measure of erosion potential; Figure 44c). Note that during the strong circulation that was set up during Storm Elliot (considered a once in 10 year storm) the circulation cell formed on the west of the Island does reach as far as the middle of the Horseneck State Beach. It does not reach the tidal inlet. Any influence that the cell had on the flow out of the inlet would be to direct it offshore more sharply than it may otherwise have moved. East Beach also experiences a strong circulation cell moving anticlockwise up the side of Gooseberry Island, eastward along East Beach and then ultimately offshore in front of Little Beach and Allens pond.

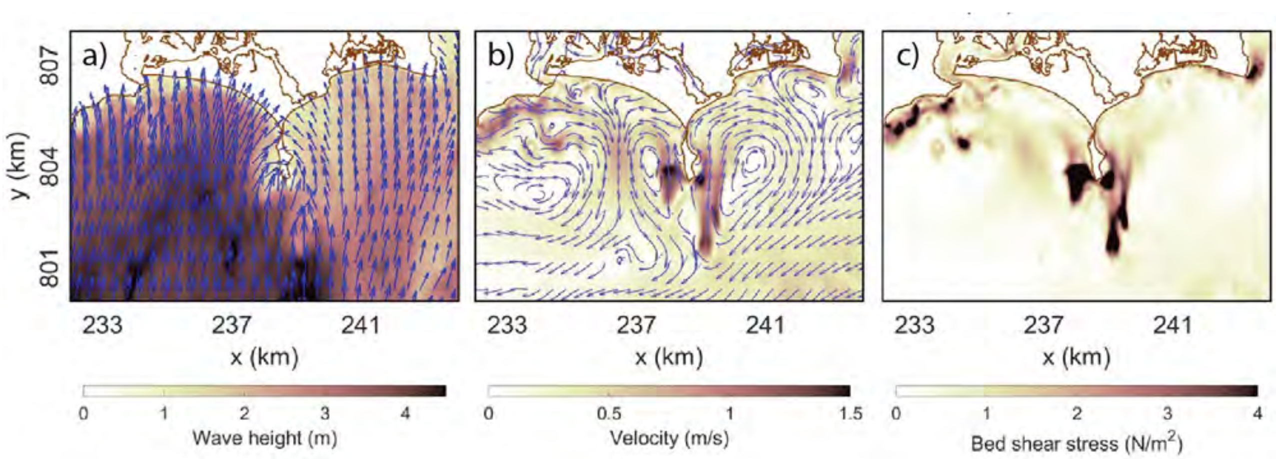

Figure 44 a) Wave propagation map, b) flow velocity field with the formation of circulation cells on both sides of the headland, and c) bed shear stress. These results are based on Storm Elliott (Dec 2022).

The impact of strong waves on circulation around the Westport inlet can be seen in Figure 45. Here the model was used to compare tide and wave generated flows, and sediment erosion under a reference storm (8m waves), the reference conditions were then broken into the component parts to see their relative impacts: tide only, storm surge only and waves only.

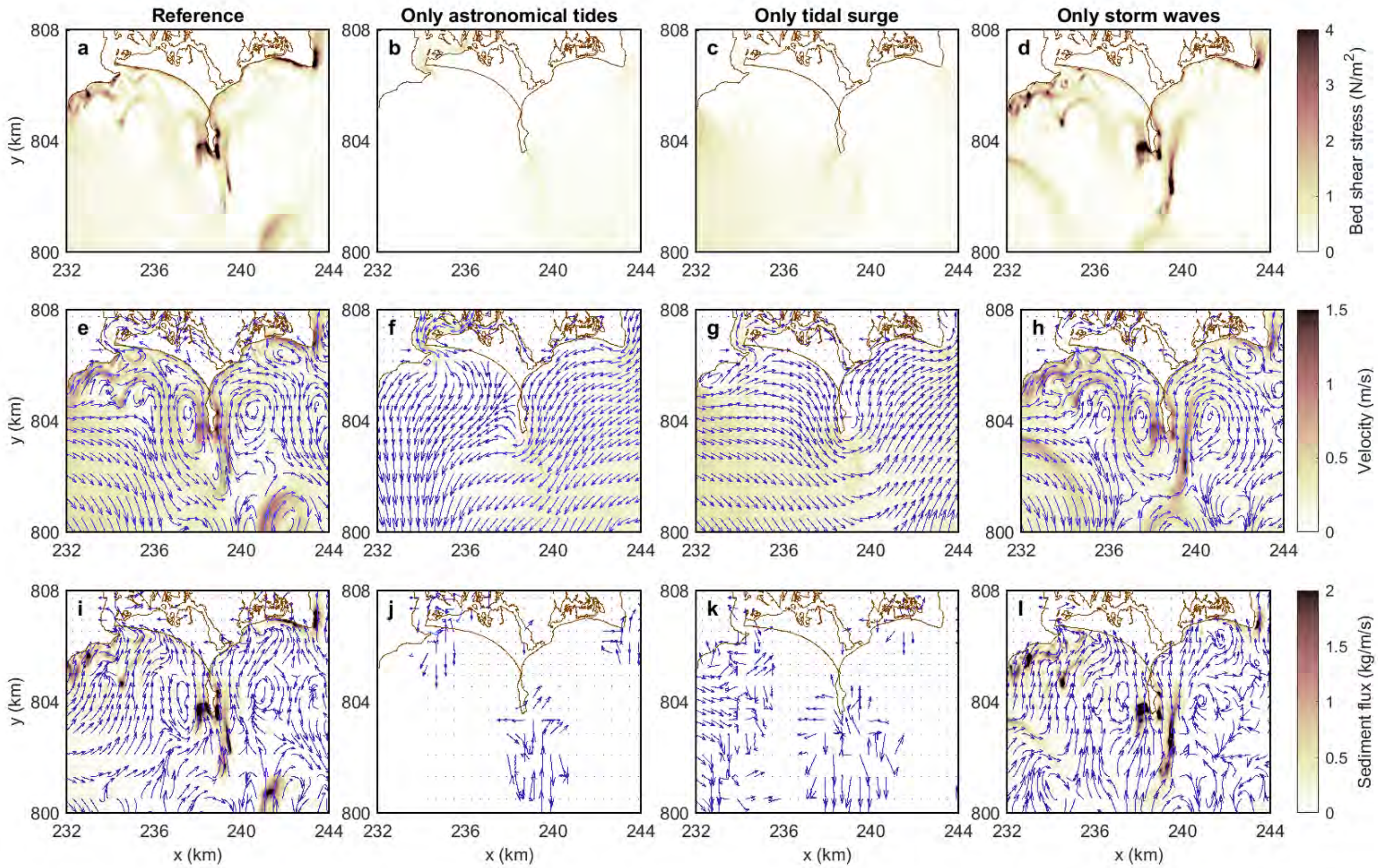

Figure 45. Bed shear stress (top row), velocity and direction of flow (wave and/or tide generated; middle row) and sediment transport magnitude and direction (bottom row), for a reference storm (8 m waves, from SSW) and individual contributing factors: tides, storm surge and waves. The magnitude of the wave impacts and the similarity between the storm and the wave only conditions highlight the impact of waves along this coastline.

The circulation either side of the causeway is seen to develop when waves are present. Under a tide only scenario, no circulation cells are set up. However, there is still a convergence of westward flowing water and north-eastward flowing water towards the eastern end of Horseneck State beach, which causes an offshore flow and interrupts any longshore transport at the end of the beach. These results also highlight the fact that the westerly sediment transport, clearly evident from the development of large sand bodies on the west end of the island, and coarser sediment on the east end of the island, is a response to wave generated transport.

6.3.2 Gooseberry Causeway

We moved on to assess the impact of removing the causeway. Two versions of a small, refined grid were created, one with the causeway as it presently is and one representing the 1892 beach configuration with no causeway. The latter was created based on historical charts and was allowed to reach an equilibrium under low-wave tidal conditions (Figure 24 in the Methods Section). As with the modeling undertaken previously, we observed large circulation cells forming either side of where the causeway now sits during high wave energy conditions (i.e., storm events). Three historical storms were simulated (Hurricane Bob, 1991; Hurricane Irene, 2011; and Storm Elliot, 2022) along with 16 scenarios representing historical storm surge, wind/wave direction and wave height conditions (in a factorial design). Here the reference conditions (REF) were a storm with 4 m waves.

Examining results from the model without the causeway, we found that under most low energy and storm conditions flows were either too weak to transport a significant amount of sediment or, when waves were larger, they were dominated by the near-shore circulation cells. Some key results are provided in Figures 46 and 47. The figures show the formation of circulation cells either side of Gooseberry Island under two different idealized storm scenarios. In both storms there is an average storm surge (0.65 m) and the waves approach from the south-southwest. The circulation cell on the west of the Island flows in an anticlockwise direction. It forms close enough to the mainland shore to prevent long shore transport from west to east. This meant that flows that occurred across the tombolo came from the southwest of the island, and not from along Horseneck Beach. The area to the west of Gooseberry Island has a rocky seabed with minimal sand. Consequently, the water flows from a sediment-free area along the western shore of Gooseberry Island. Thus, moderate storm conditions results in minimal sediment transport across the tombolo due to the area they flow from, despite some cross-tombolo currents occurring. It is only when waves are larger, under hurricane conditions, that the waves were large enough to break further offshore moving the circulations cells far enough from the beach to allow longshore transport from west to east along Horseneck Beach and, therefore, across the tombolo (where the causeway sits in reality).

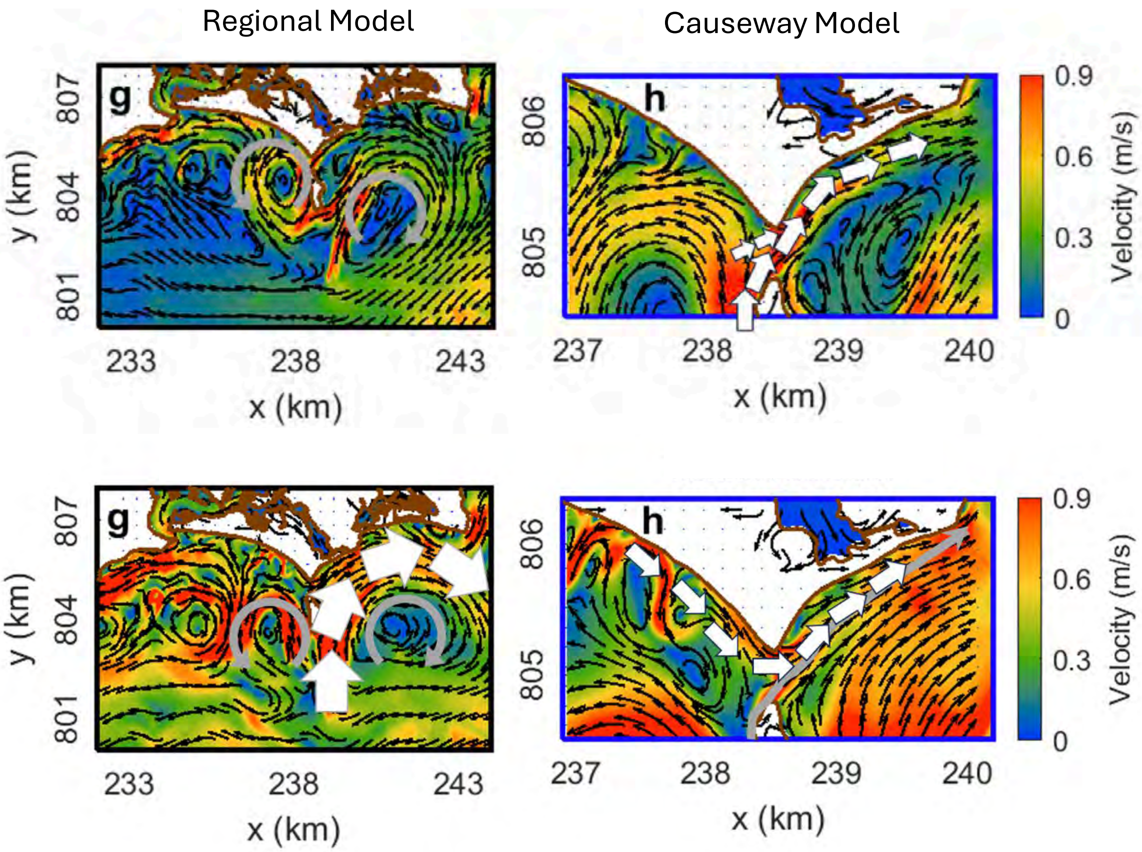

Figure 46. Water flow field during storms in the absence of the causeway. Panels A and B illustrate REF a small reference storm (see Table 4). Panels C and D show a theoretical storm with very large, "hurricane condition" waves (8.5 m from 185 degrees, i.e., SSW). Current velocity (generated by combined waves, tides and storm surge) is indicated by background color and arrow size, with direction indicated by black arrows. Grey and white arrows have been added to show the net flow and sediment transport pathways, respectively.

Figure 47 shows a comparison between the model with and without the causeway for a moderate storm condition with 4 m waves approaching from the south-southwest. The flow fields are very similar; however, water flow is observed across the tombolo when the causeway is not present because of the higher water level on the west side of the island (i.e., facing the direction the waves are approaching) compared to the east side of the island (i.e., protected from the waves by the Island). As a result, a small amount of sediment is moved from the west of the island to the east of the island. This sediment would eventually (after the storm subsided) be transported further east by lower energy conditions. However, it should be noted that the east end of East Beach will be an area of beach erosion and sediment loss because of the wave generated currents moving the sand either offshore, or along toward Little Beach. This is supported by aerial photos where the shoreline can be seen to be rocky, and shoreline change analyses, which show the shoreline retreating (Figure 43), We examined whether the sediment transported from

Horseneck Beach under the no causeway scenario would be sufficient to make up for losses from East Beach (Figure 47). Results displayed here are based on a reference scenario with south-southwest wave direction and a small storm surge. Panel c shows that in the absence of the causeway, the velocities would be higher on the west side of the island and lower on the east side. This is the result of a water level difference. With the causeway removed, the water level difference triggers a flow from the west to the east (indicated by the black arrow). The net differences in bed level shown in Panel f show a small (<10 cm) amount of deposition on East Beach close to the tombolo. This is a result of transport from both the west side and east sides of Gooseberry Island (indicated by areas of elevation loss in these areas).

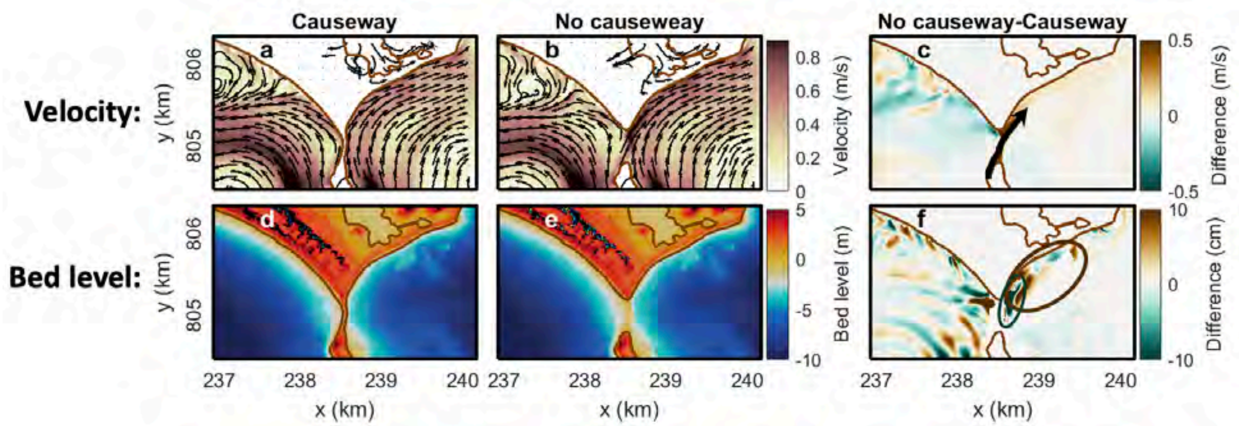

Figure 47. Comparison of flow velocity and bed level between scenarios with and without causeway. The flow velocity field (generated by a combination of waves, currents and storm surge) during peak wave height with (a) and without (b) causeway and the difference between them (c). Black arrow on c indicates water flow that would occur if the causeway did not exist. Bed level (i.e., bathymetry) at the end of simulation with (d) and without (e) the causeway and the difference between them (f). On panel f, shades of brown indicate sediment deposition while shades of blue indicate sediment erosion that would occur if the causeway did not exist.

To determine the gains and losses to East Beach (without the causeway) and the net trajectory of the beach, we tracked the transport into and out of the area. These results are shown in Figure 48. East Beach consistently loses sediment at a much greater rate than the rate of transport across the causeway, resulting in net loss from the beach. The results from the historical storms (Elliot, Irene, and Bob) indicate that the reference storms used to assess potential sediment transport in the previous section, and during which wind and wave directions were kept constant, likely overpredict compared to reality (i.e., the historical storms) where conditions vary during the storm.

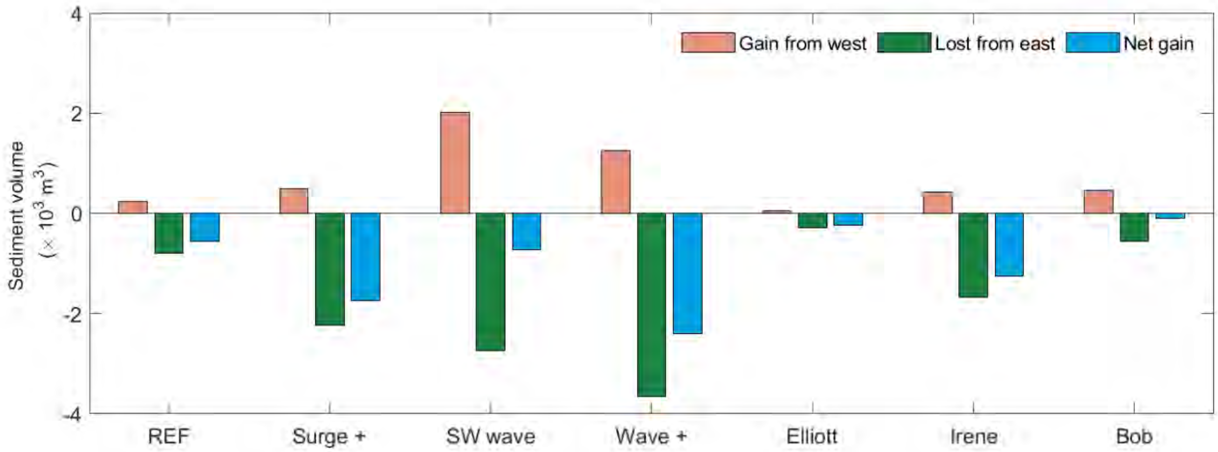

Figure 48. The total sediment thickness changes from the west sediment (warm red), east sediment (green) and total sediment change on East Beach (blue). REF is a moderate storm condition based on an assessment of historical storms. Surge + represents conditions with a higher storm surge than REF, with other conditions held the same. SW wave represents a more southwesterly wave than the normal storm conditions in REF. Wave + represents higher wave conditions (8.5 m) than REF with other conditions held the same.

The model indicates that if the causeway had not been built, transport would only be expected during large wave conditions when water level difference could drive a flow across the tombolo. The data demonstrates that even when sediment is transported across the tombolo during storms large enough to trigger the cross-shore transport, the combined loss from East Beach to the offshore and to Little Beach exceed any gains from sediment transported across the tombolo. More details of this study are provided in Xie et al (2024). The results of this section are further summarized in the synthesis below.

6.4 Climate change impacts

We examined how different climate scenarios impact the hydrodynamic environment along Horseneck and East Beach. Our findings reveal opposing behaviors of circulation cells in response to SLR (Figure 49) and higher storm wave scenarios (Figure 50), affecting both velocity and bottom shear stress on the beach and potentially influencing headland bypassing. In SLR scenarios, higher water levels allow waves to propagate farther into both beach and headland areas (Figure 49). This is due to the primary wave-breaking zone moving closer to shore simultaneously with SLR, leading to higher flow velocity and bed shear stress along the beach. In contrast, increased wave energy predominantly elevates wave height offshore rather than around the headland (Figure 50 a), reducing both velocity and bed shear stress along the beach (Figure 50 b-c). In these scenarios, the wave-breaking zone expands with intensified energy dissipation occurring at the edge of shallow areas, around 10 m depth. As a result, these distinct wave energy dissipation patterns intensify nearshore circulation cells in the SLR scenarios versus offshore circulation currents in higher storm wave scenarios (Figure 49b vs. Figure 50b). These findings align with similar studies by Mouragues et al. (2020), which also highlight that increasing wave height expands the surf zone area causing the circulation cells to move to deeper waters.

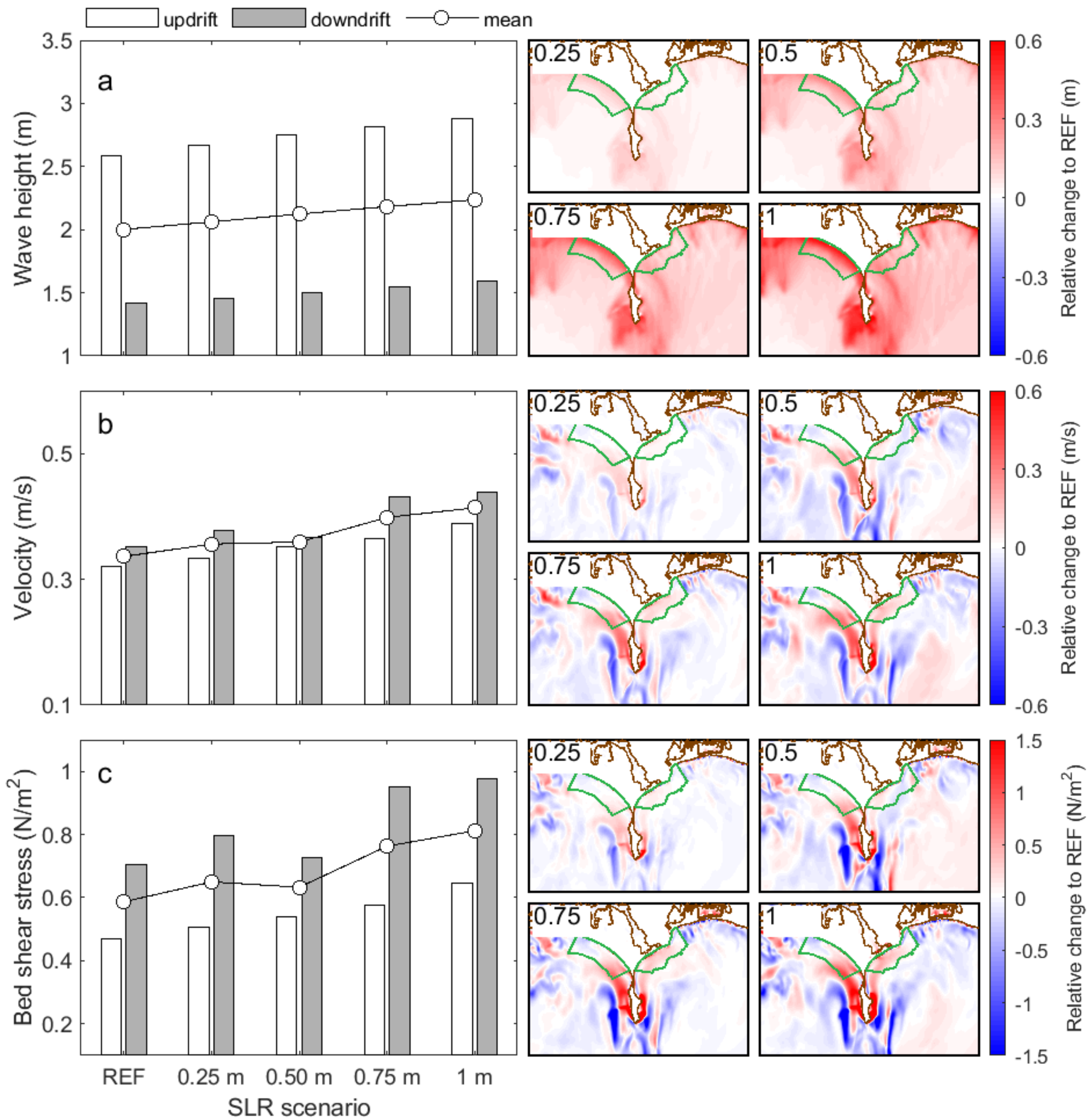

Figure 49. Changes in wave height, velocity, and bed shear stress under different sea-level rise scenarios. The bar graphs in the left panel are based on the median values of these hydrodynamic parameters in the updrift and downdrift beach regions, respectively. The mean of two bar values is represented by circles on the graph. The spatial distribution of the relative changes in these three hydrodynamic parameters is presented in the right panel. These relative changes are based on the reference results.

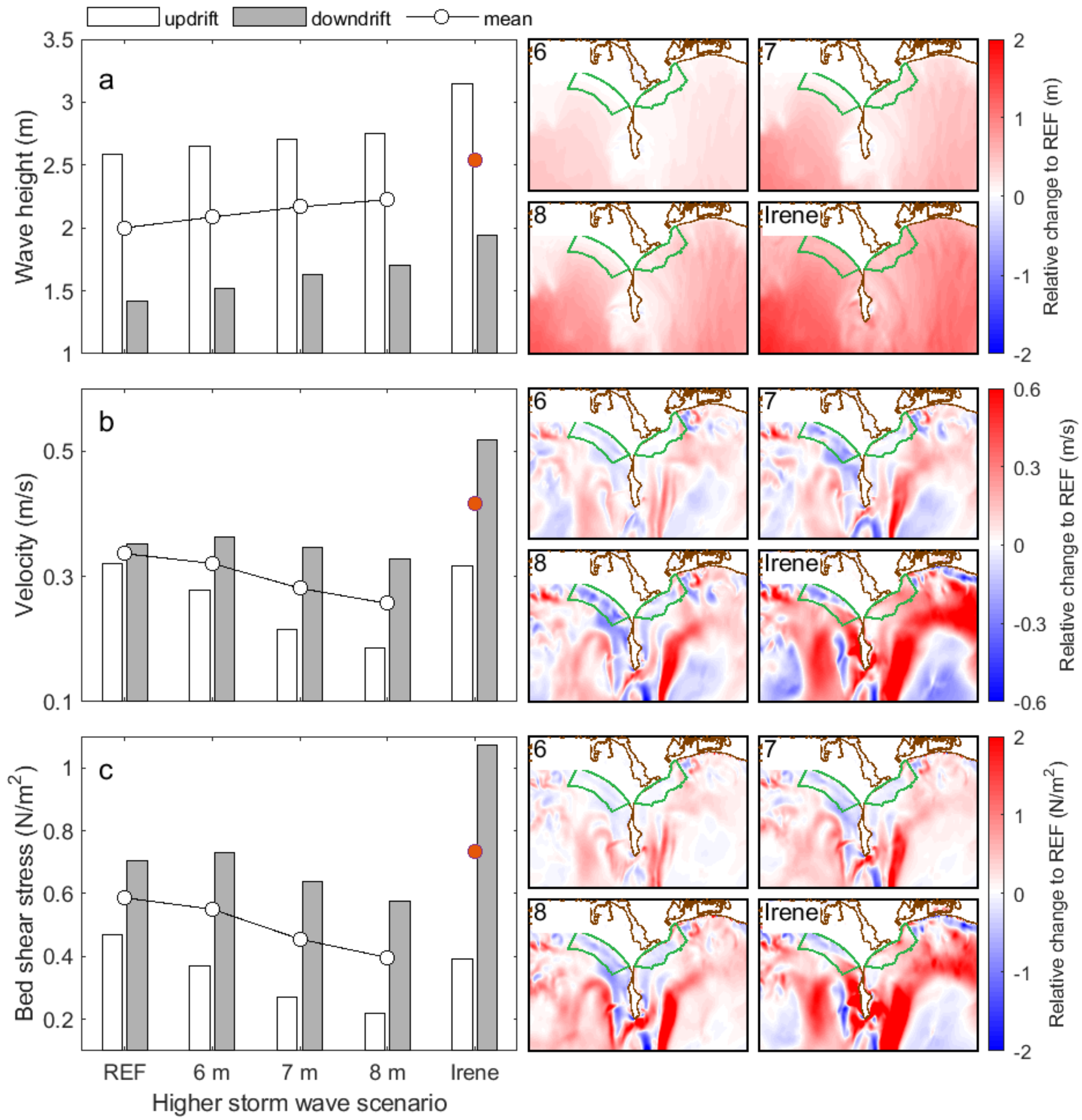

Figure 50. Changes in wave height, velocity, and bed shear stress under different scenarios of storm waves. The bar graphs in the left panel are based on the median values of these hydrodynamic parameters from the updrift beach region and the downdrift beach region, respectively. The mean of two bar values is represented by circles on the graph. The spatial distribution of the relative changes in these three hydrodynamic parameters is presented in the right panel. These relative changes are based on the reference results. Hydrodynamic parameters of Hurricane Irene are provided for a comparison.

These analyses suggest that the increase in velocity or bed shear stress close to shore due to SLR could be balanced by increasing wave height, leading to minimal changes to erosion rates under certain combinations. The exact combinations of SLR and storm waves will be critical in determining the exact hydrodynamic and morphodynamic changes along the beach in the future. Unfortunately, scientists do not yet know for certain how storms will change: will there be more, will they be stronger and more devastating? However, we do know that sea level is rising and is likely to rise faster in the future. Therefore, it is safest to assume the worst in terms of erosion and assume that sea level rise will increase rates of shoreline retreat.

Headland bypassing, the movement of sand around the southern point of Gooseberry Island, is another mechanism by which sand could theoretically move from Horseneck Beach to East Beach. We also wanted to assess the likelihood of this process. To assess sediment bypassing around the headland, we considered a hypothetical system with a seabed composed entirely of sand. We calculated the potential sediment flux across a transect in front of the headland (Figure 51). Our simulations indicate that headland bypassing is primarily facilitated by higher storm waves rather than SLR. This is because higher waves expand the surf zone, a phenomenon known to enhance headland bypassing. These results are supported by previous research (King et al., 2021). Nonetheless, the extent of headland bypassing is also controlled by factors such as spatial sediment coverage and sediment grain size (George et al., 2019; Klein et al., 2020; King et al., 2021). Given that the primary sediment composition around the headland is sedimentary rocks, our domain of only sand will overestimate the amount of headland bypassing (Limber & Murray, 2011; Davis & FitzGerald, 2020; Ramesh et al., 2021). Wave energy is usually believed to be the primary driver of headland bypassing, with tides playing a secondary role (King et al., 2021). Our study further suggests an additional factor that can enhance headland bypassing: storm surges. For example, in scenarios involving a storm surge twice as large as the reference scenario, we observe a threefold increase in headland bypassing, as illustrated in Fig. 51b (8-meter higher wave scenario vs. Hurricane Irene). These results suggest that if sand were available, there is potential for sand to move from Horseneck beach to East Beach around the Island, despite the presence of the Causeway, however, this is limited due to a lack of sand in the system.

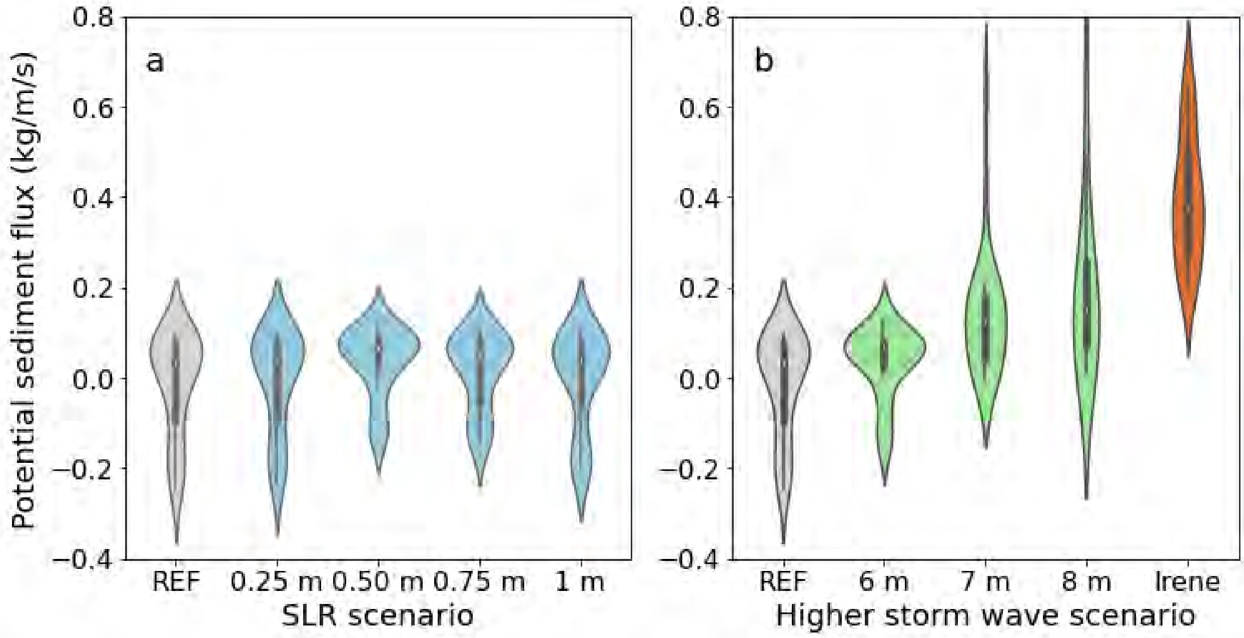

Figure 51. Potential sediment flux along the transect offshore, around the headland under different SLR scenarios (a) and higher storm wave scenarios (b). A positive sediment flux indicates sediment movement from the updrift coastal area to the downdrift area. Violin thickness corresponds to probability density. Endpoints of the violin depict minimum and maximum values. The box plot inside each violin covers the first to third quartiles, with a square representing the median value.

6.5 Synthesis of findings

The project results indicate that sediment transport along the Westport-Dartmouth shoreline relates strongly to circulation cells created by waves. During moderate to large wave conditions these cells create westward sediment transport on Horseneck Beach and eastward sediment transport on East Beach (Figure 52 A and B). The presence or absence of the Gooseberry Island Causeway has little impact on the creation of these cells, they result from the presence of the Island itself. Transport between coastal cells primarily occurs during exceptionally large storms. In the absence of the causeway, minimal sediment would be transported across the tombolo from Horseneck Beach to East Beach because under most conditions, except the highest energy events, the circulation cells force the currents to flow north from the west shore of Gooseberry Island where there is little sediment to erode and transport (Figure 52, C and D). Equally, this circulation suppresses longshore transport from west to east and likely creates east to west transport along Horseneck Beach. Under very large wave conditions (i.e., 12 m), the circulation cells move offshore, allowing some west to east longshore transport including transport of sand across the tombolo.

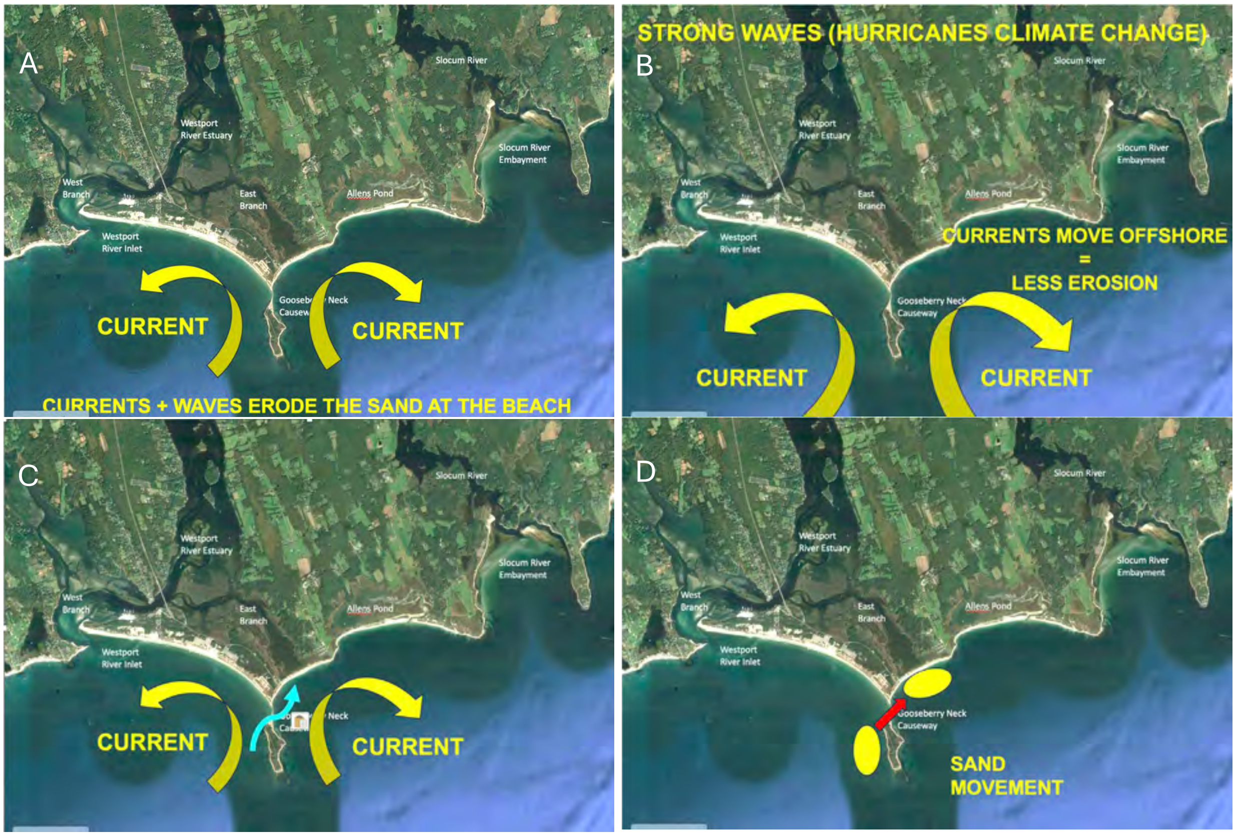

Figure 52. Panels show the direction of water currents (yellow arrows) when there is no causeway at different wave conditions. During normal conditions (panel A) wave-generated circulation moves water and sediment northward, either side of Gooseberry Island and to the west on the west side of the causeway and to the east on the east side of the causeway. Larger waves (hurricane conditions) move the circulation cells further offshore, reducing erosion (Panel B). Under high wave conditions, in the absence of a causeway the primary transport pathway would be north along the side of the island, and across the tombolo (Panel C), moving sediment from the side of the island, an area with little to no sediment, across to East Beach (Panel D).

Figure 53 provides an assessment of transport rates between coastal cells under small (annual) and large (10-year return period) storms based on model simulations, using a model with no causeway. During small and large storms, there would be minor sediment transport from west to east across the tombolo if the causeway did not exist. However, sediment transport across the tombolo to East Beach is significantly less than the volume of sand moving along East Beach or to the offshore due to the natural water and sediment circulation patterns. Likewise, the amounts and frequency of transport across the tombolo

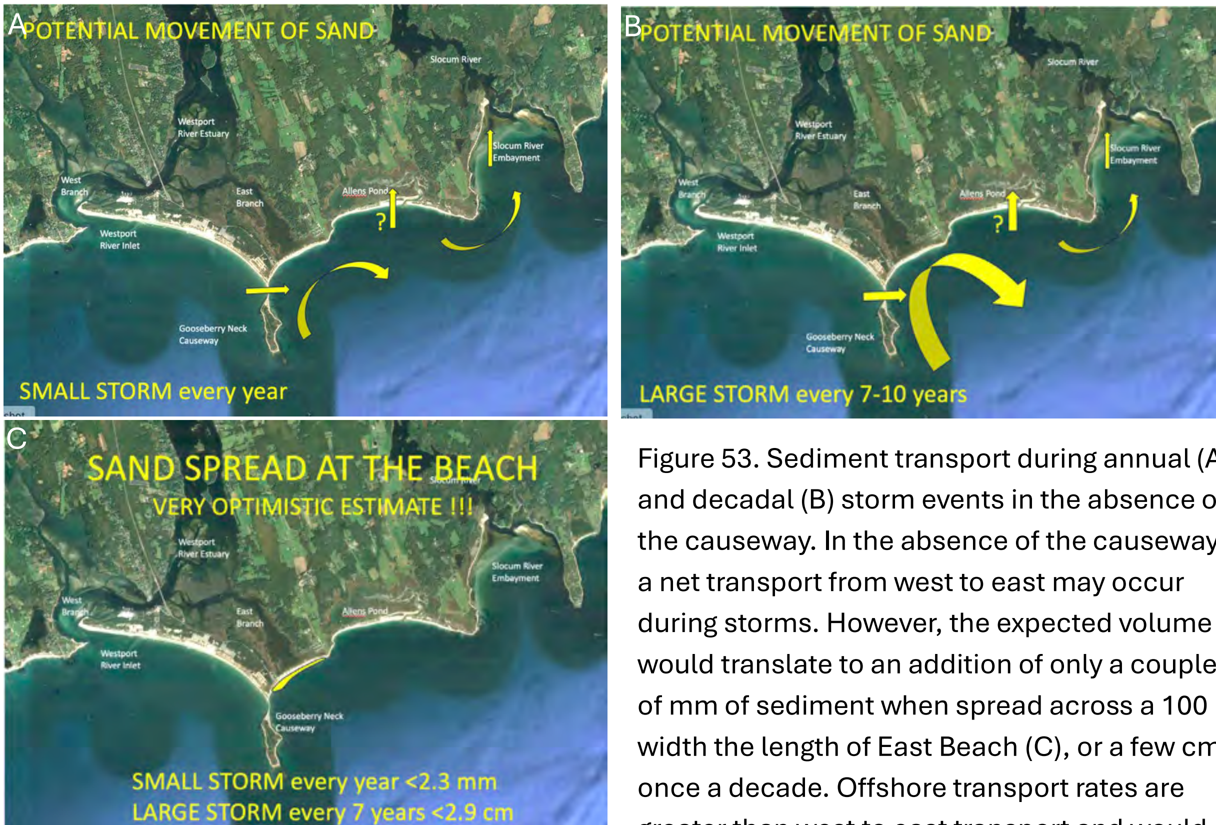

Figure 53. Sediment transport during annual (A) and decadal (B) storm events in the absence of the causeway. In the absence of the causeway, a net transport from west to east may occur during storms. However, the expected volume would translate to an addition of only a couple of mm of sediment when spread across a 100 m width the length of East Beach (C), or a few cm once a decade. Offshore transport rates are greater than west to east transport and would also rapidly remove the sediment.

mean that, even using assumptions that produce the largest transport rates, the sediment introduced across the tombolo would be only a minor contribution to the beach volume (Figure 53 C). Regardless, East Beach is a system that is experiencing barrier rollover, and the entire Westport-Dartmouth shoreline is experiencing diminished sand supply as a result of sea level rise and shoreline retreat. The strong longshore currents and offshore circulation at the east end of the beach means that this beach would be experiencing a reduction in fine grained sediment (sand) and an increase in coarser sediment supply (gravel) regardless of the presence or absence of the causeway.

7 Summary and recommendations

This project has addressed contemporary concerns in the lower Buzzards Bay region centering around the influence of the Gooseberry Causeway on the nearby beaches and bays. To do this we asked a set of questions and used a combination of remotely sensed, field and numerical modelling data to infer patterns and rates of wave and tidal flow, and sediment transport. Using a numerical model allowed us to consider conditions that either cannot be observed (e.g., comparing conditions with and without a causeway) or are difficult to measure (e.g., extreme storms). This section summarizes the answers to those questions and offers discussion around potential causes and solutions to the coastal resilience concerns that have been raised.

1. Westport River Inlet - Does the Gooseberry Causeway influence circulation at the mouth of the Westport River in a way that restricts the flow of water into/out of the Westport River mouth?

    The circulation patterns are the same at the Westport inlet with and without the causeway. Due to the protection of the Cape and the Elizabeth Islands, the highest wave conditions at Westport always approach from the southwest. When waves are large, they push a great deal of water toward the shore that then needs to flow back offshore somehow. The presence of the Island-tombolo system creates a flow northward to the beach along the island's shoreline, because the waves approach from a southerly angle. This sets up an anticlockwise circulation west of Gooseberry Island. During non-storm, low-wave conditions, the anticlockwise circulation is negligible compared to the flow of water through the Westport Inlet, thus the inlet is dominated by the tides with no influence from Gooseberry Island/Causeway. Existing model runs with and without Gooseberry Island show that this circulation pattern would exist whether the Causeway was there or not.

    The anticlockwise circulation west of Gooseberry Island/Causeway creates longshore transport of sediment from east to west along Horseneck Beach. This causes the spit at the west-end of Horseneck Beach to lengthen and widen into the Westport River inlet. However, the building of the beach into the inlet is limited by the tidal flow that has to get through the inlet. There is a large volume of water that comes into and has to go back out of the Westport Rivers with each tidal cycle (known as the tidal prism). The force of this water flowing in and out will limit the build-up of sand in the river inlet and tend to move the sand offshore to the delta and potentially back to shore on either side of the inlet. This creates the 'recurve spit' seen on the west end of Horseneck beach, with sediment that is pushed into the inlet being moved along the spit shoreline and curving round into the Westport River.

    The size of the tidal prism is the dominant factor influencing the flushing of the Westport Rivers with cleaner Buzzards Bay waters. The influence of the Gooseberry Island headland is felt through the anti-clockwise wave-driven circulation cells it creates. This circulation produces westward transport of sand and makes sand available for tidal currents to move it into the Westport Rivers. This sand would then move either onto the recurve spit at the end of Horseneck Beach or on sandy deltas (sand banks) inside the inlet. This infilling would reduce the tidal volume of the Westport Rivers only very, very slightly as the volume of the Westport Rivers is massive in comparison to the volumes of sediment being moved into the inlet.

2. East Beach – Is the Gooseberry Causeway causing or accelerating the erosion of East Beach?

   Gooseberry Island itself sets up a circulation pattern that tends to pull sand off of East Beach to the southeast. Under normal conditions and small storms, sediment would not move from west-to-east across the tombolo even if the Causeway did not exist. Under large storm (e.g., hurricane) conditions, there would be a small amount of transport of sand from west-to-east if the Causeway did not exist. However, in the model runs there is still a net loss of sand from East Beach in these large storm scenarios because the amount of sand moving across the tombolo is smaller than the amount pulled along or offshore. The sediment supply to East Beach, and the entire region, has coarsened over time as offshore deposits are depleted. Deepening water due to sea level rise is exacerbating the problem because it prevents sand from getting onshore.

3. Climate Change – How will increased sea level rise change sediment movement in lower Buzzards Bay and will the Causeway exacerbate future effects of climate change?

   Gooseberry Island and the tombolo and the shape of the shore control the movement of water and sediments, not the causeway. Under climate change scenarios, the causeway still will not strongly influence sediment transport in the region. The model shows that deeper water due to sea level rise will move the circulation cells closer to the beach resulting in more erosion/transport throughout lower Buzzards Bay. More storms and more intense storms mean more frequent events when the waves are big enough to create the divergent flows away from the causeway on either side – and around the point from the Allens pond system into Slocums River Embayment.

   Examination of marsh sediment cores indicate that Westport salt marshes are not building sediment height as fast as sea levels are rising, so they are susceptible to drowning as sea level rises.

7.1 Further observations

1. There are several warning signs of potential low resilience or continued deterioration in the lower Buzzards Bay region:
   a. Sediment will continue to coarsen on East and Horseneck beaches close to Gooseberry Neck Island, and over time, where the coarsening occurs will move further and further away from the island. There is no source to replace the sand naturally. Nourishment options are from offshore or areas of sediment accumulations. Because sand will continue to naturally move along and

offshore from the beaches, if beach nourishment is performed, it will need to be repeated regularly and is a large investment.

   b. Sand will continue to move into both the Westport Inlet and Allens Pond as these areas are acting as sinks. Some of this sediment will be needed to build marsh platforms as the system evolves. It's possible that the dredged material from Westport Inlet could be used to nourish beaches. In this system the area most in need of nourishment would be the central portion of the system (either side of Gooseberry Neck).
   c. Low salt marsh accretion means that marsh platform areas will be lost as sea level rises. If the marsh platform areas are to be preserved, efforts need to be made to protect marsh areas and increase sediment deposition onto the marshes.

2. Unanswered questions that were not within the scope of the project
   a. Are there areas of sediment offshore that could be used to nourish beaches?
   b. Is sediment building up in the Let behind the barrier, and if so, could it be redistributed to the front of the beach?

8 List of deliverables

The following is a list of deliverables from this project.

1. Report documenting findings regarding the impact of the causeway and the drivers of the observed coastal trends. [This document]
2. Four validated and calibrated modeling domains, with a suite of results from simulations undertaken for this project.
3. Extensive geodatabase of rectified aerial images and LiDAR from 1938-2021.
4. Geodatabase of mapped coastal geomorphology from Westport to Slocums embayment.
5. Extensive field and lab data set of bathymetry, hydrodynamics and morphology.
6. Twelve (12) marsh accretion rates throughout the system (to be published during 2025).
7. Three (3) journal publications (Appendix B)

   Xie, D., Hughes, Z.J., FitzGerald, D., Tas, S., Zaman Asik, T., and Fagherazzi, S., 2024. Longshore Sediment Transport Across a Tombolo Determined by Two Adjacent Circulation Cells. Journal of Geophysical Research: Earth Surface. 29:10. https://doi.org/10.1029/2024JF007709.

   Xie, D., Hughes, Z.J., FitzGerald, D.M., Tas, S., Zaman Asik, T., and Fagherazzi, S., 2024, Impacts of climate change on coastal hydrodynamics around a headland and potential headland sediment bypassing. Geophysical Research Letters, 51, e2023GL105323. https://doi.org/10.1029/2023GL105323.

   Tas, S.A.J., Hughes, Z.J., FitzGerald, D.M., Xie, D, Asik Zaman, T. and Fagherazzi, S, 2025. Headland bypassing: Moderate storms dominate extreme events. Journal of Geophysical Research: Oceans. *In review post-revision*.

8. Two (2) publications in preparation
   Asik Zaman, T., FitzGerald, D., Hughes, Z.J, Georgiou, I.Y, Fagherazzi, S., Xie, D., and Tas, S. (2024). Storm Impacts on Sediment Infilling at Allens Pond Inlet, Massachusetts. *In prep*

   Van Dongen, A., Hein, C.J., FitzGerald, D., Hughes, Z.J, and Saylor, J. (2025) Spatial Variability in Coastal Saltmarsh Resilience to Sea-Level Rise near Westport and Slocums Rivers, Massachusetts. *In prep.*

9. Seven (7) Conference presentations

   Van Dongen, A., Hein, C.J., FitzGerald, D., Hughes, Z.J, and Saylor, J. (2025) Spatial Variability in Coastal Saltmarsh Resilience to Sea-Level Rise near Westport and

Slocums Rivers, Massachusetts. S.E. GSA section meeting, Harrisonburg, Virginia, USA, March 2025

Asik Zaman, T., FitzGerald, D., Hughes, Z.J, Georgiou, I.Y, Fagherazzi, S., Xie, D., and Tas, S. (2024). Storm Impacts on Sediment Infilling at Allens Pond Inlet, Massachusetts. AGU. Washington DC, USA December 2024

Xie, D., Hughes, Z.J, FitzGerald, D., Tas, S., Zaman Asik, T., and Fagherazzi, S. (2023), Implications of Causeway Removal on Longshore Sediment Transport During Storms in a Complex Shoreline System, AGU. San Francisco, USA, December 2023.

Giess, M., FitzGerald D.M, Hughes, Z., & Staro, A. (2023). The contribution of reworking extensive offshore glaciofluvial deposits in the geomorphological development of the western Buzzard's Bay coast. CERF Biennial Conference, Nov. 2023. Portland, OR.

Tas, S.A.J., Hughes, Z.J., FitzGerald, D.M., Xie, D, Asik Zaman, T. and Fagherazzi, S, (2023). Spit and beach ridge evolution driven by headland bypassing in Slocums River Embayment, Massachusetts, USA. 13th River, Coastal and Estuarine Morphodynamics Symposium (RCEM 2023) in Urbana-Champaign, IL, USA, 25-28 September 2023.

Xie, D., Hughes, Z.J., FitzGerald, D., Tas, S., Zaman Asik, T., and Fagherazzi, S. (2023), Beyond the shoreline: The importance of coastal headlands on reducing nearshore hydrodynamic forces under climate change, 13th River, Coastal and Estuarine Morphodynamics Symposium (RCEM 2023) in Urbana-Champaign, IL, USA, 25-28 September 2023.

Tas, S., Hughes, Z., FitzGerald, D., Xie, D., Asik Zaman, T., & Fagherazzi, S. (2024, April). Linking headland bypassing to the evolution of a spit and beach ridge system-Slocums River Embayment, Buzzards Bay, Massachusetts, USA. In EGU General Assembly Conference Abstracts (p. 19644).

9 Citations

Aagaard, T., Hughes, M., Baldock, T., Greenwood, B., Kroon, A., & Power, H. (2012). Sediment transport processes and morphodynamics on a reflective beach under storm and non-storm conditions. Marine Geology, 326, 154-165.

Amante, C. J., Love, M., Carignan, K., Sutherland, M. G., MacFerrin, M., & Lim, E. (2023). Continuously Updated Digital Elevation Models (CUDEMs) to Support Coastal Inundation Modeling. Remote Sensing, 15(6), 1702. https://doi.org/10.3390/rs15061702

Andualem, T. G., Hewa, G. A., Myers, B. R., Peters, S., & Boland, J. (2023). Erosion and Sediment Transport Modeling: A Systematic Review. Land, 12(7), 1396.

Appleby, P.G., 2001. Chronostratigraphic techniques in recent sediments. In: Last, W.M., Smol, J.P. (Eds.), Tracking Environmental Change Using Lake Sediments. Springer, Dordrecht, pp. 171–203 https://doi.org/10.1007/0-306-47669-X_9.

Ashton, A. D., & Murray, A. B. (2006). High-angle wave instability and emergent shoreline shapes: 1. Modeling of sand waves, flying spits, and capes. *Journal of Geophysical Research: Earth Surface*, *111*(F4).

Backstrom, J., Jackson, D., Cooper, A., & Loureiro, C. (2015). Contrasting geomorphological storm response from two adjacent shorefaces: Earth Surface Processes and Landforms. Earth Surface Processes and Landforms, 40(15), 2112–2120. https://doi.org/10.1002/esp.3788

Bacon, J., Vincent, C., Dolphin, T., Taylor, J., Pan, S., & O'Connor, B. (2007). Shore-parallel breakwaters in meso-tidal conditions: tidal controls on sediment transport and their longer term, regional impacts at Sea Palling, UK. Journal of Coastal Research, 369-373.

Bai, X., Jiang, H., Li, C., & Huang, L. (2020). Joint probability distribution of coastal winds and waves using a log-transformed kernel density estimation and mixed copula approach. Ocean Engineering, 216, 107937.

Bastos, A., Collins, M., & Kenyon, N. (2003). Water and sediment movement around a coastal headland: Portland Bill, Southern UK. Ocean Dynamics, 53, 309-321.

Bent, G. C. (1995). Streamflow, ground-water recharge and discharge, and characteristics of surficial deposits in Buzzards Bay Basin, Southeastern Massachusetts. US Geological Survey.

Booij, N., Ris, R. C., & Holthuijsen, L. H. (1999). A third-generation wave model for coastal regions: 1. Model description and validation. Journal of Geophysical Research: Oceans, 104(C4), 7649-7666. https://doi.org/https://doi.org/10.1029/98JC02622

Brenner, O. T., Lentz, E. E., Hapke, C. J., Henderson, R. E., Wilson, K. E., & Nelson, T. R. (2018). Characterizing storm response and recovery using the beach change envelope: Fire Island, New York. Geomorphology, 300, 189-202. https://doi.org/https://doi.org/10.1016/j.geomorph.2017.08.004

Butt, T., & Russell, P. (2000). Hydrodynamics and cross-shore sediment transport in the swash-zone of natural beaches: a review. Journal of Coastal Research, 255-268.

Cheung, K. F., Tang, L., Donnelly, J. P., Scileppi, E. M., Liu, K. B., Mao, X. Z., Houston, S. H., & Murnane, R. J. (2007). Numerical modeling and field evidence of coastal overwash in southern New England from Hurricane Bob and implications for paleotempestology. Journal of Geophysical Research: Earth Surface, 112(F3).

Chi, S., Zhang, C., & Zheng, J. (2023). Sandy shoreline recovery ability after breakwater removal. Frontiers in Marine Science, 10, 1191386.

Chowdhury, P., Behera, M. R., & Reeve, D. E. (2020). Future wave-climate driven longshore sediment transport along the Indian coast. Climatic Change, 162, 405-424.

Cialone, M. A., Massey, T. C., Anderson, M. E., Grzegorzewski, A. S., Jensen, R. E., Cialone, A., Mark, D. J., Pevey, K. C., Gunkel, B. L., & McAlpin, T. O. (2015). North Atlantic Coast Comprehensive Study (NACCS) coastal storm model simulations: Waves and water levels. Available at: https://chs.erdc.dren.mil/Home. [Coastal Hazards System].

CIRES. (2014). Cooperative Institute for Research in Environmental Sciences (CIRES) at the University of Colorado, Boulder. Continuously Updated Digital Elevation Model (CUDEM) - 1/9 Arc-Second Resolution Bathymetric-Topographic Tiles. In: NOAA National Centers for Environmental Information.

Clamflats. (2019). Old Postcards and Photos of Westport, Mass. and surroundings. Available at: https://pbase.com/clamflats/gooseberry_bar_rock. [PBase]

Corbett, D.R., Walsh, J.P., 2015. 210Lead and 137Cesium: establishing a chronology for the last century. In: Shennan, I., Long, A.J., Horton, B.P. (Eds.), Handbook of Sea-level Research. JohnWiley & Sons, Ltd., Chichester, UK, pp. 361–372 https://doi.org/10.1002/9781118452547.ch24.

Costa, W. L. L., Silveira, L. F., & Klein, A. H. F. (2019). Influence of wave climate and tidal regime on headland bypassing - Study case: Northern São Francisco do Sul Island, SC, Brazil. In Coastal Sediments (pp. 488-501).

Cuadrado, D. G., Gómez, E. A., & Ginsberg, S. S. (2005). Tidal and longshore sediment transport associated to a coastal structure. Estuarine, Coastal and Shelf Science, 62(1), 291-300. https://doi.org/https://doi.org/10.1016/j.ecss.2004.09.010

D'Alpaos, A., Lanzoni, S., Marani, M., & Rinaldo, A. (2009). On the O'Brien–Jarrett–Marchi law. Rendiconti Lincei. Scienze Fisiche e Naturali, 20(3), 225–236. https://doi.org/10.1007/s12210-009-0052-x

da Silva, A. P., da Silva, G. V., Strauss, D., Murray, T., Woortmann, L. G., Taber, J., Cartwright, N., & Tomlinson, R. (2021). Headland bypassing timescales: Processes and driving forces. Science of the Total Environment, 793, 148591.

Deltares. (2014). Simulation of multi-dimensional hydrodynamic flows and transport phenomena, including sediments - User Manual (Version: 3.15.34158). Deltares. Available at: https://oss.deltares.nl/. [Delft3D Software].

Dodet, G., Melet, A., Ardhuin, F., Bertin, X., Idier, D., & Almar, R. (2019). The contribution of wind-generated waves to coastal sea-level changes. Surveys in Geophysics, 40(6), 1563-1601.

Dubois, R. N. (1988). Seasonal changes in beach topography and beach volume in Delaware. Marine Geology, 81(1-4), 79-96.

Dullaart, J. C., Muis, S., De Moel, H., Ward, P. J., Eilander, D., & Aerts, J. C. (2023). Enabling dynamic modelling of coastal flooding by defining storm tide hydrographs. Natural Hazards and Earth System Sciences, 23(5), 1847-1862.

Emanuel, K. (2017). Will global warming make hurricane forecasting more difficult? Bulletin of the American Meteorological Society, 98(3), 495-501.

Emery, K. O., & Kuhn, G. G. (1982). Sea cliffs: Their processes, profiles, and classification. Geological Society of America Bulletin, 93(7), 644. https://doi.org/10.1130/0016-7606(1982)93<644:SCTPPA>2.0.CO;2

Fagherazzi, S., Mariotti, G., Leonardi, N., Canestrelli, A., Nardin, W., & Kearney, W. S. (2020). Salt Marsh Dynamics in a Period of Accelerated Sea Level Rise. Journal of Geophysical Research: Earth Surface, 125(8), e2019JF005200. https://doi.org/https://doi.org/10.1029/2019JF005200

FitzGerald, D. M., Baldwin, C. T., Ibrahim, N. A., & Humphries, S. M. (1992). Sedimentologic and morphologic evolution of a beach ridge barrier along an indented coast: Buzzards Bay, Massachusetts.

FitzGerald, D. M., Baldwin, C. T., Ibrahim, N. A., & Sand, D. R. (1987). Development of the Northwestern Buzzards Bay Shoreline, Massachusetts. In D. M. FitzGerald & P. S. Rosen (Eds.), Glaciated Coasts (pp. 327). Academic Press INC.

FitzGerald, D. M., Buynevich, I. V., Davis, R. A., & Fenster, M. S. (2002). New England tidal inlets with special reference to riverine-associated inlet systems. Geomorphology, 48(1), 179-208.

FitzGerald, D. M., Hughes, Z. J., Georgiou, I. Y., Black, S., & Novak, A. (2020). Enhanced, Climate-Driven Sedimentation on Salt Marshes. Geophysical Research Letters, 47(10), e2019GL086737. https://doi.org/https://doi.org/10.1029/2019GL086737

FitzGerald, D.M., *Saiz, A., Baldwin, C.T., and *Sands, D.M., 1986, Spit breaching at Slocums River Inlet: Buzzards Bay, MA, Shore and Beach, v. 56, p. 11-17.

Foster, D. S. (2014). Sediment-Texture Units of the Sea Floor for Buzzards Bay, Massachusetts (BuzzardsBay_sedcover, polygon shapefile, Geographic, WGS84).

Franz, G., Delpey, M. T., Brito, D., Pinto, L., Leitão, P., & Neves, R. (2017). Modelling of sediment transport and morphological evolution under the combined action of waves and currents. Ocean Science, 13(5), 673-690.

Ganju, N. K., Lentz, S. J., Kirincich, A. R., & Farrar, J. T. (2011). Complex mean circulation over the inner shelf south of Martha's Vineyard revealed by observations and a high-resolution model. Journal of Geophysical Research: Oceans, 116(C10).

Garner, A.J., Mann, M.E., Emanuel, K.A., Kopp, R.E., Lin, N., Alley, R.B., Horton, B.P., DeConto, R.M., Donnelly, J.P., Pollard, D., 2017. Impact of climate change on New York City's coastal flood hazard: Increasing flood heights from the preindustrial to 2300 CE. Proceedings of the National Academy of Sciences, v. 114, p. 11861-11866.

George, D. A., Largier, J. L., Pasternack, G. B., Barnard, P. L., Storlazzi, C. D., & Erikson, L. H. (2019). Modeling sediment bypassing around idealized rocky headlands. Journal of Marine Science and Engineering, 7(2), 40.

George, D. A., Largier, J. L., Storlazzi, C. D., & Barnard, P. L. (2015). Classification of rocky headlands in California with relevance to littoral cell boundary delineation. Marine Geology, 369, 137–152. https://doi.org/10.1016/j.margeo.2015.08.010

Giosan, L., Bokuniewicz, H., Panin, N., & Postolache, I. (1999). Longshore sediment transport pattern along the Romanian Danube delta coast. Journal of Coastal Research, 859-871.

Goddard, P. B., Yin, J., Griffies, S. M., & Zhang, S. (2015). An extreme event of sea-level rise along the Northeast coast of North America in 2009–2010. Nature Communications, 6(1), 6346.

Goman, M., Joyce, A., & Mueller, R. (2005). Stratigraphic evidence for anthropogenically induced coastal environmental change from Oaxaca, Mexico. Quaternary Research, 63(3), 250-260.

Grasso, F., Michallet, H., & Barthélemy, E. (2011). Experimental simulation of shoreface nourishments under storm events: A morphological, hydrodynamic, and sediment grain size analysis. Coastal Engineering, 58(2), 184-193.

Goodwin, I. D., Freeman, R., & Blackmore, K. (2013). An insight into headland sand bypassing and wave climate variability from shoreface bathymetric change at Byron Bay, New South Wales, Australia. Marine Geology, 341, 29-45.

Grant, W. D., & Madsen, O. S. (1979). Combined wave and current interaction with a rough bottom. Journal of Geophysical Research: Oceans, 84(C4), 1797-1808.

Greer, M. N., & Madsen, O. S. (1978). Longshore sediment transport data: a review. Coastal Engineering 1978, 1563-1576.

Guillou, N., & Chapalain, G. (2010). Numerical simulation of tide-induced transport of heterogeneous sediments in the English Channel. Continental Shelf Research, 30(7), 806-819.

Gutmann, E.D., Rasmussen, R.M., Liu, C., Ikeda, K., Bruyere, C.L., Done, J.M., Garrè, L., Friis-Hansen, P. and Veldore, V., 2018. Changes in Hurricanes from a 13-Yr Convection-Permitting Pseudo– Global Warming Simulation, Journal of Climate, v. 31, p. 3643-3657. https://doi.org/10.1175/JCLI-D-17-0391.1.

Hallegatte, S., Green, C., Nicholls, R. J., & Corfee-Morlot, J. (2013). Future flood losses in major coastal cities. Nature Climate Change, 3(9), 802-806.

Hallermeier, R. J. (1978). Uses for a calculated limit depth to beach erosion. In Coastal Engineering 1978 (pp. 1493-1512).

Hamilton, D. G., & Ebersole, B. A. (2001). Establishing uniform longshore currents in a large-scale sediment transport facility. Coastal Engineering, 42(3), 199-218.

Han, X., Dong, S., & Wang, Y. (2021). Interaction between oblique waves and arc-shaped breakwater: Wave action on the breakwater and wave transformation behind it. Ocean Engineering, 234, 109252.

Harley, M. D., Masselink, G., Ruiz De Alegría-Arzaburu, A., Valiente, N. G., & Scott, T. (2022). Single extreme storm sequence can offset decades of shoreline retreat projected to result from sea-level rise. Communications Earth & Environment, 3(1), 112. https://doi.org/10.1038/s43247-022-00437-2

Hequette, A., Desrosiers, M., Hill, P. R., & Forbes, D. L. (2001). The influence of coastal morphology on shoreface sediment transport under storm-combined flows, Canadian Beaufort Sea. Journal of Coastal Research, 507-516.

Hoque, A., Hossain, N., Ali, S., & Rahman, M. (2019). Wave breaking and bubble formation associate energy dissipation and wave setup. Ocean Dynamics, 69, 913-923.

Hsu, T.-W., Hsu, J. R.-C., Weng, W.-K., Wang, S.-K., & Ou, S.-H. (2006). Wave setup and setdown generated by obliquely incident waves. Coastal Engineering, 53(10), 865-877.

Huang, Y., Weisberg, R. H., Zheng, L., & Zijlema, M. (2013). Gulf of Mexico hurricane wave simulations using SWAN: Bulk formula-based drag coefficient sensitivity for Hurricane Ike. Journal of Geophysical Research: Oceans, 118(8), 3916-3938.

Hubbard, D. K. (1992). Hurricane-induced sediment transport in open-shelf tropical systems; an example from St. Croix, US Virgin Islands. Journal of Sedimentary Research, 62(6), 946-960.

Huisman, B., Ruessink, B., De Schipper, M., Luijendijk, A., & Stive, M. (2018). Modelling of bed sediment composition changes at the lower shoreface of the Sand Motor. Coastal Engineering, 132, 33-49.

Idier, D., Bertin, X., Thompson, P., & Pickering, M. D. (2019). Interactions between mean sea level, tide, surge, waves and flooding: mechanisms and contributions to sea level variations at the coast. Surveys in Geophysics, 40, 1603-1630.

Jing, L., & Ridd, P. V. (1996). Wave-current bottom shear stresses and sediment resuspension in Cleveland Bay, Australia. Coastal Engineering, 29(1-2), 169-186.

Kaliraj, S., Chandrasekar, N., & Magesh, N. (2014). Impacts of wave energy and littoral currents on shoreline erosion/accretion along the south-west coast of Kanyakumari, Tamil Nadu using DSAS and geospatial technology. Environmental Earth Sciences, 71, 4523-4542.

Kemp, A.C., Sommerfield, C.K., Vane, C.H., Horton, B.P., Chenery, S., Anisfeld, S., Nikitina, D., 2012. Use of lead isotopes for developing chronologies in recent salt-marsh sediments. Quaternary Geochronology, v. 12, p. 40–49. https://doi.org/10.1016/j.quageo.2012.05.004.

Kim, G. H., Jho, M. H., & Yoon, S. B. (2017). Improving the performance of SWAN modelling to simulate diffraction of waves behind structures. Journal of Coastal Research(79), 349-353.

King, E. V., Conley, D. C., Masselink, G., Leonardi, N., McCarroll, R. J., Scott, T., & Valiente, N. G. (2021). Wave, tide and topographical controls on headland sand bypassing. Journal of Geophysical Research: Oceans, 126(8), e2020JC017053.

Klein, A. H., da Silva, G. V., Taborda, R., da Silva, A. P., & Short, A. D. (2020). Headland bypassing and overpassing: form, processes and applications. Sandy Beach Morphodynamics, 557-591.

Knutson, T.R., Sirutis, J.J., Zhao, M., Tuleya, R.E., Bender, M., Vecchi, G.A., Villarini, G. and Chavas, D., 2015. Global projections of intense tropical cyclone activity for the late twenty-first century from dynamical downscaling of CMIP5/RCP4. 5 scenarios. Journal of Climate, v. 28, p. 7203-7224.

Kobayashi, N., Agarwal, A., & Johnson, B. D. (2007). Longshore current and sediment transport on beaches. Journal of Waterway, Port, Coastal, and Ocean Engineering, 133(4), 296-304.

Kopp, R.E., DeConto, R.M., Bader, D.A., Hay, C.C., Horton, R.M., Kulp, S., Oppenheimer, M., Pollard, D., Strauss, B.H., 2017. Evolving understanding of Antarctic ice-sheet physics and ambiguity in probabilistic sea-level projections. Earth's Future, v. 5, p. 1217–1233. https://doi.org/10.1002/2017EF000663.

Lavaud, L., Bertin, X., Martins, K., Pezerat, M., Coulombier, T., & Dausse, D. (2022). Wave Dissipation and Mean Circulation on a Shore Platform Under Storm Wave Conditions. Journal of Geophysical Research: Earth Surface, 127(3), e2021JF006466. https://doi.org/https://doi.org/10.1029/2021JF006466

Lerma, A. N., Pedreros, R., Robinet, A., & Sénéchal, N. (2017). Simulating wave setup and runup during storm conditions on a complex barred beach. Coastal Engineering, 123, 29-41.

Lesser, G. R., Roelvink, J. A., van Kester, J. A. T. M., & Stelling, G. S. (2004). Development and validation of a three-dimensional morphological model. Coastal Engineering, 51(8-9), 883-915. https://doi.org/10.1016/j.coastaleng.2004.07.014

Limber, P. W., Brad Murray, A., Adams, P. N., & Goldstein, E. B. (2014). Unraveling the dynamics that scale cross-shore headland relief on rocky coastlines: 1. Model development. Journal of Geophysical Research: Earth Surface, 119(4), 854-873.

Lin, J.-G. (2013). An improvement of wave refraction-diffraction effect in SWAN. Journal of Marine Science and Technology, 21(2), 198-208.

Lin, N., Emanuel, K., Oppenheimer, M., & Vanmarcke, E. (2012). Physically based assessment of hurricane surge threat under climate change. Nature Climate Change, 2(6), 462–467. https://doi.org/10.1038/nclimate1389

Little, C.M., Horton, R.M., Kopp, R.E., Oppenheimer, M., Vecchi, G.A. and Villarini, G., 2015. Joint projections of US East Coast sea level and storm surge. Nature Climate Change, v. 5, p. 1114-1120. https://doi.org/10.1038/nclimate2801.

Longuet-Higgins, M. S. (1970). Longshore currents generated by obliquely incident sea waves: 1. Journal of Geophysical Research (1896-1977), 75(33), 6778-6789. https://doi.org/https://doi.org/10.1029/JC075i033p06778

Lorenzo-Trueba, J., & Ashton, A. D. (2014). Rollover, drowning, and discontinuous retreat: Distinct modes of barrier response to sea-level rise arising from a simple morphodynamic model. Journal of Geophysical Research: Earth Surface, 119(4), 779–801. https://doi.org/10.1002/2013JF002941

Luijendijk, A., Hagenaars, G., Ranasinghe, R., Baart, F., DMa, H., Xu, L., Okon, S. U., Hu, P., Li, W., Shi, H., & He, Z. (2024). Sediment transport and bed erosion during storm surge using a coupled hydrodynamic and morphodynamic model considering wave and current interaction. Coastal Engineering, 187, 104409.

Makar, A., Specht, C., Specht, M., Dąbrowski, P., Burdziakowski, P., & Lewicka, O. (2020). Seabed topography changes in the Sopot Pier Zone in 2010–2018 influenced by Tombolo Phenomenon. Sensors, 20(21), 6061.

Malliouri, D. I., Petrakis, S., Vandarakis, D., Kikaki, K., Hatiris, G.-A., Gad, F.-K., Panagiotopoulos, I. P., & Kapsimalis, V. (2022). The Role of Sea State to the Morphological Changes of Prasonisi Tombolo, Rhodes Island, Greece. Water, 14(13), 2016. https://www.mdpi.com/2073-4441/14/13/2016

Mangor, K., Drønen, N. K., Kaergaard, K. H., & Kristensen, N. E. (2017). Shoreline Management Guidelines. DHI: Hirschholm.

Marchesiello, P., Nguyen, N. M., Gratiot, N., Loisel, H., Anthony, E. J., San Dinh, C., Nguyen, T., Almar, R., & Kestenare, E. (2019). Erosion of the coastal Mekong delta: Assessing natural against man induced processes. Continental Shelf Research, 181, 72-89.

Masselink, G., Scott, T., Poate, T., Russell, P., Davidson, M., & Conley, D. (2016). The extreme 2013/2014 winter storms: hydrodynamic forcing and coastal response along the southwest coast of England. Earth Surface Processes and Landforms, 41(3), 378-391.

McCarroll, R., Masselink, G., Wiggins, M., Scott, T., Billson, O., Conley, D., & Valiente, N. (2019). High-efficiency gravel longshore sediment transport and headland bypassing over an extreme wave event. Earth Surface Processes and Landforms, 44(13), 2720-2727.

McCarroll, R. J., Masselink, G., Valiente, N. G., Scott, T., King, E. V., & Conley, D. (2018). Wave and tidal controls on embayment circulation and headland bypassing for an exposed, macrotidal site. Journal of Marine Science and Engineering, 6(3), 94.

McCarroll, R. J., Masselink, G., Valiente, N. G., Wiggins, M., Scott, T., Conley, D. C., & King, E. V. (2020). Impact of a headland-associated sandbank on shoreline dynamics. Geomorphology, 355, 107065.

Mariño-Tapia, I., Aird, N., Davidson, M., Kingston, K., & Ganderton, P. (2004). Tidally modulated sediment transport processes on a shore-attached sandbar. Journal of Coastal Research, 395-400.

Marsooli, R., & Lin, N. (2018). Numerical modeling of historical storm tides and waves and their interactions along the US East and Gulf Coasts. *Journal of Geophysical Research: Oceans*, *123*(5), 3844-3874.

McLaren, P., & Bowles, D. (1985). The effects of sediment transport on grain-size distributions. Journal of Sedimentary Research, 55(4), 457-470.

Moraff, K. & United States Environmental Protection Agency. (2019, October 10). Approval of the Slocums and Little Rivers Embayment System TMDL for Total Nitrogen. https://www.epa.gov/sites/default/files/2019-12/documents/slocums-little-rivers-tmdl-approval-docs.pdf

Mouragues, A., Bonneton, P., Castelle, B., Marieu, V., Jak McCarroll, R., Rodriguez-Padilla, I., Scott, T., & Sous, D. (2020). High-energy surf zone currents and headland rips at a geologically constrained mesotidal beach. Journal of Geophysical Research: Oceans, 125(10), e2020JC016259.

Murray, A.S. and Wintle, A.G., 2000. Luminescence dating of quartz using an improved single-aliquot regenerative-dose protocol. Radiation Measurements, v. 32, p. 57-73.

NDBC. (2023). Wind and wave data collected from National Data Buoy Center (Station No.: BUZM3 & 44085) ([Dataset]. NDBC. https://www.ndbc.noaa.gov/

NOAA. (2023). Historical tidal level data retrieved from Newport tidal gauge under National Oceanic and Atmospheric Administration (Station No.:8452660) ([Dataset]. NOAA. https://tidesandcurrents.noaa.gov/

NOAA. (2024). NOAA's Historical Map & Chart Collection ([Dataset]. United States Office of Coast Survey. https://historicalcharts.noaa.gov/about.php

Nordstrom, K. F. (2014). Living with shore protection structures: a review. Estuarine, Coastal and Shelf Science, 150, 11-23.

Nyberg, B., & Howell, J. A. (2016). Global distribution of modern shallow marine shorelines. Implications for exploration and reservoir analogue studies. Marine and Petroleum Geology, 71, 83-104.
Office for Coastal Management (OCM) Partners. (2009). 2005—2007 US Army Corps of Engineers (USACE) Topo/Bathy Lidar: Maine, Massachusetts, and Rhode Island [dataset]. https://www.fisheries.noaa.gov/inport/item/50052
Office for Coastal Management (OCM) Partners. (2010). 2010 USACE NCMP Topobathy Lidar: Northeast Atlantic Coast (CT, MA, ME, NH, RI) [dataset]. https://www.fisheries.noaa.gov/inport/item/50089
Office for Coastal Management (OCM) Partners. (2013). 2012 USACE Post Sandy Topographic LiDAR: Rhode Island and Massachusetts Coast [dataset]. https://www.fisheries.noaa.gov/inport/item/49609
Office for Coastal Management (OCM) Partners. (2015a). 2013-2014 U.S. Geological Survey CMGP LiDAR: Post Sandy (MA, NH, RI) [dataset]. https://www.fisheries.noaa.gov/inport/item/49846
Office for Coastal Management (OCM) Partners. (2015b). 2015 NOAA NGS Topobathy Lidar DEM: Buzzards Bay Block3 (MA) [dataset]. https://www.fisheries.noaa.gov/inport/item/48378
Office for Coastal Management (OCM) Partners. (2018). 2018 USACE NCMP Topobathy Lidar DEM: East Coast (CT, MA, ME, NC, NH, RI, SC) [dataset]. https://www.fisheries.noaa.gov/inport/item/55882
Palinkas, C. M., Halka, J. P., Li, M., Sanford, L. P., & Cheng, P. (2014). Sediment deposition from tropical storms in the upper Chesapeake Bay: Field observations and model simulations. Continental Shelf Research, 86, 6-16. https://doi.org/https://doi.org/10.1016/j.csr.2013.09.012
Pattiaratchi, C., Hegge, B., Gould, J., & Eliot, I. (1997). Impact of sea-breeze activity on nearshore and foreshore processes in southwestern Australia. Continental Shelf Research, 17(13), 1539-1560.
Pattiaratchi, C., Olsson, D., Hetzel, Y., & Lowe, R. (2009). Wave-driven circulation patterns in the lee of groynes. Continental Shelf Research, 29(16), 1961-1974.
Peregrine, D. H. (1983). Breaking waves on beaches. Annual review of fluid mechanics, 15(1), 149-178. and their dynamics along the coasts of India – A review. Journal of Coastal Conservation, 25(2), 31.
Putnam, J. A., Munk, W. H., & Taylor, M. (1949). The prediction of longshore currents. Eos, Transactions American Geophysical Union, 30(3), 337-345.
Ramesh, R., Purvaja, R., Rajakumari, S., Suganya, G. M. D., Sarunjith, K. J., & Vel, A. S. (2021). Sediment cells and their dynamics along the coasts of India – A review. *Journal of Coastal Conservation*, *25*(2), 31.
Roberts, T. M., Wang, P., & Puleo, J. A. (2013). Storm-driven cyclic beach morphodynamics of a mixed sand and gravel beach along the Mid-Atlantic Coast, USA. Marine Geology, 346, 403-421. https://doi.org/https://doi.org/10.1016/j.margeo.2013.08.001
Roy, P., Cowell, P., Ferland, M., & Thom, B. (1994). Wave-dominated coasts. Coastal evolution: Late Quaternary shoreline morphodynamics, 121-186.
Sankaranarayanan, S. (2007). Modeling the tide and wind-induced circulation in Buzzards Bay. Estuarine, Coastal and Shelf Science, 73(3-4), 467-480.
Shetty, A., & Jayappa, K. (2020). Seasonal variation in longshore sediment transport rate and its impact on sediment budget along the wave-dominated Karnataka coast, India. Journal of Earth System Science, 129, 1-14.
Short, A. D., & Masselink, G. (1999). Embayed and Structurally Controlled Beaches. In Handbook of beach and shoreface morphodynamics (pp. 230–249). John Wiley.

Siegle, E., Huntley, D. A., & Davidson, M. A. (2004). Physical controls on the dynamics of inlet sandbar systems. Ocean Dynamics, 54, 360-373.
Siegle, E., Huntley, D. A., & Davidson, M. A. (2007). Coupling video imaging and numerical modelling for the study of inlet morphodynamics. Marine Geology, 236(3-4), 143-163.
Sierra, J., & Casas-Prat, M. (2014). Analysis of potential impacts on coastal areas due to changes in wave conditions. Climatic Change, 124, 861-876.
Specht, C., Lewicka, O., Specht, M., Dąbrowski, P., & Burdziakowski, P. (2020). Methodology for carrying out measurements of the tombolo geomorphic landform using unmanned aerial and surface vehicles near Sopot Pier, Poland. Journal of Marine Science and Engineering, 8(6), 384.
Stone, J.R., Stone, B.D., DiGiacomo-Cohen, M.L., and Mabee, S.B., comps., 2018, Surficial materials of Massachusetts—A 1:24,000-scale geologic map database: U.S. Geological Survey Scientific Investigations Map 3402, 189 sheets, scale 1:24,000; index map, scale 1:250,000; 58-p. pamphlet; and geodatabase files, https://doi.org/10.3133/sim3402.
Sun, Y., Chen, C., Beardsley, R. C., Xu, Q., Qi, J., & Lin, H. (2013). Impact of current-wave interaction on storm surge simulation: A case study for Hurricane Bob. Journal of Geophysical Research: Oceans, 118(5), 2685-2701.
Svendsen, I. A. (1984). Wave heights and set-up in a surf zone. Coastal Engineering, 8(4), 303-329.
Soulsby, R. L., Hamm, L., Klopman, G., Myrhaug, D., Simons, R. R., & Thomas, G. P. (1993). Wave-current interaction within and outside the bottom boundary layer. Coastal Engineering, 21(1), 41-69.
Stockdonf, H. F., Sallenger Jr, A. H., List, J. H., & Holman, R. A. (2002). Estimation of shoreline position and change using airborne topographic lidar data. Journal of Coastal Research, 502-513.
Swart, D. H. (1974). Offshore sediment transport and equilibrium beach profiles.
Sweet, W. V., Hamlington, B. D., Kopp, R. E., Weaver, C. P., Barnard, P. L., Bekaert, D., Brooks, W., Craghan, M., Dusek, G., & Frederikse, T. (2022). Global and regional sea level rise scenarios for the United States: updated mean projections and extreme water level probabilities along US coastlines. National Oceanic and Atmospheric Administration.
SWAN, S. (2015). technical documentation (SWAN Cycle III version 41.01 A). Delft University of Technology.
Thom, B. G., Eliot, I., Eliot, M., Harvey, N., Rissik, D., Sharples, C., Short, A. D., & Woodroffe, C. D. (2018). National sediment compartment framework for Australian coastal management. Ocean & Coastal Management, 154, 103-120.
Toffoli, A., McConochie, J., Ghantous, M., Loffredo, L., & Babanin, A. V. (2012). The effect of wave-induced turbulence on the ocean mixed layer during tropical cyclones: Field observations on the Australian North-West Shelf. Journal of Geophysical Research: Oceans, 117(C11).
Trenhaile, A. (2016). Rocky coasts — their role as depositional environments. Earth-Science Reviews, 159, 1-13. https://doi.org/https://doi.org/10.1016/j.earscirev.2016.05.001
Tsai, C.-P., Chen, Y.-C., & Ko, C.-H. (2023). Prediction of Bay-Shaped Shorelines between Detached Breakwaters with Various Gap Spacings. Sustainability, 15(7), 6218. https://www.mdpi.com/2071-1050/15/7/6218
Toimil, A., Camus, P., Losada, I., Le Cozannet, G., Nicholls, R., Idier, D., & Maspataud, A. (2020). Climate change-driven coastal erosion modelling in temperate sandy beaches: Methods and uncertainty treatment. Earth-Science Reviews, 202, 103110.
USGS. (2023). Current water data for Massachusetts under United States Geological Survey [Dataset]. USGS. https://waterdata.usgs.gov/ma/nwis/rt

US Geological Survey. (1984). Geographic Names Information System. Paskamanset and Slocums River. [dataset]. https://doi.org/10.3133/70039514
US Geological Survey. (2023). Paskamanset River Near South Dartmouth, MA - 01105933 [dataset]. Water Data for the Nation. http://dx.doi.org/10.5066/F7P55KJN
Valiente, N. G., Masselink, G., Scott, T., Conley, D., & McCarroll, R. J. (2019). Role of waves and tides on depth of closure and potential for headland bypassing. Marine Geology, 407, 60-75.
van Rijn, L. C., Walstra, D. J. R., & Ormondt, M. (2004). Description of TRANSPOR2004 and implementation in Delft3D-online. Z3748.
van Rijn, L. C. (2011). Coastal erosion and control. Ocean & Coastal Management, 54(12), 867-887.
Vieira da Silva, G., Toldo Jr, E. E., Klein, A. H. d. F., & Short, A. D. (2018). The influence of wave-, wind- and tide-forced currents on headland sand bypassing – Study case: Santa Catarina Island north shore, Brazil. Geomorphology, 312, 1-11.
van Wiechen, P., de Vries, S., Reniers, A., & Aarninkhof, S. (2023). Dune erosion during storm surges: A review of the observations, physics and modelling of the collision regime. Coastal Engineering, 104383.
Vieira da Silva, G., Toldo, E. E., Klein, A. H. D. F., Short, A. D., & Woodroffe, C. D. (2016). Headland sand bypassing—Quantification of net sediment transport in embayed beaches, Santa Catarina Island North Shore, Southern Brazil. Marine Geology, 379, 13–27. https://doi.org/10.1016/j.margeo.2016.05.008
Vieira da Silva, G., Toldo Jr, E. E., Klein, A. H. d. F., & Short, A. D. (2018). The influence of wave-, wind- and tide-forced currents on headland sand bypassing – Study case: Santa Catarina Island north shore, Brazil. Geomorphology, 312, 1-11. https://doi.org/https://doi.org/10.1016/j.geomorph.2018.03.026
Villarini, G., Vecchi, G. A., Knutson, T. R., & Smith, J. A. (2011). Is the recorded increase in short-duration North Atlantic tropical storms spurious? Journal of Geophysical Research: Atmospheres, 116(D10).
Vincent, C. E., Young, R. A., & Swift, D. J. (1983). Sediment transport on the Long Island shoreface, North American Atlantic Shelf: role of waves and currents in shoreface maintenance. Continental Shelf Research, 2(2-3), 163-181.
Vousdoukas, M. I., Almeida, L. P. M., & Ferreira, Ó. (2012). Beach erosion and recovery during consecutive storms at a steep-sloping, meso-tidal beach. Earth Surface Processes and Landforms, 37(6), 583-593.
Vu, M., Lacroix, Y., & Nguyen, V. (2018). Investigating the effects of sea-level rise on morphodynamics in the western Giens tombolo, France. IOP Conference Series: Earth and Environmental Science,
Wang, K., Hou, Y., Li, S., Du, M., Chen, J., & Lu, J. (2020). A comparative study of storm surge and wave setup in the East China Sea between two severe weather events. Estuarine, Coastal and Shelf Science, 235, 106583.
Warner, J. C., Geyer, W. R., & Lerczak, J. A. (2005). Numerical modeling of an estuary: A comprehensive skill assessment. Journal of Geophysical Research: Oceans, 110, C05001.
Willmott, C. J. (1981). On the validation of models. Physical geography, 2(2), 184-194.
Wishaw, D., Leon, J. X., Barnes, M., & Fairweather, H. (2020). Tropical Cyclone Impacts on Headland Protected Bay. Geosciences, 10(5), 190.
Woodworth, P. L., Melet, A., Marcos, M., Ray, R. D., Wöppelmann, G., Sasaki, Y. N., Cirano, M., Hibbert, A., Huthnance, J. M., & Monserrat, S. (2019). Forcing factors affecting sea level changes at the coast. Surveys in Geophysics, 40(6), 1351-1397.
Wornom, S. F., Welsh, D. J., & Bedford, K. W. (2001). On coupling the SWAN and WAM wave models for accurate nearshore wave predictions. Coastal Engineering Journal, 43(03), 161-201.

Xie, D., Hughes, Z., FitzGerald, D., Tas, S., Asik, T. Z., & Fagherazzi, S. (2024). Impacts of Climate Change on Coastal Hydrodynamics Around a Headland and Potential Headland Sediment Bypassing. Geophysical Research Letters, 51(4), e2023GL105323. https://doi.org/https://doi.org/10.1029/2023GL105323

Xie, D. (2023). Model setup for a reference scenario and the hydrodynamic data around Buzzards Bay domain (v2). [Dataset]. Zenodo. https://doi.org/10.5281/zenodo.8122222

Xie, D., Schwarz, C., Brückner, M. Z. M., Kleinhans, M. G., Urrego, D. H., Zhou, Z., & van Maanen, B. (2020). Mangrove diversity loss under sea-level rise triggered by bio-morphodynamic feedbacks and anthropogenic pressures. Environmental Research Letters, 15(11), 114033.

Xie, D., Schwarz, C., Kleinhans, M. G., Zhou, Z., & van Maanen, B. (2022). Implications of Coastal Conditions and Sea-Level Rise on Mangrove Vulnerability: A Bio-Morphodynamic Modeling Study. Journal of Geophysical Research: Earth Surface, 127(3), e2021JF006301.

Yang, S., Bouma, T. J., Xu, K., Shi, B., Yang, H., Zhang, W., Luo, X., Li, P., Huang, Y., & Tian, M. (2023). Storms dominate the erosion of the Yangtze Delta and southward sediment transport. Science Bulletin, 68(6), 553-556.

Yasso, W. E. (1965). Plan geometry of headland-bay beaches. The Journal of geology, 73(5), 702-714.

Zhang, Q.-H., Bing, Y., & Onyx, W. (2009). Fine sediment carrying capacity of combined wave and current flows. International journal of sediment research, 24(4), 425-438.

Zhang, Z., Chen, C., Song, Z., Zhang, D., Hu, D., & Guo, F. (2020). A FVCOM study of the potential coastal flooding in apponagansett bay and clarks cove, Dartmouth Town (MA). Natural Hazards, 103, 2787-2809.

Zhou, Z., Wu, Y., Fan, D., Wu, G., Luo, F., Yao, P., Gong, Z., & Coco, G. (2022). Sediment sorting and bedding dynamics of tidal flat wetlands: Modeling the signature of storms. Journal of Hydrology, 610, 127913.

Zhu, Q., & Wiberg, P. L. (2022). The importance of storm surge for sediment delivery to microtidal marshes. Journal of Geophysical Research: Earth Surface, 127(9), e2022JF006612.

APPENDICES

APPENDIX A

Geomorphic and Sedimentological Mapping

In order to document the variability in shore morphology, including the nearshore, beach, dune, and other natural physiological features, the sediment composition of the beach, and engineering features, we mapped the entire project shoreline from Acoaxet Point east to Slocum River Estuary. An example of this mapping is illustrated for Gooseberry Island in a generalized form (Figure A1) and in more detailed in Figure A2. This dataset has provided important input parameters for the modeling studies but can be used by the Towns of Westport and South Dartmouth for general information about their shores and for aiding possible management issues.

Figure A1. Generalized shoreline map of Gooseberry Island showing the shoreline morphological elements and sedimentological composition as well as artificial structures.

Waypoints

Mixed Sand and Gravel

Predominantly Sand

Predominantly Gravel

Ammophila breviligulata

Freshwater Wetland

Boulder Retreat Lag

Overwash

Till Outcrop

Artificial Structures

Dunes

Boulders

Notes:

1. Gravel beach; former dune system
2. Cobbles and boulders on beach; Till dune behind berm
3. End of beach; West side of causeway
4. East side of causeway
5. North of boat ramp; Coarse sand w/ granules
6. Mix of sand and gravel; Granite boulders; Large amounts of wrack
7. Size of gravel on berm increases; Backed by phragmites-dominated wetland

Notes:

8. Gravel beach

9. Mix of cobbles and sand; Cobbles with sandy dunes behind berm

10. Sandy LTT; Cobbles and boulders on beach face; Boulders in subtidal

11. Indications of artificial cobble removal; Abrupt transitions with cobble on top of sand and boulders

12. Transition to gravel beach. Dunes are vegetated with *Rosa rugosa* and *Lathyrus japonicus*

13. Transition from gravel beach to sand. Groin-like feature.

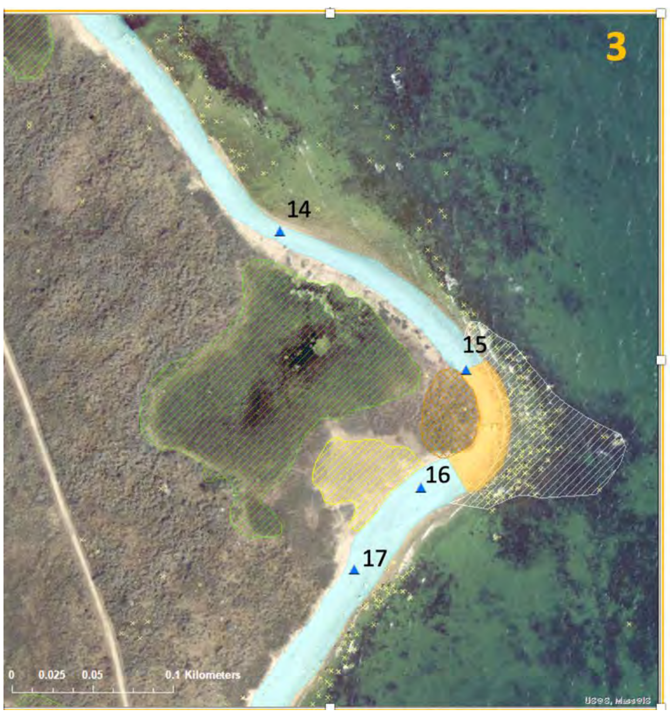

Notes:

14. Steeper gradient on beach face; More gravel on beach face and berm; Freshwater wetland behind beach shows sandy composition

15. Gravel beach; Boulder retreat lag fronting till outcrop.

16. Washover fan, contains cobbles up to 40 cm; Sandy berm 5-6m width; Sand and cobble on beach face; Pebbles and boulders on LTT

17. Boulders in subtidal

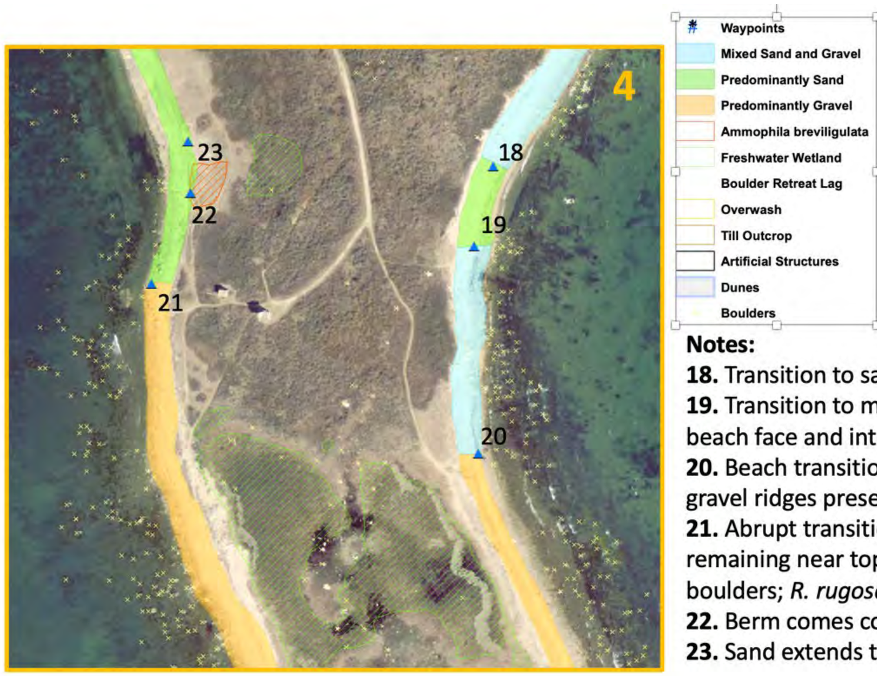

Notes:

18. Transition to sandy beach

19. Transition to mix of sand and gravel with boulders on beach face and intertidal

20. Beach transitions to pebbles and cobbles; Two distinct gravel ridges present; Backed by phragmites wetland

21. Abrupt transition from gravel to sand, with gravel remaining near top of beach profile; Fronted by large boulders; *R. rugosa* on top of sand dunes

22. Berm comes coarser-grained; Backed by sand dunes

23. Sand extends to LTT with sporadic gravel

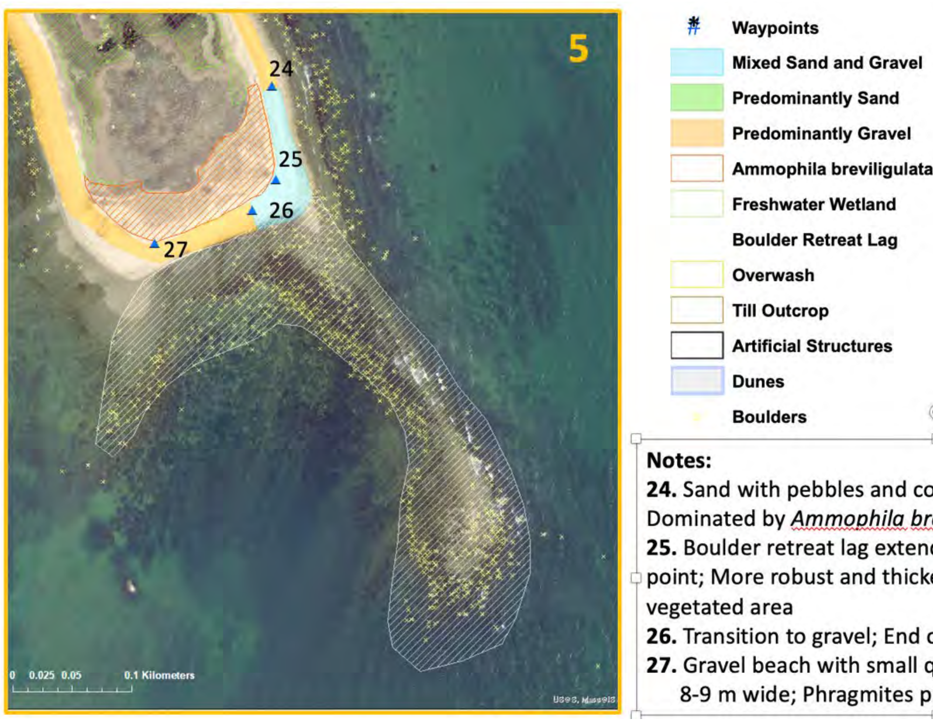

Notes:

24. Sand with pebbles and cobbles beneath vegetation; Dominated by *Ammophila breviligulata*

25. Boulder retreat lag extending ~400m offshore; Sandy point; More robust and thicker vegetation at edge of vegetated area

26. Transition to gravel; End of sand supply

27. Gravel beach with small quantity of sand on LTT; Beach 8-9 m wide; Phragmites present behind beach.

Figure A2. Segmented Geomorphic-Sedimentologic map of Gooseberry Island with notations that add considerable detail for describing changes in sediment type and eco-geomorphic features.

Radioisotopic coring data

Table A1. 210Pb Core Data Summary

Site		WMA-01	WMA-02	WMA-03	WMA-04	WMA-05	WMA-06	WMA-07	WMA-08	WMA-09	WMA-10	WMA-11	WMA-12
Latitude		41.51257	41.54211	41.54543	41.54805	41.51332	41.5132	41.51299	41.51299	41.51448	41.53514	41.53465	41.53347
Longitude		-71.05144	-71.1198	-71.12185	-71.12227	-71.05325	-71.05512	-71.01342	-71.01102	-71.00741	-70.98129	-70.98257	-70.98389
Elevation (m NAVD88)		0.193	0.526	0.453	0.471	0.307	0.342	0.371	0.329	0.326	0.561	0.661	0.662
Elevation (m MSL)		0.077	0.41	0.337	0.355	0.191	0.226	0.255	0.213	0.21	0.445	0.545	0.546
^{210}Pb Accretion Rates	Rate (mm/yr)	3.06	3.54	1.23	1.32	2.37	2.82	2.04	2.38	1.29	1.40	2.79	1.21
	Error (± mm/yr)	0.10	0.11	0.05	0.05	0.03	0.04	0.07	0.05	0.06	0.04	0.11	0.07
^{137}Cs Peak Accretion Rate	Rate (mm/yr)	3.05	3.05	1.53	1.86	2.88	2.88	2.20	2.20	2.20	1.19	1.86	1.19
	Rate Error (±	0.17	0.17	0.17	0.17	0.17	0.17	0.17	0.17	0.17	0.17	0.17	0.17
Bulk Density	Wet FC (g/cm^3)	1.027	1.056	1.056	1.059	1.056	1.026	1.117	1.044	1.194	1.341	1.014	1.052
	Dry FC (g/cm^3)	0.19	0.20	0.20	0.18	0.17	0.18	0.33	0.22	0.43	0.72	0.19	0.21
	Wet 6cm (g/cm^3)	0.992	1.057	1.114	1.154	1.013	1.021	0.991	0.952	1.103	1.121	1.034	1.117
	Dry 6cm (g/cm^3)	0.182	0.209	0.286	0.226	0.177	0.177	0.166	0.219	0.202	0.362	0.234	0.273
	Wet 10cm (g/cm^3)	1.033	1.066	1.117	1.150	1.017	1.042	1.041	0.997	1.133	1.126	1.064	1.081
	Dry 10cm (g/cm^3)	0.206	0.208	0.272	0.233	0.171	0.185	0.192	0.234	0.255	0.384	0.265	0.244
Loss-on-Ignition	Full Core (%)	44.5%	40.8%	33.5%	46.3%	48.2%	49.7%	35.2%	35.6%	28.7%	16.0%	43.9%	43.7%
	Top 6cm (%)	50.0%	49.0%	34.8%	52.0%	47.1%	51.2%	56.0%	41.9%	49.8%	26.8%	45.3%	43.4%
	Top 10cm (%)	45.0%	46.6%	34.0%	47.4%	48.1%	49.7%	50.9%	39.5%	43.6%	25.0%	40.0%	46.2%
Description of core location		East branch Westport River (eastern core)	West branch Westport River (southern core)	West branch Westport River (central core)	West branch Westport River (northern core)	East branch Westport River (central core)	East branch Westport River (western core)	Allen's Pond (western core)	Allen's Pond (central core)	Allen's Pond (eastern core)	Slocum River marsh (NE core)	Slocum River marsh (central core)	Slocum River marsh (SW core)

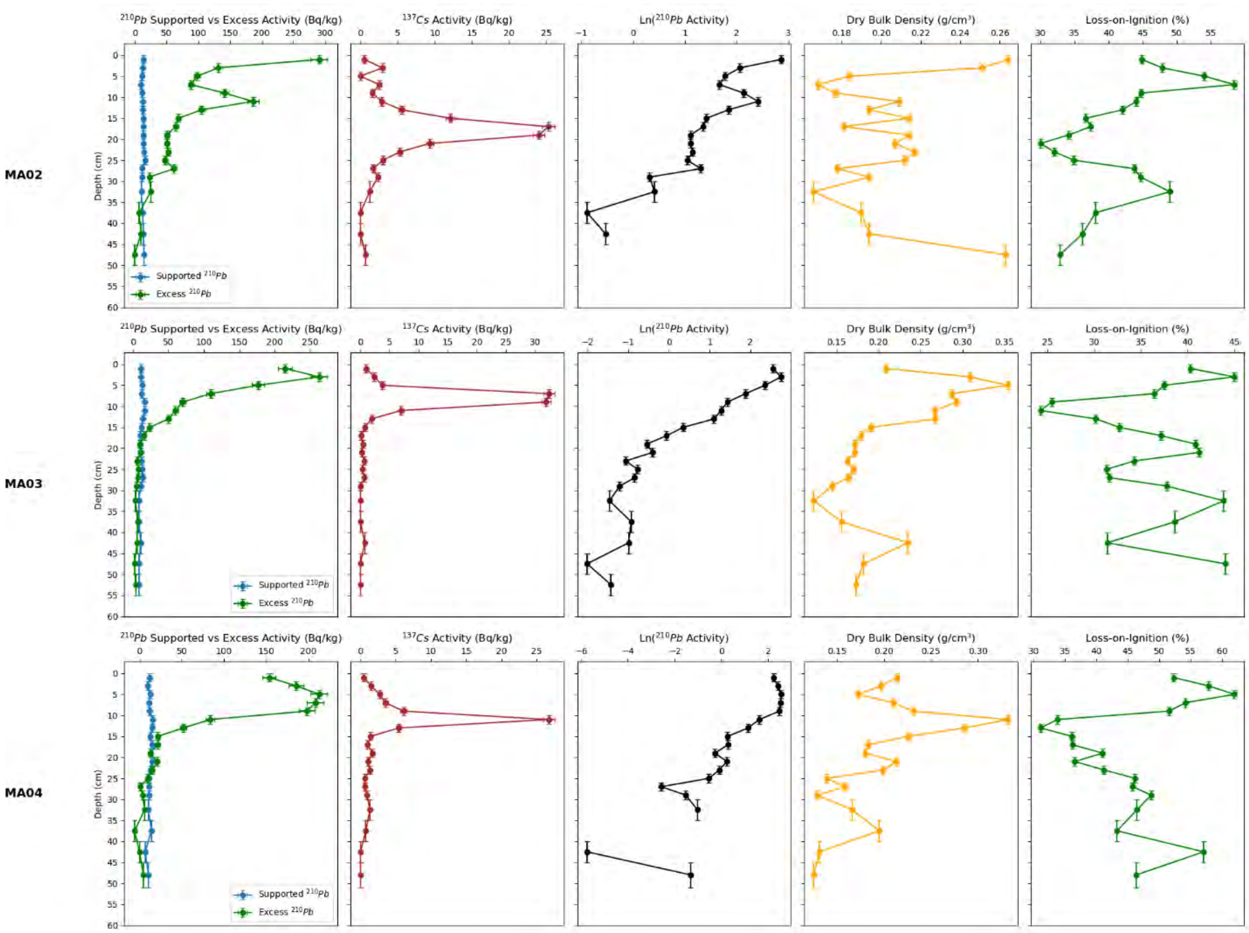

Figure A3 Accretion core data WMA-02 to 04 western branch of Westport River.

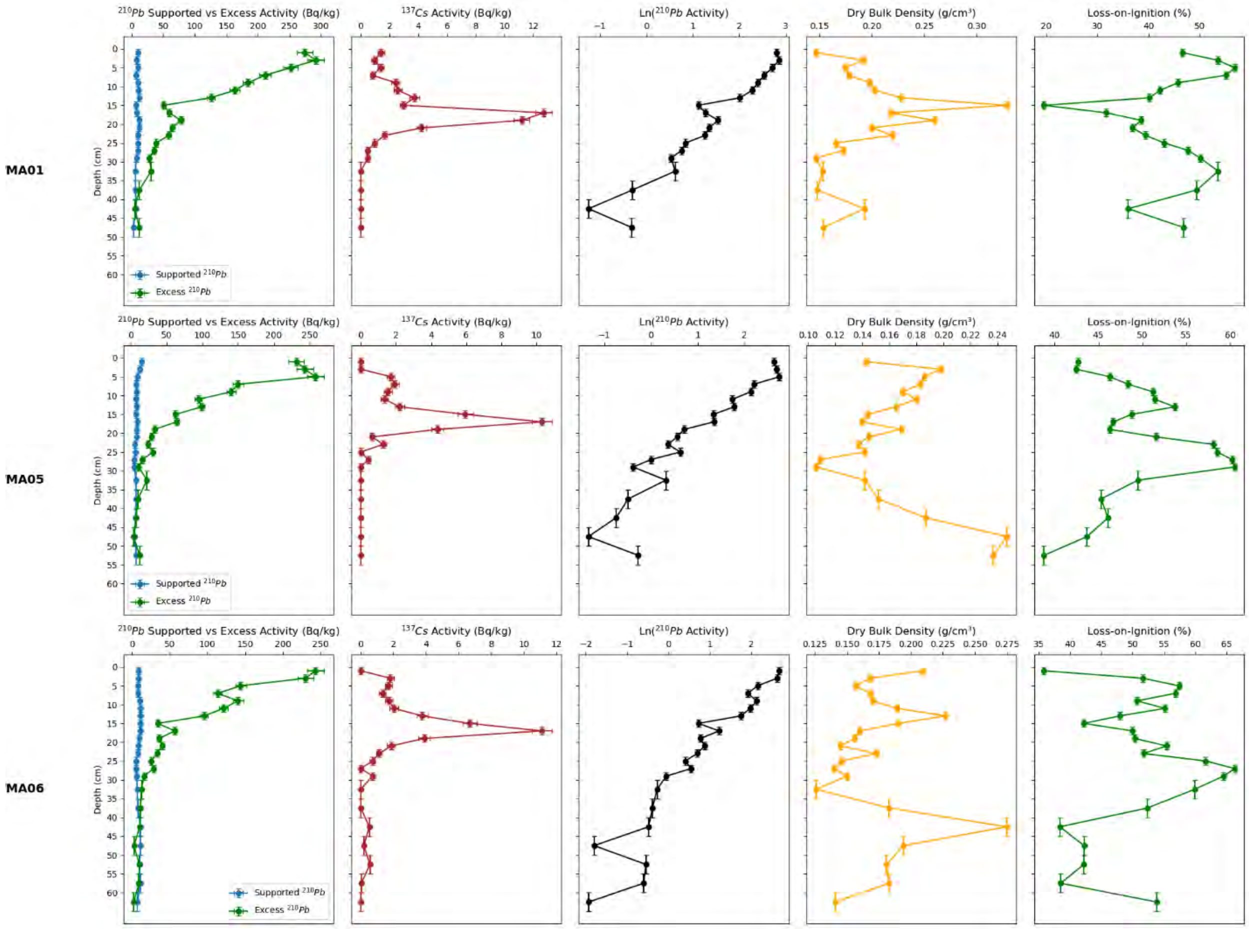

Figure A4 Accretion core data WMA-01, 05 and 06, Eastern branch of Westport River.

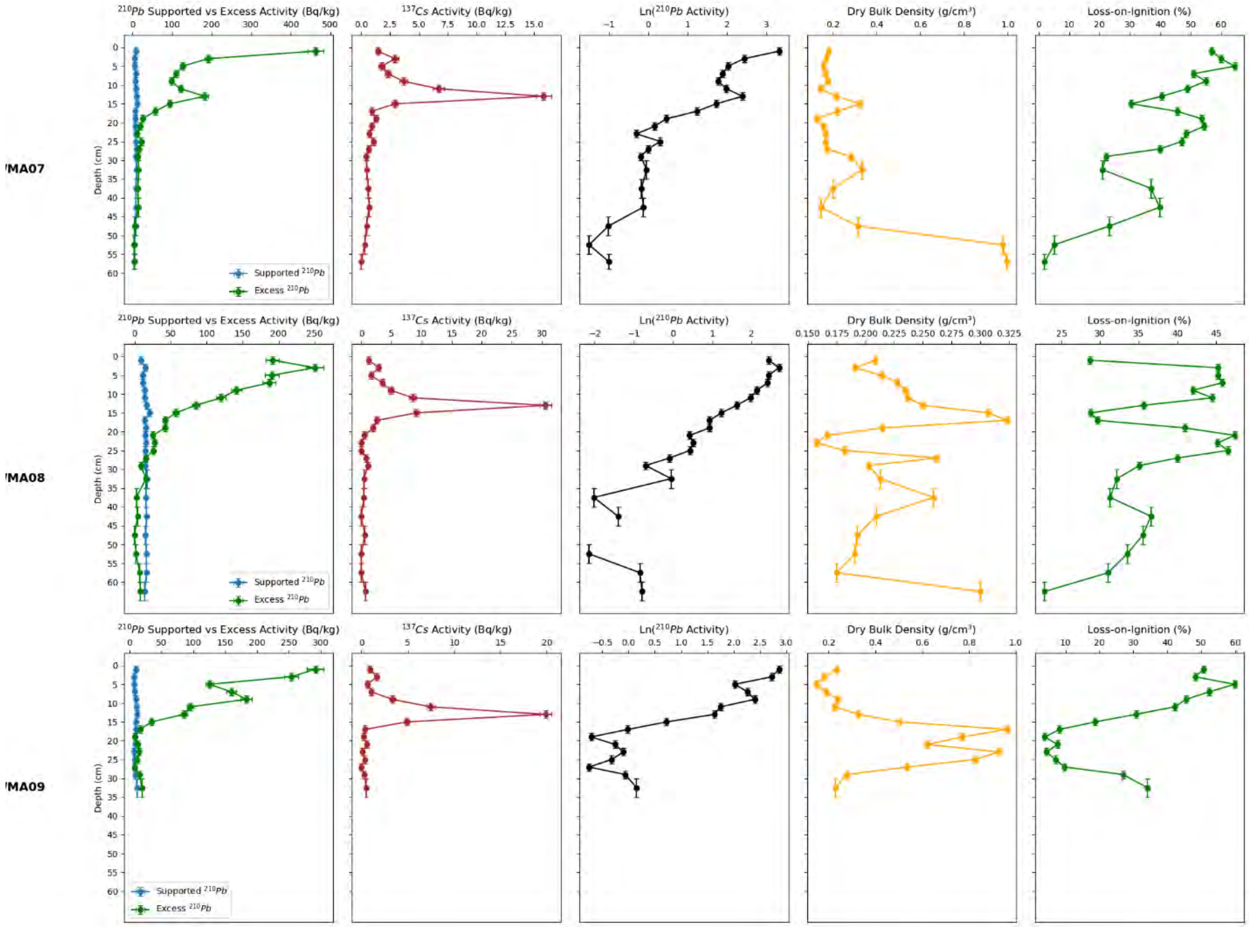

Figure A5 Accretion core data WMA-07 to 09, Allen's Pond.

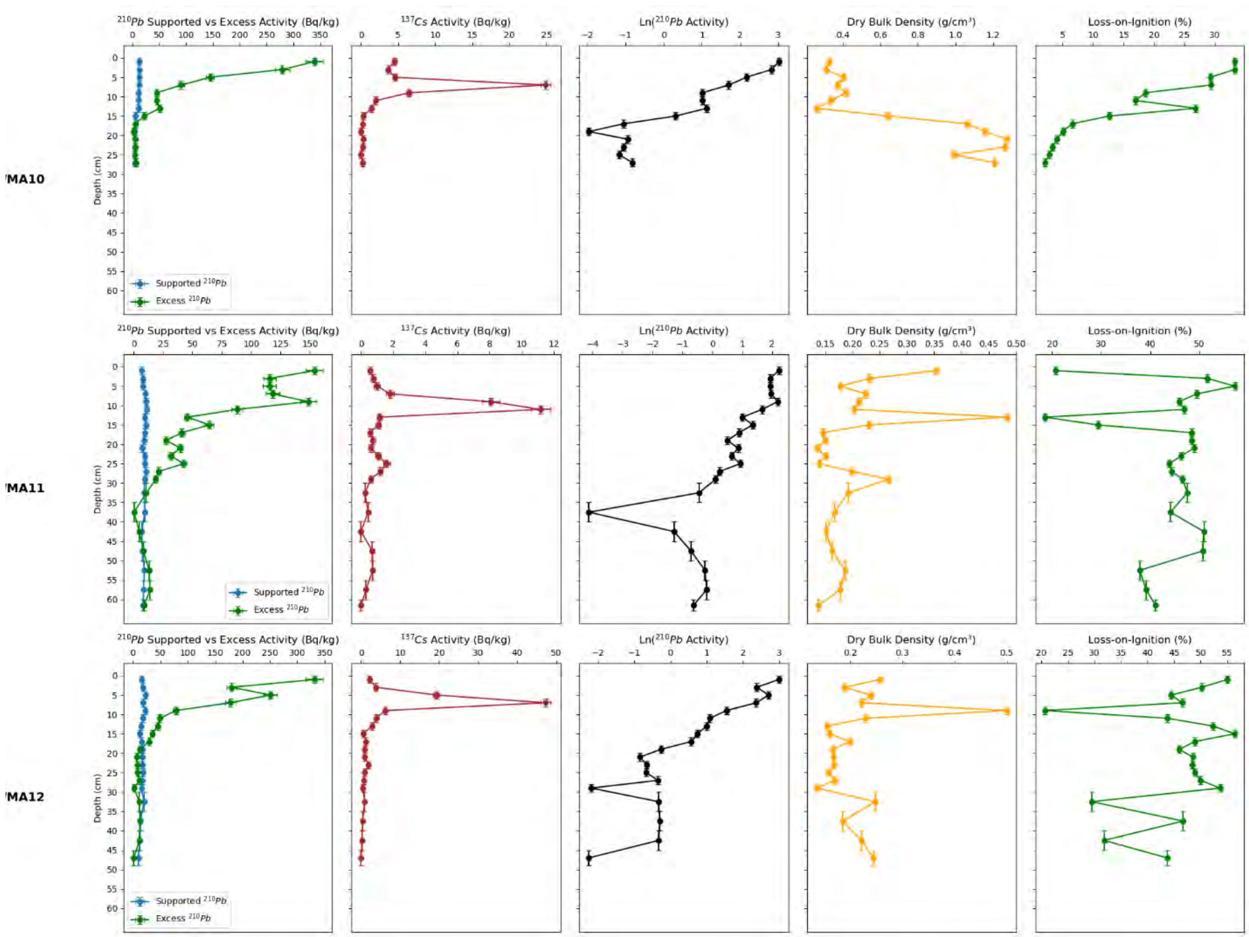

Figure A6 Accretion core data WMA-10 to 12, Slocums River Inlet.

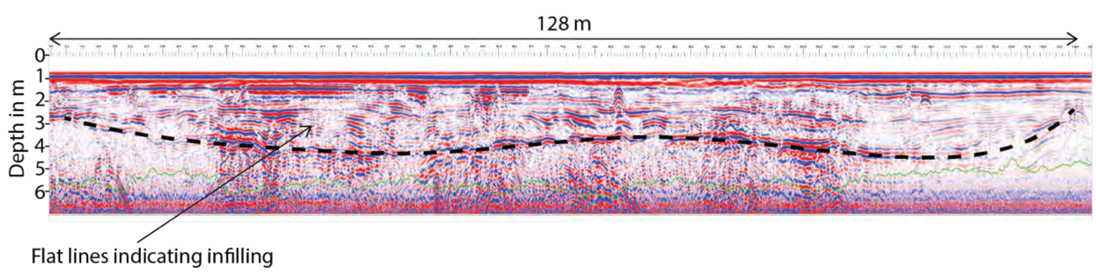

Figure A7. 128 m wide, 3 to 4 m deep channel that once opened to the let. Infilling with flat reflectors.

Next page: Figure A8. Collection of aerial photos from Clamflats (2019) showing East Beach before and after the Hurricane of 1938. The beach system historically exhibited a gravel berm landward of a sandy lower beachface and terrace. A large quantity of this sand, along with fine gravel, was moved from the foreshore to the top of the island during the hurricane.

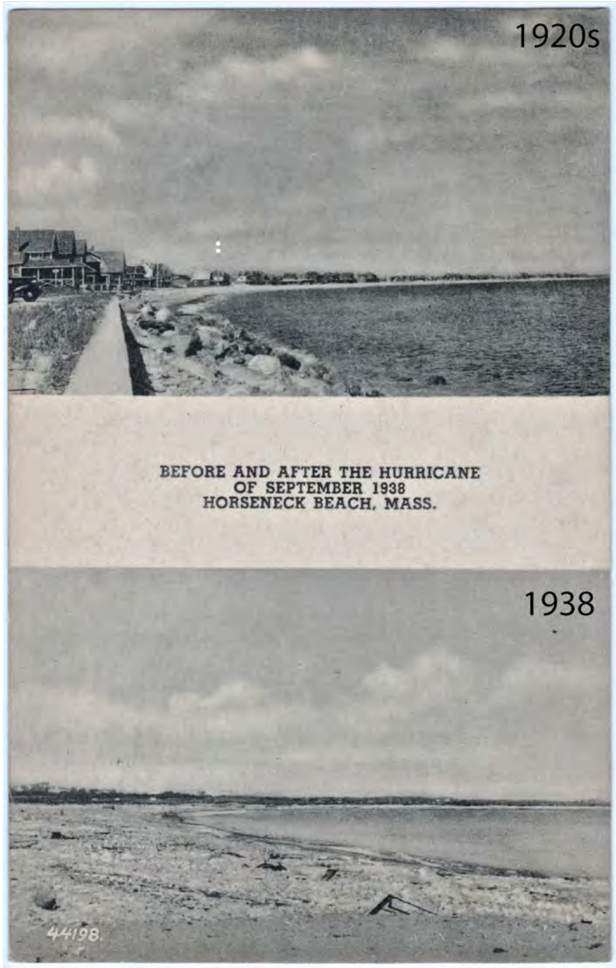

The force of the hurricane at Horseneck Beach carried the St. Rose of Lima chapel (right center) a quarter-mile from its original location.

A bent flagpole and a few fence poles are all that remained of the N. P. Tessier home at East Horseneck Beach the morning after the storm. This was one of the most palatial homes at the beach.

APPENDIX B

Attached documents:

Beach Observations.pdf
Observations of the beach on 29 Nov 2022. Observations were made during a field excursion to set up beach profiles.

Xie, D., Hughes, Z.J., FitzGerald, D., Tas, S., Zaman Asik, T., and Fagherazzi, S., 2024. Longshore Sediment Transport Across a Tombolo Determined by Two Adjacent Circulation Cells. Journal of Geophysical Research: Earth Surface. 29:10. https://doi.org/10.1029/2024JF007709

Xie, D., Hughes, Z.J., FitzGerald, D.M., Tas, S., Zaman Asik, T., and Fagherazzi, S., 2024, Impacts of climate change on coastal hydrodynamics around a headland and potential headland sediment bypassing. Geophysical Research Letters, 51, e2023GL105323. https://doi.org/10.1029/2023GL105323

Tas, S.A.J., Hughes, Z.J., FitzGerald, D.M., Xie, D, Asik Zaman, T. and Fagherazzi, S, 2025. Headland bypassing: Moderate storms dominate extreme events. Journal of Geophysical Research: Oceans. *In review post-revision*.

Observations of the beach on 29 Nov 2022

- Observations were made during a field excursion to set up beach profiles.
- The state of the beach at this time does not characterize the Summer beach conditions because of mid-November strong southerly wind/storms that eroded the beach.

Site #1 Slocum Embayment Western Spit Side

- This site is at the juncture between the inner sandy spit shoreline and outer gravel beach shoreline.
- Along much of this transition zone, gravel dominates the low-tide terrace region.

Site 2. Beach East of Allens Pond Inlet

- Note gravel in lower intertidal zone and westward along lower beach.
- Previous erosion of berm indicated by small berm scarp

Site 3. Little Beach West of Allens Pond Inlet

- Beach entirely composed of gravel (mostly cobble)
- Region contains incipient dunes mantled with gravel.
- Beach exhibits several gravel terraces
- Mobility of gravel indicated by storm gravel washovers and gravel cusps

Site 4. East Horseneck Beach

- East end of the beach is dominated by gravel
- Landward of gravel beach are well established sand dunes
- Photo on left illustrates how gravel is mantling the sand dunes

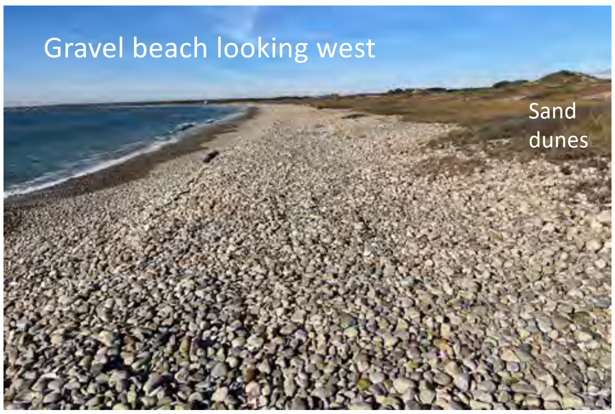

Site 5. Mid-Horseneck Beach

- Gravel exposed along lower beach; site visit during summer show beach dominated by sand.
- Likely mid-Nov storms moved sand offshore exposing gravel
- New sand in dunes blown by summer winds

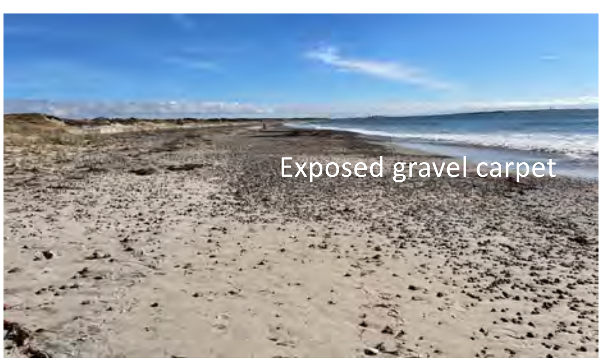

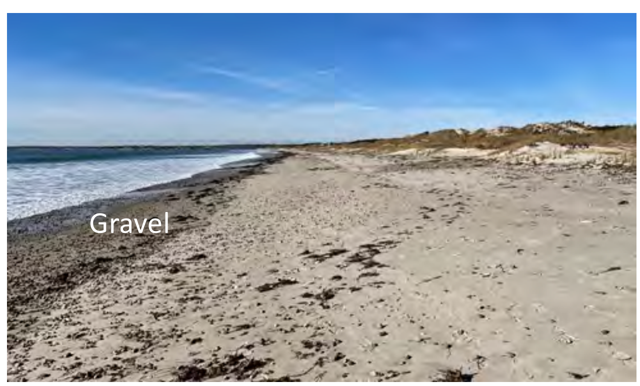

Site 6. West Horseneck Beach

- Beach dominated by sand; gravel is very sparse
- Note the berm scarp indicating recent erosion.
- Interesting, that this region extending to the inlet is the only area without extensive gravel

ADVANCING EARTH AND SPACE SCIENCES

JGR Earth Surface

RESEARCH ARTICLE
10.1029/2024JF007709

Longshore Sediment Transport Across a Tombolo Determined by Two Adjacent Circulation Cells

Danghan Xie[1,2], Zoe Hughes[1], Duncan FitzGerald[1], Silke Tas[1,3], Tansir Zaman Asik[1], and Sergio Fagherazzi[1]

[1]Department of Earth and Environment, Boston University, Boston, MA, USA, [2]Scripps Institution of Oceanography, University of California San Diego, La Jolla, CA, USA, [3]Hydrology and Environmental Hydraulics, Wageningen University and Research, Wageningen, the Netherlands

Key Points:

- The position, magnitude, and size of circulation cells on both sides of a tombolo vary with storm surge, wave height, and wave direction
- Circulation cells and storm-driven water level differences determine sediment transport across the tombolo
- Longshore sediment transport across the tombolo is negligible except during extreme storms

Supporting Information:

Supporting Information may be found in the online version of this article.

Correspondence to:

D. Xie,
danghan@ucsd.edu

Citation:

Xie, D., Hughes, Z., FitzGerald, D., Tas, S., Asik, T. Z., & Fagherazzi, S. (2024). Longshore sediment transport across a tombolo determined by two adjacent circulation cells. *Journal of Geophysical Research: Earth Surface*, *129*, e2024JF007709. https://doi.org/10.1029/2024JF007709

Received 26 FEB 2024
Accepted 15 SEP 2024

Abstract

Longshore sediment transport (LST) is essential for shaping sandy shorelines. Many shorelines are complex and indented, containing headlands, offshore islands and tombolos. Tombolos often form between islands and the mainland; however, the conditions for LST across tombolos are unclear. This question is important because tombolos are often reinforced with anthropogenic infrastructure, potentially causing sediment starvation of downdrift beaches. Along many shorelines, the return to a tombolo's natural condition has been proposed to promote sediment connectivity and counteract erosion. Nevertheless, the implications of such restorations remain uncertain. In this study, we employ the Delft3D wave-current model to investigate hydrodynamics and sediment dynamics across a tombolo, examining its role as a connector between adjacent beaches. Contrary to expectations, our simulations show only diminutive longshore currents from the updrift beach across the tombolo unless offshore wave heights exceed 8 m. Instead, predominant currents crossing the tombolo originate from offshore of the island, driven by storm-induced water level differences and circulation cells on both sides of the tombolo. The offshore island shelters the downdrift domain, resulting in higher wave energy and dissipation updrift of the tombolo. Further, increasing wave height or wave approach angle not only intensifies water level differences but also relocates circulation cells, enhancing total sediment transport from the updrift beach across the tombolo. However, in general, the deposition of sediment from the updrift side of the domain does not compensate for the sediment loss on the downdrift beach. We conclude that LST across tombolos is limited and occurs only under extreme wave conditions.

Plain Language Summary

Longshore transport, the movement of sand and fine gravel along the shoreline driven by waves and tides, plays a crucial role in building and maintaining stable and healthy beaches. Here, we focus on the potential impact of the removal of a road that obstructs water flow and sediment transport across a tombolo. Contrary to our expectations, removal of the road does not result in longshore currents across the tombolo unless the wave heights are very large. Instead, we observe water movement from the offshore of the island's updrift side toward the downdrift beach. This unexpected pattern is attributed to storm-driven water level differences bet side of the island. Additionally, storms generate circulating current patterns on both sides of the island, influencing the direction of water movement. Further investigation reveals that larger waves, particularly those moving more parallel to the beach, amplify the water level difference and alter the location of the rotating currents. Extremely large waves produce longshore currents across the tombolo, which increase the amount of sediment transferred from the updrift to the downdrift domain. However, this addition of sediment from the updrift domain does not fully compensate for sediment loss from the downdrift beach during storms.

1. Introduction

Longshore sediment transport (LST) plays a vital role in shaping the coastal landscape and influencing shoreline evolution. The process allows for sediment redistribution from one location to another, thereby buffering areas undergoing erosion (Giosan et al., 1999; Greer & Madsen, 1978; Shetty & Jayappa, 2020). LST is primarily induced by waves breaking at an oblique angle to the shoreline, resulting in a longshore current flowing within the breaker and surf zones (Hamilton & Ebersole, 2001; Kobayashi et al., 2007). In shoreline systems connected to offshore islands, current patterns may become complex because of circulation cells (Ganju et al., 2011; Klein et al., 2020; Pattiaratchi et al., 2009; da Silva et al., 2021). These cells, characterized by circulation gyres on either side of offshore islands, are formed primarily during storms by large breaking waves interacting with longshore currents along the beach. The circulation cells may shift under varying sea-level rise or storm conditions (Xie et al., 2024). Consequently, possible sediment bypassing around the islands may be limited, leading to sediment deficiencies and subsequent shoreline erosion along downdrift beaches (King et al., 2021; da Silva et al., 2021). The uneven availability of sediment can also exist in the vicinity of naturally occurring coastal features, such as tombolos and headlands, and human-made structures, such as groins and breakwaters. These features restrict water movement along the shoreline, increasing sediment deposition on the updrift side of the obstacles while reducing sediment availability on the downdrift (Bacon et al., 2007; Cuadrado et al., 2005; Specht et al., 2020). To reestablish the LST and increase sediment availability to downdrift shorelines, an increasing number of coastal managers propose removal of these obstacles (Chi et al., 2023; Nordstrom, 2014). However, questions still exist as to whether such measures would reintroduce effective downdrift sediment supply along these complex shorelines, especially during storms when circulation cells are formed.

The magnitude of LST is influenced by various factors, including wave height, wave angle, nearshore slope, and sediment composition (Chowdhury et al., 2020). For example, Pattiaratchi et al. (1997) reported that even minor increases in wave heights can lead to larger incident wave energy at the shore, potentially resulting in a ten- to hundredfold increase in LST. This is because wave energy and, thus, the resulting radiation stresses and sediment-transporting currents at the shore are proportional to the square of the wave height (Kaliraj et al., 2014). The angles at which waves approach the shoreline are crucial. When waves approach the shore perpendicularly, the resulting wave breaking and energy dissipation predominantly lead to cross-shore sediment transport (Butt et al., 2000). However, waves breaking at an angle to the shoreline create radiation stress, yielding both cross-shore and longshore components. The longshore component of the radiation stress generates longshore currents, which drive the transport of sediment parallel to the shoreline (Chowdhury et al., 2020; Putnam et al., 1949; Vincent et al., 1983). The composition of the bottom sediment plays a crucial role in determining the amount of sediment that can be resuspended. For instance, smaller sediment particles can be transported over greater distances compared to larger ones (Grasso et al., 2011).

Along open coasts, particularly in tropical and subtropical areas, storm-induced coastal sediment redistribution is known to have major geologic and ecological implications (Fagherazzi et al., 2020; FitzGerald et al., 2020; Goman et al., 2005; Hubbard, 1992). However, storm-driven LST in complex settings needs to be further investigated (Yang et al., 2023). Storms generate waves and surges, which can persist for several hours or even days (Villarini et al., 2011). Storm surges allow higher wave energy to reach the shoreline, facilitating nearshore currents that scour beach material, ultimately moving sediment to more sheltered areas (Hequette et al., 2001; Roy et al., 1994; van Wiechen et al., 2023). Storms can also redistribute sediment by resuspending material from deep water and moving it to shallow coastal regions, increasing sedimentation and buffering beaches (Roberts et al., 2013). Along shorelines connected to offshore islands, however, the distribution of wave energy can vary. Offshore islands not only provide shelter, preventing direct wave energy impact on the mainland shoreline, but also induce wave refraction and convergence (Yasso, 1965). This is because the presence of an offshore island shifts the surf zone offshore, thereby lessening the wave energy reaching the shore (Limber et al., 2014). These processes add complexity to nearshore wave energy distribution, particularly during storms. Furthermore, wave energy dissipation gives rise to circulation cells around the offshore island, which have been observed to interact with longshore currents (King et al., 2021; Xie et al., 2024). Previous studies have shown that circulation cells along with tidal currents create a morphological cycle affecting both beach sediment and offshore sandbars (Siegle et al., 2004, 2007). Specifically, in high wave energy systems, circulation cells can redistribute sediment by eroding offshore sandbars, while in low wave energy periods, ebb tidal currents are responsible for creating sandbars through offshore sediment transport. The influence of these circulation cells on LST therefore creates uncertainty in sediment transport rates to downdrift beaches, especially under varying wave energy and storm tide conditions. Further investigation is needed to assess the benefits of altering any updrift structure to promote LST, particularly in complex coastal systems with offshore islands.

In Western Buzzards Bay, Massachusetts, USA, an offshore island, Gooseberry Island, is connected to the mainland by a causeway, part of a headland system along the Westport-Dartmouth shore (Figure 1; Xie et al., 2024). The causeway was initially constructed a century ago on top of a sand and gravel tombolo and has been reinforced and elevated over the decades (Figures 1b and 1c). Currently, the causeway is approximately 10 m wide at the top and 450 m long, with the water depth at the toe being around 2 m. Large boulders (1–2 tons) have been placed along both sides of the causeway to prevent breaching during storms. At the same time, East Beach, the downdrift side of the causeway, has experienced degradation attributed to both sea-level rise and a waning sediment supply (FitzGerald et al., 1987). There are concerns that construction of the causeway diminished

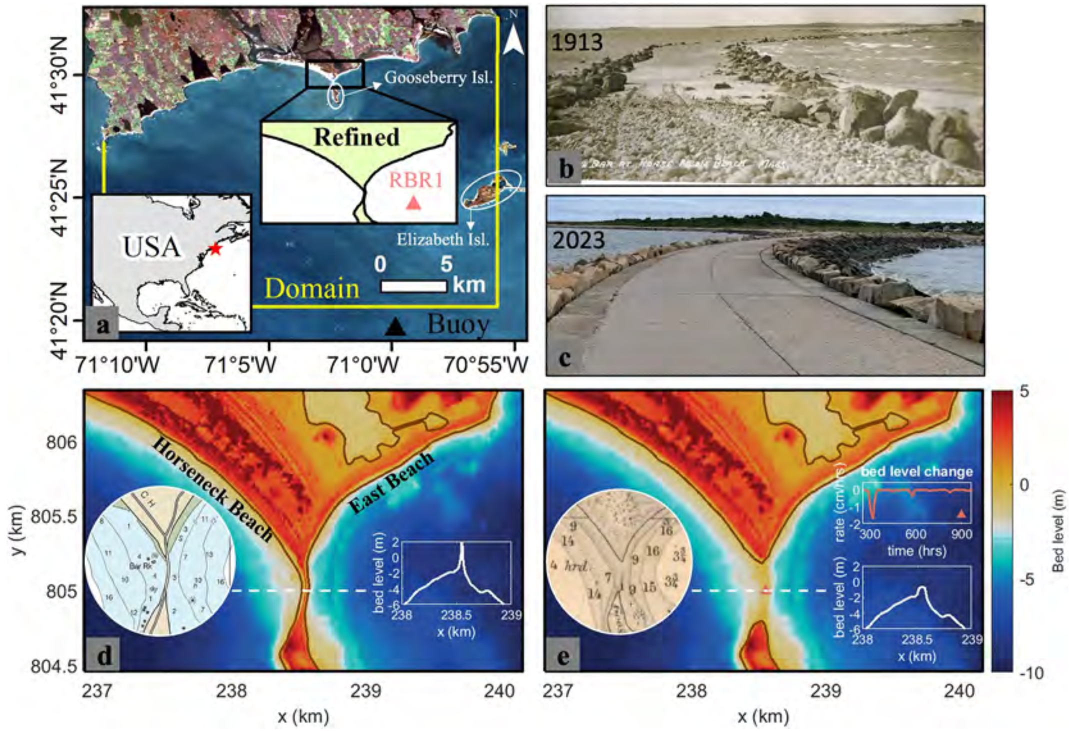

Figure 1. Maps and photos showing the study area (a) Delft3D-FLOW domain is overlayed with a Delft3D-WAVE domain (yellow box). The focus area of this research is modeled with a refined sub-domain (black box) that includes the tombolo where a causeway was constructed at the beginning of the twentieth century. An RBR (Richard Brancker Research) Solo pressure sensor was deployed on the east side of the causeway to measure storm tides and significant wave heights for model validation. The black triangle shows the location of an offshore buoy (Station BUZM3/44085; water depth 21 m) recording wave conditions (wave heights, wave period and wave direction) for model setups. The Elizabeth Islands are located to the southeast of the system. (b) Ground photograph looking southward to Gooseberry Island in 1913 (Clamflats, 2019); Residents placed boulders along the natural tombolo in order to create a path connecting to Gooseberry Island during low tide. (c) Ground photograph looking southward to Gooseberry Island in 2023 (Danghan Xie, August 2023). The causeway has been built up higher than mean high water, potentially obstructing longshore sediment transport. (d) Current bathymetry with a causeway and (e) bathymetry without causeway, which has reached an equilibrium state under non-storm conditions with the constant effects of a 20-cm wave height. Two historical sea charts in panels (d, e) depict the digital elevation model around the tombolo at different times (NOAA, 2024). The inserted line plots in these panels show the elevation across the causeway and tombolo, with modeled rate of bed level change after the bathymetry was altered to represent pre-causeway conditions until equilibrium state was reached, shown in panel (e). The bed level in the two domains is comparable with the sea charts in 2016 (d) and 1892 (e).

sediment transport to East Beach. In response, residents have proposed the removal of the causeway to restore the natural tombolo, which would reestablish sediment connectivity between Horseneck Beach (updrift side) across the tombolo to East Beach (Figure 1d). However, there is limited knowledge concerning potential sediment transport across tombolos, particularly transport associated with storms, which are known to produce circulation cells on both sides of the headland (Xie et al., 2024). This study aims to investigate transport across a natural tombolo, were the causeway not to exist. We address two key questions: (a) Would sediment transport occur across the tombolo? and (b) If so, what factors control the magnitude and direction of currents and sediment transport, including the role of storm surges, significant wave height, and wave direction.

2. Materials and Methods

In this section, we introduced the background information of the study site (Section 2.1), examined the storm characteristics based on 100 historical storm events (Section 2.2), analyzed the sediment data collected from the field, and set up the sediment bed module for the model (Section 2.3). We also determined the model parameter settings and created new bathymetry that included a tombolo (Section 2.4). Furthermore, we validated the models with measurements recorded during an extratropical storm event (Section 2.5), and designed both idealized and real storm scenarios, creating corresponding boundary conditions (Section 2.6).

2.1. Study Site

The study area is in Western Buzzards Bay along the shores of Westport and South Dartmouth, Massachusetts, USA. This region is part of an indented shoreline that includes an offshore island, Gooseberry Island, connected to the mainland by a manmade causeway (Figures 1a–1c). Along the shoreline, there are two beaches: Horseneck Beach to the west (on the updrift side) and East Beach to the east (on the downdrift side), with Gooseberry Island serving as a natural divider between them (Figure 1d). Due to the sheltering effects of Cape Cod and the Elizabeth Islands, which protect from eastern winds and waves, dominant waves typically originate from south to southwest, with an average nearshore wave height of 0.75 m and a wave period of 6.0 s in 10-m water depth (FitzGerald et al., 1992). Tides within the bay are semidiurnal, with an average tidal range of approximately 1.1 m (FitzGerald et al., 1987; Sankaranarayanan, 2007). Two small rivers on either side of the area contribute negligible amounts of fluvial input, approximately 2 m^3/s (Bent, 1995; FitzGerald et al., 1987). According to the National Oceanic and Atmospheric Administration (NOAA) hurricane database, between 1851 and 2013, a total of 55 hurricanes have impacted the southern New England. One of the most significant hurricanes, Hurricane Bob, produced a storm surge of approximately 2.8 m and peak storm waves exceeding 8 m (Sun et al., 2013). Such extreme storm events resulted in significant sediment transport and shoreline change in the coastal system (Cheung et al., 2007). In addition to hurricanes, coastal flooding and damage in this region are also frequently caused by extratropical cyclones (also known as Nor'easters or winter storms; Zhang et al., 2020).

2.2. Storm Characteristics

To characterize storm conditions in this region, we analyzed storm surge, peak storm wave height, and storm wave direction from 1938 to 2012 using data obtained from the North Atlantic Coast Comprehensive Study (NACCS) Coastal Hazards System at the buoy location (BUZM3, black triangle in Figure 1a; Cialone et al., 2015). This database includes 100 historical storms, predominantly from extratropical cyclones. We identified the frequency of storm characteristics by calculating density histograms and the probability density function (Kernel Density Estimate) for each storm, following the methodology outlined by Bai et al. (2020). A higher probability density value indicates that storm characteristics (e.g., storm surges, peak waves, or wave direction) of this magnitude have historically been more frequent.

For our study site, the most prevalent storm surge is approximately 0.65 m, and the most frequently observed peak wave height during storms is approximately 4 m (Figures 2a and 2b). The maximum storm wave height in this area can surpass 10 m, but such occurrence is highly infrequent (Figure 2b). The dominant wave direction is 185°,

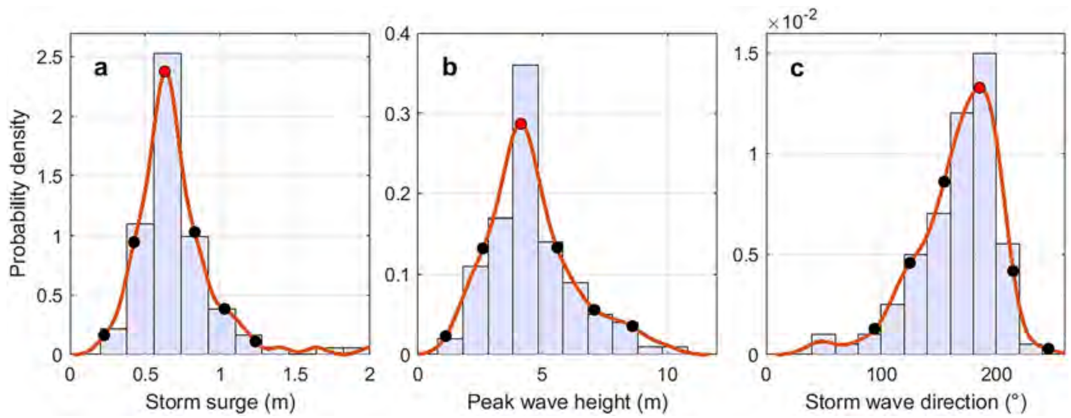

Figure 2. Normalized histogram and kernel density estimate (KDE) curve of historical storm characteristics extracted from the NACCS Coastal Hazards System (Point No. 09088). The storm characteristics examined here include (a) storm surge, (b) peak storm wave heights and (c) storm wave direction. The KDE curve provides a smooth estimate of the underlying probability density function of the data generated using a Gaussian kernel function. Wave direction in panel (c) is based on Nautical convention with 0° indicating waves coming from the north and 90° indicating waves traveling from the east.

Table 1
Model Scenarios for Synthetic and Historical Storms

No.	Group	Storm surge (m)	Storm wave height (m)	Storm wave direction (°)	Note
1	Impacts of storm surge	0.25	**4**	**185**	-
2		0.45			-
3		**0.65**			REF
4		0.85			-
5		1.05			-
6		1.25			Surge +
7	Impacts of storm wave height	**0.65**	1	**185**	-
8			2.5		-
Same as No. 3			**4**		REF
9			5.5		(extreme storm)
10			7		(extreme storm)
11			8.5		Wave + (extreme storm)
12	Impacts of storm wave direction	**0.65**	**4**	95	-
13				125	-
14				155	-
Same as No. 3				**185**	REF
15				215	-
16				245	-
17	Historical storms	0.45	5.3	193	2022- Extratropical Storm Elliott (extreme storm)
18		0.71	8.7	191	2011-Hurricane Irene (extreme storm)
19		2.77	8.8	176	1991-Hurricane Bob (extreme storm)

Note. (1) Reference idealized storm is indicated in bold; (2) Storm surge, wave heights, and wave direction vary over time in three historical storms, with the values during peak wave heights indicated in 17–19.

indicating prevailing waves coming from the south (Figure 2c). The storm characteristics provide a reference for our numerical model scenario setups. In the following text, the reference scenario is abbreviated as REF. The storm surge and wave input for the model runs are derived from the frequency distributions (black and red dots in Figure 2) covering different probability densities of each parameter (see Table 1 introduced in Section 2.6, where the bold font indicates the highest probability).

2.3. Sediment Sampling and Sediment Profile Compilation

We collected a total of 200 sediment samples, covering areas from deep water (~15-m water depth) to the beach system (see circles in Figure 3a). In agreement with a previous study by FitzGerald et al. (1992), we found that almost 85% of the Western Buzzards Bay sediment samples contained sand, with only 8% being gravel. The samples were sieved to determine the median grain size (d_{50}, Figures 3c–3f). The average d_{50} across the samples was approximately 230 μm, whereas the gravel ranged from 5,000 to 35,000 μm, with an average size of nearly 20,000 μm (Figures 3e and 3f). Thus, our numerical model considered these two grain size classes. The median grain size for sand was set to 230 μm, and for gravel, it was set to 20,000 μm.

In addition, sediment deposits in the area display upward fining, with coarser sediment underlying finer grained sand (FitzGerald et al., 1992). We therefore set up the bed module by combining two sediment layers for the sediment profiles in both large and refined model domains (Figure 3b). Sediment classes of layer 1 were determined based on the sediment texture map provided by USGS (Foster, 2014), which exhibits a similar distribution of sediment to the samples collected from the field (Figure 3a). As sand is the dominant sediment class in the study area, we assumed that the missing data region in the bottom left of the domain consists mainly of sand

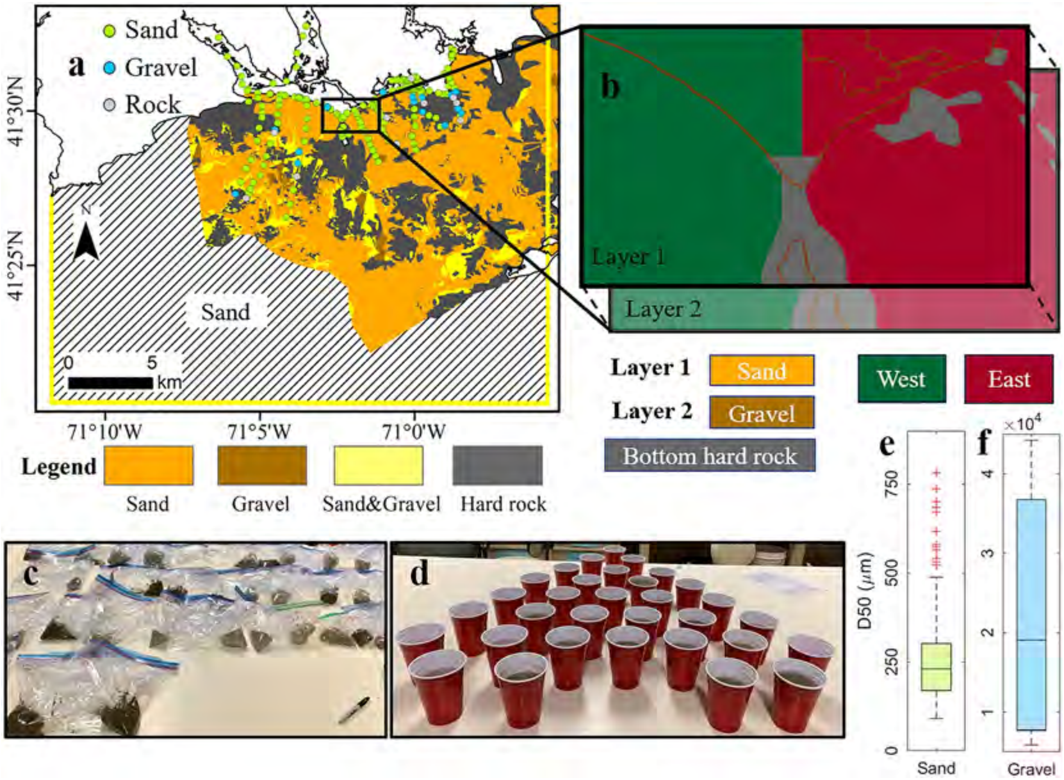

Figure 3. Domain sediment profile setups. (a) Sediment texture map and field points collected for sediment sampling. The sediment texture map indicates the spatial sediment types within Western Buzzards Bay, which mainly contains sand and gravel overlaying hard rocks (Foster, 2014). (b) Two-layer bed module in the refined model. Sediments in the west and east domains are configured separately to trace the sediment movement between the west and east regions. (c) Sediment samples collected from the field. (d) Pre-cleaning of sediment before drying. Median grain size (d_{50}) of sand (e) and gravel (f).

(see the hatched region of Figure 3a). In non-hard rock regions, a second layer was introduced under layer 1 (Figure 3b). Layer 2 was assigned as gravel to replicate the pattern of upward fining (FitzGerald et al., 1992). The thickness of each sediment layer was set to 50 cm. To identify the sources of sediment and determine the amount of sediment transported across the tombolo, sediment in the west and east domains were set up separately (Figure 3b). Transport of sand and gravel in the model used the Van Rijn transport equations, with suspended-load transport and bed-load transport calculated separately (van Rijn et al., 2004). Transport of suspended sediment was determined using the advection-diffusion equation. In this study, we refer to the area updrift of the causeway as the west domain and the area downdrift of the causeway as the east domain (Figure 3b).

2.4. Model Setup

Following our previous research investigating the formation of circulation cells in this area (Xie et al., 2024), we further explored the hydrodynamics and sediment transport around the tombolo using the spatially resolved and process-based model Delft3D (Lesser et al., 2004). We focus on wave-current interactions, including the impacts of flow on waves (via set-up, current refraction, and enhanced bottom friction) as well as the effects of waves on currents (via forcing and enhanced bed shear stress). We employed an online-coupled model between Delft3D-WAVE and Delft3D-FLOW. Delft3D-WAVE models wave propagation and wave energy dissipation based on the third-generation spectral wave model SWAN (Simulating WAves Nearshore; Booij et al., 1999), while Delft3D-FLOW simulates hydrodynamics and sediment transport by solving the depth-averaged shallow water equations. To better capture flow and sediment dynamics around the tombolo while improving computational efficiency, the domain was divided into two parts. A locally refined model domain was established around the tombolo (indicated by the black box in Figure 1a), and a larger model domain covered the rest of Western Buzzards Bay (indicated by the yellow box in Figure 1a) using the domain decomposition technique (Deltares, 2014; Zhu & Wiberg, 2022). The refined model does not extend to cover the full Gooseberry Island and its neighboring area because: (a) our main focus centers on the tombolo region, (b) computation efficiency is significantly enhanced with a smaller region, and (c) the west sediment moving onshore to East Beach through the offshore of Gooseberry Island is minimal compared to the major sediment movement across the tombolo (Figure S1 in Supporting Information S1).

The refined model domain around the tombolo contained 326 × 190 (X × Y direction) rectangular grid cells with a uniform spatial resolution of 10 m by 10 m. The large model domain consisted of 469 × 389 rectangular grid cells. Near the shoreline and island, the grid resolution was 40 m by 40 m, gradually extending to 40 m by 80 m at the southern seaward and northern landward boundaries in the cross-shore direction. The domain decomposition technique enabled parallel computation between the refined model and large model domains, with hydrodynamic information and sediment transport exchanged along the shared boundaries at each time step (Figure 1a). The initial bathymetry for the two domains was interpolated from a high-resolution digital elevation model (DEM) developed by NOAA for the USA coast (CIRES, 2014). The DEM data have a horizontal resolution ranging from 1 m to 30 m and a vertical resolution smaller than 1 m. To assess potential changes in hydrodynamics and sediment transport after the removal of the causeway, we developed new bathymetry by lowering the elevation of the causeway to the mean water level. This was followed by a long-term simulation with idealized tides and waves until the bed level change at the tombolo remained negligible (see the inserts in Figures 1d and 1e). During this simulation, the tidal range was set to 1 m and the wave height was set to 0.2 m. Compared to the historical sea chart from the year 1892, where the elevation around the tombolo was approximately 1 foot (=0.3 m) below the mean low water level (around 0.9 m below mean water level), our new bathymetry depicts a tombolo elevation of 1 m below the mean water level, nearly identical to the data shown in the sea chart (Figure 1e). Thus, we assume that the new bathymetry successfully reproduced the naturally formed tombolo. The tombolo is set to be non-erodible during simulations, enabling us to focus on the sediment transport between updrift and downdrift systems without interference from sediment erosion from the tombolo.

2.5. Model Validation

Validation encompassed both large and refined models where the causeway is present. In a previous study, validation of the large model involved comparison against two ADCPs measuring data and 43 validation points extracted from the NACCS Coastal Hazards System (Xie et al., 2024). To validate the refined model, high frequency water level and wave records were obtained using an RBR-Solo pressure sensor (RBR1) installed on the east side of the causeway from July–November 2022 (Figure 1a). RBR1 successfully captured water level and wave height during the winter storm of November 2022. To evaluate our refined model performance, we calculated the model skill index using the validation approach proposed by Willmott (1981). The skill index is defined as:

$$\text{Skill} = 1 - \frac{\sum |X_D - X_S|^2}{\sum \left(|X_D - \overline{X_S}| + |X_S - \overline{X_S}| \right)^2} \tag{1}$$

where X_D is the refined Delft3D model output and X_S is the measured data from RBR1, both of which are applied herein at hourly intervals. $\overline{X_S}$ is the temporal average of the data points from measurements. The skill index ranges between 0 and 1, where 1 indicates a perfect match between the model output and reference samples, and 0 indicates a complete failure to capture the expected behavior. Previous research suggests that a skill index higher than 0.7 to 0.8 represents a reasonable prediction, particularly for wave heights (Warner et al., 2005; Xie et al., 2024; Zhu & Wiberg, 2022). Results indicate that our local refined model could effectively capture changes in water level and wave height during storms given their high skill index (Figure 4).

2.6. Model Scenarios and Boundary Conditions

To understand the impacts of storm characteristics on hydrodynamics and sediment transport across the tombolo, we designed three groups of experiments by setting up a series of idealized storms (Table 1). A reference storm condition (indicated by the bold number in Table 1) was established using the most probable values of the storm characteristics (highlighted by the red dots in Figure 2). Subsequently, the impact of storm surge, storm waves, and storm wave direction were individually examined by varying the parameters according to the probability distributions of Figure 2. The probability occurrence of these idealized storm scenarios varies, with a higher

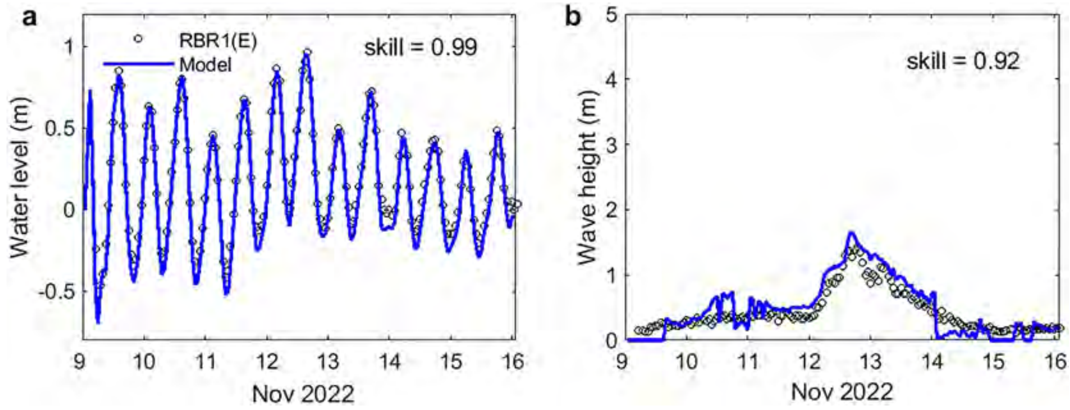

Figure 4. Comparison between Delft3D refined model output and observation data at the site of RBR1 during the winter storm of November 2022: (a) water level and (b) wave height.

likelihood of occurrence for the reference scenario (Figure S2 in Supporting Information S1). However, it is important to note that the combinations with minimum or maximum values of the examined parameter within each group rarely occur in nature. For example, a 4-m storm wave height generally appears with a storm surge ranging between 0.40 and 1.12 m, whereas a 1.25-m storm surge might be slightly beyond this range (Figure S3 in Supporting Information S1). In these idealized storms, tidal signals at the southern boundary were designed by overlaying a 0.5-m S2 tidal signal with the corresponding storm surges (Figure 5a and Figure S4 in Supporting Information S1). The storm surge period is set to 24 hr based on the probability density distribution of historical storm surge durations (Figure S4c in Supporting Information S1). Following previous studies, a cosine-shaped curve is applied to mimic the changing trend of the storm surge during the 24 hr (Dullaart et al., 2023; Ma et al., 2024; Zhou et al., 2022). Peak surge conditions were timed to coincide with high tide to maximize the storm

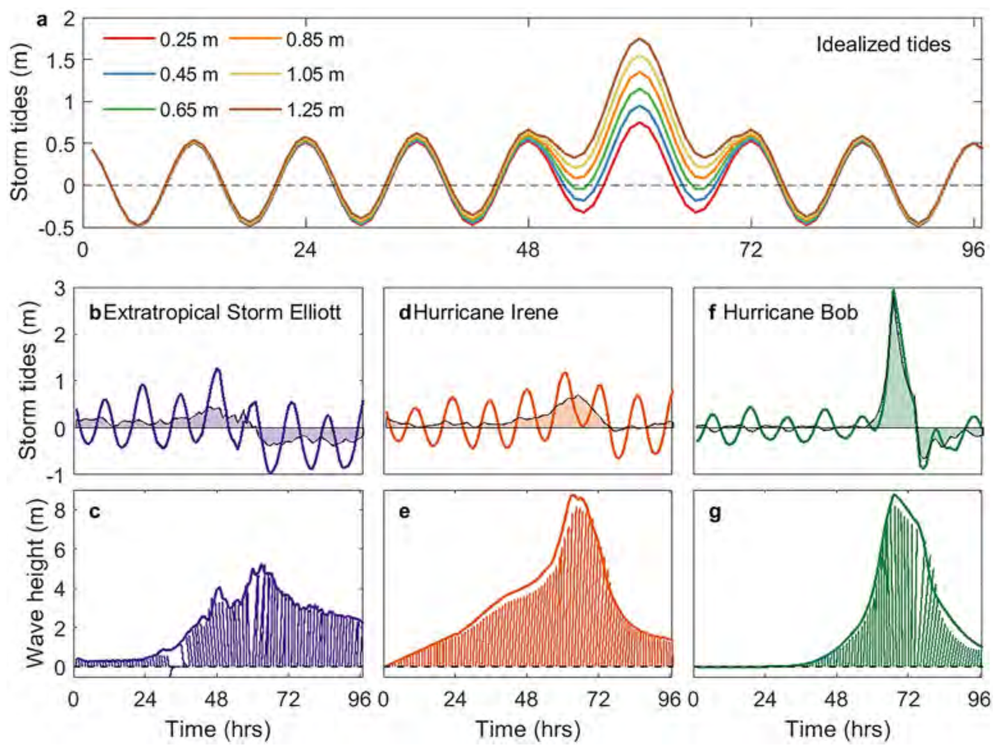

Figure 5. Boundary conditions for the model runs. Idealized storm tides (a), and three historical storms including Extratropical Storm Elliott (b, c), Hurricane Irene (d, e) and Hurricane Bob (f, g). Storm surges are indicated as shaded areas in panels (b, d, f). Line vectors in panels (c, e, g) point to the direction where the waves are propagating toward.

Table 2
Joint Probability of the Examined Model Scenarios

Scenario name	Storm surge (m) [bin range]	Wave height (m) [bin range]	Wave direction (°) [bin range]	Number of storms	Joint probability
REF	0.65 [0.56–0.74]	4 [3.8–4.8]	185 [180–200]	8	8%
Surge +	1.25 [>0.74]	4 [3.8–4.8]	185 [180–200]	1	1%
SW wave	0.65 [0.56–0.74]	4 [3.8–4.8]	215 [200–220]	3	3%
Wave +	0.65 [0.56–0.74]	8.5 [>6.8]	185 [180–200]	2	2%
Elliott	0.45 [0.38–0.56]	5.3 [4.8–5.8]	193 [180–200]	2	2%
Irene	0.71 [0.56–0.74]	8.7 [>6.8]	191 [180–200]	2	2%
Bob	2.77 [>0.74]	8.8 [>6.8]	176 [160–180]	2	2%

tides. The wave height, wave period, and wave direction are kept constant throughout the simulation at the boundary (Figure S5a in Supporting Information S1). Wave periods for these idealized storm scenarios are determined using a previously established empirical relationship between wave period (T_p) and wave height (H_s), given by $T_p \approx 5.3\sqrt{H_s}$ (Mangor et al., 2017). Here, a storm surge is defined as the abnormal elevation of water caused by a storm, exceeding the expected astronomical tide, and storm tides refer to the water level during a storm resulting from the combination of storm surge and astronomical tide.

In addition to the idealized storm scenarios, we also incorporated three historical storm events: Extratropical Storm Elliott (2022), Hurricane Irene (2017), and Hurricane Bob (1991) (Figures 5b–5g). Water level information during Extratropical Storm Elliott and Hurricane Irene was based on the tidal gauge at Newport (Station No.: 8452660) operated by NOAA and located 20 km away from the southern boundary (NOAA, 2023). Wave heights, wave periods, and wave direction were obtained from the offshore buoy station (Figure 1a) maintained by the National Data Buoy Center (NDBC, 2023). The boundary conditions for Hurricane Bob, including storm tides and waves, were obtained from the Massachusetts Coastal Flood Risk Modeling developed by Woods Hole Group (https://www.woodsholegroup.com/). Waves originated from the south for all the historic storms (Figures 5c–5e and 5g). The storm surge for Extratropical Storm Elliott was approximately 0.4 m, with a peak wave height of 5 m (Figures 5b and 5c). The storm surge for Hurricane Irene nearly doubled that of Elliott, reaching 0.7 m, with a peak wave height of around 8.7 m (Figures 5d and 5e). This wave height was similar to that observed during Hurricane Bob (Figure 5g). However, Hurricane Bob generated a substantial storm surge of approximately 2.8 m (Figure 5f) as simulated by the Coastal Flood Risk Modeling. During these historical storm events, wave periods varied with each storm and changed over time (Figure S5b in Supporting Information S1).

In our analysis, we modeled four idealized storms (including REF, Surge +, SW wave, and Wave +) and three historical storms (including Elliott, Irene, and Bob) (Table 1). The frequency probability of these storms is provided in Table 2. Joint probability is based on the proportion of storms having similar storm characteristics. Moreover, we established a relationship between peak storm wave height and annual exceedance probability to assess the severity of wave conditions examined in this study (Figure S6 in Supporting Information S1). Here, an extreme storm event is defined as one generating peak wave heights with a return period exceeding 1 year. Consequently, scenarios involving extreme wave climates refer to: (a) idealized storms with wave heights greater than the reference scenario, and (b) the three historical storms (Table 1).

The idealized storm simulations maintain constant wave conditions for the entire 96-hr period. In contrast, although the historical storms were also simulated for 96 hr, the duration of their peak waves varied and was notably shorter than the constant wave duration in the idealized storms (Figure 5). To mitigate instability arising from the transition from initial conditions to the dynamic boundary conditions in the hydrodynamic simulation, each scenario included a 24-hr spin-up period at the beginning, during which the effect of the sediment fluxes on the available bottom sediments were not taken into account (Deltares, 2014). In addition to the storm tides and storm wave boundary conditions, the other open boundaries in the large model domain included: (a) two upstream river discharge boundaries (set to 2 m^3/s) based on statistics of annual river discharge measurements (Bent, 1995; FitzGerald et al., 1987; Xie et al., 2024), and (b) two Neumann boundary conditions on the western and eastern boundaries.

3. Results

Results consist of two sections: Section 3.1 presents the spatial distribution of coastal hydrodynamic conditions around the tombolo during different idealized storms, and Section 3.2 quantifies the amount of sediment transported across the tombolo for different storms.

3.1. Impacts of Storms on the Hydrodynamic Conditions Around the Tombolo

Causeway removal allows currents to transport sediment across the tombolo during storms, in this case from the west to the east domain, because the predominant waves come from the south to southwest, with higher wave energy observed on the west. However, the currents connecting the two domains are dominated by offshore circulation cells driven by waves breaking along either side of the island and subsequently connecting with longshore currents along the beach (Figures 6 and 7).

The reference idealized storm generates a 4-m wave height at the wave boundary, propagating northward with a storm surge reaching up to 0.65 m. Wave vectors gradually refract toward Gooseberry Island (Figure 6a), and due to the protection of the island, wave heights at the tombolo area are smaller than the wave heights on the nearby beach (Figure 6b). Furthermore, wave heights on the west domain are higher than those on the east domain (Figures 6a and 6b). This is because the presence of the offshore Elizabeth Islands and Gooseberry Island shelters the region (see Figure 1a), thereby reducing wave energy in the east side of the system (Figure S7 in Supporting Information S1). The larger waves in the western area dissipate in the surf zone (Figures 6c and 6d), leading to a rise in local water level (wave set-up) and creating a water level differential on the two sides of the tombolo (Figures 6e and 6f). This water level difference is expected to generate horizontal currents flowing from the west domain to the east domain. However, wave-generated currents around Gooseberry Island form two circulation cells, one counterclockwise and one clockwise, symmetrically distributed on the west and east sides of the island (Figure 7a). These circulation cells interact with the current driven by the water level differential, drawing the flow along the west side of the island and across to the beach on the east side (Figure 7b).

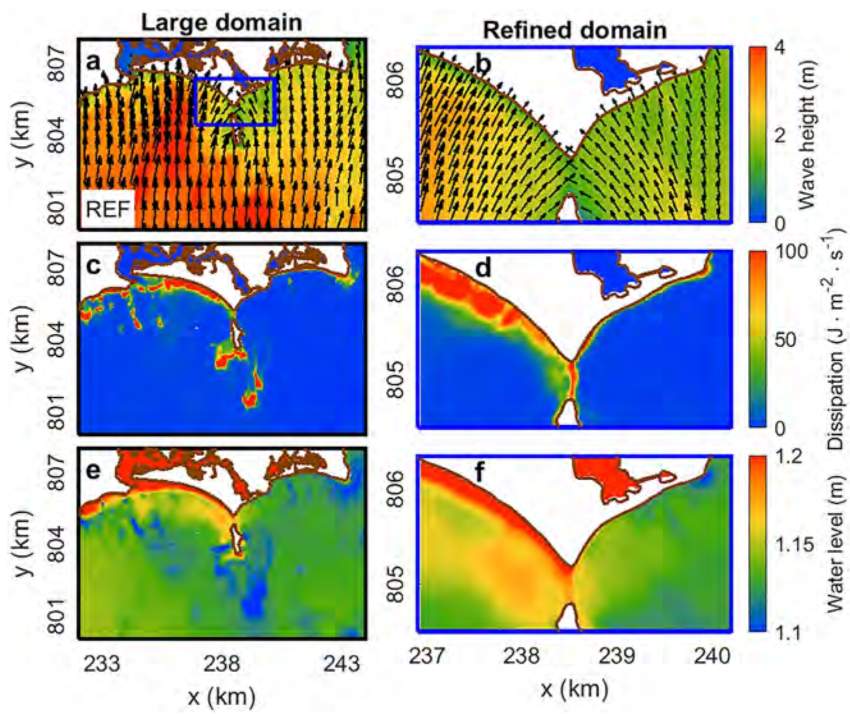

Figure 6. Hydrodynamic conditions around the tombolo in the reference scenario (REF) where waves come from the south. Wave propagation map (a, b), wave energy dissipation rate (c, d) and water level (e, f). Results are shown in two different domain sizes: large domain (a, c, e) and refined domain (b, d, f). The large domain extends beyond the island area, while the refined domain specifically focuses on the area around the tombolo.

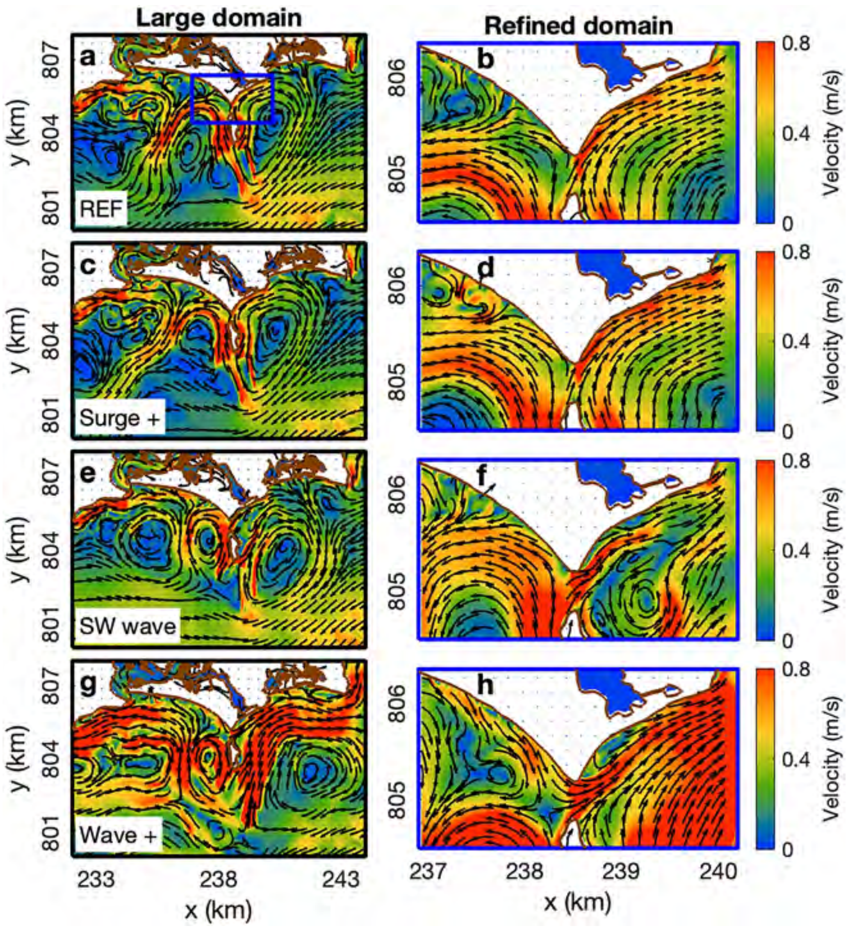

Figure 7. Flow velocity fields with the formation of circulation cells on the two sides of the island under different idealized storm scenarios. Here, Surge + refers to the scenario with 1.25 m storm surge (c, d); SW wave refers to the scenario where waves come from southwest (215°; e, f). Wave + refers to the scenario with 8.5 m wave heights (g, h).

The position, magnitude, and size of the circulation cells vary with storm surge, wave height, and wave direction, which in turn influence currents across the tombolo (Figure 7). A higher storm surge shifts the two cells landward, resulting in an increase in velocity on both sides of the island (Figure 7d). Differing from the reference scenario, which creates two symmetric circulation cells (Figure 7a), the incoming waves from the southwest produce asymmetric circulation cells (Figure 7e). Specifically, the circulation cell in the west domain moves closer to the shoreline, while the east cell migrates further eastward and seaward, causing the strong flows along East Beach to shift slightly offshore (Figure 7f). Meanwhile, the landward migration of the west circulation cell not only augments nearshore currents on Horseneck Beach but also accelerates flow across the tombolo (Figure 7f). In the large wave scenarios, although the two circulation cells have migrated seaward, their magnitude and size are enhanced, particularly the eastern cell (Figure 7g). Importantly, large waves produce eastward flow along the west beach toward the tombolo, potentially creating a new sediment transport path from Horseneck Beach to East Beach (Figure 7h).

3.2. Sediment Transport Across the Tombolo

The removal of the causeway potentially enables sediment transport across the tombolo during storms. The predominant sediment flux originates from the west domain and moves toward the east domain, driven by either larger waves or waves approaching from the southwest (Figure 8).

In the reference scenario, the peak sediment flux across the tombolo from west to east is nearly three times larger than the peak flux from east to west. Sediment transport from the west to the east domain reaches a maximum of 0.15 kg/m/s, while the flux in the opposite direction remains low at 0.05 kg/m/s (see "REF" in Figure 8a). The

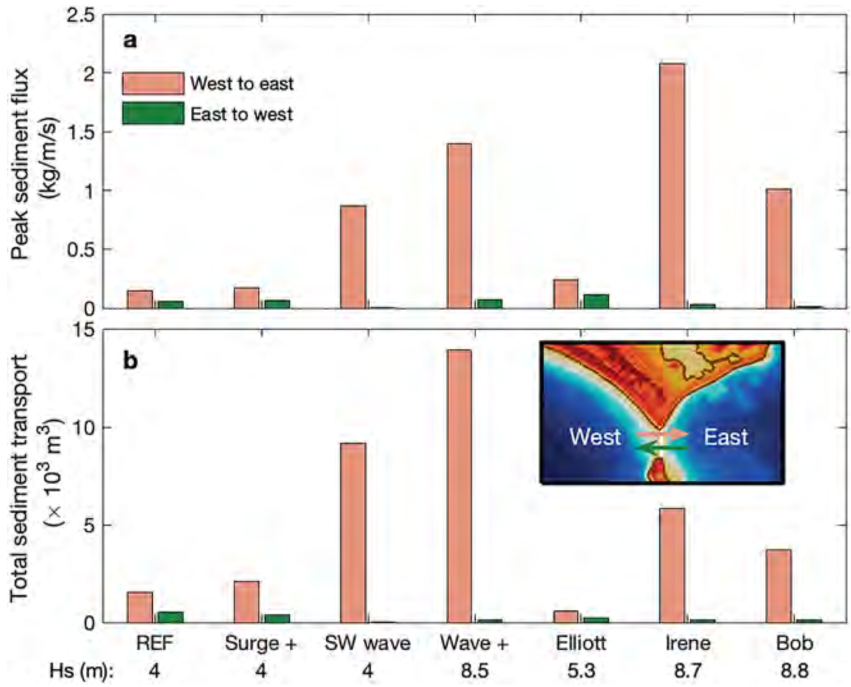

Figure 8. Peak sediment flux (a) and total cumulative sediment transport across the tombolo (b). Sediment transport across the tombolo is quantified along the transect indicated in panel (b). The magnitude of sediment transport is calculated as the sum of the suspended load and bed load. Three historical storms, including Extratropical Storm Elliott, Hurricane Irene and Hurricane Bob are also examined. The corresponding peak wave heights (Hs) are indicated below each scenario.

difference in sediment flux results in a prevailing west-to-east sediment transport under the most frequent storm conditions. Storm surge appears to have a limited role in sediment transport (see "Surge +" in Figure 8a), while significant changes are observed when waves come from the southwest or under more intense wave conditions (see "SW wave" and "Wave +" in Figure 8a). For instance, with southwest waves or with double wave height (8.5 m), the sediment transport from west to east increases by 5 and 8 times, respectively (i.e., 0.87 kg/m/s in "SW wave" and 1.39 kg/m/s in "Wave +"). Conversely, in both scenarios, the sediment flux from the east domain to the west domain is nearly negligible, approximately 0.003 kg/m/s in "SW wave" and 0.07 kg/m/s in "Wave +."

In addition to the idealized scenarios, we also examine sediment transport during three historical storm events: Extratropical Storm Elliott, Hurricane Irene, and Hurricane Bob (Figure 8a). Elliott displays a slightly higher sediment flux from west to east (0.24 kg/m/s) compared to the reference scenario, likely attributed to its 1 m higher significant wave height (see "Elliott" in Figure 8a). On the other hand, Hurricanes Irene and Bob, which exhibit nearly identical significant wave heights of approximately 8.5 m, demonstrate a substantial increase in sediment transport from west to east, reaching 2.08 kg/m/s during Hurricane Irene and 1.01 kg/m/s during Hurricane Bob. The east-to-west sediment flux during both storms is significantly lower, below 0.05 kg/m/s.

In the idealized storm settings (i.e., constant storm wave conditions), total sediment transport is a function of the peak sediment flux (see "REF," "Surge +," "SW wave" and "Wave +" in Figure 8). In the reference scenario, cumulative sediment transport from the west domain to the east domain is around 1,500 m^3 over a 72-hr storm period, while the sediment transport from the east domain to the west domain is approximately 500 m^3 ("REF" in Figure 8b). The storm surge has a limited impact on the total sediment transport ("Surge +" in Figure 8b). Furthermore, waves from the southwest or intense storm conditions (4 and 8.5 m significant wave height) cause a larger total sediment transport compared to the reference scenario, transporting cumulative sediment volumes of 9,000 and 14,000 m^3, respectively (Figure 8b).

In addition to the magnitude of wave height and the angle of wave incidence, sediment transport across the tombolo is also affected by the duration of the storm (Figure 8b). Extratropical Storm Elliott, despite having peak waves 1 m larger than the reference storm, transports only about half the total sediment, amounting to 580 m^3 ("Elliott" in Figure 8b). Hurricanes Irene and Bob produce slightly higher peak wave heights than "Wave +";

however, due to the shorter duration of large wave conditions (Figure 5), the total sediment flux from the west to the east domain is lower (5,800 m^3 during Hurricane Irene and 3,600 m^3 during Hurricane Bob). All three storms produce negligible sediment transport from the east to the west of the island (Figure 8b).

4. Discussion

Our numerical scenarios reveal that storms create water level differences in both sides of the tombolo as well as coastal circulation cells. These cells can vary in position, magnitude, and size during different storm events. The interaction between circulation cells and nearshore hydrodynamics plays a significant role in sediment transport across the tombolo.

Our scenarios include both idealized and real storm events, with variations in storm surge, peak storm wave height, and wave direction. Below, we discuss how water level differences control the horizontal velocity across the tombolo (Section 4.1.1) and how circulation cells influence the northward velocity component (Section 4.1.2). Additionally, we explore the impact of horizontal and vertical sediment grain size distribution on sediment transport across the tombolo (Section 4.2) and trace the sediment sink on the east domain, when the sediment source originates from the west domain (Section 4.3). Finally, we address other relevant processes influencing sediment transport across the tombolo and propose potential future research directions related to the tombolo systems (Section 4.4).

4.1. Impacts of Storms on the Flow Velocity Across the Tombolo

Our model simulations show that longshore currents do not cross the tombolo for moderate to low wave energies, such as during the reference and southwest-wave storm conditions (Figure 7). Such current patterns only occur during large storms (Figure 7h). We also show that velocity across the tombolo does not correlate with longshore currents (Figure S8 in Supporting Information S1). This is different from longshore currents along a straight shoreline that move parallel to the beach (Kobayashi et al., 2007; Longuet-Higgins, 1970). Instead, our model results indicate that the dominant current moves across the tombolo from the west of the island onto East Beach (Figures 7b–7d and 7f). This is likely due to (a) the water level difference between the two sides of the tombolo (Figures 6f) and (b) the circulation cells generated on either side offshore of the island, which modulate the currents across the tombolo (Figures 7a–7c and 7e and 7g). Below, we explain the factors controlling the current patterns across the tombolo in more detail.

4.1.1. Storm-Driven Water Level Differences Amplify Horizontal Velocity Across the Tombolo

In addition to storm surges, wave set-up plays a crucial role in elevating water levels during storms (Lerma et al., 2017; Wang et al., 2020). The magnitude of wave set-up in coastal areas is determined by wave energy dissipation, which leads to a radiation stress gradient transferring momentum from the wave to the water column (Hoque et al., 2019; Svendsen, 1984; Woodworth et al., 2019). In our system, variations in wave energy dissipation between the west and east domains result in differences in wave set-up, thereby generating differential water elevations on either side of the tombolo (Figures 6c–6f). This is because offshore islands, such as the Elizabeth and Gooseberry Islands, interrupt the propagation of waves toward the eastern shoreline, thereby sheltering them (Figure S7 in Supporting Information S1) and diminishing wave energy dissipation in the east domain (Figures 6c and 6d). Difference in wave set-up induced by wave height variations has also been reported in a previous field observation and modeling study by Lavaud et al. (2022).

We explore the effects of various storm parameters, including storm surge, peak wave height, and wave direction, on the water level difference between the west and east domains. Subsequently, we examine the potential correlation between horizontal velocity across the tombolo and water level difference (Figure 9). In the idealized storm scenarios, wave height controls the water level gradient across the tombolo (Figure 9b) rather than the storm surge (Figure 9a). Wave direction, while playing a secondary role, amplifies the water level differences, particularly when waves originate from the southwest (Figure 9c). This is important because a significant correlation exists between water level difference and the horizontal flow across the tombolo (Figure 9d).

The relationship between the water level gradient and flow speeds across the tombolo is further supported by hourly data points observed during the three historical storm scenarios (Figure 10a). Modulation of flow velocity, influenced by water level differences driven by wave set-up, aligns with observations from previous studies

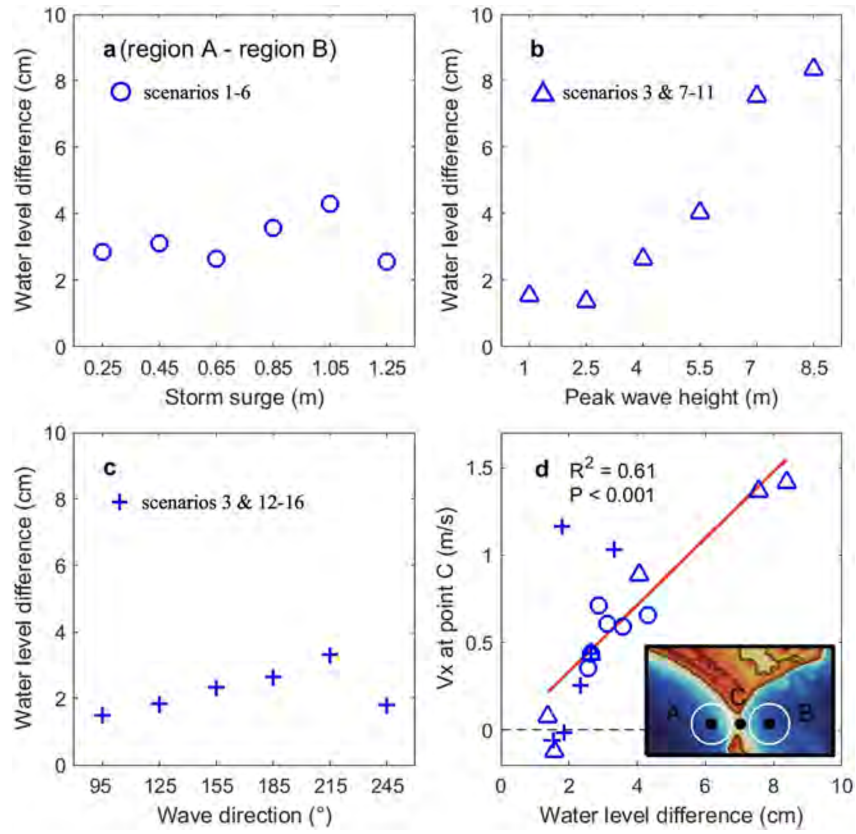

Figure 9. Relationship between the storm-driven water level difference and the horizontal velocity across the tombolo. Variations in water level difference between the west and east domains are depicted in relation to storm parameters, including storm surge (a), peak wave height (b), and wave direction (c). Panel (d) illustrates the correlation between horizontal velocity across the tombolo and water level difference. The coefficient of determination (R^2) and p value for the linear regression are annotated. As indicated in the inserted map in panel (d), the water level difference is calculated based on the 90th percentile of the water level in regions of A and B represented by the white circle around the black points, and the horizontal velocity at the tombolo is extracted from point C. Data points represent conditions at the peak of the storm surge.

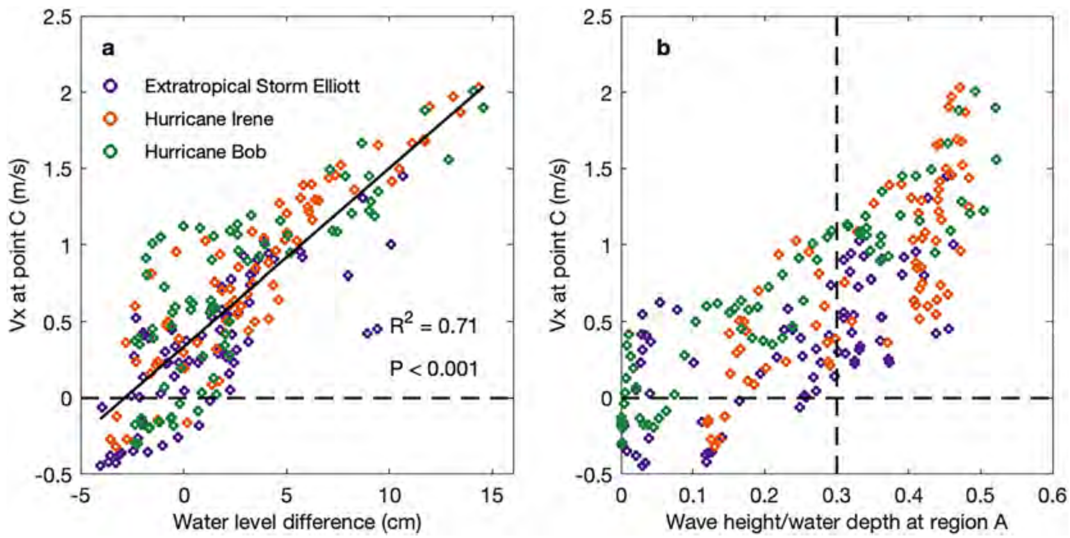

Figure 10. Relationship between horizontal velocity across the tombolo and water level difference (a), and the ratio of wave height to water depth (b). Data points are based on hourly data over the entire storm period. The vertical dashed line in panel (b) indicates a threshold above which the horizontal velocity across the tombolo is always positive.

(Dodet et al., 2019; Idier et al., 2019; Woodworth et al., 2019). Moreover, analysis reveals that flow across the tombolo is influenced by the ratio of wave height to water depth at region A (Figure 10b). Specifically, when this ratio exceeds 0.3, the velocity remains positive, indicating that currents move from the west domain to the east domain.

4.1.2. Storm-Driven Circulation Cells Amplify the Northward Velocity Component Across the Tombolo

A significant finding in our study is the emergence of two circulation cells west and east of Gooseberry Island during storms (Figure 7). Formation of circulation cells has also been observed in previous studies of similar sandy bay-headland systems, disturbing local current patterns (George et al., 2019; Klein et al., 2020; McCarroll et al., 2018). The existence of these cells is linked to waves breaking around the offshore island or headland, where currents are intensified (Vieira da Silva et al., 2018). This process can be seen in our model results, where wave dissipation around Gooseberry Island accelerates local currents (Figures 6c and 6d and 7). These circulation cells induce counterclockwise rotating currents in the west domain and clockwise rotation in the east (Figure 7). As a result, currents traversing the tombolo, driven by water level differences, interact with the circulation cells, flowing cross-shore from the west side of Gooseberry Island to East Beach, rather than moving parallel to the mainland shoreline, from the beach across the tombolo (Figures 7b–7d and 7f and 7h).

Our findings also indicate that the position, magnitude, and size of the two circulation cells are affected by storm characteristics. For example, an increase in storm surge accelerates northward velocity along the west side of Gooseberry Island (Figure 11a), which can be attributed to the landward shift of the circulation cells. This phenomenon is aligned with a previous study that presented a landward shift of circulation cells driven by sea-level rise (Xie et al., 2024). Higher water levels allow waves to propagate further onshore and move the primary

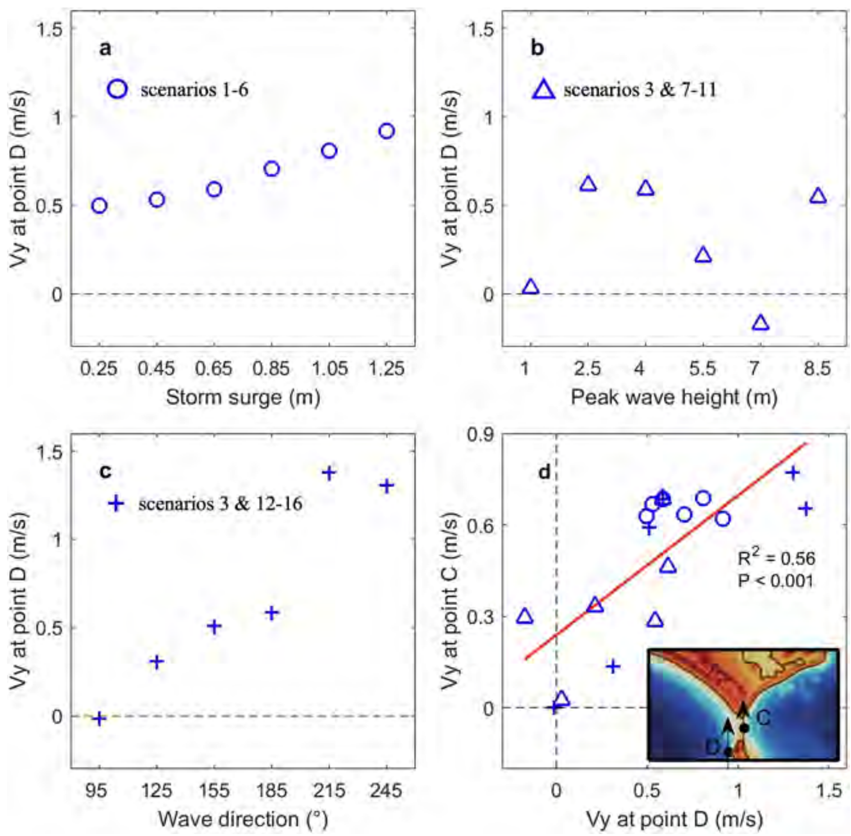

Figure 11. Relationship between the northward velocity along the west side of Gooseberry Island and the northward velocity component across the tombolo. Northward velocity at point D as a function of storm parameters, including storm surge (a), peak wave height (b) and wave direction (c), respectively. Correlation between the northerly velocity across the tombolo and the northerly velocity at point D (d). The coefficient of determination (R^2) and p value for the linear regression are annotated. Data points presented here are computed at the peak of the storm surge.

wave-breaking zone closer to the shore. Previous studies also suggest that larger waves shift the circulation cell seaward, reducing nearshore currents (Mouragues et al., 2020). This phenomenon is also observed in our results indicated by the blue triangles in Figure 11b. However, we further propose that a potential expansion of the velocity field around the circulation cell occurs simultaneously with the seaward shift (Figure 7a vs. Figure 7g). For example, in the "Wave +" scenario, the expansion of the velocity field around the circulation cells amplifies the nearshore current in the west side of the tombolo and East Beach (Figure 7b vs. Figures 7h and 11b).

In addition to the effects of storm surge and wave height, wave direction is a critical factor in modulating circulation currents. Previous studies found that the amount of wave energy reaching the shoreline and subsequent energy dissipation are highly dependent on the direction of wave propagation (Han et al., 2021; Hsu et al., 2006). In our study area, shallow zones around islands and bedrock shoals act as regions of high wave energy dissipation. When waves approach perpendicular to the shoreline, two symmetrical circulation cells form (Figure 7a). However, when waves propagate obliquely, the circulation cells become asymmetrical (Figure 7e). This phenomenon supports findings from prior studies, where oblique wave input around headlands generates asymmetrical current patterns (George et al., 2019; Klein et al., 2020; McCarroll et al., 2018). Landward migration of the west circulation cell amplifies the velocity on the west domain, as observed in the scenario with a wave direction of 215° or 245° in Figure 11c. Furthermore, we show that the northward flow across the tombolo is primarily influenced by the circulation cell on the west domain (Figure 11d).

4.2. Horizontal and Vertical Bottom Sediment Grain Size Distribution Influence Sediment Movement Across the Tombolo

Our model shows that the primary direction of sediment movement is west to east, whereas little sediment moves in the opposite direction (Figure 8). The transport of sediment from west to east is dependent on two key factors: (a) the strength and path of the current, and (b) bottom sediment grain size distribution in both horizontal and vertical dimensions. Several numerical studies have incorporated spatial variations in sediment composition within the seabed to achieve accurate sediment transport estimates (Guillou & Chapalain, 2010; Huisman et al., 2018). This consideration is crucial as finer sediment particles typically exhibit greater transport potential than coarser ones (Andualem et al., 2023; McLaren & Bowles, 1985). Coastal areas characterized by mixed sediment and rocky surfaces have received limited attention in transport studies due to their complexity (Trenhaile, 2016). Moreover, an accurate identification of rocky areas is critical to prevent overestimation of sediment transport (Xie et al., 2024). In the reference scenario of our study, the prevailing currents originate from the west side of Gooseberry Island (Figure 7b). However, this beach is predominantly rocky (Figures 3a and 3b) and there is limited sand in the nearshore to be resuspended and transported to the east domain (Figure 8).

In contrast, in scenarios characterized by a large wave environment or waves coming from the southwest, there is an increase in water level difference, intensifying the cross-tombolo velocities (Figure 9). Given that the sediment composition in the west domain is predominantly gravel and sand, stronger currents result in a noticeable increase in the potential sediment transport to the east domain (Figure 8). This also explains why Hurricane Bob exhibited a smaller peak sediment flux than Hurricane Irene, which had a more oblique wave angle, despite both having identical peak wave heights (Figure 8a). More specifically, the wave direction for Hurricane Irene during peak wave height is ~190°, compared to roughly 180° for Hurricane Bob (Figures 5e and 5g). Hurricane Irene produced strong longshore currents capable of transporting gravel and sand from the western Horseneck Beach to East Beach, whereas Hurricane Bob generated currents originating from the rocky western side of Gooseberry Island (Figure S9 in Supporting Information S1). This is because Hurricane Irene was dominated by large wave heights, similar to the "Wave +" scenario (Figures 7g and 7h vs. Figures S9a and S9b in Supporting Information S1), whereas Hurricane Bob was characterized by both large storm waves and a significant storm surge, generating a current pattern more similar to the "Surge +" scenario (Figures 7c and 7d vs. Figures S9c and S9d in Supporting Information S1). This difference is noteworthy, especially considering that Hurricane Bob created a higher storm surge compared to Hurricane Irene (Figures 5d and 5f).

In addition to the impact of horizontal sediment grain size distribution, their vertical distribution could also affect the amount of sediment deposition on East Beach. In this study, we incorporated a two-layer sediment profile to mimic the vertical sediment gradient observed in the field (Figure 3) and in previous studies (FitzGerald et al., 1992). Gravel is more resistant to movement, so the transported sediment is mostly sand (Figure S10 in Supporting Information S1). Although the general erosion and deposition patterns are similar regardless of the initial sediment layer thickness, a thinner sand layer reduces the total sediment deposition along East Beach (Figure S11 in Supporting Information S1). For instance, a 25-cm sand layer may result in less sediment deposition compared to the current model setting with a 50-cm sand layer (Figure S11d in Supporting Information S1). Conversely, increasing the initial sand thickness does not significantly alter the sand deposition in the east domain (Figure S11e in Supporting Information S1). For more accurate estimations of sediment deposition along East Beach, future studies should incorporate precise measurements of sediment layer thickness.

4.3. Source-To-Sink Sediment Movement Driven by Circulation Cells

To better understand the specific role of sediment distribution in sediment transport rates across the tombolo, we first identify locations where sediment deposition occurs in the east domain. Then, we quantify changes in sediment volume for the respective sediment compositions in the eastern beach region (Figure 12). Our analysis suggests that during storms, sediment in the western domain is transported across the tombolo and deposited along the eastern shoreline near the tombolo (Figures 12a–12g). Under typical storm conditions, whether idealized storms or those occurring annually (e.g., Extratropical Storm Elliott), west domain sediment only leads to relatively thin deposition along a narrow nearshore area having an average thickness of less than 10 cm (Figures 12a and 12e). The limited amount of sediment transported across the tombolo during the reference storm agrees with previous modeling studies (Tsai et al., 2023). In contrast, during extreme storms or when waves come from the southwest, deposition increases to around 20 cm (Figures 12c, 12d and 12f, 12g). The high rate of sediment deposition highlights the significance of wave height and wave direction on the sediment transport regime across the tombolo, as demonstrated in prior research by Malliouri et al. (2022). Moreover, the impact of tidal currents on sediment transport is minimal in this wave-dominated system (Figure S12 in Supporting Information S1). However, in areas where tidal currents are strong, especially near tidal inlets, ebb tidal currents can counteract circulation cells, move sediment offshore and contribute to the formation of offshore sandbars (Siegle et al., 2004, 2007).

We have further calculated changes in sediment volume in East Beach region resulting from the deposition of sediment from the west domain and local erosion (Figure 12h). We find that existing sediment on East Beach is eroded during storms (depicted by the green bars in Figure 12h), which aligns with previous observations and numerical studies, where storms erode sediment at the beach face (Brenner et al., 2018; Palinkas et al., 2014). We further show that sediment erosion from East Beach increases with storm surge, wave height, and waves from the

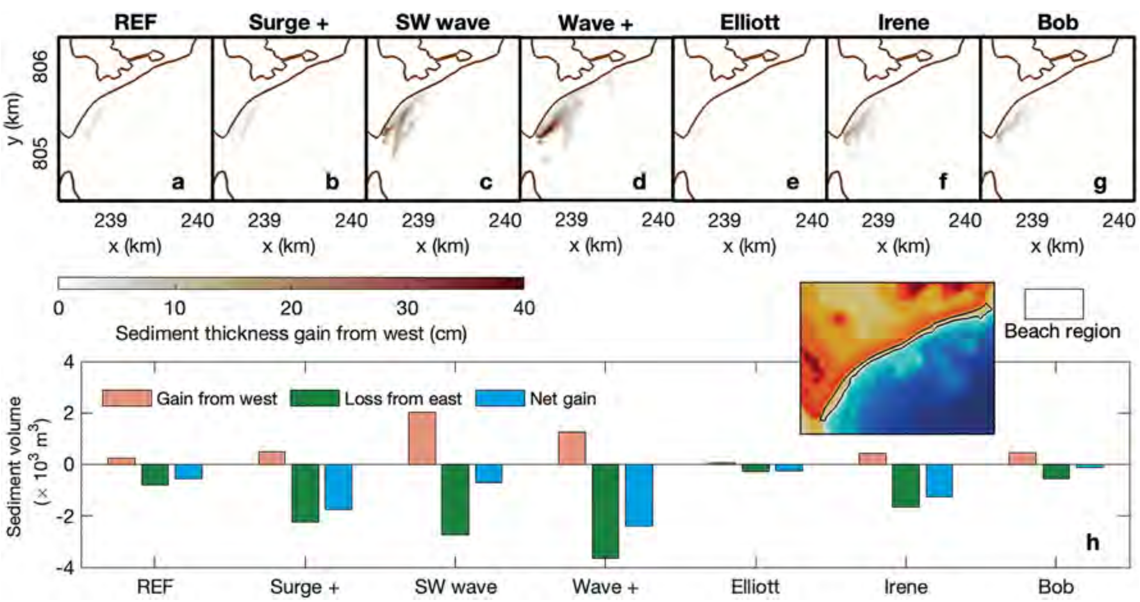

Figure 12. Variations in sediment thickness in the east domain. Spatial distribution of sediment thickness resulting from sediment transported from the west domain (a–g). The bottom bar plot illustrates the sediment volume gained from west sediments, sediment volume lost from East Beach, and the net sediment volume change (i.e., gain from west minus loss from east). These calculations are based on the east beach region, as per previous studies (Xie et al., 2024). The seaward water depth of the beach region is set to 2 m.

southwest (Figure 12h). Sediment from the west domain can only partially offset sediment loss (Figure 12). Previous studies have quantified storm erosion of beach sediment, but here we demonstrate that human activity, such as causeway removal, has the potential to exacerbate sediment erosion from East Beach region (Figure 13). More specifically, while removing the causeway would enhance sediment contribution to East Beach from Horseneck Beach (Figures 12a–12g), the additional longshore (along the shore of Gooseberry Island and the tombolo) currents across the tombolo (Figure 13c) would increase sediment erosion to the western end of East Beach (see blue area near the tombolo in Figure 13f). The eroded sediment is likely deposited nearby (see brown area near the tombolo in Figure 13f). This suggests that variations in sediment thickness near the tombolo are sensitive to the causeway removal.

Our results show that erosion primarily occurs in the areas offshore of Gooseberry Island where the substrate consists of erodible sediment, while sedimentation takes place onshore of these eroded areas (Figure S13 in Supporting Information S1). These patterns are likely driven by the circulation cells on the two sides of Gooseberry Island, which move sediment onshore by sourcing offshore sandy areas (Siegle et al., 2007). Although there are no large sandbars in our study site, onshore currents from circulation cells could potentially erode sand from these sandbars and redistribute it along the shorelines (Figure 7). This process can not only affect LST and the formation of salients/tombolos but also alter the shape of offshore sandbars (Siegle et al., 2004, 2007).

In our modeling work, we focused on sediment volume in East Beach during a single storm. It is important to note that sediment may also move back onshore during the fair weather season, potentially restoring the sediment lost from the beach (Aagaard et al., 2012; Dubois, 1988; Roberts et al., 2013). Beach recovery mainly occurs within the active beach profile, which extends to the depth of closure including the upper shoreface. Beyond this depth, coastal morphological changes due to wave impacts are observed to remain limited (Hallermeier, 1978). The depth of closure of East Beach is approximately 8 m, according to our previous study (Xie et al., 2024), and was calculated based on annual hourly wave data recorded at the buoy station (Figure 1a). A net sediment gain is found when considering a larger region with an 8-m water depth (see the blue bars in Figures S14 and S15 in Supporting Information S1). Here the incoming west sediments exceed sediment losses (orange bars vs. green bars in Figures S14 and S15 in Supporting Information S1). This is because sediment from the west domain is primarily deposited on the upper shoreface of the east domain, as shown in Figures 12a–12g. Future studies should also investigate the residence time of sediment transported into the east domain across the tombolo along with the associated morphological changes, especially considering the impact of consecutive storms (Vousdoukas et al., 2012).

4.4. Additional Processes Affecting Sediment Transport Across the Tombolo and Future Research Directions

We further explored the effect of the wave period on sediment transport. We found that an increase in wave period enhances the peak sediment flux (Figure S16a in Supporting Information S1), which eventually leads to a higher

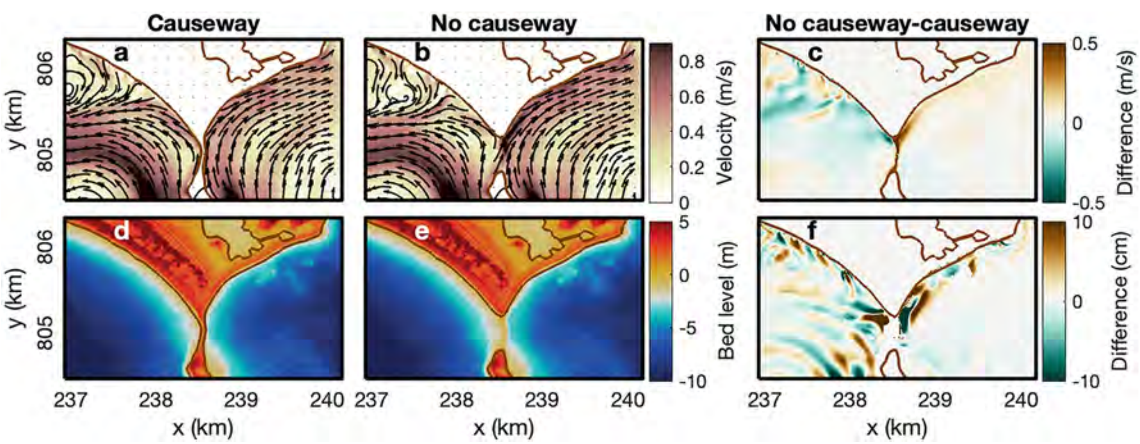

Figure 13. Comparison of velocity field and bed level between scenarios with and without causeway. Velocity field during peak wave height (a–b) and their difference (c). Bed level at the end of simulation (d–e) and their difference (f). Results displayed here are based on the REF (scenario 3).

10.1029/2024JF007709

total sediment transport, particularly from the west domain to the east domain (Figure S16b in Supporting Information S1). This aligns with early findings that longer wave periods (swell waves) can increase sediment transport capacity by altering bottom orbital velocity (Jing & Ridd, 1996; Zhang et al., 2009). Larger wave heights result in higher sediment flux and total sediment transport regardless of wave period (REF scenario vs. Wave + scenario in Figure S16 in Supporting Information S1). Another important process, local wind-wave generation, is not considered in the model simulations. This is to avoid overestimation of wave heights when applying spatially uniform wind fields over the entire domain (Figure S17 in Supporting Information S1). This could likely be improved by using spatially varying wind fields, particularly near the coastline (Huang et al., 2013). Given that our domain has a limited wind fetch, excluding local wind waves still allows us to produce relatively reasonable wave fields (Figure S17b in Supporting Information S1). However, for larger domains on a continental scale, incorporating wind-wave generation is crucial for providing accurate wave height distributions (Huang et al., 2013; Wornom et al., 2001).

In addition, Delft3D-WAVE employs SWAN for wave propagation to the coast, which has been widely used for its robustness in simulating wave transformation processes such as refraction, shoaling, and breaking (George et al., 2019; Huisman et al., 2018; King et al., 2021). However, SWAN has known limitations in simulating wave diffraction, particularly around headlands and other complex coastal features (SWAN, 2015). SWAN can properly account for diffraction if the grid size is refined to less than 1/10-1/5 of the wavelength (SWAN, 2015). This necessitates a very fine wave grid, especially for storm events with short wavelengths. The wavelength around the causeway ranges between 50 and 200 m and increases with storm wave height and storm surge (Figure S18 in Supporting Information S1). Our grid resolution (40 m) may provide a relatively accurate evaluation of wave diffraction during severe storm events such as Hurricane Bob but may fail to do so during typical storm events such as the recent Extratropical Storm Elliott. This limitation could potentially lead to an underestimation of wave energy distribution, particularly on the downdrift side of the system, given that the dominant waves in our study area come from the south to the southwest. This inaccuracy could ultimately affect wave attenuation and set-up, and subsequently influence the amount of sediment flux across the tombolo. Future studies could benefit from incorporating models with enhanced diffraction capabilities or using hybrid approaches that combine SWAN with other modules that better represent diffraction processes, thereby improving accuracy in such complex coastal environments (Kim et al., 2017; Lin, 2013).

Our model solves the depth-averaged shallow water equations; however, the three-dimensional effects might play an important role in sediment transport. For example, the potential impacts of offshore-directed undertow currents arising from set-up gradients during storms are neglected. Undertow currents could displace beach sediment offshore, facilitating the formation of offshore sandbars (Mariño-Tapia et al., 2004). Changes in wave period could also affect three-dimensional wave propagation processes such as wave-induced turbulence, shoaling, refraction, and diffraction, subsequently modifying sediment transport patterns (Sierra & Casas-Prat, 2014; Toffoli et al., 2012). Future modeling research should investigate the interactions of circulation cells with the three-dimensional flow field (Franz et al., 2017).

The model simulations were based on a modified bathymetry, where the current causeway was lowered followed by a long-term simulation to obtain an equilibrium state (Figures 1d and 1e). The historical morphology of the tombolo, which was documented in 1892, was used as a reference to lower the causeway. However, over the past 130 years, potential impacts of climate change such as sea-level rise have likely influenced the tombolo morphology. The conditions for forming a submerged tombolo occurred during a slow rise and subsequent stagnation of sea level in the Holocene (Benac et al., 2019). Nevertheless, accelerated rising sea levels along with larger and more frequent storms could erode and submerge the tombolo (Vu et al., 2018). Given the uncertain future of the tombolo under climate change, it is reasonable for our models to approximate the tombolo elevation based on historical maps. Future research could explore how climate change affects tombolo evolution, particularly under projected sea-level rise and increased storm activity (Emanuel, 2017; Goddard et al., 2015).

5. Conclusions

Our numerical simulations reveal that sediment transport across a tombolo is largely governed by circulation cells on both sides of the tombolo. These circulation cells, which form due to wave energy dissipation during storms, play a critical role in determining the patterns of hydrodynamics and sediment dynamics across the tombolo. Sediment transport across the tombolo only occurs during very large storms (e.g., with an 8-m offshore wave height). In typical storm scenarios with waves coming from the south, predominant currents are observed from the west side of the offshore island flushing toward the beach on the downdrift side. This current strength intensifies when waves approach from the southwest, causing a landward migration of the west circulation cell. However, the offshore of the island is predominantly rocky, limiting the amount of sediment that can be resuspended and transported across the tombolo.

Our results indicate that the existence of offshore islands shelters the east domain, resulting in lower wave energy and less wave dissipation on the east compared to the west side of the tombolo. During extreme storms, this imbalance increases water level differences between the two sides, which, in turn, creates west to east flow across the tombolo. In addition, the northward component of velocity from along the island across the tombolo is determined by the position, magnitude, and size of the two circulation cells. Under common storm wave conditions, with waves from the south, the circulation cells are symmetrical. However, as the wave height increases, the circulation cells shift offshore, expanding the velocity field of the east circulation cell and creating strong currents along the eastern shoreline. Conversely, when waves approach from the southwest, the west cell moves closer to the shore while the east cell moves offshore, enhancing currents across the tombolo. Although removing the anthropogenic structures such as causeway would facilitate sediment transport across the tombolo during large storms, it should be noted that the same storm waves also increase erosion along the downdrift beach. As a result, the amount of sediment from the west domain reaching the east domain may not fully offset storm-induced sediment losses.

Data Availability Statement

The wave data are collected from an offshore buoy station (Station No.: BUZM3 & 44085) maintained by the National Data Buoy Center (NDBC, 2023). The historical tidal level is retrieved from the Newport tidal gauge (Station No.: 8452660) operated by NOAA (NOAA, 2023). The sediment texture map indicating the spatial sediment types within the Western Buzzards Bay is obtained from USGS (Foster, 2014). Storm surge, peak wave height and wave direction of 100 historical storm events are obtained from a regional modeling data set by the NACCS Coastal Hazards System (Cialone et al., 2015). Delft3D is an open-source code available online (Deltares, 2014).

Acknowledgments

Funding for this project was gratefully received from the Buzzards Bay Coalition through a grant from The Rathmann Family Foundation.

References

Aagaard, T., Hughes, M., Baldock, T., Greenwood, B., Kroon, A., & Power, H. (2012). Sediment transport processes and morphodynamics on a reflective beach under storm and non-storm conditions. *Marine Geology*, *326*, 154–165. https://doi.org/10.1016/j.margeo.2012.09.004

Andualem, T. G., Hewa, G. A., Myers, B. R., Peters, S., & Boland, J. (2023). Erosion and sediment transport modeling: A systematic review. *Land*, *12*(7), 1396. https://doi.org/10.3390/land12071396

Bacon, J., Vincent, C., Dolphin, T., Taylor, J., Pan, S., & O'Connor, B. (2007). Shore-parallel breakwaters in meso-tidal conditions: Tidal controls on sediment transport and their longer term, regional impacts at sea Palling, UK. *Journal of Coastal Research*, 369–373.

Bai, X., Jiang, H., Li, C., & Huang, L. (2020). Joint probability distribution of coastal winds and waves using a log-transformed kernel density estimation and mixed copula approach. *Ocean Engineering*, *216*, 107937. https://doi.org/10.1016/j.oceaneng.2020.107937

Benac, Č., Bočić, N., & Ružić, I. (2019). On the origin of both a recent and submerged tombolo on Prvić Island in the Kvarner area (Adriatic Sea, Croatia). *Geologia Croatica*, *72*(3), 195–203. https://doi.org/10.4154/gc.2019.14

Bent, G. C. (1995). *Streamflow, ground-water recharge and discharge, and characteristics of surficial deposits in Buzzards Bay Basin, Southeastern Massachusetts*. US Geological Survey.

Booij, N., Ris, R. C., & Holthuijsen, L. H. (1999). A third-generation wave model for coastal regions: 1. Model description and validation. *Journal of Geophysical Research*, *104*(C4), 7649–7666. https://doi.org/10.1029/98JC02622

Brenner, O. T., Lentz, E. E., Hapke, C. J., Henderson, R. E., Wilson, K. E., & Nelson, T. R. (2018). Characterizing storm response and recovery using the beach change envelope: Fire Island, New York. *Geomorphology*, *300*, 189–202. https://doi.org/10.1016/j.geomorph.2017.08.004

Butt, T., Russell, P., Miles, J., & Turner, I. (2000). Hydrodynamics and cross-shore sediment transport in the swash-zone of natural beaches: A review. *Journal of Coastal Research*, *50*(sp1), 255–268. https://doi.org/10.2112/jcr-si50-120.1

Cheung, K. F., Tang, L., Donnelly, J. P., Scileppi, E. M., Liu, K. B., Mao, X. Z., et al. (2007). Numerical modeling and field evidence of coastal overwash in southern New England from Hurricane Bob and implications for paleotempestology. *Journal of Geophysical Research*, *112*(F3). https://doi.org/10.1029/2006jf000612

Chi, S., Zhang, C., & Zheng, J. (2023). Sandy shoreline recovery ability after breakwater removal. *Frontiers in Marine Science*, *10*, 1191386. https://doi.org/10.3389/fmars.2023.1191386

Chowdhury, P., Behera, M. R., & Reeve, D. E. (2020). Future wave-climate driven longshore sediment transport along the Indian coast. *Climatic Change*, *162*(2), 405–424. https://doi.org/10.1007/s10584-020-02693-7

Cialone, M. A., Massey, T. C., Anderson, M. E., Grzegorzewski, A. S., Jensen, R. E., Cialone, A., et al. (2015). North Atlantic coast comprehensive study (NACCS) coastal storm model simulations: Waves and water levels (Version 2.0) [Software]. *U.S. Army Corps of Engineers*. https://chs.erdc.dren.mil/Home/Index

CIRES. (2014). Cooperative institute for research in environmental sciences (CIRES) at the University of Colorado, boulder. Continuously updated digital elevation model (CUDEM) - 1/9 arc-second resolution bathymetric-topographic tiles. In *NOAA national centers for environmental information*.

Clamflats. (2019). Old postcards and photos of Westport, Mass. And surroundings (Version 1) [Dataset]. *PBase*. https://pbase.com/clamflats/gooseberry_bar_rock

Cuadrado, D. G., Gómez, E. A., & Ginsberg, S. S. (2005). Tidal and longshore sediment transport associated to a coastal structure. *Estuarine, Coastal and Shelf Science*, *62*(1), 291–300. https://doi.org/10.1016/j.ecss.2004.09.010

da Silva, A. P., da Silva, G. V., Strauss, D., Murray, T., Woortmann, L. G., Taber, J., et al. (2021). Headland bypassing timescales: Processes and driving forces. *Science of the Total Environment*, *793*, 148591. https://doi.org/10.1016/j.scitotenv.2021.148591

Deltares. (2014). Simulation of multi-dimensional hydrodynamic flows and transport phenomena, including sediments (Version 3.15.34158) [Software]. *Deltares*. https://oss.deltares.nl/

Dodet, G., Melet, A., Ardhuin, F., Bertin, X., Idier, D., & Almar, R. (2019). The contribution of wind-generated waves to coastal sea-level changes. *Surveys in Geophysics*, *40*(6), 1563–1601. https://doi.org/10.1007/s10712-019-09557-5

Dubois, R. N. (1988). Seasonal changes in beach topography and beach volume in Delaware. *Marine Geology*, *81*(1–4), 79–96. https://doi.org/10.1016/0025-3227(88)90019-9

Dullaart, J. C., Muis, S., De Moel, H., Ward, P. J., Eilander, D., & Aerts, J. C. (2023). Enabling dynamic modelling of coastal flooding by defining storm tide hydrographs. *Natural Hazards and Earth System Sciences*, *23*(5), 1847–1862. https://doi.org/10.5194/nhess-23-1847-2023

Emanuel, K. (2017). Will global warming make hurricane forecasting more difficult? *Bulletin of the American Meteorological Society*, *98*(3), 495–501. https://doi.org/10.1175/bams-d-16-0134.1

Fagherazzi, S., Mariotti, G., Leonardi, N., Canestrelli, A., Nardin, W., & Kearney, W. S. (2020). Salt marsh dynamics in a period of accelerated sea level rise. *Journal of Geophysical Research: Earth Surface*, *125*(8), e2019JF005200. https://doi.org/10.1029/2019JF005200

FitzGerald, D. M., Baldwin, C. T., Ibrahim, N. A., & Humphries, S. M. (1992). Sedimentologic and morphologic evolution of a beach ridge barrier along an indented coast: Buzzards Bay, Massachusetts. *Quaternary Coasts of the United States*, 65–75. https://doi.org/10.2110/pec.92.48.0065

FitzGerald, D. M., Baldwin, C. T., Ibrahim, N. A., & Sand, D. R. (1987). Development of the northwestern Buzzards bay shoreline, Massachusetts. In D. M. FitzGerald & P. S. Rosen (Eds.), *Glaciated coasts* (p. 327). Academic Press INC.

FitzGerald, D. M., Hughes, Z. J., Georgiou, I. Y., Black, S., & Novak, A. (2020). Enhanced, climate-driven sedimentation on salt marshes. *Geophysical Research Letters*, *47*(10), e2019GL086737. https://doi.org/10.1029/2019GL086737

Foster, D. S. (2014). Sediment-texture units of the sea floor for Buzzards bay, Massachusetts (BuzzardsBay_sedcover, polygon shapefile, geographic, WGS84) (Version 1) [Dataset]. *USGS*. https://data.usgs.gov/datacatalog/data/USGS:fd6bb70a-1ad6-44b3-9a70-8a6057c3b755

Franz, G., Delpey, M. T., Brito, D., Pinto, L., Leitão, P., & Neves, R. (2017). Modelling of sediment transport and morphological evolution under the combined action of waves and currents. *Ocean Science*, *13*(5), 673–690. https://doi.org/10.5194/os-13-673-2017

Ganju, N. K., Lentz, S. J., Kirincich, A. R., & Farrar, J. T. (2011). Complex mean circulation over the inner shelf south of Martha's Vineyard revealed by observations and a high-resolution model. *Journal of Geophysical Research*, *116*(C10), C10036. https://doi.org/10.1029/2011jc007035

George, D. A., Largier, J. L., Pasternack, G. B., Barnard, P. L., Storlazzi, C. D., & Erikson, L. H. (2019). Modeling sediment bypassing around idealized rocky headlands. *Journal of Marine Science and Engineering*, *7*(2), 40. https://doi.org/10.3390/jmse7020040

Giosan, L., Bokuniewicz, H., Panin, N., & Postolache, I. (1999). Longshore sediment transport pattern along the Romanian Danube delta coast. *Journal of Coastal Research*, 859–871.

Goddard, P. B., Yin, J., Griffies, S. M., & Zhang, S. (2015). An extreme event of sea-level rise along the Northeast coast of North America in 2009–2010. *Nature Communications*, *6*(1), 6346. https://doi.org/10.1038/ncomms7346

Goman, M., Joyce, A., & Mueller, R. (2005). Stratigraphic evidence for anthropogenically induced coastal environmental change from Oaxaca, Mexico. *Quaternary Research*, *63*(3), 250–260. https://doi.org/10.1016/j.yqres.2005.02.008

Grasso, F., Michallet, H., & Barthélemy, E. (2011). Experimental simulation of shoreface nourishments under storm events: A morphological, hydrodynamic, and sediment grain size analysis. *Coastal Engineering*, *58*(2), 184–193. https://doi.org/10.1016/j.coastaleng.2010.09.007

Greer, M. N., & Madsen, O. S. (1978). Longshore sediment transport data: A review. *Coastal Engineering*, *1978*, 1563–1576. https://doi.org/10.1061/9780872621909.095

Guillou, N., & Chapalain, G. (2010). Numerical simulation of tide-induced transport of heterogeneous sediments in the English Channel. *Continental Shelf Research*, *30*(7), 806–819. https://doi.org/10.1016/j.csr.2010.01.018

Hallermeier, R. J. (1978). Uses for a calculated limit depth to beach erosion. *Coastal Engineering*, *1978*, 1493–1512.

Hamilton, D. G., & Ebersole, B. A. (2001). Establishing uniform longshore currents in a large-scale sediment transport facility. *Coastal Engineering*, *42*(3), 199–218. https://doi.org/10.1016/s0378-3839(00)00059-4

Han, X., Dong, S., & Wang, Y. (2021). Interaction between oblique waves and arc-shaped breakwater: Wave action on the breakwater and wave transformation behind it. *Ocean Engineering*, *234*, 109252. https://doi.org/10.1016/j.oceaneng.2021.109252

Hequette, A., Desrosiers, M., Hill, P. R., & Forbes, D. L. (2001). The influence of coastal morphology on shoreface sediment transport under storm-combined flows, Canadian Beaufort Sea. *Journal of Coastal Research*, 507–516.

Hoque, A., Hossain, N., Ali, S., & Rahman, M. (2019). Wave breaking and bubble formation associate energy dissipation and wave setup. *Ocean Dynamics*, *69*(8), 913–923. https://doi.org/10.1007/s10236-019-01279-x

Hsu, T.-W., Hsu, J. R.-C., Weng, W.-K., Wang, S.-K., & Ou, S.-H. (2006). Wave setup and setdown generated by obliquely incident waves. *Coastal Engineering*, *53*(10), 865–877. https://doi.org/10.1016/j.coastaleng.2006.05.002

Huang, Y., Weisberg, R. H., Zheng, L., & Zijlema, M. (2013). Gulf of Mexico hurricane wave simulations using SWAN: Bulk formula-based drag coefficient sensitivity for Hurricane Ike. *Journal of Geophysical Research: Oceans*, *118*(8), 3916–3938. https://doi.org/10.1002/jgrc.20283

Hubbard, D. K. (1992). Hurricane-induced sediment transport in open-shelf tropical systems; an example from St. Croix, US Virgin Islands. *Journal of Sedimentary Research*, *62*(6), 946–960.

Huisman, B., Ruessink, B., De Schipper, M., Luijendijk, A., & Stive, M. (2018). Modelling of bed sediment composition changes at the lower shoreface of the Sand Motor. *Coastal Engineering*, *132*, 33–49. https://doi.org/10.1016/j.coastaleng.2017.11.007

Idier, D., Bertin, X., Thompson, P., & Pickering, M. D. (2019). Interactions between mean sea level, tide, surge, waves and flooding: Mechanisms and contributions to sea level variations at the coast. *Surveys in Geophysics*, *40*(6), 1603–1630. https://doi.org/10.1007/s10712-019-09549-5

Jing, L., & Ridd, P. V. (1996). Wave-current bottom shear stresses and sediment resuspension in Cleveland Bay, Australia. *Coastal Engineering*, *29*(1–2), 169–186. https://doi.org/10.1016/s0378-3839(96)00023-3

Kaliraj, S., Chandrasekar, N., & Magesh, N. (2014). Impacts of wave energy and littoral currents on shoreline erosion/accretion along the south-west coast of Kanyakumari, Tamil Nadu using DSAS and geospatial technology. *Environmental Earth Sciences*, *71*(10), 4523–4542. https://doi.org/10.1007/s12665-013-2845-6

Kim, G. H., Jho, M. H., & Yoon, S. B. (2017). Improving the performance of SWAN modelling to simulate diffraction of waves behind structures. *Journal of Coastal Research*, *79*(79), 349–353. https://doi.org/10.2112/si79-071.1

King, E. V., Conley, D. C., Masselink, G., Leonardi, N., McCarroll, R. J., Scott, T., & Valiente, N. G. (2021). Wave, tide and topographical controls on headland sand bypassing. *Journal of Geophysical Research: Oceans*, *126*(8), e2020JC017053. https://doi.org/10.1029/2020jc017053

Klein, A. H., da Silva, G. V., Taborda, R., da Silva, A. P., & Short, A. D. (2020). Headland bypassing and overpassing: Form, processes and applications. *Sandy Beach Morphodynamics*, 557–591. https://doi.org/10.1016/b978-0-08-102927-5.00023-0

Kobayashi, N., Agarwal, A., & Johnson, B. D. (2007). Longshore current and sediment transport on beaches. *Journal of Waterway, Port, Coastal, and Ocean Engineering*, *133*(4), 296–304. https://doi.org/10.1061/(asce)0733-950x(2007)133:4(296)

Lavaud, L., Bertin, X., Martins, K., Pezerat, M., Coulombier, T., & Dausse, D. (2022). Wave dissipation and mean circulation on a shore platform under storm wave conditions. *Journal of Geophysical Research: Earth Surface*, *127*(3), e2021JF006466. https://doi.org/10.1029/2021JF006466

Lerma, A. N., Pedreros, R., Robinet, A., & Sénéchal, N. (2017). Simulating wave setup and runup during storm conditions on a complex barred beach. *Coastal Engineering*, *123*, 29–41. https://doi.org/10.1016/j.coastaleng.2017.01.011

Lesser, G. R., Roelvink, J. A., van Kester, J. A. T. M., & Stelling, G. S. (2004). Development and validation of a three-dimensional morphological model. *Coastal Engineering*, *51*(8–9), 883–915. https://doi.org/10.1016/j.coastaleng.2004.07.014

Limber, P. W., Brad Murray, A., Adams, P. N., & Goldstein, E. B. (2014). Unraveling the dynamics that scale cross-shore headland relief on rocky coastlines: 1. Model development. *Journal of Geophysical Research: Earth Surface*, *119*(4), 854–873. https://doi.org/10.1002/2013jf002950

Lin, J.-G. (2013). An improvement of wave refraction-diffraction effect in SWAN. *Journal of Marine Science and Technology*, *21*(2), 198–208.

Longuet-Higgins, M. S. (1970). Longshore currents generated by obliquely incident sea waves: 1. *Journal of Geophysical Research (1896-1977)*, *75*(33), 6778–6789. https://doi.org/10.1029/JC075i033p06778

Ma, H., Xu, L., Okon, S. U., Hu, P., Li, W., Shi, H., & He, Z. (2024). Sediment transport and bed erosion during storm surge using a coupled hydrodynamic and morphodynamic model considering wave and current interaction. *Coastal Engineering*, *187*, 104409. https://doi.org/10.1016/j.coastaleng.2023.104409

Malliouri, D. I., Petrakis, S., Vandarakis, D., Kikaki, K., Hatiris, G.-A., Gad, F.-K., et al. (2022). The role of sea state to the morphological changes of Prasonisi tombolo, Rhodes island, Greece. *Water*, *14*(13), 2016. https://doi.org/10.3390/w14132016

Mangor, K., Drønen, N. K., Kaergaard, K. H., & Kristensen, N. E. (2017). *Shoreline management guidelines*. DHI: Hirschholm.

Mariño-Tapia, I., Aird, N., Davidson, M., Kingston, K., & Ganderton, P. (2004). Tidally modulated sediment transport processes on a shore-attached sandbar. *Journal of Coastal Research*, 395–400.

McCarroll, R. J., Masselink, G., Valiente, N. G., Scott, T., King, E. V., & Conley, D. (2018). Wave and tidal controls on embayment circulation and headland bypassing for an exposed, macrotidal site. *Journal of Marine Science and Engineering*, *6*(3), 94. https://doi.org/10.3390/jmse6030094

McLaren, P., & Bowles, D. (1985). The effects of sediment transport on grain-size distributions. *Journal of Sedimentary Research*, *55*(4), 457–470.

Mouragues, A., Bonneton, P., Castelle, B., Marieu, V., Jak McCarroll, R., Rodriguez-Padilla, I., et al. (2020). High-energy surf zone currents and headland rips at a geologically constrained mesotidal beach. *Journal of Geophysical Research: Oceans*, *125*(10), e2020JC016259. https://doi.org/10.1029/2020jc016259

NDBC. (2023). Wind and wave data collected from national data buoy center (station No.: BUZM3 & 44085) (Version 1) [Dataset]. *NDBC*. https://www.ndbc.noaa.gov/

NOAA. (2023). Historical tidal level data retrieved from Newport tidal gauge under National Oceanic and Atmospheric Administration (station No.:8452660) (Version 1) [Dataset]. *National Oceanic and Atmospheric Administration*. https://tidesandcurrents.noaa.gov/

NOAA. (2024). NOAA's historical map & chart collection (Version 1) [Dataset]. *United States Office of Coast Survey*. https://historicalcharts.noaa.gov/about.php

Nordstrom, K. F. (2014). Living with shore protection structures: A review. *Estuarine, Coastal and Shelf Science*, *150*, 11–23. https://doi.org/10.1016/j.ecss.2013.11.003

Palinkas, C. M., Halka, J. P., Li, M., Sanford, L. P., & Cheng, P. (2014). Sediment deposition from tropical storms in the upper Chesapeake Bay: Field observations and model simulations. *Continental Shelf Research*, *86*, 6–16. https://doi.org/10.1016/j.csr.2013.09.012

Pattiaratchi, C., Hegge, B., Gould, J., & Eliot, I. (1997). Impact of sea-breeze activity on nearshore and foreshore processes in southwestern Australia. *Continental Shelf Research*, *17*(13), 1539–1560. https://doi.org/10.1016/s0278-4343(97)00016-2

Pattiaratchi, C., Olsson, D., Hetzel, Y., & Lowe, R. (2009). Wave-driven circulation patterns in the lee of groynes. *Continental Shelf Research*, *29*(16), 1961–1974. https://doi.org/10.1016/j.csr.2009.04.011

Putnam, J. A., Munk, W. H., & Taylor, M. (1949). The prediction of longshore currents. *Eos, Transactions American Geophysical Union*, *30*(3), 337–345. https://doi.org/10.1029/TR030i003p00337

Roberts, T. M., Wang, P., & Puleo, J. A. (2013). Storm-driven cyclic beach morphodynamics of a mixed sand and gravel beach along the Mid-Atlantic Coast, USA. *Marine Geology*, *346*, 403–421. https://doi.org/10.1016/j.margeo.2013.08.001

Roy, P., Cowell, P., Ferland, M., & Thom, B. (1994). Wave-dominated coasts. *Coastal evolution: Late Quaternary shoreline morphodynamics*, 121–186. https://doi.org/10.1017/cbo9780511564420.006

Sankaranarayanan, S. (2007). Modeling the tide and wind-induced circulation in Buzzards Bay. *Estuarine, Coastal and Shelf Science*, *73*(3–4), 467–480. https://doi.org/10.1016/j.ecss.2006.12.022

Shetty, A., & Jayappa, K. (2020). Seasonal variation in longshore sediment transport rate and its impact on sediment budget along the wave-dominated Karnataka coast, India. *Journal of Earth System Science*, *129*, 1–14. https://doi.org/10.1007/s12040-020-01504-y

Siegle, E., Huntley, D. A., & Davidson, M. A. (2004). Physical controls on the dynamics of inlet sandbar systems. *Ocean Dynamics*, *54*(3–4), 360–373. https://doi.org/10.1007/s10236-003-0062-7

Siegle, E., Huntley, D. A., & Davidson, M. A. (2007). Coupling video imaging and numerical modelling for the study of inlet morphodynamics. *Marine Geology*, *236*(3–4), 143–163. https://doi.org/10.1016/j.margeo.2006.10.022

Sierra, J., & Casas-Prat, M. (2014). Analysis of potential impacts on coastal areas due to changes in wave conditions. *Climatic Change*, *124*(4), 861–876. https://doi.org/10.1007/s10584-014-1120-5

Specht, C., Lewicka, O., Specht, M., Dąbrowski, P., & Burdziakowski, P. (2020). Methodology for carrying out measurements of the tombolo geomorphic landform using unmanned aerial and surface vehicles near Sopot Pier, Poland. *Journal of Marine Science and Engineering*, *8*(6), 384. https://doi.org/10.3390/jmse8060384

Sun, Y., Chen, C., Beardsley, R. C., Xu, Q., Qi, J., & Lin, H. (2013). Impact of current-wave interaction on storm surge simulation: A case study for hurricane Bob. *Journal of Geophysical Research: Oceans*, *118*(5), 2685–2701. https://doi.org/10.1002/jgrc.20207

Svendsen, I. A. (1984). Wave heights and set-up in a surf zone. *Coastal Engineering*, *8*(4), 303–329. https://doi.org/10.1016/0378-3839(84)90028-0

SWAN, S. (2015). *Technical documentation (SWAN Cycle III version 41.01 A)*. Delft University of Technology.
Toffoli, A., McConochie, J., Ghantous, M., Loffredo, L., & Babanin, A. V. (2012). The effect of wave-induced turbulence on the ocean mixed layer during tropical cyclones: Field observations on the Australian North-West Shelf. *Journal of Geophysical Research*, *117*(C11). https://doi.org/10.1029/2011jc007780
Trenhaile, A. (2016). Rocky coasts —— Their role as depositional environments. *Earth-Science Reviews*, *159*, 1–13. https://doi.org/10.1016/j.earscirev.2016.05.001
Tsai, C.-P., Chen, Y.-C., & Ko, C.-H. (2023). Prediction of bay-shaped shorelines between detached breakwaters with various gap spacings. *Sustainability*, *15*(7), 6218. https://doi.org/10.3390/su15076218
van Rijn, L. C., Walstra, D. J. R., & Ormondt, M. (2004). Description of TRANSPOR2004 and implementation in Delft3D-online. Z3748.
van Wiechen, P., de Vries, S., Reniers, A., & Aarninkhof, S. (2023). Dune erosion during storm surges: A review of the observations, physics and modelling of the collision regime. *Coastal Engineering*, *186*, 104383. https://doi.org/10.1016/j.coastaleng.2023.104383
Vieira da Silva, G., Toldo Jr, E. E., Klein, A. H. D. F., & Short, A. D. (2018). The influence of wave-wind- and tide-forced currents on headland sand bypassing – Study case: Santa Catarina Island north shore, Brazil. *Geomorphology*, *312*, 1–11. https://doi.org/10.1016/j.geomorph.2018.03.026
Villarini, G., Vecchi, G. A., Knutson, T. R., & Smith, J. A. (2011). Is the recorded increase in short-duration North Atlantic tropical storms spurious? *Journal of Geophysical Research*, *116*(D10), D10114. https://doi.org/10.1029/2010jd015493
Vincent, C. E., Young, R. A., & Swift, D. J. (1983). Sediment transport on the long island shoreface, north American Atlantic shelf: Role of waves and currents in shoreface maintenance. *Continental Shelf Research*, *2*(2–3), 163–181. https://doi.org/10.1016/0278-4343(83)90014-6
Vousdoukas, M. I., Almeida, L. P. M., & Ferreira, Ó. (2012). Beach erosion and recovery during consecutive storms at a steep-sloping, meso-tidal beach. *Earth Surface Processes and Landforms*, *37*(6), 583–593. https://doi.org/10.1002/esp.2264
Vu, M., Lacroix, Y., & Nguyen, V. (2018). Investigating the effects of sea-level rise on morphodynamics in the western Giens tombolo, France. *IOP Conference Series: Earth and Environmental Science*, *167*, 012027. https://doi.org/10.1088/1755-1315/167/1/012027
Wang, K., Hou, Y., Li, S., Du, M., Chen, J., & Lu, J. (2020). A comparative study of storm surge and wave setup in the East China Sea between two severe weather events. *Estuarine, Coastal and Shelf Science*, *235*, 106583. https://doi.org/10.1016/j.ecss.2020.106583
Warner, J. C., Geyer, W. R., & Lerczak, J. A. (2005). Numerical modeling of an estuary: A comprehensive skill assessment. *Journal of Geophysical Research*, *110*(C5), C05001. https://doi.org/10.1029/2004jc002691
Willmott, C. J. (1981). On the validation of models. *Physical Geography*, *2*(2), 184–194. https://doi.org/10.1080/02723646.1981.10642213
Woodworth, P. L., Melet, A., Marcos, M., Ray, R. D., Wöppelmann, G., Sasaki, Y. N., et al. (2019). Forcing factors affecting sea level changes at the coast. *Surveys in Geophysics*, *40*(6), 1351–1397. https://doi.org/10.1007/s10712-019-09531-1
Wornom, S. F., Welsh, D. J., & Bedford, K. W. (2001). On coupling the SWAN and WAM wave models for accurate nearshore wave predictions. *Coastal Engineering Journal*, *43*(03), 161–201. https://doi.org/10.1142/s0578563401000335
Xie, D., Hughes, Z., FitzGerald, D., Tas, S., Asik, T. Z., & Fagherazzi, S. (2024). Impacts of climate change on coastal hydrodynamics around a headland and potential headland sediment bypassing. *Geophysical Research Letters*, *51*(4), e2023GL105323. https://doi.org/10.1029/2023GL105323
Yang, S., Bouma, T. J., Xu, K., Shi, B., Yang, H., Zhang, W., et al. (2023). Storms dominate the erosion of the Yangtze Delta and southward sediment transport. *Science Bulletin*, *68*(6), 553–556. https://doi.org/10.1016/j.scib.2023.03.005
Yasso, W. E. (1965). Plan geometry of headland-bay beaches. *The Journal of Geology*, *73*(5), 702–714. https://doi.org/10.1086/627111
Zhang, Q.-H., Bing, Y., & Onyx, W. (2009). Fine sediment carrying capacity of combined wave and current flows. *International Journal of Sediment Research*, *24*(4), 425–438. https://doi.org/10.1016/s1001-6279(10)60015-7
Zhang, Z., Chen, C., Song, Z., Zhang, D., Hu, D., & Guo, F. (2020). A FVCOM study of the potential coastal flooding in apponagansett bay and clarks cove, Dartmouth Town (MA). *Natural Hazards*, *103*(3), 2787–2809. https://doi.org/10.1007/s11069-020-04102-9
Zhou, Z., Wu, Y., Fan, D., Wu, G., Luo, F., Yao, P., et al. (2022). Sediment sorting and bedding dynamics of tidal flat wetlands: Modeling the signature of storms. *Journal of Hydrology*, *610*, 127913. https://doi.org/10.1016/j.jhydrol.2022.127913
Zhu, Q., & Wiberg, P. L. (2022). The importance of storm surge for sediment delivery to microtidal marshes. *Journal of Geophysical Research: Earth Surface*, *127*(9), e2022JF006612. https://doi.org/10.1029/2022jf006612

AGU ADVANCING EARTH AND SPACE SCIENCES

Geophysical Research Letters

RESEARCH LETTER
10.1029/2023GL105323

Key Points:

- The formation of circulation cells and wave energy convergence around headlands during storms reduce bottom shear stress at the beach
- Sea-level rise increases wave heights, currents, and bed shear stress in the nearshore because of landward shifting of the circulation cells
- Higher storm waves expand the surf zone, shift circulation cells seaward, and enhance potential headland sediment bypassing

Supporting Information:

Supporting Information may be found in the online version of this article.

Correspondence to:
D. Xie,
danghan@bu.edu

Citation:

Xie, D., Hughes, Z., FitzGerald, D., Tas, S., Asik, T. Z., & Fagherazzi, S. (2024). Impacts of climate change on coastal hydrodynamics around a headland and potential headland sediment bypassing. *Geophysical Research Letters*, *51*, e2023GL105323. https://doi.org/10.1029/2023GL105323

Received 6 JULY 2023
Accepted 27 JAN 2024

Impacts of Climate Change on Coastal Hydrodynamics Around a Headland and Potential Headland Sediment Bypassing

Danghan Xie[1], Zoe Hughes[1], Duncan FitzGerald[1], Silke Tas[1,2], Tansir Zaman Asik[1], and Sergio Fagherazzi[1]

[1]Department of Earth and Environment, Boston University, Boston, MA, USA, [2]Hydrology and Environmental Hydraulics Group, Wageningen University and Research, Wageningen, The Netherlands

Abstract Shorelines face growing threats due to climate change and diminishing sand supply. Coastal headlands, common rocky features along coastlines, are crucial in shaping hydrodynamics and sediment transport. Yet, the influence of future climate conditions, including sea-level rise (SLR) and intensified storm energy on complex shorelines with headlands has remained relatively unexplored. In this study, we model changes in hydrodynamics and headland bypassing under different SLR and higher storm wave scenarios. Our findings reveal the formation of circulation cells on both sides of a headland, where wave energy converges around the headland zone. Future climate conditions result in larger storm waves on the beach. However, SLR enhances nearshore currents through a landward shifting of the circulation cells, while higher storm waves intensify offshore flow currents due to the seaward movement of the cells. This effect, in turn, increases the potential for headland sediment bypassing.

Plain Language Summary Coastal headlands, prominent rocky features along open coastlines, play a crucial role in protecting nearby beaches from strong waves and erosion. They also affect how sand is exchanged between different beaches. We use a model to explore how future climate conditions including sea-level rise (SLR) and larger storm waves influence coastal waves, littoral currents, and the transport of sand around headlands. Our findings reveal that headlands converge wave energy forming circulation flow cells. SLR results in stronger nearshore currents, driven by the landward movement of the rotating flow cells. In contrast, larger storm waves can move the rotating flow cells seaward, thereby increasing offshore current strength and the potential for sand transport around the headland. Understanding how coastal waves, flow and sediment transport change under future climate conditions will help determine coastal resilience.

1. Introduction

The coastal zone contains a variety of landforms that provide valuable ecosystem services and recreational areas for coastal communities. However, the stability of coastlines is of growing concern because of the increasing risks posed by climate change, including the accelerating rate of sea-level rise (SLR) and the increasing frequency and intensity of storms (Church & White, 2011; Hallegatte et al., 2013; Xie et al., 2020). The consequent enhanced hydrodynamic forces are expected to cause greater erosion, further degrading the shore (Ashton & Murray, 2006; Masselink et al., 2016; Stockdonf et al., 2002).

Coastlines rarely exhibit straight profiles; instead, they often display indentations accompanied by coastal headlands, such as bay-headland coasts or embayed coasts (Davis & FitzGerald, 2020; Slott et al., 2006; van Rijn, 2011). Headlands are a common coastal landform found along nearly 80% of the ice-free shorelines worldwide (Klein et al., 2020; Luijendijk et al., 2018; Nyberg & Howell, 2016). They typically consist of sedimentary rocks which are more resistant to erosion, allowing them to protrude further into the water as the adjacent beach recedes (Davis & FitzGerald, 2020; Limber & Murray, 2011; Ramesh et al., 2021).

Previous studies have identified the key characteristics of coastal headlands, including: (a) converging points for wave energy and currents; (b) obstruction of littoral drifts; (c) blockage of wave energy, creating sheltered areas along adjacent beaches; and (d) formation of circulation cells in nearby waters (Bastos et al., 2003; da Silva et al., 2021; Klein et al., 2020; McCarroll et al., 2019; van Rijn, 1998). These characteristics not only shape local geomorphology but also significantly impact sediment dynamics throughout the coastal system (George et al., 2022). For example, the concentration of hydrodynamic forces around headlands reduces longshore currents, promoting local sedimentation (van Rijn, 2011). Additionally, sediment connectivity between adjacent embayments around a headland, accomplished through headland bypassing, strongly influences sediment availability and subsequent sedimentation patterns in the downdrift areas (Klein et al., 2020). However, the efficiency of headland bypassing varies with individual systems depending on wave incident angles, wave heights and shape of the headland (George et al., 2019). A noteworthy phenomenon that arises around headlands is the formation of circulation cells, resulting from the interactions among waves, currents, and coastal geomorphology. These circulation cells play a vital role in governing sediment transport processes as sediment is driven and redistributed by the circulation currents (George et al., 2019; Klein et al., 2020; McCarroll et al., 2018).

The dynamics of circulation cells and headland bypassing are significantly influenced by the interplay of tides and waves. Vieira da Silva et al. (2018) found that waves are the driving force producing circulation cells leading to headland bypassing, with tides playing a secondary role. This perspective is reinforced by other studies underlining the role that large waves have for the initiation of sediment bypassing (McCarroll et al., 2018; Thom et al., 2018). Tidal levels and tidal currents are also important. Research by Costa et al. (2019) suggests that tidal currents can complement and reinforce wave-driven sediment transport, thereby favoring sediment bypassing around the headland. Similar findings has been found by Valiente et al. (2019), who observed that heightened tidal levels intensify nearshore bed shear stress, augmenting headland bypassing. Despite these recent insights, the effect of climate change such as SLR and higher storm waves remains relatively unexplored (George et al., 2022; Klein et al., 2020). SLR has the potential to deepen shallow coastal areas and reduce wave attenuation, enabling greater penetration of wave energy closer to the shore (Siegle & Costa, 2017). On the other hand, larger wave energy intensifies wave heights and alter the wave breaking zone (Peregrine, 1983). Both aspects have implications for the hydrodynamics of headlands and, consequently, headland bypassing. Thus, there is a need for comprehensive research aimed at unraveling how climate change drivers may impact headlands, and by extension, the patterns of headland bypassing.

Here we investigate the impact of headlands on coastal hydrodynamics and potential headland bypassing, as well as assess how these impacts may change under rising sea level and increased storm magnitude conditions. Our study focuses on Western Buzzards Bay (Figure 1a), consisting of a major coastal headland separating two embayments (FitzGerald et al., 1987). We conduct numerical modeling to explore the impacts of coastal headlands on nearshore hydrodynamics and the effects of climate change on coastal vulnerability. This study improves our understanding of physical forces operating along indented shorelines under future climate conditions.

2. Materials and Methods

2.1. Study Area

Western Buzzards Bay, Massachusetts (USA), includes numerous tidal inlets and estuaries. The bay is characterized by indented shorelines separated by headlands and embayments (Figure 1b). The Gooseberry Island headland in this study is an offshore island attached to the shoreline by a natural tombolo and, more recently, by a manmade causeway similar to the study by Klein et al. (2020). The island shore is mantled by cobbles and boulders with a general elevation higher than 1 m, so that the island shoreline is relatively stable and unlikely to be flooded in a regime of a 1-m SLR (Figure S1 in Supporting Information S1). Where beaches do exist, they are primarily composed of fine sand and often armored by coarse sand and gravel layers (FitzGerald et al., 1992). The system is wave dominated and experiences a relatively small tidal range (~1.1 m), with a modest river discharge (~2 m^3/s) (Figure S2 in Supporting Information S1) (Bent, 1995; FitzGerald et al., 1987). Prevailing winds and waves originate from the southwest due to the sheltering effect of the Elizabeth Islands that extend southwestward from Cape Cod (Figure 1a; Figure S3 in Supporting Information S1). The area is commonly impacted by extratropical cyclones and infrequent hurricanes, both of which could generate over 5 m significant wave heights at a 21-m water depth (Figure 1c), driving sediment resuspension, shoreline retreat, and inlet breaching (FitzGerald et al., 2002).

2.2. General Description of Model Approach

Following previous studies of coastal circulation cells (McCarroll et al., 2018; Mulligan et al., 2008; van Rijn, 2011), the process-based model Delft3D was used to simulate coastal hydrodynamics, during varying storm conditions and different climate scenarios (Lesser et al., 2004). Delft3D-FLOW solves the depth-averaged shallow water equations to simulate water levels and current velocity (Lesser et al., 2004). Delft3D-WAVE

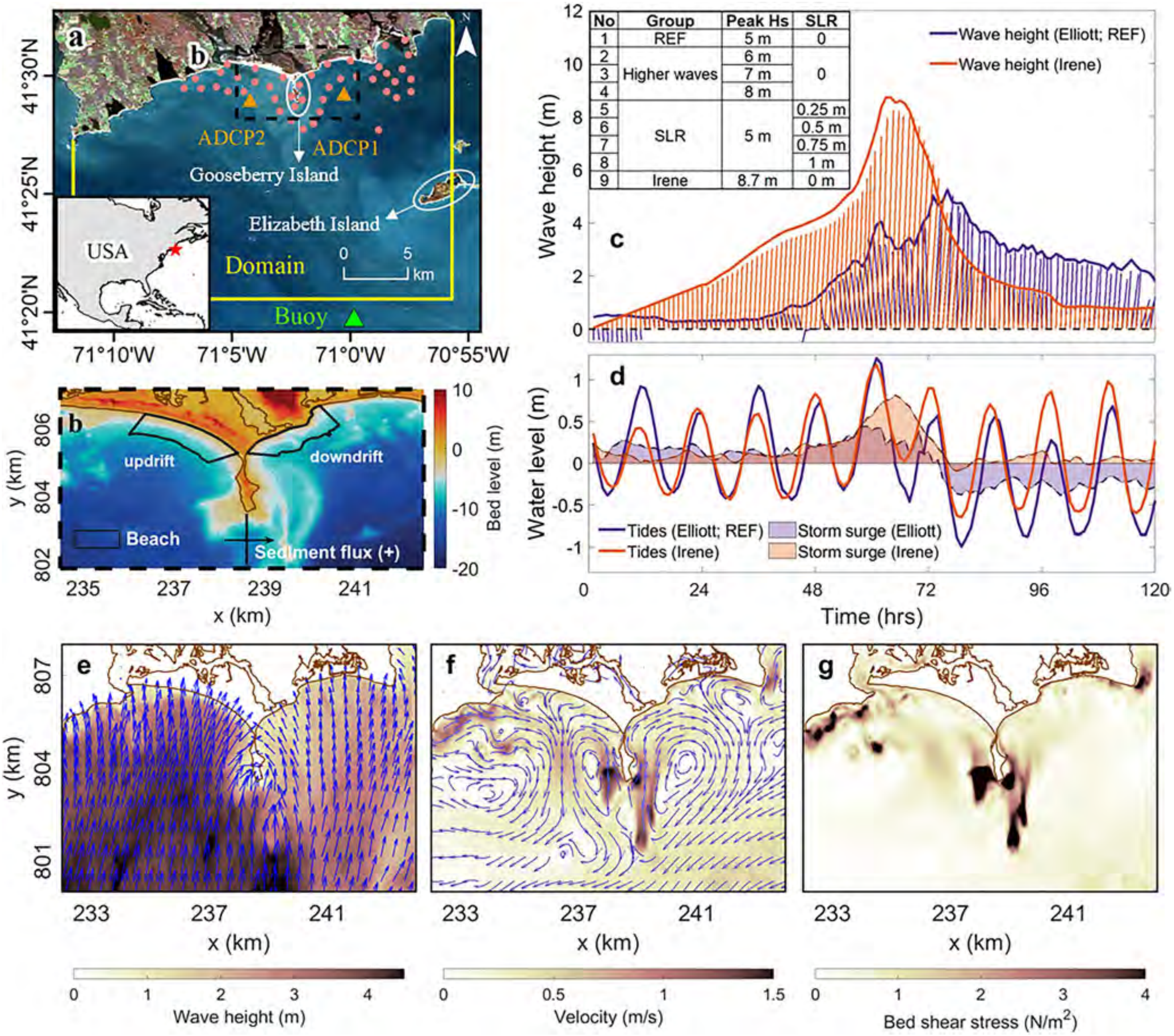

No	Group	Peak Hs	SLR
1	REF	5 m	0
2	Higher waves	6 m	0
3		7 m	
4		8 m	
5	SLR	5 m	0.25 m
6			0.5 m
7			0.75 m
8			1 m
9	Irene	8.7 m	0 m

Figure 1. Model regions in the study area (Western Buzzards Bay, MA, USA), boundary conditions and key hydrodynamic parameters around the headland during the present-day storm conditions. (a) The Delft3D-FLOW and Delft3D-WAVE domains overlap in the region depicted by the yellow box. Black dashed box highlights the focus area of this research, consisting of two coastal cells separated by a headland. Red dots are validation points extracted from the North Atlantic Coast Comprehensive Study Coastal Hazards System (Cialone et al., 2015) (Text S1 in Supporting Information S1). Two Acoustic Doppler Current Profiler (ADCPs) are deployed updrift and downdrift of the headland, measuring water level and waves (e.g., significant wave height [Hs], peak wave period and wave direction); this data set is used to validate the model setup. Green triangle shows the location of an offshore buoy (Station No.: BUZM3 & 44085; 21-m water depth) recording hydrodynamic and meteorological data for model setup. (b) Topographic map of the focus area indicating both updrift and downdrift beaches (black outline). The offshore boundary of each region is based on the 8-m water line determined by the Depth of Closure (see Text S4 in Supporting Information S1) (Hallermeier, 1978; King et al., 2021; Valiente et al., 2019). (c) Wave height, and (d) water level signals at the domain boundary of two historical storms (Elliott and Irene). Lines in panel (c) point to the direction where the waves are propagating toward. In panel (c), scenarios with higher storm waves and sea-level rise (SLR) are presented, with Storm Elliott as the reference (REF). (e) Wave propagation map, (f) flow velocity field with the formation of circulation cells on both sides of the headland, and (g) bed shear stress. Panels (e)–(g) are based on the Elliott storm (2022) and serve as reference results in Figures 2 and 3.

simulates wave propagation and dissipation (whitecapping, bottom friction, and depth-induced breaking) as well as wave-current interactions, based on the third-generation spectral wave model Simulating WAves Nearshore (Booij et al., 1999). Delft3D-FLOW and Delft3D-WAVE were coupled in a two-way manner using overlapping grids (Figure 1a). This allows for the consideration of the impacts of flow on waves (via set-up, current refraction and enhanced bottom friction), as well as the effects of waves on currents (via forcing and enhanced bed shear stress) (Deltares, 2014). Since the river discharge is small in our study site, vertical stratification of the water column is assumed to be negligible and is not included (Garrison, 2014).

Bottom shear stress are enhanced due to the non-linear interaction between the boundary layer at the bed associated with the waves and the current (Grant & Madsen, 1979). The enhancement of the bed shear stress (τ_m) is calculated using Soulsby et al. (1993) formula:

$$\tau_m = \tau_c\left[1 + 1.2\left(\frac{\tau_w}{\tau_w + \tau_c}\right)^{3/2}\right] \tag{1}$$

where the bed shear stress driven by current alone (τ_c) is related to the Chézy friction value (C) and current velocity (u):

$$\tau_c = \frac{g\rho u^2}{C^2} \tag{2}$$

and τ_w is the wave-induced bed shear stress:

$$\tau_w = \frac{1}{2}\rho f_w u_{\mathrm{orb}}^2 \tag{3}$$

where $g = 9.81$ m/s^2 is the gravitational acceleration and ρ is the density of water, set to 1,025 kg/m^3. Wave friction (f_w) is calculated in Delft3D-FLOW using Swart (1974) formula after the wave orbital velocity near the bottom (u_{orb}) is computed from Delft3D-WAVE. Other details on grid development, bathymetry sources, boundary conditions and model validation are provided in Supporting Information S1 (Texts S2 and S3 in Supporting Information S1).

2.3. Model Scenario Setups

Previous studies indicate that climate change is responsible for SLR and higher wave energy, which can intensify hydrodynamic forces around coastal areas (FitzGerald et al., 2020). To investigate these effects, we divided modeling simulations into three groups: present-day scenarios (the reference run with Storm Elliott), future climate change scenarios (derived from the reference run), and another real storm event (Hurricane Irene) (see table in Figure 1c). In the climate change scenarios, we simulated different peak wave heights and various SLR magnitudes. The storm wave heights were selected using the annual wave exceedance probability for wave heights from the North Atlantic Coast Comprehensive Study (NACCS) (Figure S4a in Supporting Information S1) (Cialone et al., 2015). The SLR scenarios for the model were based on the NOAA technical report for the United States coast (Figure S4b in Supporting Information S1) (Sweet et al., 2022).

We investigated the effects of different values of SLR by setting up four additional runs, where the mean water level during the Storm Elliott was increased by 0.25, 0.5, 0.75, and 1 m. These values represent future projections of mean water levels along the US coastline. Sea level will increase by 0.3 m in 2050 and 1 m by 2090 based on the IPCC Intermediate climate scenario, which anticipates global mean sea level reaching 1 m by 2100 (Figure S4b in Supporting Information S1).

The peak wave height of Storm Elliott at the buoy is around 5 m, which corresponds to a storm with yearly frequency (Figure S4a in Supporting Information S1). To assess the effects of higher storm waves on the system resulting from climate change, we conducted additional simulations using peak storm wave heights of 6, 7, and 8 m at the buoy, representing return periods of approximately 2, 3, and 5 years, respectively (Figure S4a in Supporting Information S1).

3. Results

3.1. Effects of Sea-Level Rise and Higher Storm Waves on Coastal Circulation Cells

We show that coastal headlands concentrate wave energy and induce two circulation cells at the two sides. The cells lead to higher hydrodynamic forces around the headland than adjacent beaches during storms (Figures 1e–

1g). For the present-day scenario, the headland creates a shadow zone downdrift when waves come from the south to southwest, causing higher wave height in the updrift beach (Figure 1e). In addition, the headland produces wave refraction that redistributes wave energy along the adjacent nearshore (Figure 1e). Circulation cells caused by wave breaking along both sides of the headland diverge the flow current from the headland thereby lessening current magnitude along the bordering embayments (Figure 1f). The presence of circulation cells and convergence of wave energy create higher bed shear stress around the headland than along the adjacent beaches (Figure 1g).

Both SLR and the presence of higher storm waves increase nearshore wave heights, yet the two climate change scenarios display distinct impacts on coastal currents and bottom shear stress, as depicted in Figures 2 and 3.

Higher water levels during storms extend the propagation of waves closer to the shoreline, resulting in higher wave heights along both updrift and downdrift beaches and in proximity to the headland (Figure 2a). SLR causes the onshore migration of the circulation cells. This migration intensifies currents in shallow areas, and augments bed shear stress along the beach and in the vicinity of the headland (Figures 2b and 2c). Conversely, scenarios featuring higher storm waves produce an increase in wave heights along the beach while maintaining relatively consistent conditions around the headland (Figure 3a). However, these scenarios present a seaward migration of circulation cells, causing a reduction in flow strength and bed shear stress near the shoreline and along both sides of the headland, accompanied by an increase in flow strength and bed shear stress around the seaward side of the headland (Figures 3b and 3c). In the event of both high storm surge and storm waves, as exemplified by the Irene scenario, the beach and the headland are exposed to higher waves, leading to the expansion of the circulation cells, especially on the downdrift side of the headland (Figures 3a and 3b). This expansion contributed to increased current velocity and stronger bed shear stress in the downdrift beach, contrasting with the relatively minimal changes observed in flow strength and bed shear stress in the updrift beach (Figures 3b and 3c).

3.2. How Sea-Level Rise and Higher Storm Waves Affect Potential Headland Bypassing

To assess sediment bypassing around the headland, we consider a hypothetical system with a seabed composed entirely of sand. We calculate the potential sediment flux across a transect in front of the headland (see Figure 1b). This flux is primarily influenced by storm wave height, as shown in Figure 4.

In the present-day scenario, the sediment flux is nearly negligible (gray violin in Figure 4), and SLR has limited impact on it (blue violins in Figure 4a). In contrast, larger storm waves significantly enhance the potential sediment flux (green violins in Figure 4b). In addition, our results show that a storm surge has a significant impact on headland passing. The storm surge from Hurricane Irene is nearly double that of Storm Elliott (Figure 1d). Compared to an 8-m wave height scenario, a similar wave height scenario with a larger storm surge (i.e., hurricane Irene) could almost triple the potential sediment flux (Figure 4b).

4. Discussion and Conclusions

The role of headlands in the coastal system has been a topic of interest for decades, yet the effects of future climate conditions on coastal hydrodynamics around headlands and on the potential headland bypassing remain relatively unexplored. Our modeling findings indicate that future climate conditions are likely to result in increased wave heights nearshore. Nevertheless, our findings reveal that distinct patterns of flow and hydrodynamic forces around the headland can emerge under different climate scenarios, such as SLR and higher storm waves. These differing behaviors can lead to contrasting responses in terms of headland bypassing.

The presence of a coastal headland is known to concentrate waves, resulting in decreased wave energy in adjacent beach regions (Goodwin et al., 2013; McCarroll et al., 2020; Wishaw et al., 2020). The shallow areas surrounding these headlands not only mitigate wave heights but also intensify flow currents due to wave breaking, creating additional forces on currents (Dobbelaere et al., 2022; McCarroll et al., 2020). These effects are consistent with our simulations, which reveal the development of circulation cells around the headland, characterized by accelerated flow currents along the shallow zones (Figure 1f). This phenomenon aligns with previous studies (Valiente et al., 2019) and is essential in directing offshore flows and redistributing sediment within the coastal system (George et al., 2019; Mouragues et al., 2020). Our simulation suggests that bed shear stress is strongly related to the circulation cells (Figure 1g), potentially controlling sediment transport patterns, coastal erosion, and shoreline stability (Marchesiello et al., 2019).

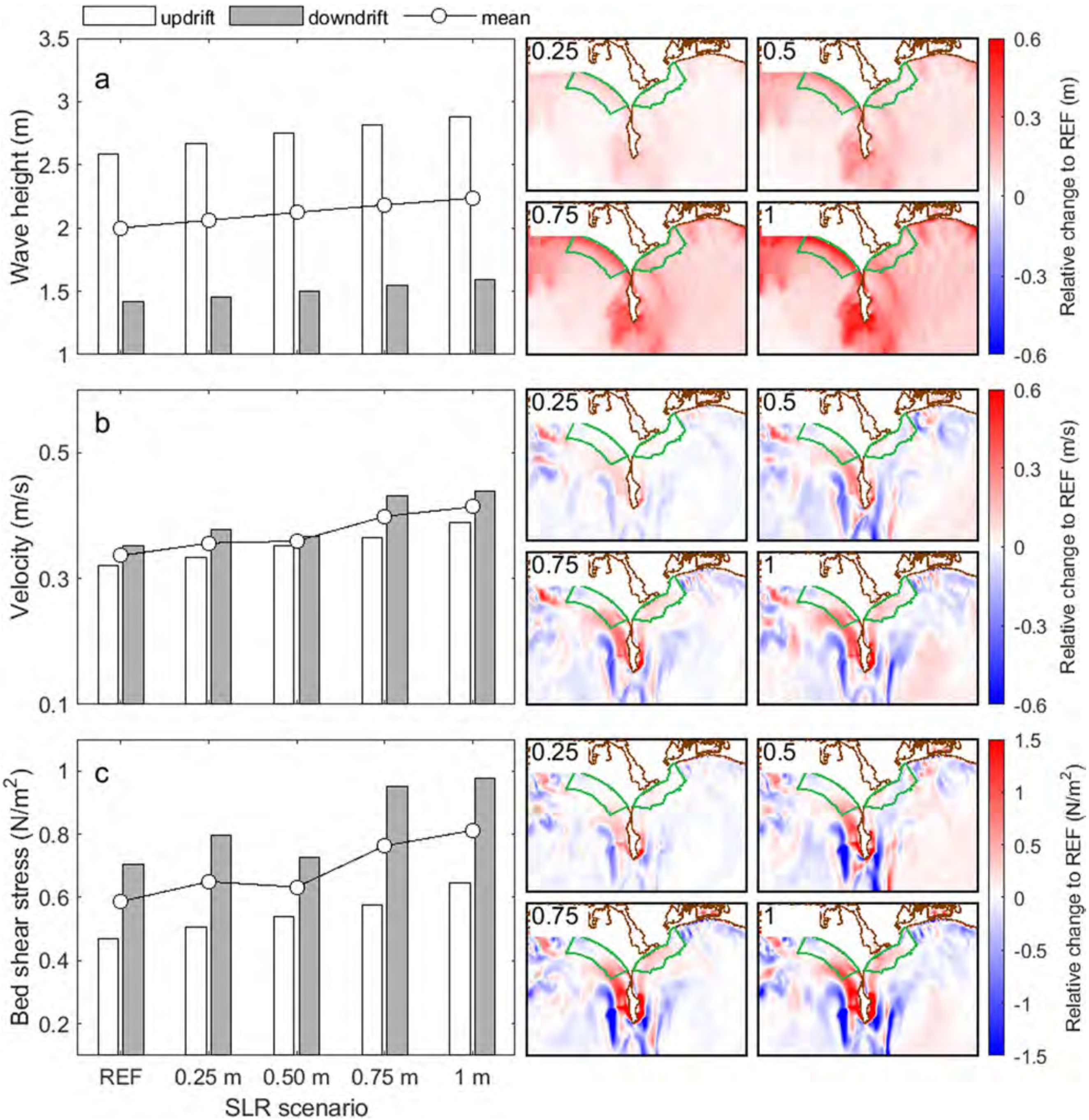

Figure 2. Changes in wave height, velocity, and bed shear stress under different sea-level rise (SLR) scenarios. The bar graphs in the left panel are based on the median values of these hydrodynamic parameters in the updrift and downdrift beach regions, respectively. The mean of two bar values is represented by circles on the graph. The spatial distribution of the relative changes in these three hydrodynamic parameters is presented in the right panel. These relative changes are based on the reference results from Figures 1e–1g.

We have also examined how different climate scenarios impact the hydrodynamic environment around the headland. Our findings reveal opposing behaviors of circulation cells in response to SLR and higher storm wave scenarios, affecting both velocity and bottom shear stress on the beach (Figures 2 and 3) and potentially influencing headland bypassing (Figure 4). In the SLR scenarios, higher water levels allow waves to propagate farther into both beach and headland areas (Figure 2a). This is due to the primary wave-breaking zone moving closer to the shore simultaneously with SLR, leading to higher flow velocity and bed shear stress along the beach

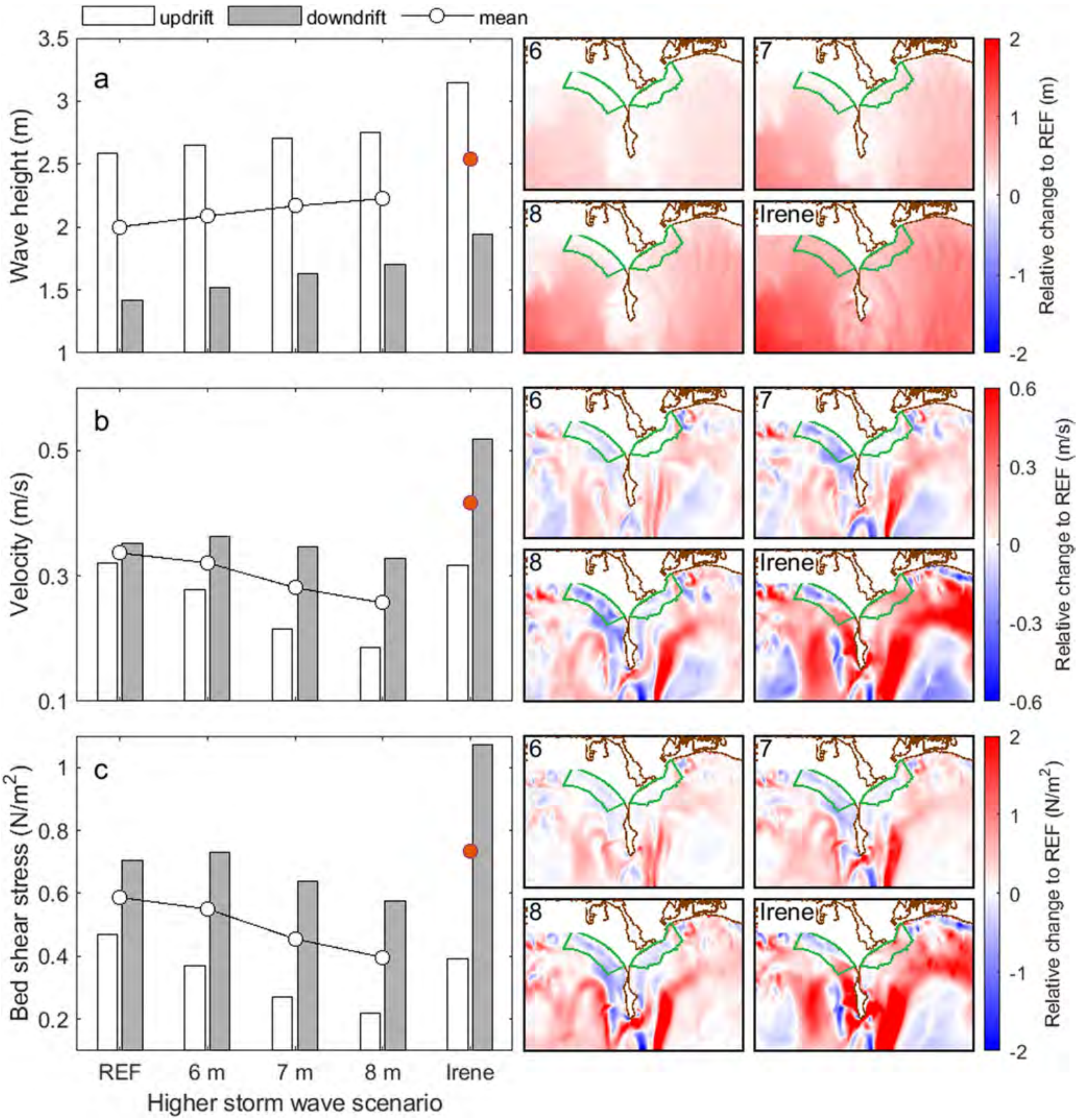

Figure 3. Changes in wave height, velocity, and bed shear stress under different scenarios of storm waves. The bar graphs in the left panel are based on the median values of these hydrodynamic parameters from the updrift beach region and the downdrift beach region, respectively. The mean of two bar values is represented by circles on the graph. The spatial distribution of the relative changes in these three hydrodynamic parameters is presented in the right panel. These relative changes are based on the reference results from Figures 1e–1g. Hydrodynamic parameters of Hurricane Irene are provided for a comparison.

(Figures 2b and 2c). In contrast, increased wave energy predominantly elevates wave height offshore of the beach rather than around the headland (Figures 2a and 3a), reducing both velocity and bed shear stress along the beach (Figures 3b and 3c). In these scenarios, the wave-breaking zone expands with intensified energy dissipation occurring at the edge of shallow areas, around the 10-m isobath (Figure S5 in Supporting Information S1). As a result, these distinct wave energy dissipation patterns intensify nearshore circulation cells in the SLR scenarios versus offshore circulation currents in higher storm wave scenarios (Figure 2b vs. Figure 3b). These findings align

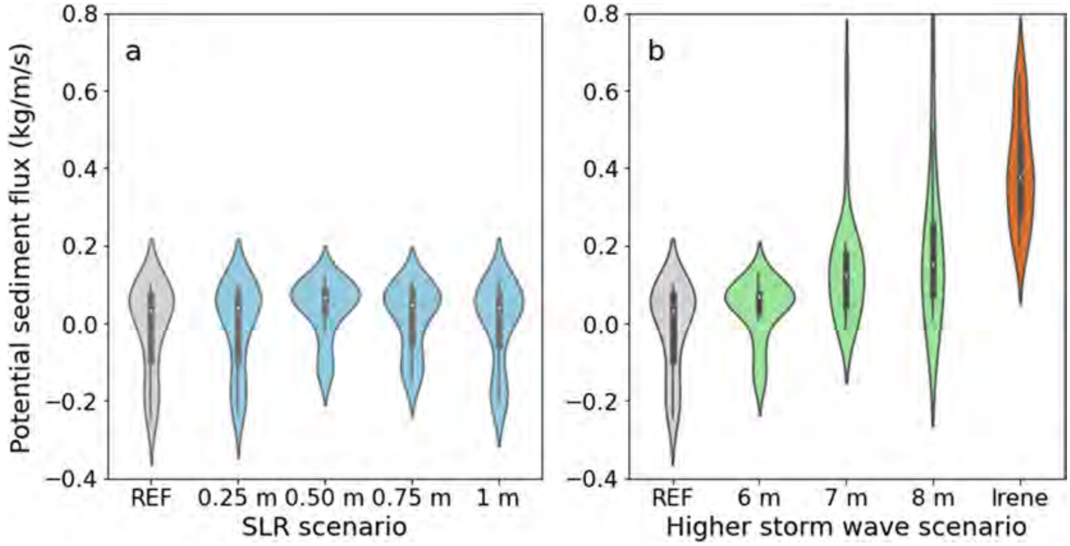

Figure 4. Potential sediment flux along the transect in front of the headland under different sea-level rise (SLR) scenarios (a) and higher storm wave scenarios (b). A positive sediment flux indicates sediment movement from the updrift coastal area to the downdrift area. Violin thickness corresponds to probability density. Endpoints of the violin depict minimum and maximum values. The box plot inside each violin covers the first to third quartiles, with a square representing the median value.

with similar studies by Mouragues et al. (2020), which also highlight that increasing wave height expands the surf zone area and causes the circulation cells to move to deeper waters. Our additional analysis further suggests that the increase in velocity or bed shear stress due to SLR is balanced by increasing wave height, leading to minimal changes in these two variables under certain combinations (Figure S6 in Supporting Information S1). Hence, the combinations of SLR and wave height are of critical importance in determining hydrodynamic changes along the beach in the future.

Potential headland bypassing is examined by evaluating the sediment flux along a transect near the headland (Figure 4). Our simulations indicate that headland bypassing is primarily facilitated by higher storm waves rather than SLR. The reason is that higher waves expand the surf zone, a phenomenon known to enhance headland bypassing, as demonstrated in both our Figure S5 in Supporting Information S1 and previous research (King et al., 2021). Nonetheless, the extent of headland bypassing is also controlled by factors such as spatial sediment coverage and sediment grain size (George et al., 2019; King et al., 2021; Klein et al., 2020). Given that the primary sediment composition around the headland is sedimentary rocks, our domain of only sand might overestimate the amount of headland bypassing (Davis & FitzGerald, 2020; Limber & Murray, 2011; Ramesh et al., 2021). Wave energy is usually believed to be the primary driver of headland bypassing, with tides playing a secondary role (King et al., 2021). Our study further suggests an additional factor that can enhance headland bypassing: storm surges. For example, in scenarios involving a storm surge twice as large as the reference scenario, we observe a threefold increase in headland bypassing, as illustrated in Figure 4b (8-m higher wave scenario vs. Hurricane Irene).

Recent studies have explored the impact of future climate change on coastal processes (Toimil et al., 2020). Coastal headlands, a common feature in shoreline systems worldwide, play a unique role in shaping these processes (Klein et al., 2020; Luijendijk et al., 2018; Nyberg & Howell, 2016). Climate-driven variations in hydrodynamics and sediment availability at the shore are crucial for coastal morphological development and will have dramatic ecological and economic implications (Xie et al., 2022). Our study highlights the complexities of physical forces operating along indented shorelines and different roles played by varying climate conditions in altering wave energy, circulation cells and the potential bypassing around headlands.

Data Availability Statement

The wind and wave data are collected from an offshore buoy station (Station No.: BUZM3 & 44085) maintained by National Data Buoy Center (NDBC, 2023). Historical tidal level is retrieved from Newport tidal gauge (Station

No.: 8452660) operated by National Oceanic and Atmospheric Administration (NOAA, 2023). Annual river discharge is measured at the Paskamanset River near South Dartmouth, Massachusetts, USA (Station No. 01105933, Location: 41°35′07″N, 70°59′27″W) managed by United States Geological Survey (USGS, 2023). Delft3D is an open-source code available online (Deltares, 2014). The model setup for a reference scenario and the hydrodynamic data utilized in this research are available in the Zenodo repository with open access under the MIT license (Xie, 2023). Model validation data includes the field observation (Acoustic Doppler Current Profiler) and regional modeling data set by NACCS Coastal Hazards System (Cialone et al., 2015).

Acknowledgments
Funding for this project was gratefully received from the Buzzards Bay Coalition through a grant from The Rathmann Family Foundation.

References

Ashton, A. D., & Murray, A. B. (2006). High-angle wave instability and emergent shoreline shapes: 1. Modeling of sand waves, flying spits, and capes. *Journal of Geophysical Research*, *111*(F4), F04011. https://doi.org/10.1029/2005jf000422

Bastos, A., Collins, M., & Kenyon, N. (2003). Water and sediment movement around a coastal headland: Portland Bill, Southern UK. *Ocean Dynamics*, *53*(3), 309–321. https://doi.org/10.1007/s10236-003-0031-1

Bent, G. C. (1995). *Streamflow, ground-water recharge and discharge, and characteristics of surficial deposits in Buzzards Bay Basin, Southeastern Massachusetts*. US Geological Survey.

Booij, N., Ris, R. C., & Holthuijsen, L. H. (1999). A third-generation wave model for coastal regions: 1. Model description and validation. *Journal of Geophysical Research*, *104*(C4), 7649–7666. https://doi.org/10.1029/98jc02622

Church, J. A., & White, N. J. (2011). Sea-level rise from the late 19th to the early 21st century. *Surveys in Geophysics*, *32*(4–5), 585–602. https://doi.org/10.1007/s10712-011-9119-1

Cialone, M. A., Massey, T. C., Anderson, M. E., Grzegorzewski, A. S., Jensen, R. E., Cialone, A., et al. (2015). North Atlantic Coast Comprehensive Study (NACCS) coastal storm model simulations: Waves and water levels. Retrieved from https://chs.erdc.dren.mil/Home. [Coastal Hazards System].

Costa, W. L. L., Silveira, L. F., & Klein, A. H. F. (2019). Influence of wave climate and tidal regime on headland bypassing - Study case: Northern São Francisco do Sul Island, SC, Brazil. In *Coastal sediments* (pp. 488–501).

da Silva, A. P., da Silva, G. V., Strauss, D., Murray, T., Woortmann, L. G., Taber, J., et al. (2021). Headland bypassing timescales: Processes and driving forces. *Science of the Total Environment*, *793*, 148591. https://doi.org/10.1016/j.scitotenv.2021.148591

Davis, R. A. J., & FitzGerald, D. M. (2020). *Beaches and coasts* (2nd ed.). John Wiley & Sons.

Deltares. (2014). Simulation of multi-dimensional hydrodynamic flows and transport phenomena, including sediments - User manual (Version: 3.15.34158) [Delft3D Software]. Deltares. Retrieved from https://oss.deltares.nl/

Dobbelaere, T., Curcic, M., Le Hénaff, M., & Hanert, E. (2022). Impacts of Hurricane Irma (2017) on wave-induced ocean transport processes. *Ocean Modelling*, *171*, 101947. https://doi.org/10.1016/j.ocemod.2022.101947

FitzGerald, D. M., Baldwin, C. T., Ibrahim, N. A., & Humphries, S. M. (1992). Sedimentologic and morphologic evolution of a beach ridge barrier along an indented coast: Buzzards Bay, Massachusetts.

FitzGerald, D. M., Baldwin, C. T., Ibrahim, N. A., & Sands, D. R. (1987). Development of the northwestern Buzzards Bay shoreline, Massachusetts. In *Glaciated coasts* (pp. 327–357). Academic Press, Inc. 18 fig, 38 ref.

FitzGerald, D. M., Buynevich, I. V., Davis, R. A., & Fenster, M. S. (2002). New England tidal inlets with special reference to riverine-associated inlet systems. *Geomorphology*, *48*(1), 179–208. https://doi.org/10.1016/s0169-555x(02)00181-2

FitzGerald, D. M., Hughes, Z. J., Georgiou, I. Y., Black, S., & Novak, A. (2020). Enhanced, Climate-driven sedimentation on salt marshes. *Geophysical Research Letters*, *47*(10), e2019GL086737. https://doi.org/10.1029/2019gl086737

Garrison, T. S. (2014). *Essentials of oceanography*. Cengage Learning.

George, D. A., Castelle, B., & Mulligan, R. P. (2022). Crossing the boundaries: How key advancements in understanding of headland sediment bypassing improves definition of littoral cells. *Journal of Geophysical Research: Oceans*, *127*(8), e2021JC018269. https://doi.org/10.1029/2021jc018269

George, D. A., Largier, J. L., Pasternack, G. B., Barnard, P. L., Storlazzi, C. D., & Erikson, L. H. (2019). Modeling sediment bypassing around idealized rocky headlands. *Journal of Marine Science and Engineering*, *7*(2), 40. https://doi.org/10.3390/jmse7020040

Goodwin, I. D., Freeman, R., & Blackmore, K. (2013). An insight into headland sand bypassing and wave climate variability from shoreface bathymetric change at Byron Bay, New South Wales, Australia. *Marine Geology*, *341*, 29–45. https://doi.org/10.1016/j.margeo.2013.05.005

Grant, W. D., & Madsen, O. S. (1979). Combined wave and current interaction with a rough bottom. *Journal of Geophysical Research*, *84*(C4), 1797–1808. https://doi.org/10.1029/jc084ic04p01797

Hallegatte, S., Green, C., Nicholls, R. J., & Corfee-Morlot, J. (2013). Future flood losses in major coastal cities. *Nature Climate Change*, *3*(9), 802–806. https://doi.org/10.1038/nclimate1979

Hallermeier, R. J. (1978). Uses for a calculated limit depth to beach erosion. In *Coastal engineering 1978* (pp. 1493–1512).

King, E. V., Conley, D. C., Masselink, G., Leonardi, N., McCarroll, R. J., Scott, T., & Valiente, N. G. (2021). Wave, tide and topographical controls on headland sand bypassing. *Journal of Geophysical Research: Oceans*, *126*(8), e2020JC017053. https://doi.org/10.1029/2020jc017053

Klein, A. H., da Silva, G. V., Taborda, R., da Silva, A. P., & Short, A. D. (2020). Headland bypassing and overpassing: Form, processes and applications. In *Sandy beach morphodynamics* (pp. 557–591).

Lesser, G. R., Roelvink, J. A., van Kester, J. A. T. M., & Stelling, G. S. (2004). Development and validation of a three-dimensional morphological model. *Coastal Engineering*, *51*(8–9), 883–915. https://doi.org/10.1016/j.coastaleng.2004.07.014

Limber, P. W., & Murray, A. B. (2011). Beach and sea-cliff dynamics as a driver of long-term rocky coastline evolution and stability. *Geology*, *39*(12), 1147–1150. https://doi.org/10.1130/g32315.1

Luijendijk, A., Hagenaars, G., Ranasinghe, R., Baart, F., Donchyts, G., & Aarninkhof, S. (2018). The state of the world's beaches. *Scientific Reports*, *8*(1), 1–11. https://doi.org/10.1038/s41598-018-24630-6

Marchesiello, P., Nguyen, N. M., Gratiot, N., Loisel, H., Anthony, E. J., San Dinh, C., et al. (2019). Erosion of the coastal Mekong delta: Assessing natural against man induced processes. *Continental Shelf Research*, *181*, 72–89. https://doi.org/10.1016/j.csr.2019.05.004

Masselink, G., Scott, T., Poate, T., Russell, P., Davidson, M., & Conley, D. (2016). The extreme 2013/2014 winter storms: Hydrodynamic forcing and coastal response along the southwest coast of England. *Earth Surface Processes and Landforms*, *41*(3), 378–391. https://doi.org/10.1002/esp.3836

McCarroll, R. J., Masselink, G., Valiente, N. G., Scott, T., King, E. V., & Conley, D. (2018). Wave and tidal controls on embayment circulation and headland bypassing for an exposed, macrotidal site. *Journal of Marine Science and Engineering*, *6*(3), 94. https://doi.org/10.3390/jmse6030094

McCarroll, R. J., Masselink, G., Valiente, N. G., Wiggins, M., Scott, T., Conley, D. C., & King, E. V. (2020). Impact of a headland-associated sandbank on shoreline dynamics. *Geomorphology*, *355*, 107065. https://doi.org/10.1016/j.geomorph.2020.107065

McCarroll, R. J., Masselink, G., Wiggins, M., Scott, T., Billson, O., Conley, D., & Valiente, N. (2019). High-efficiency gravel longshore sediment transport and headland bypassing over an extreme wave event. *Earth Surface Processes and Landforms*, *44*(13), 2720–2727. https://doi.org/10.1002/esp.4692

Mouragues, A., Bonneton, P., Castelle, B., Marieu, V., Jak McCarroll, R., Rodriguez-Padilla, I., et al. (2020). High-energy surf zone currents and headland rips at a geologically constrained mesotidal beach. *Journal of Geophysical Research: Oceans*, *125*(10), e2020JC016259. https://doi.org/10.1029/2020jc016259

Mulligan, R. P., Hay, A. E., & Bowen, A. J. (2008). Wave-driven circulation in a coastal bay during the landfall of a hurricane. *Journal of Geophysical Research*, *113*, C05026. https://doi.org/10.1029/2007jc004500

NDBC. (2023). Wind and wave data collected from National Data Buoy Center (Station No.: BUZM3 & 44085) [Dataset]. NDBC. Retrieved from https://www.ndbc.noaa.gov/

NOAA. (2023). Historical tidal level data retrieved from Newport tidal gauge under National Oceanic and Atmospheric Administration (Station No.:8452660) [Dataset]. NOAA. Retrieved from https://tidesandcurrents.noaa.gov/

Nyberg, B., & Howell, J. A. (2016). Global distribution of modern shallow marine shorelines. Implications for exploration and reservoir analogue studies. *Marine and Petroleum Geology*, *71*, 83–104. https://doi.org/10.1016/j.marpetgeo.2015.11.025

Peregrine, D. H. (1983). Breaking waves on beaches. *Annual Review of Fluid Mechanics*, *15*(1), 149–178. https://doi.org/10.1146/annurev.fl.15.010183.001053

Ramesh, R., Purvaja, R., Rajakumari, S., Suganya, G. M. D., Sarunjith, K. J., & Vel, A. S. (2021). Sediment cells and their dynamics along the coasts of India – A review. *Journal of Coastal Conservation*, *25*(2), 31. https://doi.org/10.1007/s11852-021-00799-3

Siegle, E., & Costa, M. B. (2017). Nearshore wave power increase on reef-shaped coasts due to sea-level rise. *Earth's Future*, *5*(10), 1054–1065. https://doi.org/10.1002/2017ef000624

Slott, J. M., Murray, A. B., Ashton, A. D., & Crowley, T. J. (2006). Coastline responses to changing storm patterns. *Geophysical Research Letters*, *33*, L18404. https://doi.org/10.1029/2006gl027445

Soulsby, R. L., Hamm, L., Klopman, G., Myrhaug, D., Simons, R. R., & Thomas, G. P. (1993). Wave-current interaction within and outside the bottom boundary layer. *Coastal Engineering*, *21*(1), 41–69. https://doi.org/10.1016/0378-3839(93)90045-a

Stockdonf, H. F., Sallenger, A. H., Jr., List, J. H., & Holman, R. A. (2002). Estimation of shoreline position and change using airborne topographic lidar data. *Journal of Coastal Research*, 502–513.

Swart, D. H. (1974). Offshore sediment transport and equilibrium beach profiles.

Sweet, W. V., Hamlington, B. D., Kopp, R. E., Weaver, C. P., Barnard, P. L., Bekaert, D., et al. (2022). *Global and regional sea level rise scenarios for the United States: Updated mean projections and extreme water level probabilities along US coastlines*. National Oceanic and Atmospheric Administration.

Thom, B. G., Eliot, I., Eliot, M., Harvey, N., Rissik, D., Sharples, C., et al. (2018). National sediment compartment framework for Australian coastal management. *Ocean & Coastal Management*, *154*, 103–120. https://doi.org/10.1016/j.ocecoaman.2018.01.001

Toimil, A., Camus, P., Losada, I., Le Cozannet, G., Nicholls, R., Idier, D., & Maspataud, A. (2020). Climate change-driven coastal erosion modelling in temperate sandy beaches: Methods and uncertainty treatment. *Earth-Science Reviews*, *202*, 103110. https://doi.org/10.1016/j.earscirev.2020.103110

USGS. (2023). Current water data for Massachusetts under United States Geological Survey [Dataset]. USGS. Retrieved from https://waterdata.usgs.gov/ma/nwis/rt

Valiente, N. G., Masselink, G., Scott, T., Conley, D., & McCarroll, R. J. (2019). Role of waves and tides on depth of closure and potential for headland bypassing. *Marine Geology*, *407*, 60–75. https://doi.org/10.1016/j.margeo.2018.10.009

van Rijn, L. C. (1998). Principles of coastal morphology.

van Rijn, L. C. (2011). Coastal erosion and control. *Ocean & Coastal Management*, *54*(12), 867–887. https://doi.org/10.1016/j.ocecoaman.2011.05.004

Vieira da Silva, G., Toldo, E. E., Jr., Klein, A. H. D. F., & Short, A. D. (2018). The influence of wave-wind- and tide-forced currents on headland sand bypassing – Study case: Santa Catarina Island north shore, Brazil. *Geomorphology*, *312*, 1–11. https://doi.org/10.1016/j.geomorph.2018.03.026

Wishaw, D., Leon, J. X., Barnes, M., & Fairweather, H. (2020). Tropical cyclone impacts on headland protected bay. *Geosciences*, *10*(5), 190. https://doi.org/10.3390/geosciences10050190

Xie, D. (2023). Model setup for a reference scenario and the hydrodynamic data around Western Buzzards Bay (v3) [Dataset]. Zenodo. https://doi.org/10.5281/zenodo.10621597

Xie, D., Schwarz, C., Brückner, M. Z. M., Kleinhans, M. G., Urrego, D. H., Zhou, Z., & van Maanen, B. (2020). Mangrove diversity loss under sea-level rise triggered by bio-morphodynamic feedbacks and anthropogenic pressures. *Environmental Research Letters*, *15*(11), 114033. https://doi.org/10.1088/1748-9326/abc122

Xie, D., Schwarz, C., Kleinhans, M. G., Zhou, Z., & van Maanen, B. (2022). Implications of coastal conditions and sea-level rise on mangrove vulnerability: A bio-morphodynamic modeling study. *Journal of Geophysical Research: Earth Surface*, *127*(3), e2021JF006301. https://doi.org/10.1029/2021jf006301

References From the Supporting Information

Brakenhoff, L., Schrijvershof, R., van der Werf, J., Grasmeijer, B., Ruessink, G., & van der Vegt, M. (2020). From ripples to large-scale sand transport: The effects of bedform-related roughness on hydrodynamics and sediment transport patterns in Delft3D. *Journal of Marine Science and Engineering*, *8*(11), 892. https://doi.org/10.3390/jmse8110892

CIRES. (2014). *Cooperative Institute for Research in Environmental Sciences (CIRES) at the University of Colorado, Boulder. Continuously Updated Digital Elevation Model (CUDEM) - 1/9 arc-second resolution bathymetric-topographic tiles*. NOAA National Centers for Environmental Information.

Dean, R. G., & Dalrymple, R. A. (2004). *Coastal processes with engineering applications*. Cambridge University Press.

Marsooli, R., & Lin, N. (2018). Numerical modeling of historical storm tides and waves and their interactions along the US East and Gulf Coasts. *Journal of Geophysical Research: Oceans*, *123*(5), 3844–3874. https://doi.org/10.1029/2017jc013434

Warner, J. C., Geyer, W. R., & Lerczak, J. A. (2005). Numerical modeling of an estuary: A comprehensive skill assessment. *Journal of Geophysical Research*, *110*, C05001. https://doi.org/10.1029/2004jc002691

Willmott, C. J. (1981). On the validation of models. *Physical Geography*, *2*(2), 184–194. https://doi.org/10.1080/02723646.1981.10642213

Xie, D., Schwarz, C., Kleinhans, M. G., Bryan, K. R., Coco, G., Hunt, S., & van Maanen, B. (2023). Mangrove removal exacerbates estuarine infilling through landscape-scale bio-morphodynamic feedbacks. *Nature Communications*, *14*(1), 7310. https://doi.org/10.1038/s41467-023-42733-1

Zhu, Q., & Wiberg, P. L. (2022). The importance of storm surge for sediment delivery to microtidal marshes. *Journal of Geophysical Research: Earth Surface*, *127*(9), e2022JF006612. https://doi.org/10.1029/2022jf006612

Headland bypassing: Moderate storms dominate extreme events

Silke Tas[1,2], Zoe Hughes[1], Duncan FitzGerald[1], Danghan Xie[1], Tansir Zaman Asik[1], Sergio Fagherazzi[1]

[1]Department of Earth and Environment, Boston University, Boston, MA, USA
[2]Hydrology and Environmental Hydraulics, Wageningen University and Research, Wageningen, The Netherlands

Key Points:

- The sediment budget of an embayment is driven by frequent, moderate bypassing events rather than rare extreme events
- Tides can influence headland bypassing even in a microtidal regime
- Climate change can have a dual impact on headland bypassing, either increasing or decreasing transport rates

Corresponding author: Silke Tas, `silke.tas@wur.nl`

Abstract

Natural headlands form obstacles to longshore sediment transport between neighbouring coastal cells. Sediment connectivity around headlands only occurs for certain wave and tidal conditions. This study investigates the thresholds and pathways for sediment transport into Slocums Embayment, an enclosed bay situated at the mouth of Buzzards Bay, Massachusetts, USA. The embayment is isolated from the surrounding shoreline by two headlands. A numerical model is validated with field observations and sediment volumes estimated from LIDAR images. Modelling reveals that Slocums Embayment is a completely closed coastal cell under regular conditions, only receiving sediment during storms (return period ¿ 1 year). The cumulative effect of less intense but more frequent storms (once per 1 or 2 years) outweighs the higher rates of sediment transported during the most extreme events. Despite the microtidal regime, tidal currents, possibly enhanced by storm surges that fill and empty Buzzards Bay, heavily influence the total volume of sediment deposited inside Slocums Embayment. The impact of climate change on these sediment pathways is twofold: more frequent or larger wave events increase the sediment volumes deposited inside the embayment, while sea-level rise and higher surge levels reduce the availability of offshore sediment for transport. These findings have important implications for coastal management and the prediction of long-term coastal change, as it shifts the focus from the rare, extreme events to the more frequent, moderate events. Understanding the exact thresholds for sediment bypassing, and their associated occurrence probabilities, is key for robust sediment budget calculations.

Plain Language Summary

Headlands are irregular, mostly rocky features that protrude into the sea and become obstacles for the movement of sand along the coast. This study looks at Slocums Embayment, a small, enclosed bay in Buzzards Bay, Massachusetts, USA. Using a computer model and real-world data, we find that, under normal wave conditions, little sand is moved into Slocums Embayment, the process only occurs during high wave conditions that happen once a year or less frequently. Interestingly, even though large waves move more sand, the combined effect of smaller storms that happen often (once every 1 or 2 years) results in more sand moved into the bay. Tidal currents, sometimes together with storm surges, have a major impact on the total amount of sediment moved into Slocums Embayment. Climate change could lead to larger and more frequent storms, which can move more sand into the bay, but rising sea levels might limit how much sand can be picked up from the seabed. These findings are important for managing coastal areas and predicting how coastlines will change over time. Instead of only focusing on rare, extreme events, this research highlights the importance of more frequent, smaller events.

1 Introduction

Approximately half of the world's coastlines are characterised by rocky headlands and embayments (King et al., 2021), exhibiting high ecological, recreational, and commercial value. The sheltering effect of these headlands creates ideal conditions for harbors and pocket beaches. Sediment along irregular shorelines is often trapped between headlands, forming pocket beaches and embayments (Short & Masselink, 1999). In addition to small sediment inputs from possible rivers and reworking of glacial deposits and eroding cliffs, the sediment budget of these coastal cells is a function of headland bypassing (Valiente et al., 2019). Understanding headland bypassing is therefore crucial for robust sediment budget calculations, and hence valuable knowledge for coastal management and predicting long-term coastal change (da Silva et al., 2023; Woodroffe et al., 2022; R. J. McCarroll et al., 2021; Wishaw et al., 2021; Valiente et al., 2019; Cooper et al., 2002; Motyka & Brampton, 1993).

Under most conditions, headlands block sediment transport between neighbouring coastal cells, and transport around them occurs only under certain wave and tidal conditions (Klein et al., 2020; Valiente et al., 2019; Short & Masselink, 1999). Sediment connectivity, i.e. the pathways and thresholds for sediment transport between littoral cells, has been the topic of many studies: for an overview of more than 40 headland bypassing studies see Klein et al. (2020). Despite several efforts to develop conceptual models, e.g., R. J. McCarroll et al. (2021); D. George et al. (2015); Short and Masselink (1999), local studies are still necessary to determine the exact sediment transport thresholds and pathways in and out of most embayments R. McCarroll et al. (2019); Wishaw et al. (2021).

In this paper, thresholds and pathways for sediment transport around headlands are investigated, using Slocums Embayment as a case study. Slocums Embayment is an enclosed bay situated at the mouth of Buzzards Bay, Massachusetts, USA. A numerical model, validated with field observations and sediment volumes estimated from LIDAR images, is used to study a range of idealised and realistic storm scenarios, and their impact on the sediment budget of an enclosed embayment.

2 Methods

Sediment transport in the vicinity of Slocums Embayment is explored using a coupled Delft3D-FLOW/ WAVE model. Delft3D-FLOW solves the unsteady shallow water equations (Lesser et al., 2004) and Delft3D-WAVE uses the third-generation numerical wave model SWAN (Booij et al., 1999). Delft3D has been successfully used for sediment transport simulations around headlands (Vieira da Silva et al., 2016; R. McCarroll et al., 2018; D. A. George et al., 2019). A full description and validation of the model set-up can be found in Xie et al. (2024). A short description of the model set-up, validation and run scenarios is provided below. Model boundary conditions are derived from the North Atlantic Coast Comprehensive Study (NACCS), a coastal storm wave and water level modelling study of the US North Atlantic coast (Cialone et al., 2005). Sediment volume changes of the spit at the Slocums River Inlet based on a series of LIDAR DEMs were used to validate the modelled sediment transport.

2.1 Study Area

Northwestern Buzzards Bay in Massachusetts, USA (Figure 1a), is a complex coastal system consisting of multiple headlands, producing several coastal cells containing tidal inlets and mixed-sediment beaches. While these compartments form mostly closed sediment cells during regular wave conditions, high-energy events like severe winter storms or rare tropical storms can generate sediment pulses past headlands (FitzGerald et al., 1992). Near the mouth of Buzzards Bay, Slocums River Embayment is delimited by Mishaum Point to the east and Barneys Joy Point to the west (see Figure 1b). The embayment shoreline is dominated by gravel and bedrock, except on the inner western side of Slocums River inlet, where sandy beaches, a spit and a series of beach ridges are present. The beach ridges represent historic positions of the shoreline, as it progressed seaward. Aerial images covering the last 30 years (1991-2021, Figure 1c-f) show a dynamic spit system gradually accumulating sand. Since Slocums River drains a small basin, and has a small discharge of ca. 5 m^3/s (US Geological Survey, 2023a), the sediment accumulating near Slocums River inlet is likely marine in origin, entering the embayment via headland bypassing. The Paskamanset/Slocums River (the freshwater portion of Slocums River maintained its Native American name (US Geological Survey, 1984)) has been heavily polluted in the past. A landfill near Dartmouth, responsible for most of the pollution, has been capped off to prevent run-off into the river (Moraff & United States Environmental Protection

Agency, 2019). Local communities are worried that further water quality issues may occur as a result of the sediment accumulating near the river inlet triggering a reduction in tidal flushing. Predicting the future sedimentation around the inlet requires a better grasp of the sources and pathways of sediment transport into Slocums Embayment and an improved understanding of headland bypassing thresholds; this is the focus of this study.

At the mouth of Buzzards Bay, the tidal regime is semi-diurnal and microtidal, with a tidal range between 0.7-1.3 m (neap and spring tides respectively, NOAA (2023)). Offshore, the average wave height is approximately 1.0 m with a peak wave period of 7.1 s (NDBC, 2023). The shoreline is only exposed to waves approaching from the south to southwest. Due to the low wave and tidal energy, it has generally been assumed that infrequent, large-magnitude events (hurricanes) may have a large impact on the overall sediment transport patterns in the embayment (FitzGerald et al., 1992).

Previous studies in this area were mostly qualitative or focused on individual coastal cells (FitzGerald et al., 1986, 1992). This research aims to map pathways and quantify thresholds for headland bypassing around Barneys Joy Point into Slocums River Embayment, using a combined approach of numerical modelling (Xie et al., 2024), field observations, and remote sensing.

2.2 Model set-up

For this study, two separate grids were developed: a larger one for the WAVE calculations (dashed line in Figure 2), and a smaller FLOW grid nested inside the WAVE domain (solid line in Figure 2). The southern boundary of the WAVE domain is located offshore to avoid strong bed level gradients at the boundary and to avoid any sheltering effects of the nearby islands. Its position was chosen close to output point 9740 of the NACCS model (green square marker in Figure 2), facilitating the use of NACCS results as input to our simulations. The lateral boundaries of the WAVE domain were selected so that wave shadow zones would not affect the region of interest around Slocums Embayment. Grid cell size varies from 80 m near the boundaries to 40 m in the region of interest.

The FLOW domain was extended far enough south to capture flow into and out of Buzzards Bay. The lateral boundaries extend slightly beyond the region of interest, and the northern boundary allows for the inclusion of a reasonable tidal prism inside the Slocums

Figure 1. **(a)** Location of the area of interest in Northwestern Buzzards Bay, South Massachusetts, USA. The red rectangle indicates the location of panel b. **(b)** Slocums Embayment at the mouth of Buzzards Bay, bounded by two headlands: Barneys Joy Point and Mishaum Point. West of Barneys Joy Point is Allens Beach and Allens Pond. The red rectangle indicates the location of panels c-f. **(c-f)** Temporal evolution of the spit at Slocums River inlet, in 1991, 2001, 2012 and 2021 (Google Earth, 2023).

and Westport Rivers. Along the southern boundary, a water level is prescribed based on the water level at output point 9088 in the NACCS ADCIRC model. A velocity boundary condition is applied to the eastern and western FLOW domain boundaries, based on linear interpolation between NACCS output points 10414, 1219, 9143, 1003, 9086, 1275,

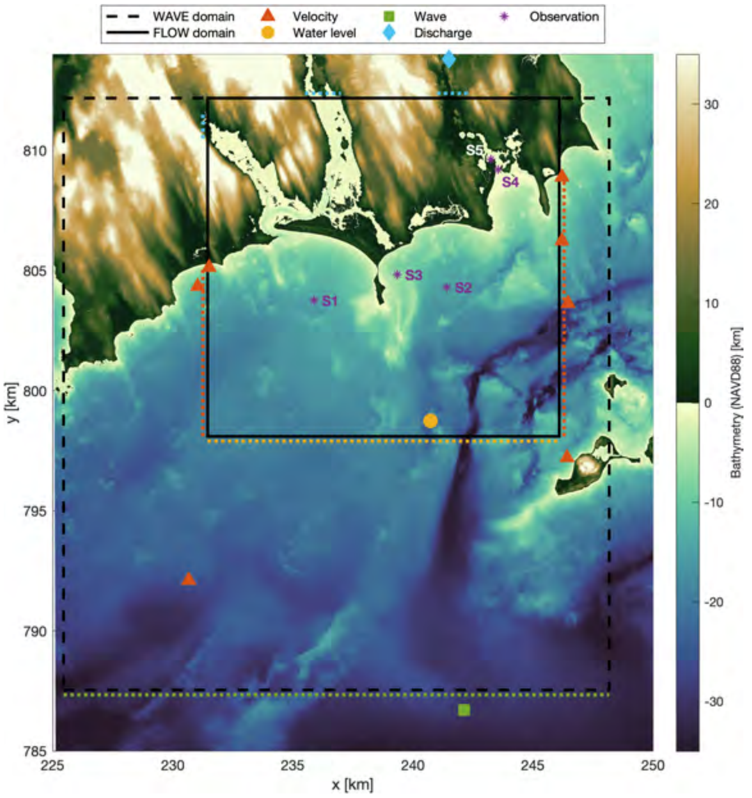

Figure 2. Delft3D model domains for WAVE (dashed black rectangle) and FLOW (solid black rectangle). The NACCS output points (Cialone et al., 2005) that serve as boundary conditions are indicated by the markers, with the color representing the type of output (orange triangles: velocity, yellow dot: water level, green squares: waves and wind). Measuring stations (S1-S5) are visualised with purple asterisks.

8967 (counterclockwise, starting along the west boundary). The model was run in depth-averaged mode.

The bathymetry is based on the Continuously Updated Digital Elevation Model (CIRES, 2014; Amante et al., 2023). This bathymetry was validated with point measurements collected in September 2022 (see Figure S1). The boundary conditions for the scenario runs are based on annual exceedance probability curves for wave heights and water levels from NACCS, see Table 1. The river discharge boundary conditions used in the analysis are based on a stream gauge located in Paskamanset River (gauge 01105933, US Geological Survey (2023a).

A single sediment fraction is included in the model, medium sand with a D50 of 350 μm, based on sediment samples (see dots in Figure 3a, as well as Text S2 and Folk (1966)).

The spatial distribution of sediment in the model domain is based on a sediment texture map by Foster et al. (2016). All patches that contained predominantly sand were included as sandy patches in the model (see blue colors in Figure 3a). The sand coverage derived from this map was checked against our field samples and an alternative method developed by King et al. (2021), using the smoothness of a high-resolution bathymetry as an indicator of loose sediment (see SupText S2). In our model, the sand was divided into 5 geographic zones, allowing us to determine the source of the sediment deposited inside Slocums Embayment. The first zone is Allens Beach (yellow patch in Figure 3b), which includes the intertidal beach and supratidal dunes east and west of Allens Pond inlet. Towards the headlands on each side, the beach composition changes to gravel; the extent of the sandy patch in the model is based on field observations and sediment samples. The second zone is the nearshore area in front of Allens Pond (orange patch in Figure 3b), surrounded by patches of bedrock. The third zone (pink) represents the sediment inside Slocums Embayment, delimited by Barneys Joy Point on the west and Mishaum Point on the east. The offshore sediment is divided into a westerly (magenta) and easterly (purple) zone, separated by a bedrock outcrop south of Barneys Joy Point. The sediment thickness of the 4 submerged sediment zones is set to 2 m, while the sediment thickness of the Allens Beach patch is set to 0.5 m.

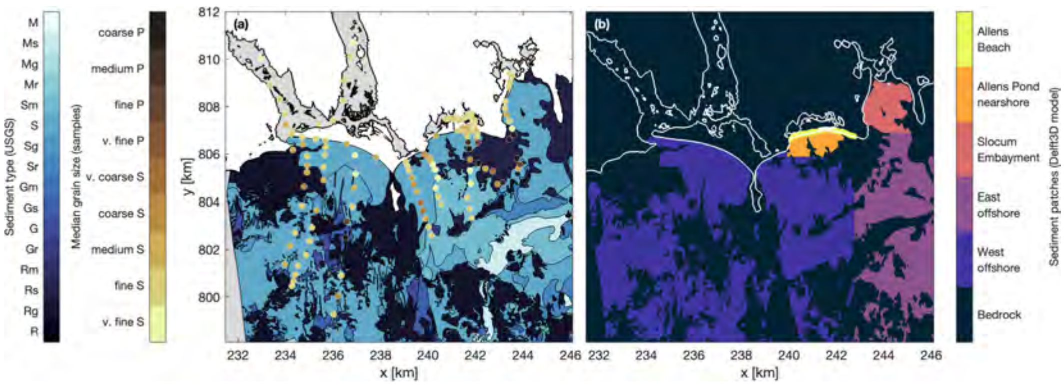

Figure 3. **(a)** Sediment type based on USGS sediment texture map of Buzzards Bay (Foster et al. (2016), in blue shades). Median grain size based on sediment samples from this study in yellow-brown dots. **(b)** Sediment zones implemented in the model. Darkest color is bedrock (i.e., no sediment available in the model), all other zones contain medium sand.

2.3 Model scenarios

Different wave and water level conditions are explored through multiple idealised model scenarios. The peak wave height and wind speed for four return periods (1, 2, 10 and 50 years) are derived from the annual exceedance probability curves at NACCS output point 9740, near the offshore WAVE boundary (green marker in Figure 2). The wave period corresponding to each wave height is calculated using a linear relationship between wave height and wave period at the offshore NACCS output location (green square in Figure 2), based on 100 storms reported in the NACCS database. The wave and wind conditions are kept constant throughout each simulation.

Return period [yr]	H_s [m]	T_p [s]	u_{10} [m/s]
1	4.7	11.6	12.8
2	6.2	12.3	15.9
10	9.5	13.8	22.6
50	12.4	15.1	28.6

Table 1. Offshore peak wave and wind conditions for storms with different return periods (based on NACCS exceedance probability curves, Cialone et al. (2005)).

Due to the orientation of the coastline and the presence of offshore islands (see Figure 2), our project area is only exposed to waves coming from south to southwest. Therefore, only three wave directions are considered in the simulations: 180°, 210°and 240°. Three water level scenarios are developed to assess the influence of tides and storms: constant water level (MSL, no tide or storm surge), tide-only and tide + storm surge. The latter two scenarios are derived from a NACCS storm time series. Combining 4 storm strengths, 3 wave directions and 3 water level scenarios results in 36 model scenarios (Table 2). In each scenario, the wave and wind conditions are constant in time and space, only the water level varies in the tide-only and tide + storm surge simulations. This approach allows us to isolate the impact of each storm characteristic (wave height, direction and surge) on headland bypassing. In addition to these 36 idealised storm scenarios, two additional scenarios were simulated: an idealised non-storm, low-wave scenario which occurs multiple times per year ($H_S = 1.5$ m), and a realistic storm scenario.

Storm return periods [yr]	1, 2, 10, 50
Wave direction [°]	180, 210, 240
Water level	MSL, tide-only, tide + surge

Table 2. Overview of the 36 model scenarios with all possible combinations of storm return period (4), wave direction (3) and water level (3) scenario. Wave direction is defined according to the nautical convention (180° waves are coming from the south).

2.4 Model validation

Observations at 5 locations in the model domain (stations S1-S5 in Figure 2) were recorded between October and December 2022, using the following instruments: 1. Acoustic Doppler Current Profiler (ADCP) with wave gauge (stations S1 and S2), 2. wave gauge (S3), 3. ADCP (S4), and 4. pressure sensor (S5). For model validation, a period coincident with a higher wave energy was selected: 8-15 November 2022 (see Figure S4). The comparison between modelled and observed values was quantified by using the skill score as proposed by Willmott (1981) (see Text S3).

Measured and simulated water levels and wave conditions compared well. The velocity magnitude was of the correct order of magnitude and showed similar trends, despite having a relatively low skill score. However, the modelled velocity direction at S1 (and S2 in December) lacks the distinct tidal signature of the observations. Note that for these validation model runs, we did not use inputs for the east and west boundaries of the FLOW domain; we instead adopted Neumann boundary conditions. Therefore, these runs do not include the effect of the tide filling and emptying Buzzards Bay, which explains the strong tidal signal in the observed velocities.

For the extreme storm scenarios in this study, boundary conditions (including velocities at the east and west boundaries of the FLOW domain) were derived from the NACCS study. Xie et al. (2024) compared the output of our model with several NACCS output points located in our model domain and showed good agreement.

3 Results

3.1 Net sediment transport volume estimate from LIDAR

Aerial images dating back to 1938 suggest that Slocums inlet has gained sediment. However, it is only since 2005 that LIDAR data allow us to quantify the sediment volume change around Slocums inlet (OCM Partners, 2009, 2010, 2013, 2015b, 2018). The earlier LIDAR-derived DEMs stopped at the water surface, and therefore were taken around low tide to include as much as possible of the emerged part of the spit. To allow consistent comparison with these older data sets, the lowest elevation that was included in all LIDAR DEMs was -0.4 m NAVD88 (MLW is -0.58 m NAVD88, NOAA (2023)). The images were corrected for differences in Geoid used for processing the raw data (see Text S4). The western side of the river inlet was divided into 4 polygons (see Figure S5), and for each LIDAR DEM, the volume above -0.4 m NAVD88 was calculated (see Figure 4).

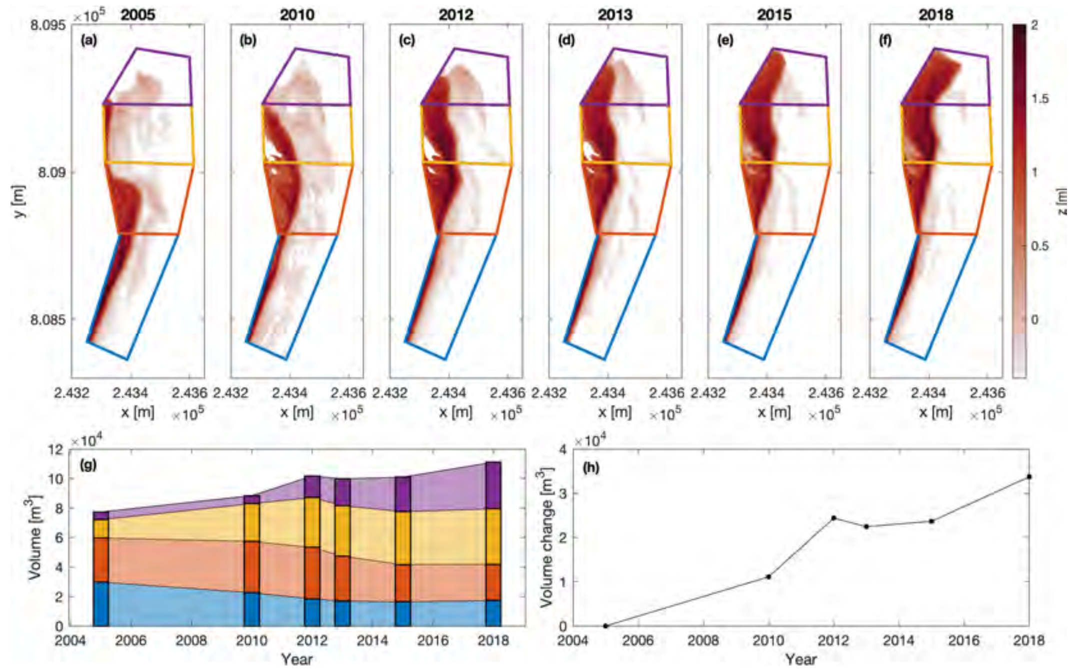

Figure 4. **(a-f)** Evolution of the spit volume near the inlet of Slocums River between 2005 and 2018, based on LIDAR (see Figure 1 for the location of the spit), **(g)** total volume of the spit above -0.4m NAVD88, separated in four sub-volumes along the shore (see panels a-f for division subvolumes), and **(h)** total volume change of the spit compared to initial volume in 2005.

Figure 4a-f shows that a pulse of sediment has moved north along the shoreline between 2005 and 2018, accumulating in the northernmost polygon. This is also confirmed by the volume of each subpolygon in Figure 4g. Initially, the two southern polygons (blue and orange) contained most sediment, gradually losing material to the northern polygons (yellow and purple). The last two LIDAR images show that only the northern polygon is still gaining sediment, while the three southern polygons maintain a stable volume. Over a period of 13 years, the spit system gained a volume of ca. 33700 m^3 (Figure 4h), with an average gain of approximately 2600 m^3/year.

3.2 Threshold for sediment transport into Slocums Embayment

Figure 5 shows the currents (vector field) and maximum bed shear stresses (colormap) at 4 different time steps over the tidal cycle (columns) for 3 different wave conditions (rows). The first row represents a tide-only scenario, the middle row a non-storm, low-wave scenario ($H_s = 1.5$m), which occurs multiple times per year and the bottom row represents wave conditions occurring once every 10 years (see Table 1).
For tide-only and low-wave conditions (top two rows in Figure 5, panels a-h), the flow completely bypasses Slocums Embayment, and the bed shear stresses are too low within most of the domain to suspend sediment (default critical bed shear stress for erosion in Delft3D is 0.5 N/m^2). The current patterns are similar for the tide-only and low-wave scenarios, which implies that, under relatively calm conditions, the currents are dominated by the tidal filling and emptying of Buzzards Bay. It is only under storm conditions (bottom row Figure 5, panel i-l) that the flow curves around Barneys Joy Point, opening a pathway for sediment transport into Slocums Embayment. This confirms that sediment transport into Slocums Embayment is event-driven and only occurs during storms, when the wave-driven currents are large enough to modify the tidal flow in and out of Buzzards Bay.

3.3 Scenario analysis

The 36 scenarios are run for 72 hours, of which the first 24 hours are morphostatic spin-up, followed by 48 hours of morphodynamic simulation. Figure 6 shows the resulting sediment fluxes (vector field) and bed level changes (colormap) for the tide-only scenarios (4 storm strengths, columns, and 3 wave directions, rows). Most of the sediment transported into the embayment during a storm is deposited just around the headland.

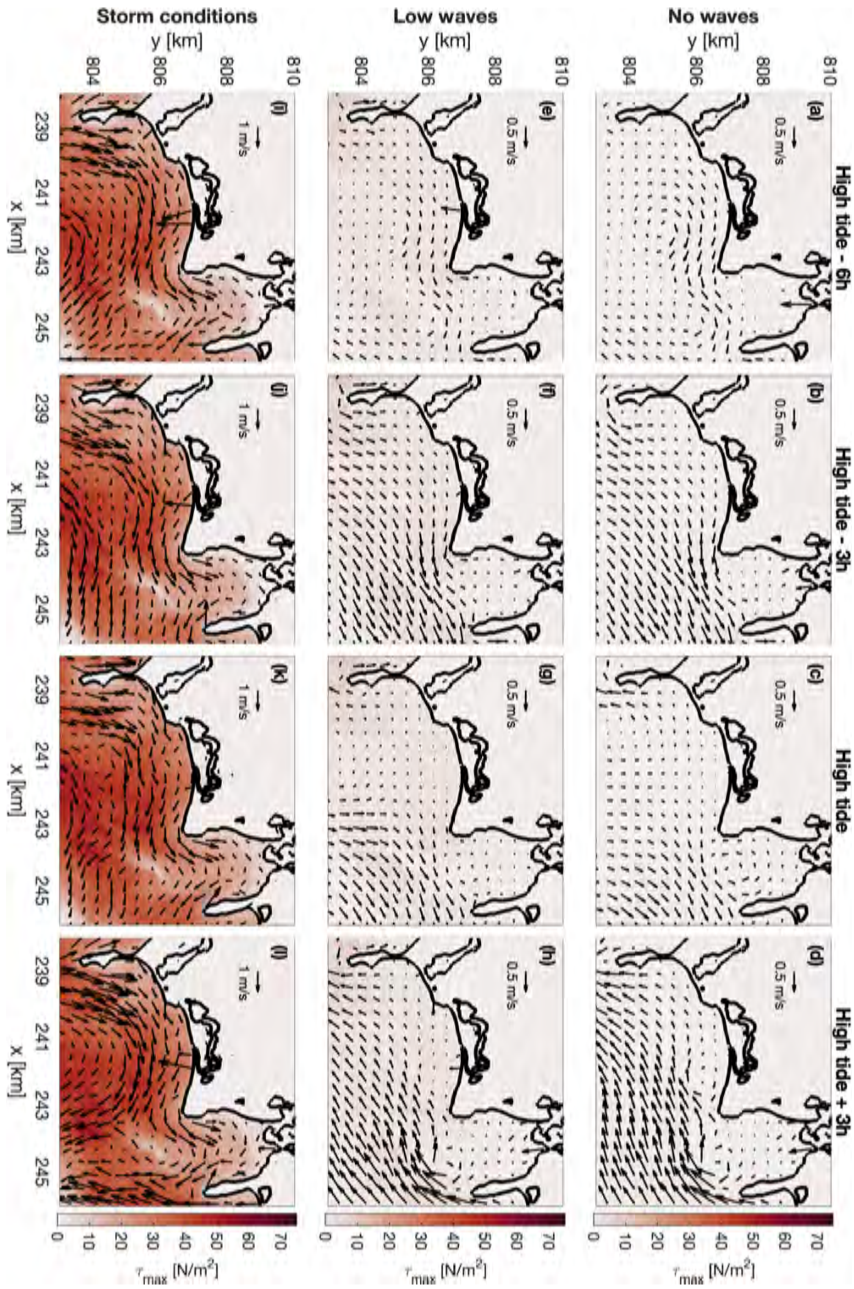

Figure 5. Current patterns (vector field) and maximum bed shear stress (colormap) under 3 different wave conditions. (a-d) Tide-only, (e-h) low-wave scenario ($H_s = 1.5$ m), and (i-l) 1 in 10-year wave conditions ($H_s = 9.5$ m). The columns show different time steps in the tidal cycle: from 6 hours before high tide to 3 hours after high tide.

The volume of sediment deposited near the headland increases with wave height, and is lowest for waves coming from the south (180°, top row in Figure 6).
While sustained peak storm conditions lasting 48 hours are highly unlikely, this approach was adopted such that the tide-only and tide + storm surge scenarios could be compared

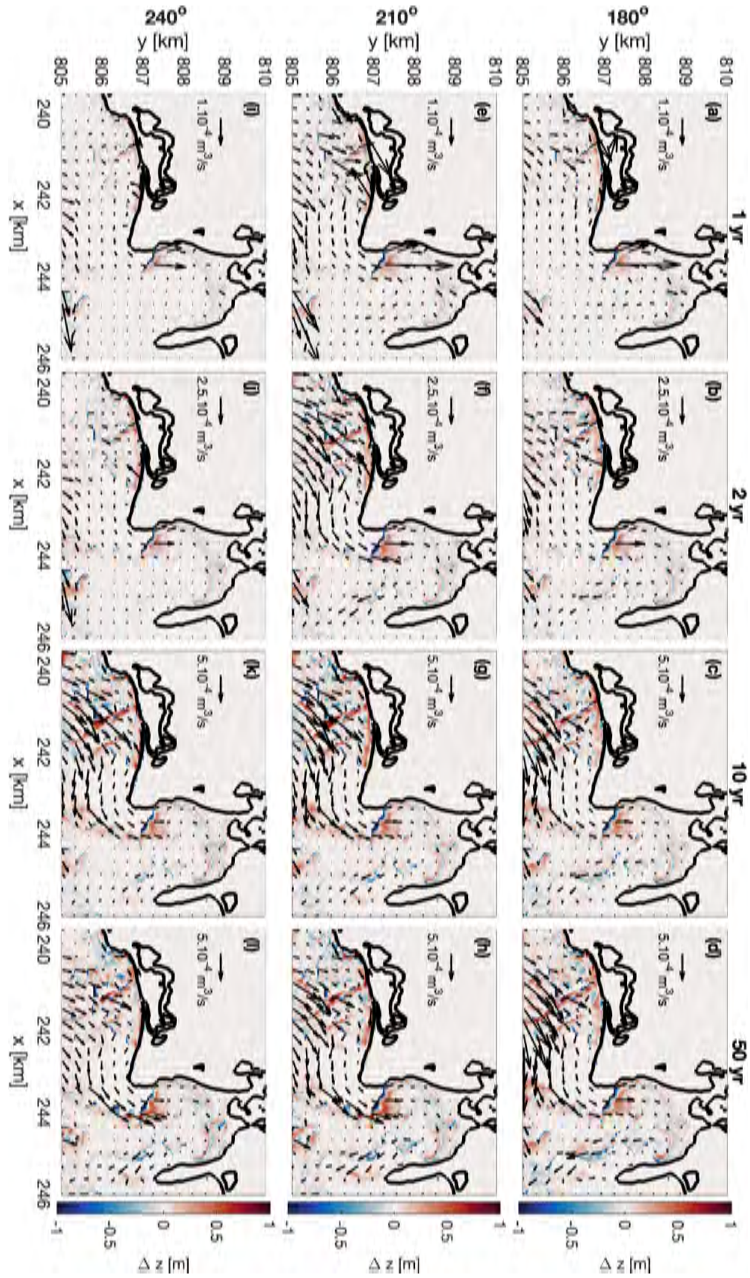

Figure 6. Residual sediment fluxes (vector field) and bed level changes (colormap) under different wave conditions. The columns show different return periods of the wave height and wind speed (ranging from 1 to 50 years). The rows represent different wave directions (180°, 210°, and 240°). For clarity, the vector scale changes among wave conditions, see arrow in top left corner of each panel.

to the constant water level scenario. At the end of each scenario, the change in sediment volume inside Slocums Embayment is calculated, where Slocums Embayment is delineated by a fictional line between the headlands of Barneys Joy Point and Mishaum Point (following the same line that separates the sediment fractions of Slocums Embayment and East offshore in Figure 3). This sediment volume is then divided by the duration of the storm (48 hours) to obtain an average hourly net sediment transport, see Equation 1:

$$Q_i = \frac{\Delta V_{Slocums}}{\Delta t_{storm}} \tag{1}$$

Where Q_i is the average hourly net transport rate [m^3/hr], $\Delta V_{Slocums}$ is the total sediment volume change inside Slocums Embayment [m^3] and Δt_{storm} is the storm duration [hr].

In Figure 7 the average hourly net transport is plotted for each scenario, with the wave height on the horizontal axis (and the corresponding return period on the secondary horizontal axis at the top of the figure).

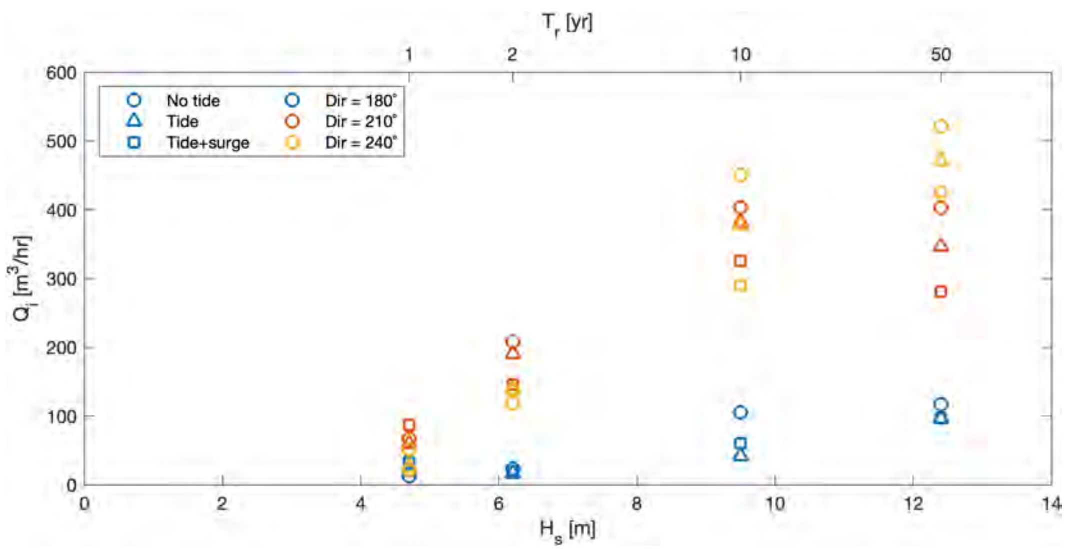

Figure 7. Average hourly net sediment transport (Q_i) into Slocums Embayment for all 36 scenarios. The bottom horizontal axis gives the peak wave height (H_s) of each scenario, the top horizontal axis the corresponding return period (T_r). The symbols represent water level scenarios and the colors wave direction.

Higher waves generate more net transport into the embayment, although this relationship is weaker for waves coming from the south (180°, blue markers). For the lower wave heights, a wave direction of 210°generates the highest net transport, however for extreme storms the westerly waves generate more net transport. While the gross transport into the embayment increases with wave height for all wave directions, a transport pathway out of the embayment opens up for higher waves coming from 210°, reducing the net transport in these scenarios (see Figure 8).

In almost every combination of wave height and direction, there is less net transport for the tide-only scenario than the constant water level scenario. First, due to the modulating effect of varying water levels, and second, because some of the sediment entering the embayment is only passing through due to the strong tidal currents. Only in the lowest wave height scenario do the tide + storm surge scenario generates more transport than the scenarios without storm surge. However it should be noted that in these hypothetical scenarios, the wave height is constant in time. In reality, the timing of the peak wave conditions with respect to the surge will have a significant impact on sediment transport, resulting in higher or lower net transport volumes.

Although larger waves transport more sediment, the recurrence of these conditions decreases with increasing storm magnitude, as seen in Figure 7 (secondary x-axis). Consequently, a cumulative transport rate was calculated, which incorporates the hourly net transport rate and the annual exceedance probability of the corresponding wave conditions, see Equation 2:

$$Q_c = \frac{\Delta V_{Slocums}}{\Delta t_{storm} * T_r} \tag{2}$$

Where Q_c is the cumulative transport rate [m^3/hr/yr] and T_r is the return period of the wave conditions [yr].

Figure 8a shows that a storm with a return period of 2 years and wave direction 210° is responsible for most net sediment transport into the embayment over longer time scales. While the 1 in 50-year wave conditions will generate most net transport per hour, these conditions are so rare that their total contribution to sediment deposition inside Slocums Embayment is minor. Note that a positive sediment transport rate indicates sediment import into Slocums Embayment, whereas the negative values in Figure 8d correspond to sediment export. However, these rates of sediment loss never exceed the total sediment import from the other regions, thus leading to net positive transports for all scenarios.

The sediment in Slocums Embayment at the end of each 48-hour storm simulation is traced back to its region of origin (Figure 8b-f). Even though Allens Beach and the nearshore area of Allens Pond represent only a small portion of the entire model domain, together they are responsible for more than half of the sediment that ends up in Slocums Embayment. Allens Beach provides the most sediment under westerly waves in scenarios with

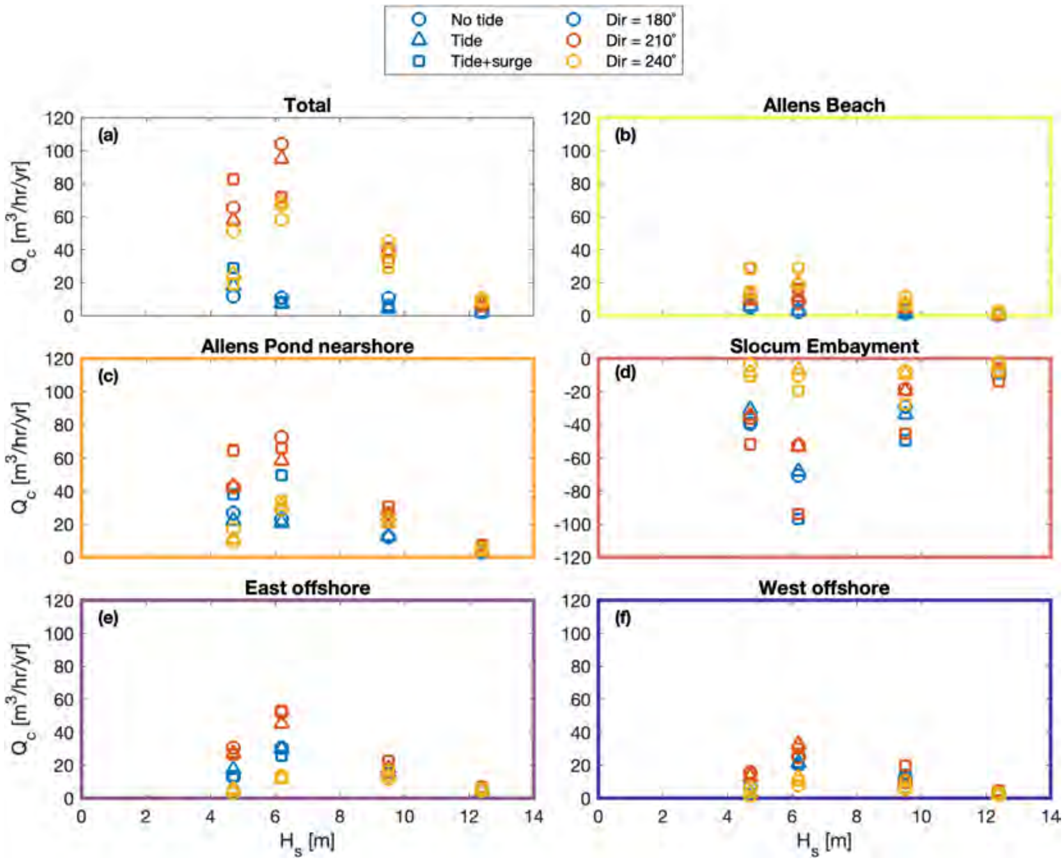

Figure 8. Cumulative transport rate, i.e. the average hourly net sediment transport divided by the return period (see Equation 2). The sediment volume change inside Slocums Embayment **(a)** is split up into the contributions of each region of origin **(b-f)**, the colored outlines corresponding to the patches in Figure 3b. The shapes represent water level scenarios and the colors wave directions.

surge, since the westerly waves generate the strongest longshore currents and the surge allows the waves to erode sediment from the upper beach and dune foot. The largest contributions from the Allens Pond nearshore zone occur for a wave direction of 210°, because although 240°generates the strongest longshore currents, Gooseberry Island shelters the more westerly waves, resulting in lower wave heights nearshore, and therefore less erosion.

3.4 Realistic storm scenario

The previous model scenarios considered time-varying water levels but constant wave conditions. However, during real storms the timing of peak wave conditions relative to the timing of the storm surge and tide varies, which can significantly affect sediment transport. Therefore, we also modelled a more realistic storm scenario. We selected a representative storm from the NACCS dataset of hypothetical hurricanes, whose storm track follows a path similar to the 1938 hurricane (NACCS track 78, storm 492, Cialone et al. (2005)). The 1938 hurricane significantly impacted the area and is the storm of record for the southeastern coast of Connecticut, Rhode Island, and Western Buzzards Bay. The hypothetical hurricane has a peak wave height of 9 m and peak storm surge levels of 3.5 m above MSL, see Figure 9a. Peak wave conditions occurred after the peak water levels. Figure 9b shows the instantaneous sediment volume change inside Slocums Embayment (dashed line), divided into the contributions of each sediment region (different colors). Figure 9c gives the cumulative volume change inside the embayment.

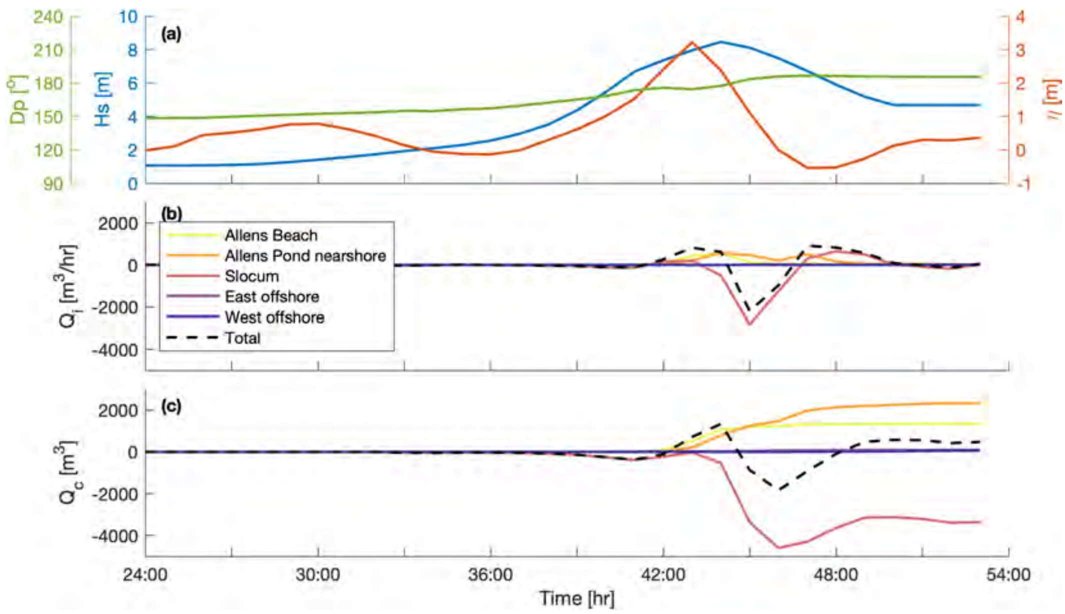

Figure 9. **(a)** Left y-axes: wave height (blue) and wave direction (green), right axis: water level (orange) during a NACCS hypothetical hurricane. Instantaneous **(b)** and cumulative **(c)** sediment volume change inside Slocums Embayment (dashed black line) and split up into the contributions of each region of origin (same colours as in Figures 3b and 8).

The net effect of the storm is a deposition of 1000 m^3, most of this sediment was eroded from Allens Beach and Allens Pond nearshore. The pink line shows that during the peak of the storm surge, the conditions inside the embayment are energetic enough to erode sediment, which is then exported out of the embayment. In fact, around t = 45 hours, there is a strong sediment flux out of the embayment, due to a combination of high wave energy and ebb tide.

4 Discussion

Traditionally, the sediment budget of enclosed embayments has often been treated as a closed coastal cell (van Rijn, 2010; Hsu & Evans, 1989). Over the last 30 years, an increasing number of studies have described processes of headland bypassing (Short & Masselink, 1999; Smith, 2001; Goodwin et al., 2013; Ribeiro et al., 2014; Duarte et al., 2014; bin Ab Razak, 2015; Vieira da Silva et al., 2016). These studies have focused on identifying the conditions producing headland bypassing, which generally occurs during extreme events. The current study, however, reveals that sediment transport into Slocums Embayment is dominated by small volumes transported during frequent storms (occurring every 1-5 years), rather than the larger volume moved into the embayment during rare extreme events, as illustrated in Figure 10a-b. King et al. (2021) modelled bypassing rates around 29 headlands in Cornwall, UK under various wave and tide conditions. Combining these bypassing rates and their corresponding exceedance probabilities (see Text S5) allowed us to test whether the sediment budget of enclosed embayments are driven by moderate rather than extreme conditions, see Table 3.

Scenario	Number	Percentage
Total scenarios	348	100%
Scenarios with sediment transport around headland	311/348	89%
Bypassing under large and extreme waves (no bypassing median waves)	119/311	38%
Most instantaneous bypassing under extreme waves	116/119	97%
Most cumulative bypassing under large waves	90/116	78%

Table 3. Analysis of the headland bypassing rates calculated by King et al. (2021), see also Text S5.

King et al. (2021) calculated headland bypassing rates for three wave conditions: median waves (wave height exceeded 50% of the time), large waves (exceedance probability 5%) and extreme waves (exceedance probability 0.14%). These 3 wave conditions were applied to 348 different scenarios (29 headlands, 2 water levels, 3 wave directions, wave-

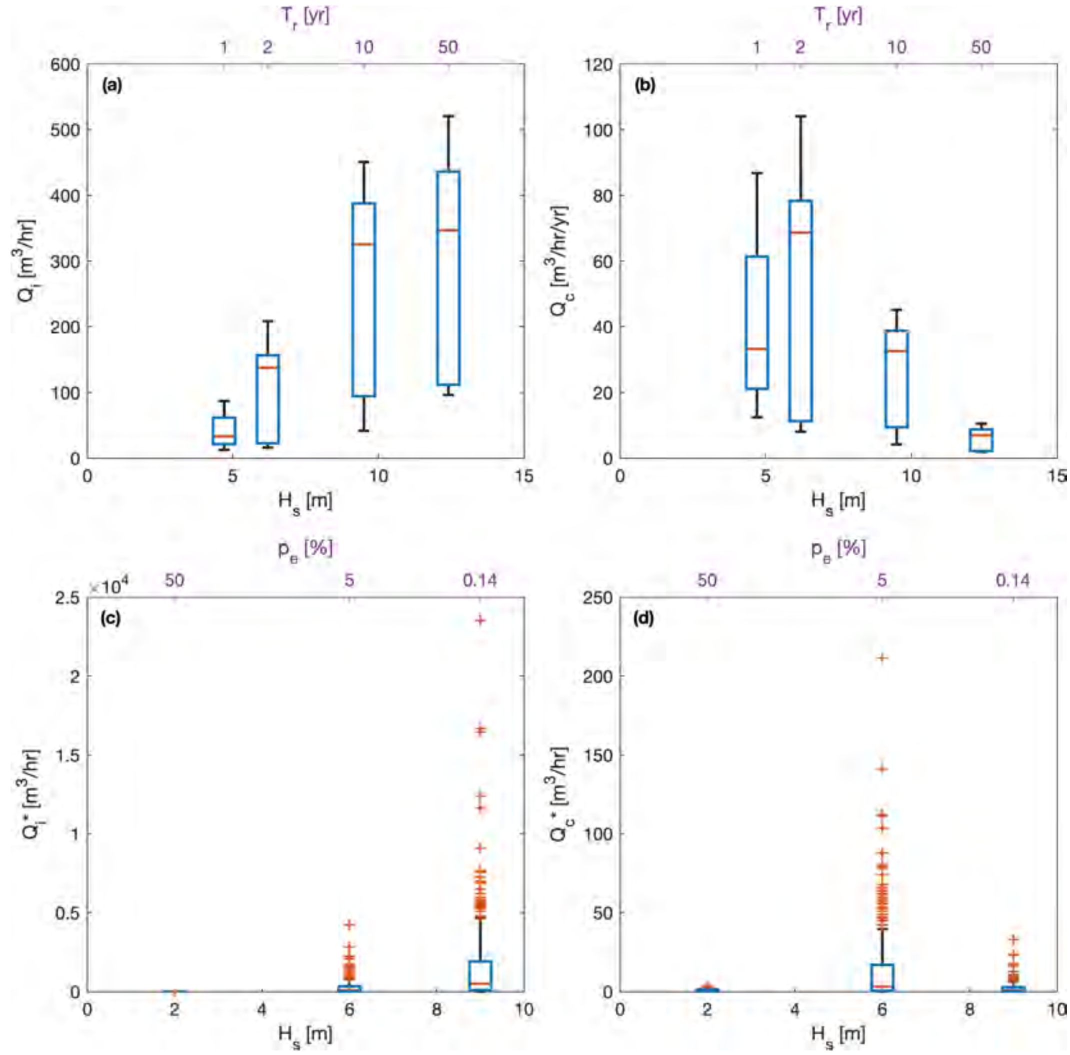

Figure 10. Boxplot of the instantaneous (Q_i, left column) and cumulative (Q_c, right column) headland bypassing rates in Slocums Embayment (top row) and in the study of King et al. (2021) (bottom row). Note that the absolute values of Slocums Embayment and King et al. (2021) cannot be compared one-on-one, due to different definitions of the bypassing rates (sediment deposited in embayment vs. sediment passing through headland transect) and frequency (return period peak value vs. hourly exceedance probability), hence the bypassing rates of King et al. (2021) are denoted by $Q*$.

only and wave+tide). Sediment transport around the headland occurred in 89% of these scenarios, but only 119 scenarios are considered as true headland bypassing cases (headland blocks all sediment transport during regular conditions, bypassing only takes place during large and/or extreme wave conditions). Almost all cases of headland bypassing

(97%) had the highest instantaneous bypassing rates during the highest waves (see Figure 10c). Interestingly, in 78% of those simulations, the large waves contributed more to the cumulative bypassing volumes than the extreme waves (see Figure 10d). This corroborates findings of the current study, that the sediment budget of an embayment enclosed by headlands is driven by frequent, moderate storms rather than rare, extreme events. Understanding the thresholds for headland bypassing, and bypassing rates in relation to their frequency of occurrence, is therefore significant for coastal management.

One of the challenges of studying headland bypassing and sediment dynamics during storms is the lack of field observations during extreme conditions. Previous studies, e.g., Backstrom et al. (2015); Harley et al. (2022); da Silva et al. (2023), used detailed pre- and post-storm bathymetries to investigate headland bypassing. However, detailed topo-bathymetric surveys are often not available. This study proposes an alternative method to validate sediment transport rates. Given that Slocums Embayment is a closed littoral cell most of the time (see Figure 5) and Slocums River has a nearly negligible discharge, we assumed that the sediment accumulating at Slocums River Inlet could be linked to headland bypassing. The modelled average hourly net transport rates are an order of magnitude smaller than the average yearly volume increase of the spit at the inlet of Slocums River, derived from LIDAR images (Figure 4). Given that storm conditions often last 6-12 hours, this results in the same order of magnitude of sediment deposition inside the embayment, $O(10^3\ \mathrm{m}^3)$.

This study assumed constant wave conditions to facilitate comparison between scenarios. In reality the wave height varies over time during a storm. Due to the location of the embayment at the mouth of Buzzards Bay, the filling and emptying of the bay has a large impact on the resulting sediment transport patterns. Based on a database of 100 historical storms (Cialone et al., 2005), peak surge levels usually precede peak wave conditions (see Figure 11). Moreover, the storms with the highest waves (peak wave height > 10 m, the largest 25%) are over-represented in storms with a time lag between 3 and 9 hours between peak water level and peak wave height.

As illustrated by the realistic storm scenario, peak wave conditions following the peak water level may result in higher rates of sediment export from the embayment and consequently lower rates of net sediment deposition. Therefore, the sediment transport rates based on constant wave conditions likely represent the upper limit of expected sediment transport volumes into the embayment during the long term.

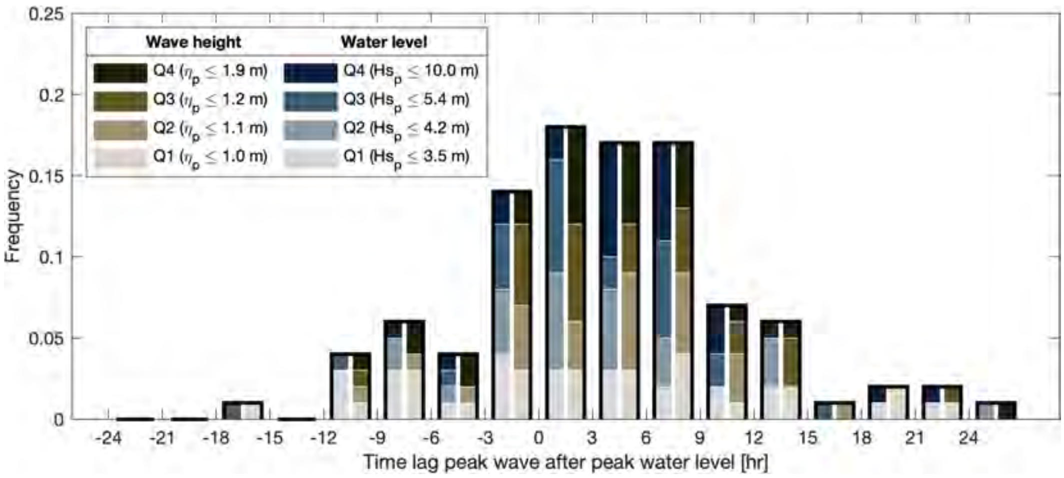

Figure 11. Histogram of the time lag between peak water level and peak wave height for a database of 100 historical storms (Cialone et al., 2005). A positive time lag corresponds to the peak water level preceding the peak wave height. The stacked bars represent the quartile distribution of the wave heights (blue) and water levels (brown) in each histogram bin.

It is generally predicted that climate change will increase storm intensity and frequency (Lin et al., 2012). Moreover, slower moving storm systems could generate higher storm surge levels, and thus, exceedance probability of peak wave conditions could increase. While higher or more frequent extreme wave conditions have the potential to increase sediment deposition inside Slocums Embayment, the relationship with increasing surge levels is not straightforward. On one hand, higher water levels may erode previously inaccessible sand in the dunes between Allens Pond and Barneys Joy Point. On the other hand, higher water levels move the depth of closure line closer to shore, potentially preventing sand from offshore being picked up, and thus reducing the volume of sand available for headland bypassing. This complex response to water level is also confirmed by King et al. (2021), with some headlands experiencing higher bypassing rates around spring high water, whereas bypassing rates were higher around spring low water for other headlands.

5 Conclusion

Slocums Embayment is a sediment sink at the mouth of Buzzards Bay. Based on LIDAR images, the spit near the river inlet is accumulating ca. 2600 m^3 sand per year. A numerical model (Delft3D) was used to analyse the thresholds and pathways of sediment into Slocums Embayment. Under day-to-day conditions, the tidal filling and emptying of Buzzards Bay dominates the current patterns outside of the embayment, and as a result the flow bypasses Slocums Embayment. Model results reveal that only under extreme wave conditions (occurring once per year or less) do the currents curve around Barneys Joy Point producing a sediment transport pathway into the embayment.

The role of wave conditions, tide and surge was investigated through 36 model scenarios (4 wave height, 3 wave direction and 3 water level scenarios). The amount of sediment deposited in the embayment increases with wave height. However, when taking into account the occurrence frequency of the wave conditions, our results indicate that smaller, more frequent moderate wave events (with a return period of one or two years) cumulatively contribute more sediment to the embayment than the most extreme events (return period 10-50 years). Applying our method to bypassing rates of 29 headlands in Cornwall (King et al., 2021) revealed dominance of smaller, more frequent bypassing events in a large majority (78%) of the scenarios. This is crucial information for coastal managers and the prediction of long-term coastal change, as it shifts the focus from the rare, extreme events to the more frequent, moderate events. Understanding the exact thresholds for sediment bypassing, and their associated occurrence probabilities, is key for robust sediment budget calculations.

Headland bypassing studies in other locations have suggested that headland bypassing in microtidal regimes is mostly wave driven (R. McCarroll et al., 2018; Vieira da Silva et al., 2018). However, sediment transport around Barneys Joy Point is heavily influenced by the filling and emptying of Buzzards Bay. Furthermore, a storm surge can significantly increase the amount of sediment entering Slocums Embayment, although the timing between the peak water levels and peak wave conditions can also open a sediment pathway out of the embayment, as illustrated with the realistic storm scenario. This study therefore shows that even in a microtidal regime, headland bypassing is not necessarily wave-driven, and tides and storm surges can influence the net sediment transport.

Open Research Section

The following data was accessed through various public repositories: LIDAR-derived DEMs were downloaded from the NOAA Data Access Viewer (OCM Partners, 2009, 2010, 2013, 2015a, 2015b, 2018); aerial images were accessed through the USGS EarthExplorer (US Geological Survey, 2023b) and Google Earth (Google Earth, 2023); river discharge data is measured at a stream gauge located in Paskamanset River (gauge 01105933, US Geological Survey (2023a)); tides and water levels are retrieved from the NOAA tidal station in Newport, RI (station 8452660, NOAA (2023)); wave and wind data are measured at a NDBC offshore station (station 44085 and BUZM3, NDBC (2023)); the bathymetry is based on the NOAA Continuously Updated DEM (CIRES, 2014); and the sediment texture map of Buzzards Bay was downloaded from the USGS Science Data Catalog (Foster et al., 2016). The NACCS model data used as boundary conditions for the model simulations in this study was downloaded from the Coastal Hazards System (Nadal-Caraballo et al., 2020; Cialone et al., 2005).

Measurement data used for model validation, as well as the Delft3D model input files and Matlab scripts for pre- and post-processing are uploaded to the repository of 4TU.ResearchData and currently undergoing quality control. The editor and reviewers can already access the dataset via the following private link: `https://tinyurl.com/2ttxpncw` after quality control the dataset will be published with the DOI: `doi.org/10.4121/5232674a-4255-465f-bd36-306e9a0a9a97` (Tas et al., 2024). The measurement data includes bathymetry measurements and ADCP wave and current measurements (both collected by WHG as part of this project), grain size distributions of sediment samples, RBR wave data, Nortek AquaDopp water level and current data and HOBO water level data. Delft3D is open-source software developed by Deltares (Lesser et al., 2004).

Acknowledgments

This research is funded by the Buzzards Bay Coalition through a grant from The Rathmann Family Foundation. We would like to thank Sarah Black, Sophia Tigges, Matt Gies, Abbi Sloot, Ellie Bortman, Brooke Tillotson, Simone Fishman, Evie Usich and Rebecca Rudolph for their assistance collecting and analysing field measurements.

References

Amante, C. J., Love, M., Carignan, K., Sutherland, M. G., MacFerrin, M., & Lim, E. (2023, March). Continuously Updated Digital Elevation Models (CUDEMs) to Support Coastal Inundation Modeling. *Remote Sensing*, *15*(6), 1702. doi: 10.3390/rs15061702

Backstrom, J., Jackson, D., Cooper, A., & Loureiro, C. (2015, December). Contrasting geomorphological storm response from two adjacent shorefaces: Earth

Surface Processes and Landforms. *Earth Surface Processes and Landforms*, *40*(15), 2112–2120. doi: 10.1002/esp.3788

bin Ab Razak, M. S. (2015). *Natural headland sand bypassing: Towards identifying and modelling the mechanisms and processes* (Doctoral dissertation, CRC Press Taylor & Francis Group, Boca Raton London New York). Retrieved 2023-02-03, from `http://resolver.tudelft.nl/uuid:4b126111-3f1b-4986-949e-4a174ebf7322`

Booij, N., Ris, R. C., & Holthuijsen, L. H. (1999, April). A third-generation wave model for coastal regions: 1. Model description and validation. *Journal of Geophysical Research: Oceans*, *104*(C4), 7649–7666. doi: 10.1029/98JC02622

Cialone, M. A., Massey, T. C., Anderson, M. E., Grzegorzewski, A. S., Jensen, R. E., Cialone, A., ... Ratcliff, J. J. (2005). *North Atlantic Coast Comprehensive Study (NACCS) Coastal Storm Model Simulations: Waves and Water Levels* (Tech. Rep.). Vicksburg, MS, USA: U.S. Army Engineer Research and Development Center Coastal and Hydraulics Laboratory.

CIRES. (2014). *Continuously Updated Digital Elevation Model (CUDEM) - 1/9 Arc-Second Resolution Bathymetric-Topographic Tiles. Tiles 41.25-41.50N, 71.00-71.25W.* NOAA National Centers for Environmental Information. doi: 10.25921/ds9v-ky35

Cooper, N. J., Barber, P. C., Bray, M. J., & Carter, D. J. (2002, September). Shoreline management plans: A national review and engineering perspective. *Proceedings of the Institution of Civil Engineers - Water and Maritime Engineering*, *154*(3), 221–228. doi: 10.1680/wame.2002.154.3.221

da Silva, A. P., Vieira da Silva, G., Strauss, D., & Tomlinson, R. (2023, April). Storm systems influencing sediment compartment connectivity through headland bypassing. In *Coastal Sediments 2023* (pp. 1713–1725). New Orleans, LA, USA: WORLD SCIENTIFIC. doi: 10.1142/9789811275135_0157

Duarte, J., Taborda, R., Ribeiro, M., Cascalho, J., Silva, A., & Bosnic, I. (2014). Evidences of sediment bypassing at Nazaré headland revealed by a large scale sand tracer experiment. In *Proceedings of 3.as Jornadas de Engenharia Hidrográica.* (pp. 289–292). Lisboa.

FitzGerald, D. M., Baldwin, C. T., Ibrahim, N. A., & Humphries, S. M. (1992). Sedimentologic and morphologic evolution of a beach-ridge barrier along an indented coast: Buzzards Bay, Massachusetts. *Quaternary Coasts of the United States: Marine and Lacustrine Systems*(SEPM Special Publications No. 48), 65–75. Retrieved 2023-02-03, from `https://archives.datapages.com/data/sepm_sp/SP48/Sedimentologic_and_Morphologic_Evolution.htm`

FitzGerald, D. M., Saiz, A., Baldwin, C. T., & Sands, D. M. (1986). Spit Breaching at Slocum River Inlet: Buzzards Bay, Massachusetts. *Shore and Beach*, *54*, 11–17.

Folk, R. L. (1966, March). A review of grain-size parameters. *Sedimentology*, *6*(2), 73–93. doi: 10.1111/j.1365-3091.1966.tb01572.x

Foster, D. S., Baldwin, W. E., Barnhardt, W. A., Schwab, W. C., Ackerman, S. D., Andrews, B. D., & Pendleton, E. A. (2016). *Shallow geology, sea-floor texture, and physiographic zones of Buzzards Bay, Massachusetts* (U.S. Geological Survey Open-File Report No. 2014-1220). U.S. Geological Survey. doi: 10.3133/ofr20141220

George, D., Largier, J., Storlazzi, C., & Barnard, P. (2015, November). Classification of rocky headlands in California with relevance to littoral cell boundary delineation. *Marine Geology*, *369*, 137–152. doi: 10.1016/j.margeo.2015.08.010

George, D. A., Largier, J. L., Pasternack, G. B., Barnard, P. L., Storlazzi, C. D., & Erikson, L. H. (2019, February). Modeling Sediment Bypassing around Idealized Rocky Headlands. *Journal of Marine Science and Engineering*, *7*(2), 40. doi: 10.3390/jmse7020040

Goodwin, I. D., Freeman, R., & Blackmore, K. (2013, July). An insight into headland sand bypassing and wave climate variability from shoreface bathymetric change at Byron Bay, New South Wales, Australia. *Marine Geology*, *341*, 29–45. doi: 10.1016/j.margeo.2013.05.005

Google Earth. (2023). *Satellite images of Slocums Embayment, MA between 1985 and 2022.* Retrieved 2023-02-03, from `https://earth.google.com/web/`

Harley, M. D., Masselink, G., Ruiz De Alegría-Arzaburu, A., Valiente, N. G., & Scott, T. (2022, May). Single extreme storm sequence can offset decades of shoreline retreat projected to result from sea-level rise. *Communications Earth & Environment*, *3*(1), 112. doi: 10.1038/s43247-022-00437-2

Hsu, J. R. C., & Evans, C. (1989, December). Parabolic bay shapes and applications. *Proceedings of the Institution of Civil Engineers*, *87*(4), 557–570. doi: 10

.1680/iicep.1989.3778

King, E. V., Conley, D. C., Masselink, G., Leonardi, N., McCarroll, R. J., Scott, T., & Valiente, N. G. (2021, August). Wave, Tide and Topographical Controls on Headland Sand Bypassing. *Journal of Geophysical Research: Oceans*, *126*(8). doi: 10.1029/2020JC017053

Klein, A. H., Vieira Da Silva, G., Taborda, R., Da Silva, A. P., & Short, A. D. (2020). Headland bypassing and overpassing: Form, processes and applications. In *Sandy Beach Morphodynamics* (pp. 557–591). Elsevier. doi: 10.1016/B978-0-08-102927-5.00023-0

Lesser, G., Roelvink, J., van Kester, J., & Stelling, G. (2004, October). Development and validation of a three-dimensional morphological model. *Coastal Engineering*, *51*(8-9), 883–915. doi: 10.1016/j.coastaleng.2004.07.014

Lin, N., Emanuel, K., Oppenheimer, M., & Vanmarcke, E. (2012, June). Physically based assessment of hurricane surge threat under climate change. *Nature Climate Change*, *2*(6), 462–467. doi: 10.1038/nclimate1389

McCarroll, R., Masselink, G., Valiente, N., Scott, T., King, E., & Conley, D. (2018, August). Wave and Tidal Controls on Embayment Circulation and Headland Bypassing for an Exposed, Macrotidal Site. *Journal of Marine Science and Engineering*, *6*(3), 94. doi: 10.3390/jmse6030094

McCarroll, R., Masselink, G., Wiggins, M., Scott, T., Billson, O., Conley, D., & Valiente, N. (2019, October). High-efficiency gravel longshore sediment transport and headland bypassing over an extreme wave event. *Earth Surface Processes and Landforms*, *44*(13), 2720–2727. doi: 10.1002/esp.4692

McCarroll, R. J., Masselink, G., Valiente, N. G., King, E. V., Scott, T., Stokes, C., & Wiggins, M. (2021, April). An XBeach derived parametric expression for headland bypassing. *Coastal Engineering*, *165*, 103860. doi: 10.1016/j.coastaleng.2021.103860

Moraff, K., & United States Environmental Protection Agency. (2019, October). *Approval of the Slocums and Little Rivers Embayment System TMDL for Total Nitrogen.* Retrieved 2023-12-19, from `https://www.epa.gov/sites/default/files/2019-12/documents/slocums-little-rivers-tmdl-approval-docs.pdf`

Motyka, JM., & Brampton, AH. (1993, January). *Coastal management - mapping of* *littoral cells* (Tech. Rep. No. Report SR 328). HR Wallingford. Retrieved 2023-02-03, from http://eprints.hrwallingford.com/id/eprint/339

Nadal-Caraballo, N. C., Campbell, M. O., Gonzalez, V. M., Torres, M. J., Melby, J. A., & Taflanidis, A. A. (2020, May). Coastal Hazards System: A Probabilistic Coastal Hazard Analysis Framework. *Journal of Coastal Research*, *95*(sp1), 1211. doi: 10.2112/SI95-235.1

NDBC. (2023). *Station 44085 - Buzzards Bay, MA.* Retrieved 2023-02-03, from https://www.ndbc.noaa.gov/station_page.php?station=44085

NOAA. (2023). *Station 8452660 - Newport, RI.* Retrieved 2023-02-03, from https://tidesandcurrents.noaa.gov/stationhome.html?id=8452660

OCM Partners. (2009). *2005 - 2007 US Army Corps of Engineers (USACE) Topo/Bathy Lidar: Maine, Massachusetts, and Rhode Island.* Retrieved 2023-02-03, from https://www.fisheries.noaa.gov/inport/item/50052

OCM Partners. (2010). *2010 USACE NCMP Topobathy Lidar: Northeast Atlantic Coast (CT, MA, ME, NH, RI).* Retrieved 2023-02-03, from https://www.fisheries.noaa.gov/inport/item/50089

OCM Partners. (2013). *2012 USACE Post Sandy Topographic LiDAR: Rhode Island and Massachusetts Coast.* Retrieved 2023-02-03, from https://www.fisheries.noaa.gov/inport/item/49609

OCM Partners. (2015a). *2013-2014 U.S. Geological Survey CMGP LiDAR: Post Sandy (MA, NH, RI).* Retrieved 2023-02-03, from https://www.fisheries.noaa.gov/inport/item/49846

OCM Partners. (2015b). *2015 NOAA NGS Topobathy Lidar DEM: Buzzards Bay Block3 (MA).* Retrieved 2023-02-03, from https://www.fisheries.noaa.gov/inport/item/48378

OCM Partners. (2018). *2018 USACE NCMP Topobathy Lidar DEM: East Coast (CT, MA, ME, NC, NH, RI, SC).* Retrieved 2023-02-03, from https://www.fisheries.noaa.gov/inport/item/55882

Ribeiro, M., Taborda, R., Rodrigues, A., & Silveira, T. (2014). Insights on sediment bypassing at headland-bay beaches: An example at the Portuguese west coast. In *3as Jornadas de Engenharia Hidrográfica.* Lisbon, Portugal.

Short, A. D., & Masselink, G. (1999). Embayed and Structurally Controlled Beaches. In *Handbook of beach and shoreface morphodynamics* (pp. 230–249).

New York, USA: John Wiley.

Smith, A. W. (2001). Headland bypassing. In *Coasts & Ports 2001: Proceedings of the 15th Australasian Coastal and Ocean Engineering Conference* (pp. 214–216). Australia: Institution of Engineers, Australia. Retrieved 2023-02-03, from `https://search.informit.org/doi/10.3316/informit.928362880525926`

Tas, S., Hughes, Z., FitzGerald, D., Xie, D., Asik, T. Z., & Fagherazzi, S. (2024). *Data and model files presented in "Headland bypassing: Moderate storms dominate extreme events".* doi: 10.4121/5232674a-4255-465f-bd36-306e9a0a9a97

US Geological Survey. (1984). *Geographic Names Information System. Paskamanset and Slocums River.* doi: 10.3133/70039514

US Geological Survey. (2023a). *Paskamanset River Near South Dartmouth, MA - 01105933.* Water Data for the Nation. doi: 10.5066/F7P55KJN

US Geological Survey. (2023b). *USGS EarthExplorer.* Retrieved 2023-02-03, from `https://earthexplorer.usgs.gov`

Valiente, N. G., Masselink, G., Scott, T., Conley, D., & McCarroll, R. J. (2019, January). Role of waves and tides on depth of closure and potential for headland bypassing. *Marine Geology*, *407*, 60–75. doi: 10.1016/j.margeo.2018.10.009

van Rijn, L. (2010). *Coastal erosion control based on the concept of sediment cells* (Consience Project Final Report). Retrieved 2023-02-03, from `https://www.leovanrijn-sediment.com/papers/Coastalerosion2012.pdf`

Vieira da Silva, G., Toldo, E. E., Klein, A. H. D. F., Short, A. D., & Woodroffe, C. D. (2016, September). Headland sand bypassing — Quantification of net sediment transport in embayed beaches, Santa Catarina Island North Shore, Southern Brazil. *Marine Geology*, *379*, 13–27. doi: 10.1016/j.margeo.2016.05.008

Vieira da Silva, G., Toldo Jr., E. E., Klein, A. H. D. F., & Short, A. D. (2018, July). The influence of wave-, wind- and tide-forced currents on headland sand bypassing – Study case: Santa Catarina Island north shore, Brazil. *Geomorphology*, *312*, 1–11. doi: 10.1016/j.geomorph.2018.03.026

Willmott, C. J. (1981, July). On the validation of models. *Physical Geography*, *2*(2), 184–194. doi: 10.1080/02723646.1981.10642213

Wishaw, D., Leon, J., Fairweather, H., & Crampton, A. (2021, June). Influence of wave direction sequencing and regional climate drivers on sediment headland bypassing. *Geomorphology*, *383*, 107708. doi: 10.1016/j.geomorph.2021.107708

Woodroffe, C. D., Carvalho, R. C., Oliver, T. S. N., & Thom, B. G. (2022, June). Sediment dynamics at different timescales on an embayed coast in southeastern Australia. *Journal of Coastal Conservation*, *26*(3), 21. doi: 10.1007/s11852-022-00867-2

Xie, D., Hughes, Z., FitzGerald, D., Tas, S., Asik, T. Z., & Fagherazzi, S. (2024, February). Impacts of Climate Change on Coastal Hydrodynamics Around a Headland and Potential Headland Sediment Bypassing. *Geophysical Research Letters*, *51*(4), e2023GL105323. doi: 10.1029/2023GL105323

Supporting Information for "Headland bypassing: Moderate storms dominate extreme events"

Silke Tas[1,2], Zoe Hughes[1], Duncan FitzGerald[1], Danghan Xie[1], Tansir Zaman Asik[1], Sergio Fagherazzi[1]

[1]Department of Earth and Environment, Boston University, Boston, MA, USA

[2]Hydrology and Environmental Hydraulics, Wageningen University and Research, Wageningen, The Netherlands

Contents of this file

Introduction This Supporting Information includes five sections. Text S1 contains the validation of the Continuously Updated DEM bathymetry with point bathymetry measurements collected in 2022, illustrated in Figure S1. Text S2 explains how the sediment distribution map, used in the Delft3D model, was validated in two ways: by comparing it to sediment samples collected in 2022 and 2023 (Figure S2) and by a bathymetry smoothness analysis based on King et al. (2021) (Figure S3). In Text S3 the modelled hydrodynamics are validated using wave, current and water level measurements collected in 2022 (Figure S4). Text S4 provides further detail on the calculation of the volume change of the spit at Slocums River Inlet, including a correction for different Geoid models (Table

S1 and Figure S5). Lastly, Text S5 presents the analysis of the headland bypassing rates of King et al. (2021), first instantaneous bypassing rates as function of wave height (Figure S6) and then the cumulative bypassing rates (Figure S7). All data used for validation is shared in a public repository, see Open Research Section (Tas et al., 2024).

Text S1. Bathymetry validation

The model bathymetry is based on the Continuously Updated Digital Elevation Model (CUDEM, (Amante et al., 2023; CIRES, 2014)). Supplementary Figure S1 shows a comparison of this CUDEM bathymetry with point measurements collected by Woods Hole Group (WHG) in September 2022.In general, the difference between the CUDEM and the observations is relatively small ($< 5\%$ of the water depth). The largest discrepancies are found in the most dynamic regions around the inlets of Westport and Slocums River, and the channel inside Westport River.

Text S2. Sediment distribution validation

The sediment distribution in the Delft3D model is based on a sediment texture map of Buzzards Bay by (Foster et al., 2016), which is based on seismic-reflection profiles, high-resolution bathymetry, acoustic-backscatter intensity, bottom photographs, and surficial sediment samples. In the model, the sediment texture map was simplified to a binary distribution of sand vs. bedrock (see Figure 3). The resulting sediment distribution map is validated in two ways: (1) sediment samples collected in 2022 and 2023, and (2) a smoothness analysis of the bathymetry based on (King et al., 2021).

At 200 locations offshore, nearshore, in and around the river inlets and on the beach sediment samples were collected between July 2022 and July 2023 (see Figure S2a). The samples were collected by Ponar Grab Sampler in subaqueous settings and manually on the beach. Some locations did not contain enough fine-grained material to sample (e.g. bedrock, cobbles or coarse pebbles). These locations are indicated by the red dots in FigureS2b-f. They were still included in the study as they provide relevant information about sand availability. Where the beach was poorly sorted, the collected sediment sample was only representative of the fine-grained component (medium to fine pebbles and sand), while the coarse component was visually described. Finally, the grain size distribution of each sample was determined using a RO-TAP sieve shaker with a mesh size ranging from $\phi = 4.0$ to $\phi = -4.0$. Following (Folk, 1966), these parameters were calculated for each sample: median and mean grain size, sorting (a measure of the grain size variation), skewness (a measure of the symmetry of the grain size distribution curve), and kurtosis (a measure of the peakedness of the grain size distribution curve), see Figure S2b-f. The sediment in this area is very heterogeneous, ranging from bedrock and cobbles around the headlands to very fine sand in the inlets. Generally, the median grain size agreed well with the sediment classification in the USGS sediment texture map by (Foster et al., 2016). The sediment in Slocums Embayment, Allens Pond nearshore and Allens Beach is mostly fine to medium sand, which supports the model D50 of 350 μm.(King et al., 2021) developed an alternative method to determine sand coverage from high-resolution bathymetry, which we used to further validate the USGS sediment texture map in our area of interest. It assumes that areas of loose sediment (i.e. sand) are smoother than rock. First, the original bathymetry (Figure S3a) is resampled to 10x10 m resolution for computational efficiency (Figure S3b). Next, a smoothed surface is generated by applying a 100x100 m median filter (Figure S3c). Then, a difference plot is generated between the original (resampled) bathymetry and the smoothed bathymetry (Figure S3d). The standard deviation of this difference plot is calculated (Figure S3e) and finally the maximum standard deviation over 100x100 m windows is determined (Figure S3f). Areas with a high maximum standard deviation are rougher, and therefore likely to be bedrock/gravel, while lower maximum standard deviation corresponds to smooth, sandy patches. Figure

S3f includes an overlay of the outlines of the different sediment zones of (Foster et al., 2016), which aligns very well with the rougher patches identified by the higher maximum standard deviation.

Text S3. Model validation

The comparison between modelled and observed values was quantified by using the skill score as proposed by (Willmott, 1981), see Supplementary Equation 1:

$$skill = 1 - \frac{\sum |X_{model} - X_{obs}|^2}{\sum \left(\left|X_{model} - \overline{X_{obs}}\right| + \left|X_{obs} - \overline{X_{obs}}\right|\right)^2} \tag{1}$$

Where X_{model} is the modelled value, X_{obs} the observed value and $\overline{X_{obs}}$ the average observed value over the entire time range of the validation.

Text S4. LIDAR sediment volume estimates

The volume change of the spit at Slocums River inlet was calculated based on LIDAR DEMs between 2005 and 2018. A LIDAR DEM is vertically referenced relative to a geoid, which is a surface of equal gravitational attraction and is roughly equal to mean sea level. The National Geodetic Survey regularly updates the geoid model, as a result, the LIDAR DEMs collected between 2005 and 2018 are referenced to 4 different geoid models (see Table S1, second column). Therefore, the LIDAR DEMs must first be corrected to the same vertical reference level. Assuming the elevation of Fthe parking lot of Demarest LLoyd State Park near Slocums River inlet (visible in the bottom left corner of Figure 1c-f) has not changed over time, this could be used as a reference elevation in each LIDAR DEM. The average elevation of the parking lot is calculated (see Supplementary Figure S5a-f and third column in Table S1). Geoid12B is used as reference, so the LIDAR DEMs of 2005, 2010, 2012 and 2013 are vertically corrected with the difference in elevation of the parking lot. The resulting LIDAR DEMs are shown in Supplementary Figure S5g-l, together with the -0.4 m contour line, which was used as base level for the volume calculations.

Text S5. Analysis bypassing rates King et al. (2021)

(King et al., 2021) developed and validated a coupled hydrodynamic, wave and sediment transport model (Delft3D) to calculate headland bypassing rates for 29 headlands under variable wave, tide and sediment conditions along 75 km of the macrotidal, embayed north coast of Cornwall. They conducted a wide range of scenarios by varying the following parameters:

- Wave height and period: A joint probability distribution of the significant wave height and peak wave period was fitted through 3 year wave data. Three conditions were selected: median waves (50% exceedance probability, $H_s = 2$ m, $T_p = 10.5$ s), large waves (5% exceedance probability, $H_s = 6$ m, $T_p = 15$ s) and extreme waves (0.14% exceedance probability, representing the 12-hour exceedance, $H_s = 9$ m, $T_p = 18.9$ s).

- Wave direction: The three most common wave direction bins at the offshore wave buoy were selected: 270°, 281.25°and 292.5°.

- Wave-only, tide-only and coupled wave-tide scenarios. The wave-only scenarios were conducted for two water levels corresponding to spring high water and spring low water level. Tidal scenarios were conducted over a spring-neap cycle and times where water levels were at spring high water or spring low water level were extracted for analysis.

- A uniform, homogeneous sand bed and a spatially variable sand coverage

For the current analysis, only the scenarios with waves and a spatially varying sand coverage are considered, which results in 12 scenarios per wave height (3 wave directions, 2 water levels, with/without tides), and multiplied by 29 headlands gives 348 total scenarios.

S5.1 Instantaneous bypassing rates

(King et al., 2021) determined the instantaneous bypassing rates by integrating the alongshore sediment transport component from the headland apex to the maximum depth. Additionally, two shore-normal transects were defined at the apex, defined by the shoreline orientation of the embayment on either side of the headland. The instantaneous bypassing rate was set to zero if the bypassing rates at the two shore-normal transects were divergent, or if the sand transport rate was lower than the range of validation (0.00016 m^3/m/tidal cycle). The resulting bypassing rates are given in Supplementary Figure S6, the 29 headlands are sorted based on magnitude of the maximum bypassing rate. Note that the bypassing rate is defined as positive up-coast (generally toward the northeast), due to the varying orientation of the coast, certain headlands experience negative bypassing rates (i.e. transport in down-coast direction).Sediment transport around the headland occurred in 89% of these scenarios, but only 119 scenarios are considered as true headland bypassing cases (headland blocks all sediment transport during regular conditions, bypassing only takes place during large and/or extreme wave conditions). Supplementary Figure S6 shows that in almost all cases of headland bypassing (116/119, or 97%), the highest instantaneous bypassing rates occurred during the highest waves. This is in line with most other headland bypassing studies, where headland bypassing is related to extreme events.

S5.2 Cumulative bypassing rates

For Slocums Embayment, the bypassing volumes were combined with the associated return period of the storm event to determine the cumulative effect of bypassing events on the sediment budget of the embayment, see Equation 2. The cumulative effect of the bypassing rates in (King et al., 2021) can be calculated in a similar fashion with the following equation:

$$Q_c = Q_i * p_e \tag{2}$$

where Q_c is the cumulative bypassing rate [m^3/hr], Q_i is the instantaneous bypassing rate [m^3/hr] (see Supplementary Figure S6), and p_e is the exceedance probability of the wave height. The resulting cumulative bypassing rates for each headland are given in Supplementary Figure S7.Out of the 116 scenarios where the highest instantaneous bypassing occurred during the highest waves, 90 scenarios (78%) have the highest cumulative bypassing during the large waves (rather than the extreme waves). This shows that the majority of the headland bypassing scenarios is in line with the behaviour observed in Slocums Embayment, where the sediment budget is mostly driven by moderate, more frequent events.

References

Amante, C. J., Love, M., Carignan, K., Sutherland, M. G., MacFerrin, M., & Lim, E. (2023, March). Continuously Updated Digital Elevation Models (CUDEMs) to Support Coastal Inundation Modeling. *Remote Sensing*, *15*(6), 1702. doi: 10.3390/rs15061702

CIRES. (2014). *Continuously Updated Digital Elevation Model (CUDEM) - 1/9*

Arc-Second Resolution Bathymetric-Topographic Tiles. Tiles 41.25-41.50N, 71.00-71.25W. NOAA National Centers for Environmental Information. doi: 10.25921/ds9v-ky35

Folk, R. L. (1966, March). A review of grain-size parameters. *Sedimentology*, *6*(2), 73–93. doi: 10.1111/j.1365-3091.1966.tb01572.x

Foster, D. S., Baldwin, W. E., Barnhardt, W. A., Schwab, W. C., Ackerman, S. D., Andrews, B. D., & Pendleton, E. A. (2016). *Shallow geology, sea-floor texture, and physiographic zones of Buzzards Bay, Massachusetts* (U.S. Geological Survey Open-File Report No. 2014-1220). U.S. Geological Survey. doi: 10.3133/ofr20141220

King, E. V., Conley, D. C., Masselink, G., Leonardi, N., McCarroll, R. J., Scott, T., & Valiente, N. G. (2021, August). Wave, Tide and Topographical Controls on Headland Sand Bypassing. *Journal of Geophysical Research: Oceans*, *126*(8). doi: 10.1029/2020JC017053

Tas, S., Hughes, Z., FitzGerald, D., Xie, D., Asik, T. Z., & Fagherazzi, S. (2024). *Data and model files presented in "Headland bypassing: Moderate storms dominate extreme events".* doi: 10.4121/5232674a-4255-465f-bd36-306e9a0a9a97

Willmott, C. J. (1981, July). On the validation of models. *Physical Geography*, *2*(2), 184–194. doi: 10.1080/02723646.1981.10642213

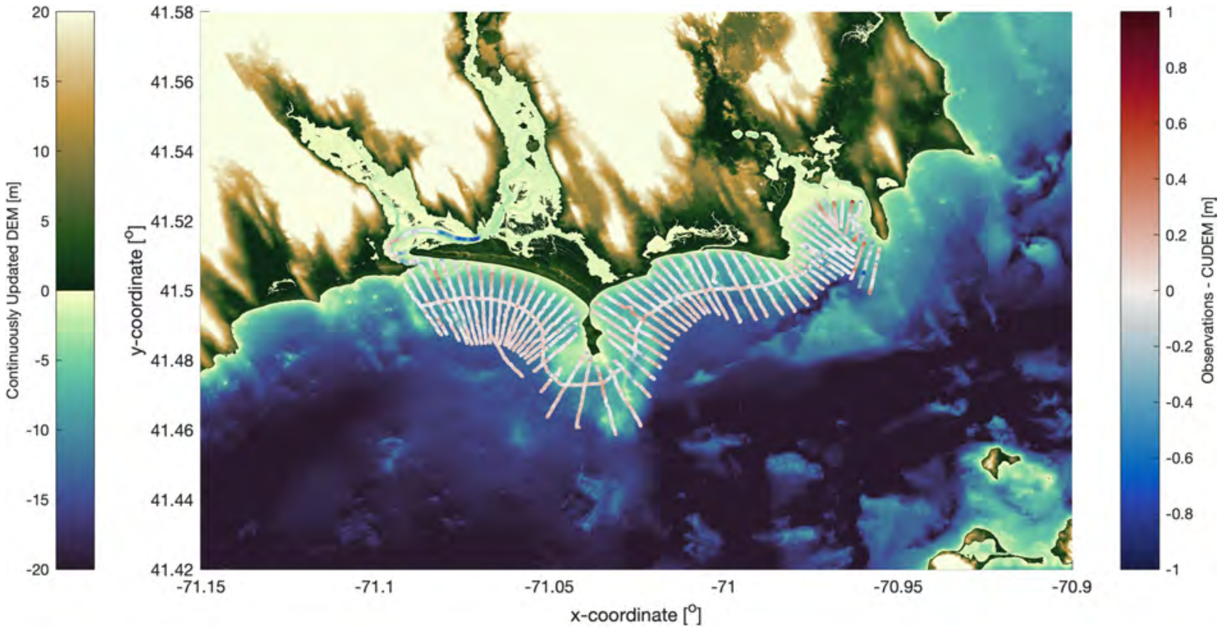

Figure S1. Continuously Updated DEM (left colormap) with overlay of comparison DEM with point measurements collected by WHG in 2022 (right colormap).

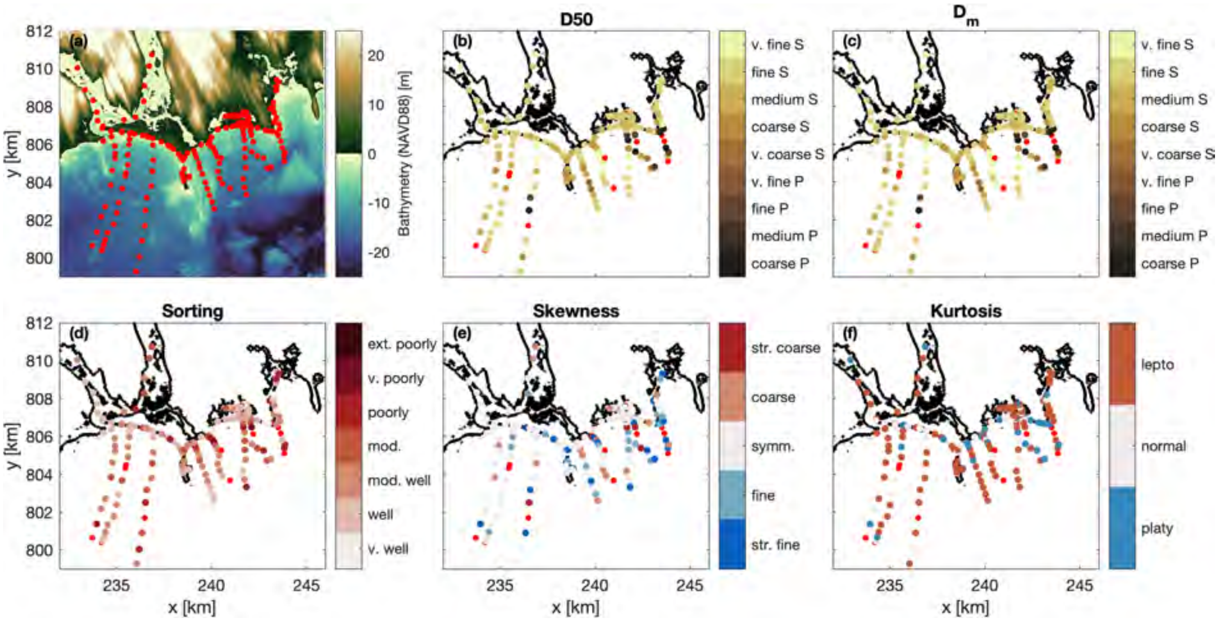

Figure S2. **(a)** 200 sediment sampling locations around the project area and their properties: **(b)** median grain size diameter, **(c)** mean grain size diameter, **(d)** sorting, **(e)** skewness, and **(f)** kurtosis.

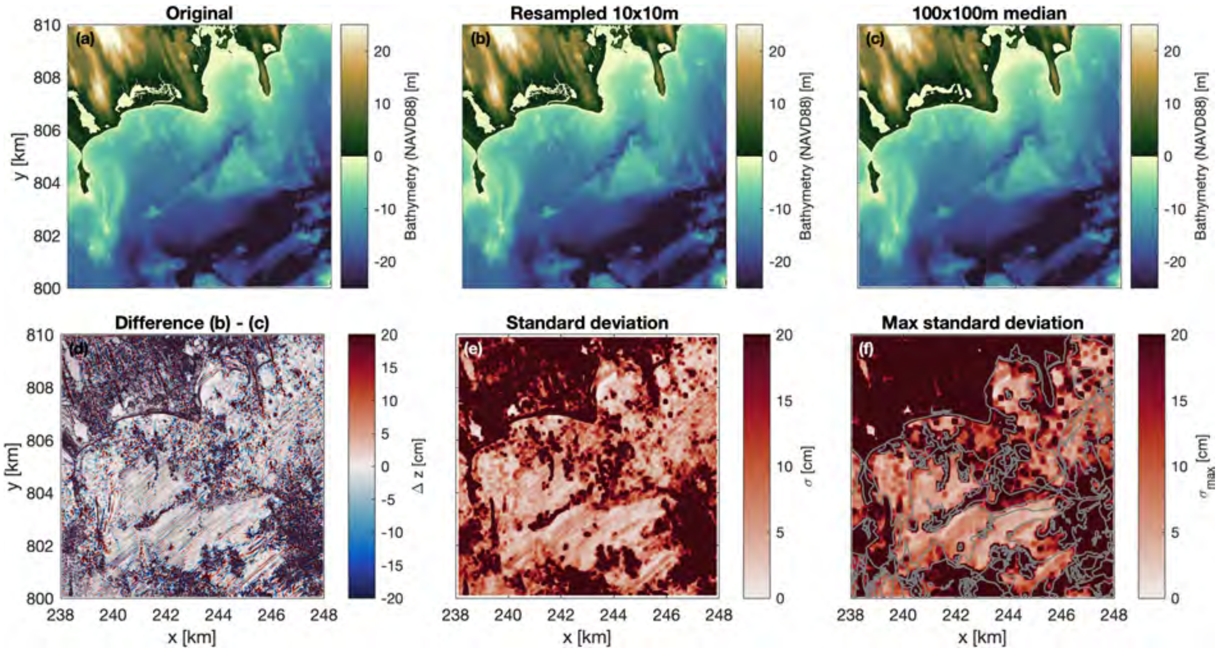

Figure S3. Method to determine sand coverage, following (King et al., 2021): **(a)** original high-resolution bathymetry, **(b)** 10x10 m resampled bathymetry, **(c)** 100x100 m smoothed bathymetry, **(d)** difference between the resampled and smoothed bathymetry (panel b minus panel c), **(e)** standard deviation of the difference between resampled and smoothed bathymetry, and **(f)** maximum standard deviation over 100x100 m window (colormap) and outlines of different sediment zones from (Foster et al., 2016) (grey lines).

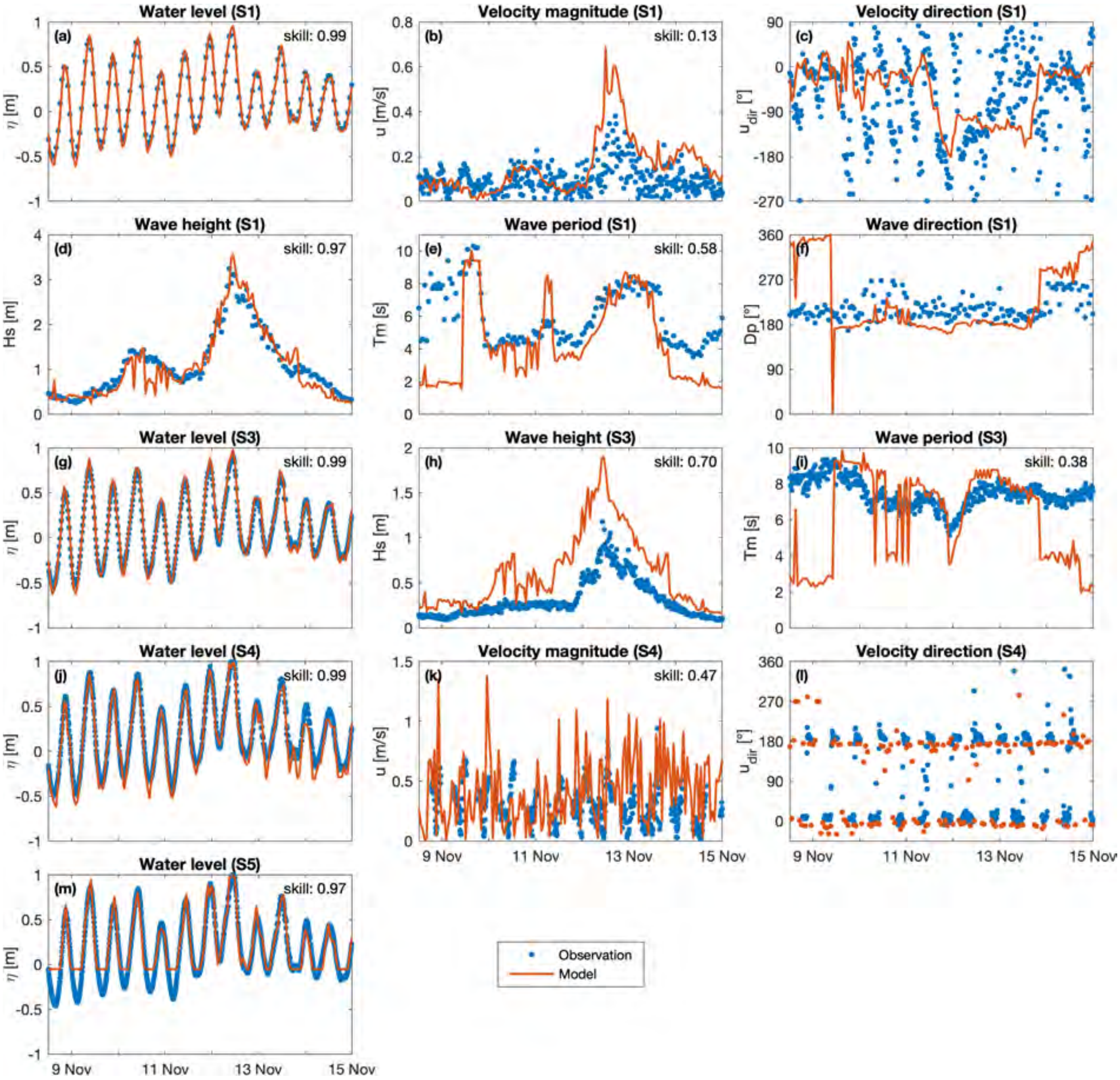

Figure S4. Comparison of measured (blue) and simulated (orange) parameters at different locations: S1 **(a-f)**, S3 **(g-i)**, S4 **(j-l)** and S5 **(m)**. See Figure 2 for the locations of the measurement stations. Skill scores are calculated using Equation 1 based on (Willmott, 1981).

LIDAR year	Geoid model	Average parking lot elevation [m above NAVD88]
2005	Geoid03	1.76
2010	Geoid09	1.62
2012	Geoid12A	1.53
2013	Geoid12A	1.59
2015	Geoid12B	1.77
2018	Geoid12B	1.76

Table S1. Geoid model and the average elevation of the parking lot in each LIDAR DEM.

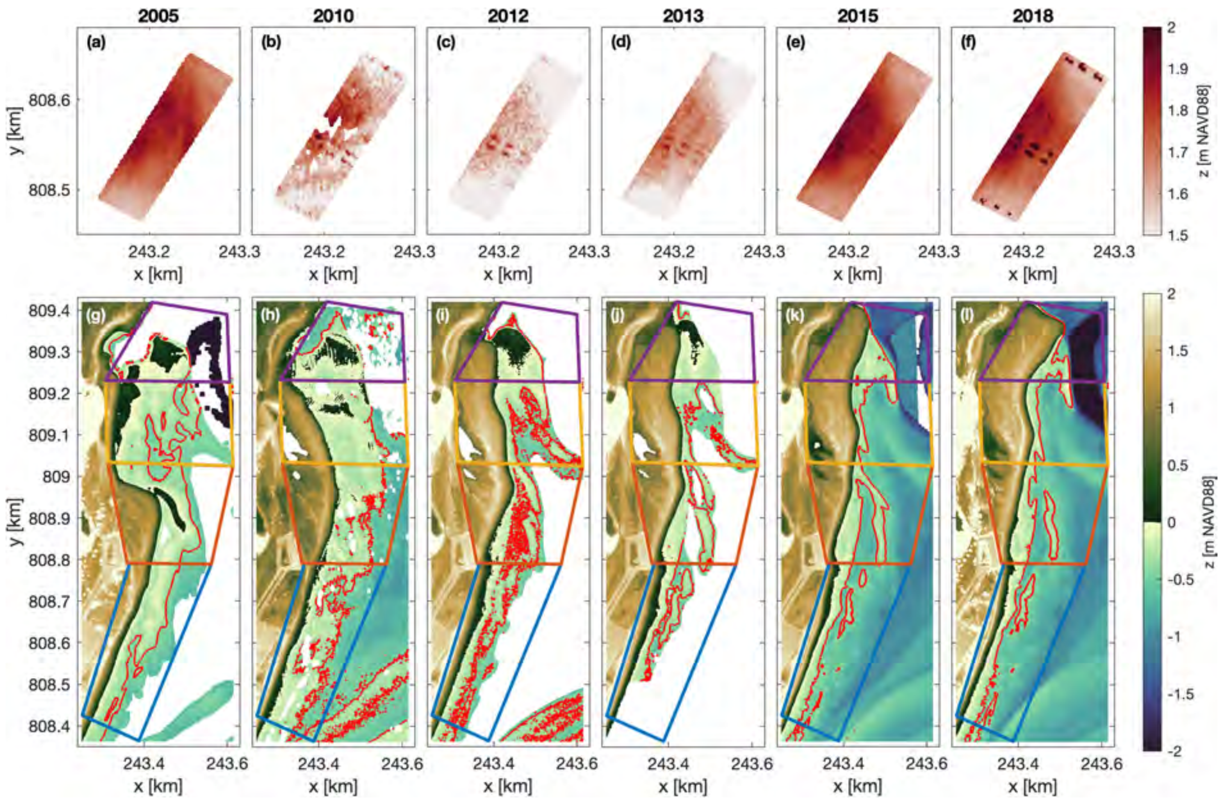

Figure S5. **(a-f)** Parking lot elevation before geoid correction. **(g-l)** LIDAR DEM after geoid correction, with the -0.4 m contour line used as base level for the volume calculations.

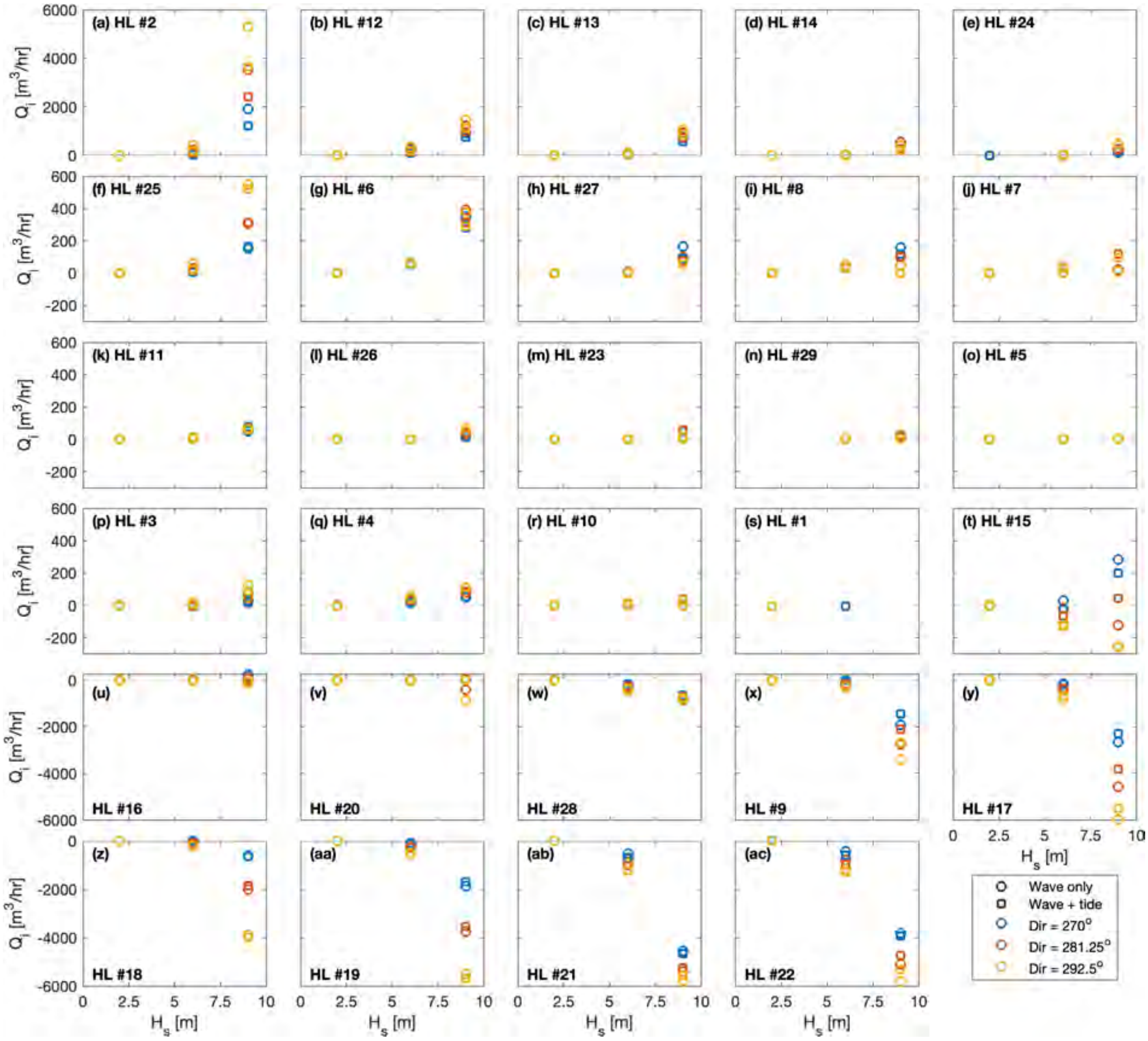

Figure S6. Instantaneous bypassing rates as a function of wave height at 29 headlands for different wave directions (colours) and with and without tide (square vs. round markers respectively). Headlands are sorted based on maximum bypassing rate, to allow for scaling of the vertical axis per row.

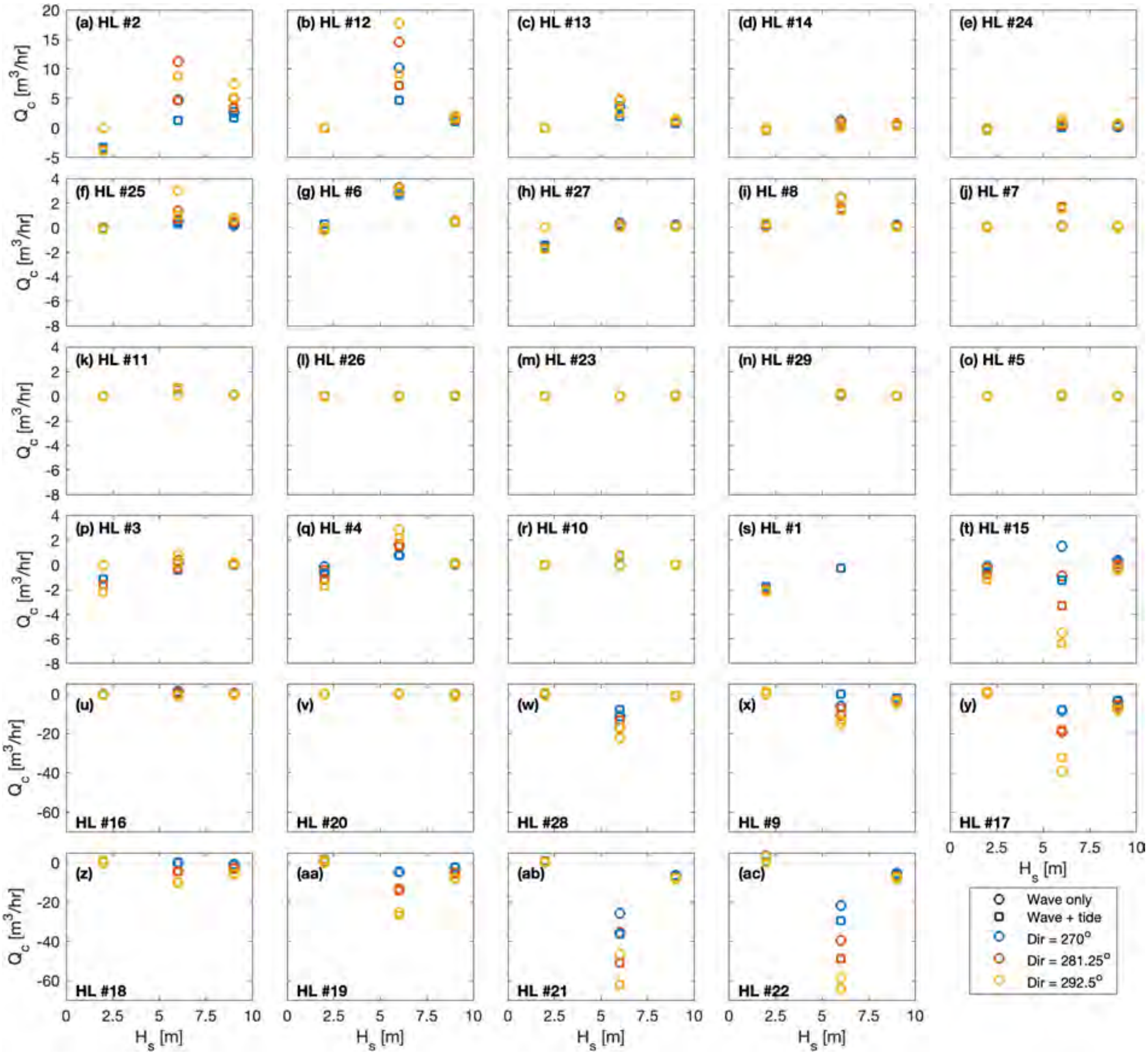

Figure S7. Cumulative bypassing rates as a function of wave height at 29 headlands for different wave directions (colours) and with and without tide (square vs. round markers, respectively). Headlands are sorted based on maximum bypassing rate, to allow for scaling of the vertical axis per row.